ISBN 0-315-95982-7

Canada

UNIVERSITÉ D'OTTAWA
UNIVERSITY OF OTTAWA

ACKNOWLEDGEMENT

This thesis work has been conducted under the guidance of Professor H. Teitelbaum since its very beginning. I would like to express my most sincere gratitude to my supervisor Professor Teitelbaum for his invaluable advice, constant inspiration and support throughout the course of this work.

Acknowledgement is made to my fellow colleagues Zhikai Cheng and Delmar Permann for their assistance and friendship, and to the departmental support staff.

I am also grateful to the University of Ottawa, the Natural Sciences and Engineering Research Council of Canada, and Canadian taxpayers for their financial aid under which I was able to undertake this study.

With gratitude, I wish to thank my brothers and sisters, who have been supportive of my education.

Special thanks to my darling wife, Xiaoling, for her comfort, patience and understanding. Thanks also to my daughter, Wei, and my parents-in-law. They have been accompanying me over a difficult time.

This thesis is dedicated to the memory of my beloved parents, who inspired me to pursue excellence.

ABSTRACT

Shock tube experiments were conducted to observe the primary reactions of methyl radicals. 0.7% -7% azomethane diluted in argon or nitrogen was used as a precursor for methyl radicals. The rate of disappearance of CH_3 radicals was measured behind incident shock waves in real time using a high resolution laser schlieren technique. The measurements covered the temperature range 1400-4000 K and the pressure range 0.1-1.1 atm. Selected experimental results were analyzed by an analytic point-by-point approach, which led to a self-consistent determination of the rate coefficient for methyl recombination, supported by the theory of unimolecular reactions. All of the experiments were then analyzed by computer simulation to evaluate the rate coefficients for the primary reactions of CH_3. The rate coefficient for $2CH_3 \rightarrow C_2H_4 + H_2$, which was basically unknown at high temperatures, was obtained by comparing experimental laser-schlieren signals with those from numerical integration of a postulated mechanism of 44 reactions coupled to the conservation equations of mass, energy, and momentum. The important reactions in the mechanism were identified by a sensitivity analysis.

Experiments were also conducted at lower temperatures of 560-1300 K. Chemical chaos and oscillation were observed in the pyrolysis of azomethane at 900-1300 K for the first time.

The fall-off effect in the decomposition of azomethane was studied theoretically on the basis of the modern theory of unimolecular reactions. The results of our calculation are in agreement with published experimental work. More exact calculations need to be done

above 2000 K.

Rate constants are calculated for CH_3 (+ Ar) = CH_2 + H (+ Ar) at the limiting low pressure, the limiting high pressure, as well as the intermediate fall-off ranges. The results show that published experimental rate constants for methyl dissociation correspond to the fall-off region close to the low pressure limit. At the low pressure limit the activation energy is less than the bond dissociation energy, in agreement with experimental results. Forward and backward rate coefficients at the high pressure limit are compared with other theoretical calculations. More theoretical and experimental work is necessary to understand the reverse reaction and its competing reactions, as well as the decomposition channel leading to CH + H_2.

CONTENTS

LIST OF FIGURES

LIST OF TABLES

CHAPTER 1

INTRODUCTION

1.1 PRACTICAL AND THEORETICAL SIGNIFICANCE

CH_3 radicals are prevalent during the combustion and pyrolysis of most hydrocarbons. CH_3 is also the most stable and important alkyl radical in the high temperature oxidation and decomposition reactions of alkanes. The reactions of CH_3 are therefore of fundamental interest for the mechanistic description of complicated combustion processes. Methyl-methyl reactions are important in flame propagation because of the high methyl concentration. Warnatz has shown that "hydrocarbon fuel is attacked by H, O, and OH in the first steps" in a fully developed flame front.[1] "The alkyl radicals formed in this way decompose rapidly to smaller alkyl radicals and alkenes. Only for the smallest alkyl radicals, such as CH_3 and C_2H_5, does the relatively slow thermal decomposition compete with recombination and with oxidation reactions involving O atoms and O_2".[2] According to Warnatz, the combustion mechanism of C_n-hydrocarbons ($n \geq 3$) can be roughly reduced to the question of "how fast CH_3 and C_2H_5 are formed" in the decomposition of these C_n-alkyl radicals, and "this part of the mechanism is rate-controlling" in the combustion of alkane and alkene.[2] In other words, methane- and ethane-air flames are the two representative cases of hydrocarbon combustion. Figure 1.1 shows a flow diagram for the oxidation of methane in methane-air flames.[2] Once

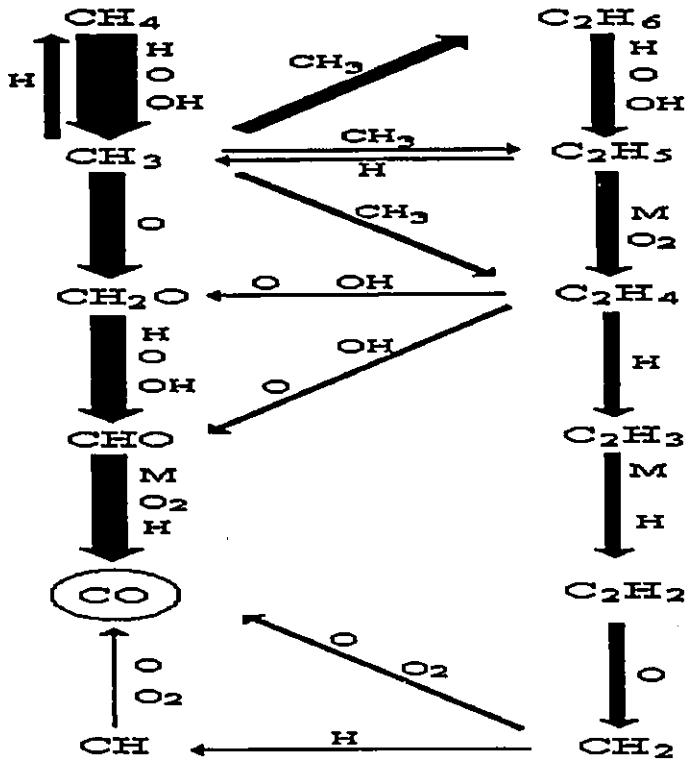

Figure 1.1 Flow diagram for the oxidation of CH_4 in methane-air flames at P = 1 bar, and T < 2000 K. (Adapted from reference 2. The thickness of the arrows is proportional to the net reaction rates.)

CH_3 and / or C_2H_5 are formed, the main reactions lead the way to CO formation. At the same time, methyl-methyl reactions, which are the central topic of this thesis, compete with the oxidation processes. The difference between CH_4 and C_2H_6 is that the ethane-air flame propagates faster than the methane-air flame since C_2H_5 is more reactive than CH_3.[1]

The recombination of methyl radicals and its reverse process, the decomposition of ethane, have long attracted the attention of both experimentalists and theoreticians. The recombination is a major termination process in the pyrolysis and oxidation of hydrocarbons. It serves as the reference reaction for measurements of other reactions of methyl radicals, and it also has been used as a model for testing and improving statistical theories of unimolecular reaction.

Recently, the chemical vapour deposition (CVD) technique has made it possible to synthesize diamond films by combustion of hydrocarbon.[3-5] Unlike the conventional method in which diamond is synthesized at extremely high pressures and high temperatures, flame synthesis of diamond films can be easily conducted in an open atmosphere. Murayama et al.[6] demonstrated the synthesis of a highly uniform film of polycrystalline diamond by a flat flame. Computational simulation[7] of diamond chemical vapour deposition is necessary to study the effects of various parameters (such as burner-to-substrate distance, flow rate, and fuel stoichiometry etc.) on diamond growth and to scale the system to larger areas. According to Miller and Melius's combustion mechanism and Coltrin and Dandy's surface chemistry mechanism, CH_3 plays the dominant role in depositing carbon.[7] Large fluxes of CH_3 and H at the surface are predicted. Gas phase methyl radical reactions will affect diamond growth rate.

In summary, the reactions of CH_3 at high temperatures are important for many aspects of pyrolysis and combustion.

1.2 LITERATURE REVIEW AND THE PROBLEMS TO BE SOLVED

1.2.1 Precursor of Methyl Radical

The reactions of methyl radicals are very fast, occurring in less than 1 millisecond. Special techniques have to be employed to generate CH_3 homogeneously on a very short time scale. This can be achieved by the flash photolysis or high-temperature pyrolysis of precursors, such as azomethane (CH_3NNCH_3), acetone (CH_3COCH_3), dimethylmercury ($Hg(CH_3)_2$), tetramethyltin ($Sn(CH_3)_4$), and methyliodide (CH_3I). These are usually diluted by inert gases. Among them, azomethane is the most frequently used precursor in the studies of methyl radical reactions.

Troe's research group has extensively used the fast thermal decomposition of azomethane at temperatures above 1300 K and flash photolysis at room temperature to investigate methyl recombination.[8-10] Back et al also applied the thermal decomposition and the photolysis of azomethane to study methyl reactions.[11-12] Pilling's group studied methyl recombination over the temperature range 296-577 K using laser flash photolysis of azomethane as a source,[13] while Wagner's group[14-17] and Frank's group[18-19] as well as Gutman, Lin et al[20] investigated high temperature reactions of CH_3 generated by the thermal decomposition of azomethane. All thermal pyrolysis studies confirm that an azomethane

molecule decomposes into two methyl radicals at temperatures higher than 1300 K; the decomposition occurs so fast that it excludes the methyl-azomethane bimolecular reaction.[8]

The rate coefficient for azomethane decomposition is available[8,15-16,21-23] over the range 500 -2200 K. Since our experiments went far beyond 2200 K, it is necessary to investigate the decomposition of azomethane up to 4000 K. The decomposition is a unimolecular reaction. Thus the rate coefficient should exhibit complicated temperature and pressure dependence. However, no one has studied the full fall-off behaviour of the decomposition of azomethane. In chapter 2, the fall-off behaviour will be addressed on the basis of the modern theory of unimolecular reactions.

The pyrolysis of azomethane below 1300 K is slow and generally recognized as occurring by a chain mechanism, though the chain is short. For the sake of investigating methyl radical reactions, low- temperature pyrolysis is not recommended. Nevertheless, for completeness it is worthwhile seeing what would happen at those lower temperatures. It turns out as an unexpected gain: We observed chemical chaos and oscillation in the pyrolysis of azomethane at 900-1300 K for the first time. Further details will be given in chapter 3.

1.2.2 Thermal Decomposition of Methyl Radical

The methyl radical is ubiquitous during the pyrolysis and combustion of hydrocarbons. However, unlike other alkyl radicals it resists thermal decomposition. Its unimolecular reactions,

$$CH_3 \xrightarrow{M} CH + H_2 \quad (1)$$

$$\xrightarrow{M} CH_2 + H \quad (2)$$

are simply too slow to compete against bimolecular reactions with itself or with oxygen-

$$2\,CH_3 \rightarrow C_2H_5 + H \quad (3)$$

$$\rightarrow C_2H_4 + H_2 \quad (4)$$

$$\xrightarrow{M} C_2H_6 \quad (5)$$

$$\rightarrow CH_4 + CH_2 \quad (6)$$

containing species such as O, O_2 and OH. It is only at elevated temperatures > 2700 K [24] that methyl decomposition need be considered among the elementary reactions needed to model the pyrolysis[25] and combustion[26-27] of CH_4 as well as the chemical vapour deposition of diamond.[28-29]

Recently, there have been two experimental[26,30] and one theoretical[31] study of the two competing channels of methyl decomposition. However, substantial disagreement exists regarding which channel has a higher energy barrier.

The rate constants for reaction (2) have been measured at the low pressure limit by means of atomic resonance absorption spectroscopy over the temperature range 1700 -2850 K.[2,32-34] It is, however, important to have further confirmation of these measurements and to extend them to higher temperatures and pressures. We have performed experiments designed to evaluate the rates of channels (3) to (6), using laser-schlieren detection of methyl reactions behind shock waves. It turns out that reactions (3-4) become important at the same high temperatures where thermal decomposition of CH_3 could compete. A proper analysis of the experiments requires a good knowledge of the rates of reaction (1-2) up to 4000 K. In

addition, Merkel and Zulicke have calculated the rate constant for reaction (2) at the high pressure limit using statistical adiabatic channel theory.[35] Their results do not agree with a recent ab initio calculation of the high-pressure limiting rate constant for the reverse of reaction (2) by Wagner and coworkers using variational transition state theory.[36] The latter found a positive activation energy in contrast to Merkel *et al.*'s and the experimental negative activation energy.[37-41] As the experiments correspond to the low-pressure limit, it seems that this controversy can be addressed only by carrying out a full calculation of the fall-off curves over a wide range of temperatures.

The theoretical study in chapter 2 is designed to evaluate the above questions. We proceed using the methods developed by Troe.[42-45]

1.2.3 Methyl-Methyl Reactions

1.2.3.1 $CH_3 + CH_3 \rightarrow C_2H_6$

Methyl radical recombination has been widely studied for many years. A comprehensive review of the experimental results prior to 1980 for the recombination and its reverse is given by Baulch and Duxbury.[46] Most experimental measurements there refer to room temperature and pressures below or close to 1 atm. They propose a temperature-independent value of 2.4×10^{13} cm^3 $mole^{-1}$ s^{-1} over the temperature range 250 - 420 K for the high pressure limit. Hippler et al felt that an experimental study at pressures above 1 atm would help to establish the high pressure limiting value,[9] and they performed the experiments

at room temperature in the bath gases Ar and N_2, over the pressure range 1-200 atm to study high-pressure effects in $CH_3 + CH_3 \rightarrow C_2H_6$. This leads to a limiting rate constant of $k_{rec,\infty}$ = (3.5 ± 0.36)×10^{13} cm^3 $mole^{-1}$ s^{-1}. There have been some experimental studies of CH_3 recombination in the fall-off region. (Knowledge of the fall-off behaviour of this reaction was derived largely from prior knowledge of ethane decomposition). Slagle et al[47] and Macpherson et al[13] investigated the recombination as a function both of temperature (296-906 K) and of pressure (0.5-600 torr), which provided a more quantitative and detailed picture of the kinetics of this important reaction over a wide range of experimental conditions. There have been only a few experimental studies of methyl recombination reaction at high temperatures.[8,14] Using UV absorption near 216 nm, Glanzer, Quack, and Troe measured the methyl recombination rate constant behind shock waves in the temperature and pressure ranges of 1200-1500 K and 0.2-25 atm,[8] while Hwang, Wagner, and Wolff did the experiment at 1200-1600 K and 10-240 atm.[14] Even at the highest pressures, the reaction was in the fall-off region. The high pressure limiting rate constants were obtained by extrapolation. Hwang et al suggested a negative temperature dependence. In contrast to extensive work on the pressure and temperature dependence of this reaction at low temperature (T < 1000 K) "data are still scarce" at higher temperatures and "reliable extrapolations to the limiting rate constant are difficult to make" above 1000 K.[32]

Methyl radical recombination has also received considerable theoretical attention. Troe has developed a systematic theory of unimolecular reactions[42-45] based on solutions of the master equation,[42] on the statistical adiabatic channel model (SACM),[48] and on RRKM theory. The statistical adiabatic channel calculations predict a nearly temperature-independent

high-pressure-limiting rate constant, $k_{rec,\infty}$, for $CH_3+CH_3 \rightarrow C_2H_6$.[43,48] The low-pressure-limiting rate coefficient and fall-off curves are analyzed on the basis of full master equation models and RRKM models. Furthermore, Troe has transformed the complicated theory into a relatively simple formalism in factorized form, which is very easy for experimentalists to use. The simplified factorization approach has been applied successfully, in practice, to many reactions. Wardlaw and Marcus developed a flexible transition state theory (FTST) which recognizes the interactions between the transitional modes.[49] Wagner and Wardlaw[50] applied the FTST model to analyze the experimental results of Slagle et al.[47] and Macpherson et al.,[13] and then fit their results over the full temperature and pressure range to Troe's factorial form. They predicted a decrease in $k_{rec,\infty}$ by a factor of 3.6 over the temperature range 300 - 2000 K. Although their result is supported by two other experimental studies,[14,51] Troe has questioned their conclusion on the basis of a SACM calculation.[43] We are in favour of Troe's temperature-independent $k_{rec,\infty}$ because Troe and coworkers[9] established the high pressure limiting value by direct measurement at the high pressure limit, and SACM modelling helps to expand the temperature range. Other studies[14,50-51] are all in the fall-off range. The high-pressure limiting rate constants are obtained by extrapolating low pressure data, and the uncertainty is, no doubt, associated with the extrapolation. The theoretical results still need to be tested experimentally, especially at temperatures above 1000 K.

Figure 1.2, taken from the National Institute of Standards and Technology (NIST) Chemical Kinetics Database,[52] outlines the previous experimental and theoretical studies of methyl recombination. The variation is very large. The apparent scatter is partially due to the pressure variations. However, even under similar pressure conditions, some discrepancies

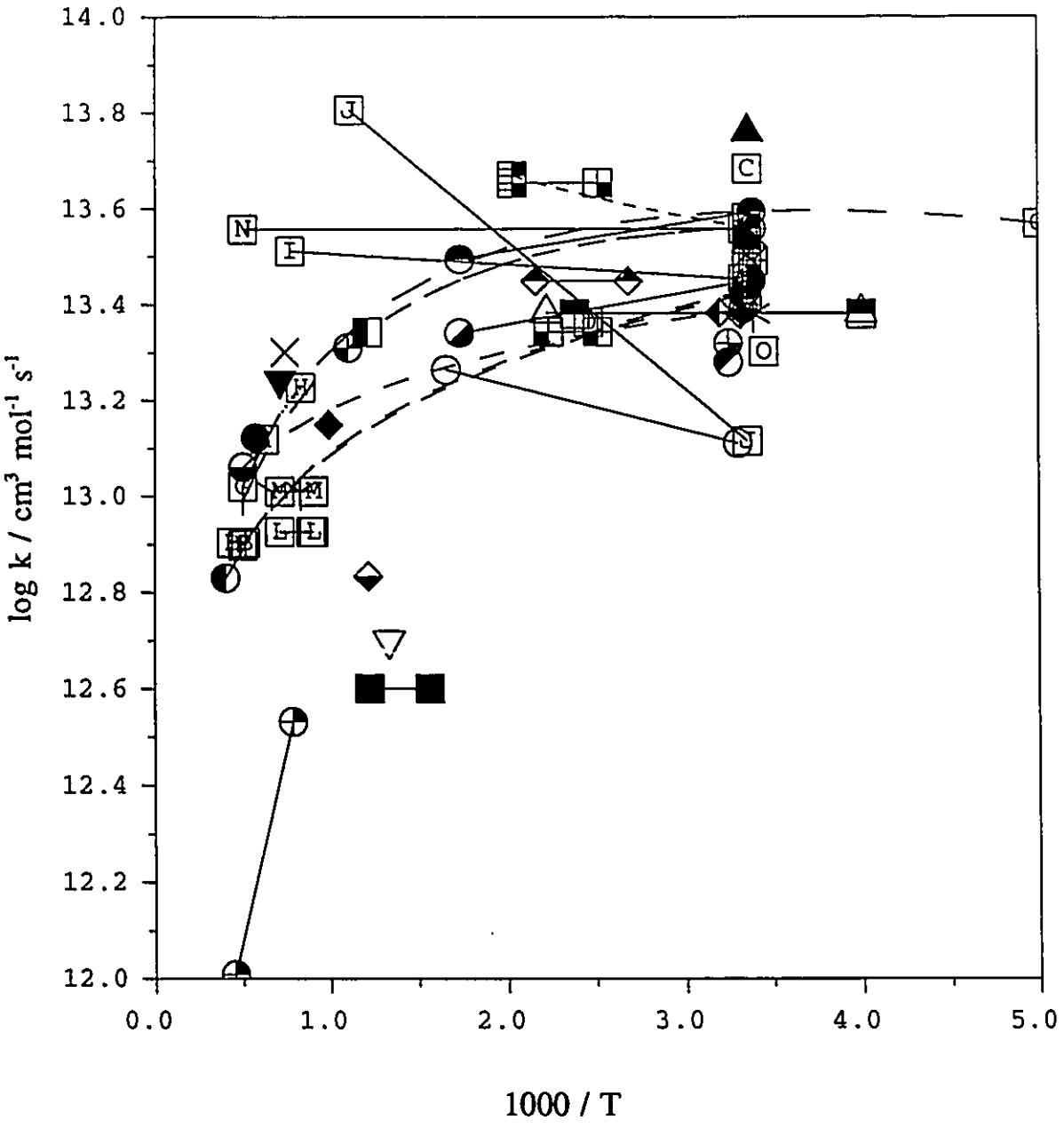

Figure 1.2 NIST Arrhenius plot of the rate coefficients for $CH_3 + CH_3 \rightarrow C_2H_6$.

(From reference 52. References therein: ◒ 2; ▾ ᛉ 8; ⬓ 9; ⊞ 10; ◓ ◒ 13; H 14; ⊕ 15; B 19; L M 21; N 32; ⬓ 46; ⊕ 47; + 50; G 51; □ 64; I 87; ◐ 109; O 145; ▲ 146; × 147; ♦ 148; ∇ ■ 149; ● 150; ◧ 151; ◒ 152; ♦ 153; ♦ 154; ⊕ 155; ⊞ 156; ⊞ 157; C 158; J 159; O 160; etc.)

are still present. There is an obvious gap concerning the high-temperature data. Only a few of the experimental studies were done at combustion temperatures. The uncertainties still leaves room for further study.

1.2.3.2 $CH_3 + CH_3 \rightarrow C_2H_5 + H$

At low temperatures, the reaction rate for $CH_3 + CH_3 \rightarrow C_2H_5 + H$ is small because this channel is endothermic. As a result the reaction proceeds via the C_2H_6 channel. As temperature increases, it becomes a concerted reaction. "At temperatures around 2000 K and at normal pressures, the C_2H_6 channel is well into the fall-off regime while the rate coefficient for formation of C_2H_5 + H has increased significantly and now makes an important contribution".[53]

There have been several studies of this reaction under high-temperature shock tube conditions.[18,54-57] Figure 1.3 shows previous experimental work, theoretical studies, as well as some authoritative evaluations. Atomic resonance absorption spectroscopy of H as well as laser schlieren detection were used to determine rate coefficients for $CH_3 + CH_3 \rightarrow C_2H_5$ + H. It was shown that hydrogen atoms were formed in the first step.[18,55] Because of the pressure dependence of methyl radical recombination, the formation of C_2H_5 + H should occur preferably at low pressure and high temperature. The rate constant from the recent, more direct measurement of Frank et al[18] is recommended over the temperature range 1300-2500 K by the updated compilation,[32] though it is not uniquely determined at T>1900 K. The computer simulation in chapter 5 will test this recommendation at very high temperatures.

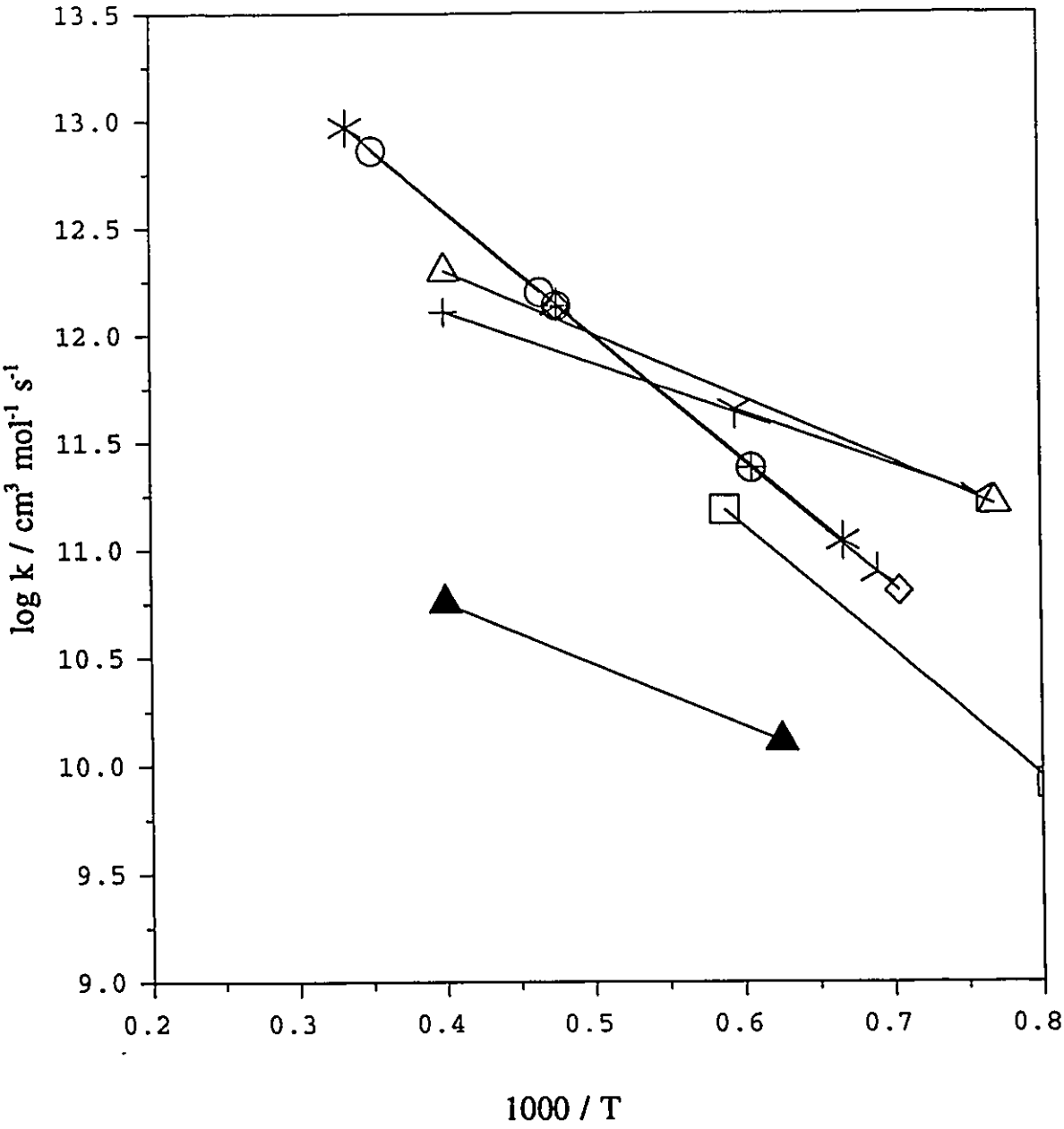

Figure 1.3 NIST Arrhenius plot of the rate coefficients for $CH_3 + CH_3 \rightarrow C_2H_5 + H$.

(From reference 52. References therein: ✱ 2; △ 32; ○ 34; ▲ 54; ⊕ 55; □ 57; + 111; etc.)

1.2.3.3 $CH_3 + CH_3 \rightarrow C_2H_4 + H_2$

Reactions of CH_3 at high temperatures are fairly complex. The formation of $C_2H_4 + H_2$ is another reaction channel for $CH_3 + CH_3$ at high temperatures where the C_2H_6 channel approaches the low pressure limit. These two channels are the only exothermic reactions for $CH_3 + CH_3$. Thermodynamics also indicates the formation of $C_2H_4 + H_2$ to be the preferable exothermic channel at high temperatures ($T > 2000$ K).

Figure 1.4 displays the experimental results from several sources. Gardiner et al[56] made the first study of $CH_3 + CH_3 \rightarrow C_2H_4 + H_2$. This was then followed with a more detailed study made by Tsuboi,[58] where he derived the sum of the rate constants for the $C_2H_5 + H$ channel and the $C_2H_4 + H_2$ channel. This accounted for the reaction products of $CH_3 + CH_3$ besides the recombination to ethane. Warnatz in his evaluation[2] recommended Roth and Just's results where the rate constant was obtained by fitting atomic resonance absorption of H atoms to a reaction mechanism in an ethane pyrolysis study.[55] Kern et al[59] gave a similar result recently, while in other studies using UV spectroscopy, Just[60] as well as Frank[19] reported a rate coefficient with a smaller activation energy. Those experimental results mentioned above, shown in the upper part of Figure 1.4, gave fairly consistent results with respect to magnitude. However, these "large" rates were not compatible with Kiefer and Budach's observations in the high temperature pyrolysis of ethane,[54] and they suggested more than an order of magnitude reduction. (They also proposed a smaller rate coefficient for $CH_3 + CH_3 \rightarrow C_2H_5 + H$). Kiefer and Budach's argument was supported by Hidaka et al's

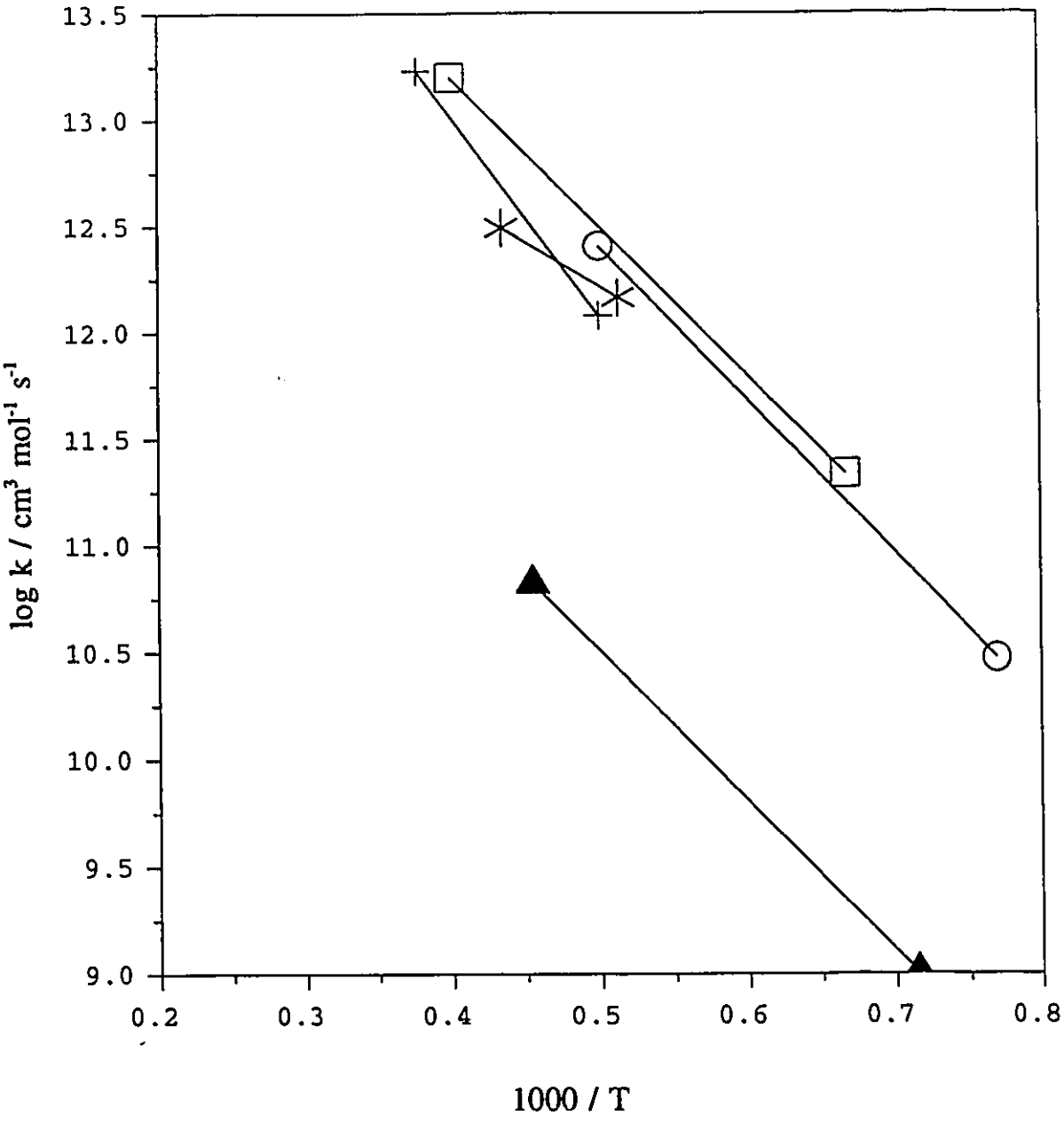

Figure 1.4 NIST Arrhenius plot of the rate coefficients for $CH_3 + CH_3 \rightarrow C_2H_4 + H_2$.

(From reference 52. References therein: □ 2; ✳ 19; + 56; ○ 59; ▲ 61; etc.)

simulation of the high temperature pyrolysis of methane[61] (shown in the lower part of Figure 1.4). The latter obtained a result 100 times smaller than that of Kern et al.[59] The controversy is worth further investigation.

Compared to that for the C_2H_6 and C_2H_5 channels, the rate coefficient for ethylene and hydrogen molecule formation is not well known. No data has been available above 2600 K. Since the rate coefficient data are still scarce, no final conclusion has yet been reached on this matter. This present study provides another set of experimental results for $CH_3 + CH_3 \rightarrow C_2H_4 + H_2$, and it is at least a step further towards the final settlement.

1.2.3.4 $CH_3 + CH_3 \rightarrow CH_4 + CH_2$

The only available data for this reaction is from Frank and Braun-Unkhoff's work,[18-19] where atomic resonance absorption spectroscopy was chosen to monitor the thermal decay of azomethane, methyliodide and ethane. At temperatures above 1900 K, their H-profiles are sensitive to this disproportionation reaction. However, there has been no reliable measurement where singlet and triplet states of CH_2 are identified. This creates uncertainties in the determination of other channels of $CH_3 + CH_3$ at high temperatures.

1.2.4 Experimental Techniques

Methyl radical reactions have been widely studied over a number of years primarily by the technique of flash photolysis at T < 1000 K and by shock tube pyrolysis at higher

temperatures, coupled with kinetic absorption spectroscopy.

The kinetics of chemical reactions taking place at high temperature can be studied conveniently by means of a shock tube, which was first used by Vieille in 1899 and is now a widespread experimental technique for investigating fast chemical reactions. A shock wave can change the physical state of matter drastically on a very short time scale. A gas sample may be heated from room temperature to 10^4 K, and pressures up to 10^3 atm can be reached within one nanosecond. These conditions may be held for a few milliseconds. During this time period chemical reactions can be monitored by kinetic measurements.

Many means are available to follow the progress of the chemical reactions of methyl radicals. Various approaches have been tried. Time-resolved absorption spectroscopy, sometimes combined with gas chromatography of the end products, has been used for measuring rate coefficients for methyl radical reactions over a wide range of conditions. The most frequently used analytical method is UV absorption of the methyl radical at 216.5 *nm*.[8-10,13-17,47,51,58,60,62-63] The next frequently used technique is mass spectrometry.[51,56,64]

The last few years have seen an increasing use of more sensitive analytical techniques. One such technique is atomic resonance absorption spectroscopy (ARAS),[18-19,26,33-34,60] which is able to detect very low concentrations of only a few ppm of H or C atoms generated by the reactions of highly dilute CH_3. The advantages offered by such low concentrations are the minimization of effects of secondary and tertiary reactions and a considerably simplified interpretation of the chemical kinetics of the investigated system.[18,26,60]

Photo-ionization mass spectrometry (PIMS)[47] is another sensitive technique suitable for the measurement of radicals at low concentration (low pressure). The gas-phase species

effuse into the ion optics of a mass spectrometer where they are ionized by the focussed output of a pulsed laser.

The role of lasers in studying chemical kinetics in shock tubes, as fully addressed by Hanson,[75] has also grown rapidly in the last few years.[26,30,65-66] Laser absorption spectroscopic methods are also able to detect very low radical concentrations with high resolution. The combination of shock heating of a reacting gas mixture with sensitive techniques for species detection offers great advantages for the study of elementary reactions at elevated temperatures. This has been demonstrated by Dean and Hanson in their recent study[26] of hydrocarbon pyrolysis, where they shock heated highly dilute mixtures (6 to 100 ppm) of ethane or methane in argon, and monitored the CH time history using narrow-linewidth laser absorption at 431 nm and the C-atom time history using ARAS.

Another successful technique, which is especially useful for reactions occurring on the submicrosecond time scale, is the laser schlieren method[67-71] with excellent time resolution and thermal sensitivities. It can monitor the time profiles of refractive index gradients and has been applied to the pyrolysis of hydrocarbons, such as C_3H_6,[68] C_2H_6,[54,65] C_2H_4,[72-73] and CH_4.[31,74]

Lasers have also been used to photolyze azomethane or acetone at 193 nm as sources of methyl radicals[9-10,13,47,51,62-63] at low temperatures (T<1000 K), and "are now also employed as photolysis sources to trigger specific radical-radical and radical-molecule reactions in shock-heated gases".[75] Since laser photolysis may produce atomic and radical reactants both directly and instantaneously, it may control reaction pathways without going through complex mechanisms, and it promotes more direct and quantitative measurements of specific reaction

rates.[75] Modern lasers provide powerful and promising techniques for the studies of chemical kinetics, and one should see their application increasing. Some day we may reach the stage when chemical reactions are fully controlled and monitored by lasers.

Despite the fact that elementary reactions of CH_3 have been studied for more than 40 years, there is a surprising amount of uncertainty and even controversy regarding the magnitude of the rate constants involving CH_3, especially at high temperatures.[2]

1.3 APPROACHES ADOPTED

The present study applies the shock tube method to heat mixtures of azomethane dilute in argon or nitrogen. The pyrolysis of azomethane provides a clean source of methyl radicals above 1300 K, and the disappearance of methyl is monitored by the laser schlieren technique. Consequently, we are able to observe the primary reactions of CH_3. They leave a distinctive signature characteristic of exothermic reactions, permitting unambiguous identification of the reactions.

With the sensitive laser schlieren technique, experiments can be conducted at lower temperatures with weaker shock waves. The low-end temperature reached 560 K in the present work, allowing us to discover a temperature regime where the pyrolysis of azomethane becomes chaotic and oscillatory.

Since no one has investigated the fall-off behaviour for the decomposition of azomethane (despite frequent use as a methyl precursor), the present author estimated the fall-

off effect under the experimental conditions using the theory of unimolecular reactions developed by Troe.[42-45] Fall-off behaviour for the decomposition of methyl was also studied theoretically by the same approach.

The majority of kinetic data deduced from the present shock tube experiments was obtained by comparing observable time profiles with profiles calculated by numerical simulation of a postulated mechanism. We shall discuss our computer simulation using a 44-step mechanism described in Chapter 5. Under some conditions, kinetic data can be obtained analytically, and such a point-by-point analysis will be given in Chapter 4.

CHAPTER 2

UNIMOLECULAR REACTIONS

In the mechanism used for the computer simulation, several reactions (or their reverses) belong to the class of unimolecular reactions. For some of the unimolecular reactions, the temperature and pressure dependence of the rate constants is well known. However, there have been no studies of the fall-off effects for the decomposition of azomethane itself or for the decomposition of methyl radicals. A proper analysis of the experiments requires a good knowledge of the decomposition rates of azomethane and methyl. This will be addressed in this chapter.

2.1 THEORY OF THERMAL UNIMOLECULAR REACTIONS

Unimolecular dissociation and the reverse recombination in the gas phase exhibit a complicated dependence on temperature, pressure, and bath gas. "Their kinetic behaviour is governed by the complex competition of unimolecular chemical changes in molecular structure with bimolecular physical collisional energization and deenergization processes".[45]

The reactions have the pattern

$$AB\ (+\ M) \rightleftharpoons A + B\ (+\ M)$$

Their forward reactions are usually called dissociations, and reverse reactions called

recombinations. AB, A, and B stand for the reacting radicals, molecules or atoms, and M represents inert collision partners which act as collisional energizers and deenergizers. Isolated dissociation reactions are described by a pseudo-first order rate law

$$k_{diss}=-\frac{1}{[AB]}\frac{d[AB]}{dt} \qquad (2.1)$$

Isolated recombination reactions are expressed by a pseudo-second order rate law

$$k_{rec}=+\frac{1}{[A]\,[B]}\frac{d[AB]}{dt} \qquad (2.2)$$

Both k_{diss} and k_{rec} are [M]-dependent. Under identical conditions, i.e., the same temperature, pressure, and diluents, the rate coefficients, k_{diss} and k_{rec}, are related to each other by the equilibrium constant, K_c

$$k_{diss}/k_{rec}=K_c \qquad (2.3)$$

A dissociation reaction consists of three steps:[45,76] collisional activation (1), collisional deactivation (-1), and fragmentation (2)

$$AB + M \rightarrow AB^* + M \qquad (1)$$

$$AB^* + M \rightarrow AB + M \qquad (-1)$$

$$AB^* \rightarrow A + B \qquad (2)$$

where AB* are excited molecules. The reverse reaction, recombination, consists of an association (-2), redissociation (2) and collisional deactivation (-1)

$$A + B \rightarrow AB^* \qquad (-2)$$

$$AB^* \rightarrow A + B \qquad (2)$$

$$AB^* + M \rightarrow AB + M \qquad (-1)$$

The limiting rate coefficients follow the relationships

$$k_{0,diss}[M] = \lim_{[M]\to 0} k_{diss} = k_1[M] \tag{2.4}$$

$$k_{0,rec}[M] = \lim_{[M]\to 0} k_{rec} = \frac{k_{-2}}{k_2} k_{-1}[M] \tag{2.5}$$

$$k_{\infty,diss} = \lim_{[M]\to \infty} k_{diss} = \frac{k_1}{k_{-1}} k_2 \tag{2.6}$$

$$k_{\infty,rec} = \lim_{[M]\to \infty} k_{rec} = k_{-2} \tag{2.7}$$

At low pressures, the dissociation rate is determined by the rate of collisional activation (1), $k_1[M]$, due to the rare chance of collision. At high pressures, the collisional activation and deactivation are so frequent that an equilibrium ratio, k_1/k_{-1} , of AB and AB* is established and that the unimolecular fragmentation (2) of AB* becomes the rate determining step. In recombination at low pressures, frequent association and redissociation of AB* establish an equilibrium between A, B, and AB*, as described by the ratio k_{-2}/k_2. Collisional stabilization (-1) of AB* is then the rate determining step. At high pressures, excited molecules AB* are stabilized by collision as soon as they are formed, and therefore the recombination rate is determined by the association step (-2).

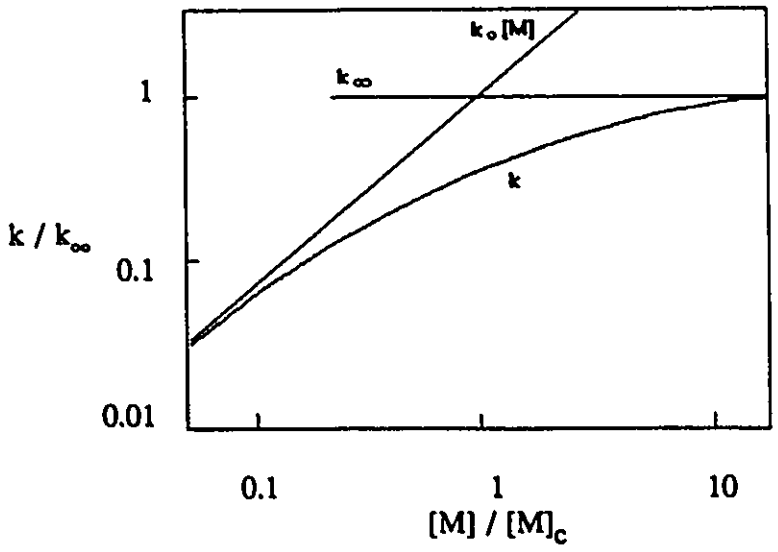

Figure 2.1 Fall-off curve of a thermal unimolecular dissociation or recombination reaction. (Adapted from reference 45)

Figure 2.1 is the fall-off curve of a unimolecular reaction. It shows the transition of the rate coefficient, k, from the "low-pressure range", where it is proportional to $[M]$, to the "high-pressure range", where it approaches the constant value k_∞. The limiting rate coefficients are clearly the key quantities characterizing the general position of fall-off curves. At the "centre of the fall-off curve", the two limiting lines, $k_0[M]$ and k_∞, intersect where the concentration equal to $[M]_C$.

A systematic theoretical study of unimolecular reactions has been made by Troe.[42-45] In the following three sections his compact formalism is presented. It "gives a realistic representation of the rate coefficients" and arrives at a set of formulae "simple enough to be incorporated into computer models".

2.1.1 Thermal Unimolecular Reactions at Low Pressure

The rate constant of a thermal unimolecular reaction in the limiting low pressure range, $k_{0,diss}$, can be expressed as a product of a strong collision rate constant, k_0^{sc}, and a collision efficiency, β_c,[42]

$$k_{0,diss} = \beta_c k_0^{sc} \qquad (2.8)$$

As discussed above, $k_{0,diss} = k_1$. k_1 is related to k_{-1} via detailed balance

$$\frac{k_1}{k_{-1}} = \left(\frac{[AB^*]}{[AB]}\right)_{eq} = f^* \qquad (2.9)$$

k_{-1} can be expressed as the product of the collision frequency at unit concentration, Z, and the effective collision efficiency, β_c. $k_{0,diss}$ can be rewritten in to the form[42,45]

$$k_{0,diss} = k_1 = \beta_c Z f^* \qquad (2.10)$$

The equilibrium fraction, f^*, of molecules having sufficient energy to dissociate is obtained by the integral

$$f^* = \int_{E_0}^{\infty} f(E)\, dE \qquad (2.11)$$

where $f(E)$ represents the Boltzmann distribution in those states of AB that have energy above E_0, the dissociation threshold energy relative to the ground state.

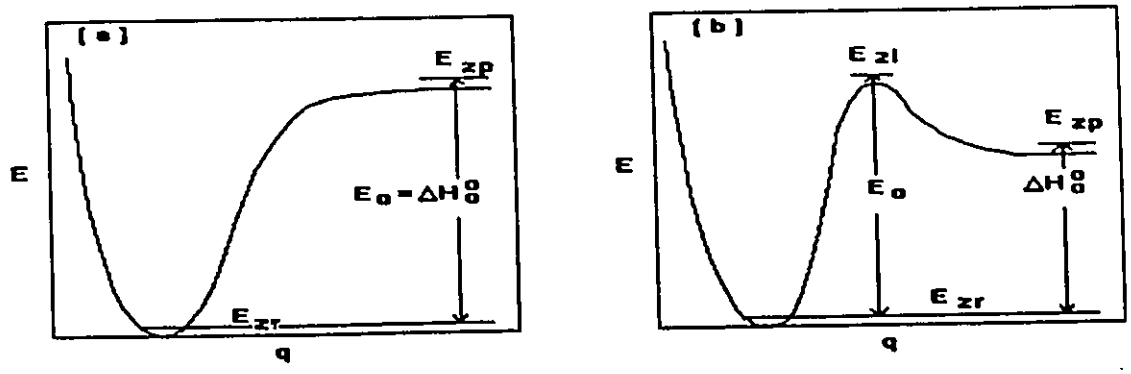

Figure 2.2 Energy as a function of reaction coordinates. (a) simple bond fission reactions (b) complex elimination reactions. (Adapted from reference 45)

Figure 2.2 shows the two types of potential energy diagrams for dissociations. E_{zr}, E_{zp}, and E_{zl} denote the zero-point energies of the reactant, product, and intermediate activated complex. The dissociation reaction where the reverse recombination has no energy barrier is a simple bond fission reaction. The dissociation where the reverse reaction has an energy barrier is a complex elimination. For a simple bond fission reaction, E_0 equals to the enthalpy change of reaction at 0 K, *ie.* ΔH°_0. For a complex elimination reaction, E_0 is equal to ΔH°_0 plus the barrier height.

2.1.1.1 Strong Collision Rate Constants

According to equations (2.8) and (2.10)

$$k_0^{sc} = Zf^\bullet \qquad (2.12)$$

By quantum statistical mechanics, f^* is split up into various factors which "include all the important contributing factors in a sufficiently accurate form, but nevertheless provide transparent and simple equations for practical application".[42] Therefore k_0^{sc} has been expressed in factorized form as[42,45]

$$k_0^{sc} = Z_{LJ} \frac{\rho_{vib,h}(E_0)\, k_B T}{Q_{vib}} \exp\left(-\frac{E_0}{k_B T}\right) F_E F_{anh} F_{rot} F_{rotint} \qquad (2.13)$$

The Lennard-Jones collision frequency, Z_{LJ}, for collisions between the reacting molecules AB and the bath gas M is used as the basis for the overall rate coefficient for perfect collisional energy transfer. As is well known, it is given by[77-78]

$$Z_{LJ} = N_A \pi \sigma_{AB-M}^2 \sqrt{\frac{8RT}{\pi \mu_{AB-M}}}\, \Omega_{AB-M}^{(2,2)^*} \qquad (2.14)$$

with Avogadro's number, N_A, the Lennard-Jones collision diameter, $\sigma_{AB-M} = (\sigma_{AB-AB}+\sigma_{M-M})/2$, the reduced mass, $\mu_{AB-M} = m_{AB}m_M/(m_{AB}+m_M)$, with the molecular weights m_{AB} and m_M, and the reduced collision integral $\Omega^{(A^2,B^2,M^2)^*}$ a function of k_BT/ε_{AB-M} where the Lennard-Jones well depth $\varepsilon_{AB-M} = (\varepsilon_{AB-AB}\varepsilon_{M-M})^{1/2}$. The reduced collision integral can be approximated by[78]

$$\Omega_{AB-M}^{(2,2)^*} = [0.697 + 0.5185 \log(k_BT/\varepsilon_{AB-M})]^{-1} \qquad (2.15)$$

which is accurate to within ±2.5% in the range $3 \le k_BT/\varepsilon_{AB-M} \le 300$.

The vibrational partition function is given by

$$Q_{vib}=\prod_{i=1}^{s}\left[1-\exp\left(-\frac{h\nu_i}{k_BT}\right)\right]^{-1} \qquad (2.16)$$

where ν_i (i = 1, 2, ..., s) are the molecular vibration frequencies ν_i (i = 1, 2, ..., s). They contribute to the harmonic oscillator density of states at the threshold energy according to

$$\rho_{vib.h}(E_0)=\frac{(E_0+\alpha(E_0)E_z)^{s-1}}{(s-1)!\prod_{i=1}^{s}(h\nu_i)} \qquad (2.17)$$

where the zero-point energy, E_z , is given by

$$E_z=\frac{1}{2}\sum_{i=1}^{s}(h\nu_i) \qquad (2.18)$$

and $\alpha(E_0)$ is a correction factor for polyatomic molecules with[45]

$$\alpha(E_0)=1-w\beta^* \qquad (2.19)$$

$$\log_{10}w=-1.0506\,(E_0/E_z)^{0.25} \qquad at\ E_0/E_z\geq 1 \qquad (2.20)$$

$$w^{-1}=5\,(E_0/E_z)+2.73\,(E_0/E_z)^{1/2}+3.51 \qquad at\ 0.1\leq E_0/E_z\leq 1 \qquad (2.21)$$

and

$$\beta^{*}=(s-1)\,(\sum_{i=1}^{s}\nu_i^2)\,/\,(\sum_{i=1}^{s}\nu_i)^2 \qquad (2.22)$$

The Boltzmann-factor, $exp(-E_0/k_BT)$, generally shows the main temperature dependence of k_0^{sc}.

F_E, accounts for the energy dependence of the density of states[42,45]

$$F_E=\frac{\int_{E_0}^{\infty}f(E)\,dE}{f(E_0)\,k_BT}=\sum_{i=0}^{s-1}\frac{(s-1)!}{(s-1-i)!}\left(\frac{k_BT}{E_0+\alpha(E_0)\,E_Z}\right)^i \qquad (2.23)$$

where $f(E)$ is the Boltzmann distribution for a total rovibrational energy, E.

The anharmonicity of the molecular vibrations is taken into account by the factor, F_{anh}. For complex elimination reactions, $F_{anh}=1$. For simple bond fissions it is given by[42,45]

$$F_{anh}=\left(\frac{s-1}{s-3/2}\right)^m \qquad (2.24)$$

where m denotes the number of the disappearing oscillators during the reaction.

F_{rot}, takes into account the contribution of external rotation of the molecule AB[45]

$$F_{rot}=F_{rot\,max}\left(\frac{I^{*}/I}{I^{*}/I-1+F_{rot\,max}}\right) \qquad (2.25)$$

where, for a linear molecule of s oscillators,

$$F_{rot\,max}=\frac{1}{s}\left(\frac{E_0+\alpha(E_0)\,E_Z}{k_BT}\right) \qquad (2.26)$$

and, for a nonlinear molecule,

$$F_{rot\ max} = \frac{(s-1)!}{(s+1/2)!}\left(\frac{E_0+\alpha(E_0)E_Z}{k_BT}\right)^{3/2} \qquad (2.27)$$

For a simple bond fission reaction, I^*/I is approximated by

$$I^*/I = 2.15(E_0/k_BT)^{1/3} \qquad (2.28)$$

but for a molecular elimination reaction one must simply guess I^*/I.

$F_{rot\ int}$ accounts for internal rotors (treated as free rotors)[42,45]

$$F_{rot\ int} = \frac{(s-1)!}{(s-1+r/2)!}\left(\frac{E_0+\alpha(E_0)E_Z}{k_BT}\right)^{r/2} \qquad (2.29)$$

where r denotes the number of internal free rotors ($s+r = 3N-6$ for a nonlinear molecule, and $s+r = 3N-5$ for a linear molecule).

2.1.1.2 Weak Collision Rate Constants

At combustion temperatures, the effective collision efficiency, β_C , is much smaller than unity. High-temperature unimolecular dissociation and the reverse recombination often occur at the weak collision limit of energy transfer, where the "strong collision assumption" ($\beta_C \approx 1$) that whole quanta are transferred in every collision has to be abandoned.[42]

The weak collision factor can be related to the average energy transferred per collision, $\langle\Delta E\rangle$, by[42,45]

$$\frac{\beta_c}{1-\sqrt{\beta_c}} = \frac{-\langle\Delta E\rangle}{F_E k_B T} \qquad (2.30)$$

which holds for $1 \le F_E \le 3$. Theoretical treatments of the energy transfer problem are far

from satisfactory. Experimental data must be relied upon in order to specify β_C. For each different bath gas, experimental studies[79-82] show that the temperature dependence of $\langle \Delta E \rangle$ is very weak and that $\beta_C \propto T^{-1}$ approximately.

2.1.2 Thermal Unimolecular Reactions at High Pressure

A simplified SACM (statistical adiabatic channel model[48]) calculation of the high pressure rate constants for unimolecular simple bond fission and the reverse radical association reactions has met with surprising success,[43] even though it is based on very general features of the potential only.

The high-pressure limiting rate constant is given by the product[43]

$$k_\infty = k_\infty^{PST} f^{rigid} \qquad (2.31)$$

where the upper limit, k_∞^{PST}, is calculated by phase space theory, or loose activated complex theory that neglects any anisotropy of the interaction potential. The rigidity factor, f^{rigid}, is smaller than unity and accounts for anisotropy restrictions of the potential. It is convenient to calculate the high pressure recombination rate constant, $k_{rec,\infty}$, first and then to convert it to the high pressure dissociation rate constant, $k_{diss,\infty}$, through the equilibrium constant, K_C.

The isotropic portion of the recombination rate coefficient is represented by the expression[43]

$$k_{rec,\infty}^{PST} = \frac{k_B T}{h} \left(\frac{h^2}{2\pi \mu k_B T} \right)^{3/2} \frac{Q_{el}(AB)}{Q_{el}(A)\, Q_{el}(B)} Q_{cent}^{\ddagger} \qquad (2.32)$$

with the reduced mass, μ, of A and B, the electronic partition functions, Q_{el}, and the

centrifugal partition function[43]

$$Q^{*}_{cent} = \sum_{J=0}^{\infty} (2J+1) \exp\left(-\frac{E_0(J) - E_0(J=0)}{k_B T}\right) = \sum_{J=0}^{\infty} f(J) \qquad (2.33)$$

For a given J, the centrifugal barriers, $E_0(J)$, are easily obtained by numerical determination of the maximum of the lowest adiabatic channel potential, $V_a(z)$, for the dissociation reaction AB→A+B.[43]

$$V_a(z) = D[1-\exp(-z)]^2 + \Delta E_z \exp\left(-\frac{\alpha}{\beta} z\right) + E_{zp} + B_e J(J+1) \left(\frac{1}{1+a_1 z + a_2 z^2}\right) \qquad (2.34)$$

with

$$D = \Delta H_0^{\circ} + E_{zz} - E_{zp} \qquad (2.35)$$

$$\beta = \sqrt{\frac{f_{RC}}{2D}} = \sqrt{\frac{2\pi^2 \mu}{D}}\, \nu_{RC} \qquad (2.36)$$

$$z = \beta (q - q_e) \qquad (2.37)$$

$$\Delta E_z = E_{zz} - E_{zp} - h\nu_{RC}/2 \qquad (2.38)$$

where D, the bond dissociation energy, and β (which is determined from the force constant, f_{RC}, for the dissociating bond) are Morse potential parameters. The vibrational frequency of the oscillator, ν_{RC}, is associated with the reaction coordinate. q denotes the reaction

coordinate and q_e the equilibrium distance between the fragments in the reactant, or the length of the associating bond. J is the total angular momentum quantum number. B_e stands for the average value of the two smallest rotational constants of the reactant molecule in the equilibrium configuration. The channel potential, V_a, is given by the sum of the Morse potential, V, and the channel eigenvalue, E_a, which is interpolated between the eigenvalues of the reactant and the product states by means of an empirical parameter, α. For a quasi-diatomic molecule[43]

$$a_1 = 2/\beta q_e \tag{2.39}$$

$$a_2 = 1/(\beta q_e)^2 \tag{2.40}$$

Centrifugal barriers can be fitted to the form

$$E_0(J) - E_0(J=0) = C_v \cdot [J(J+1)]^{v^*} \tag{2.41}$$

The maxima of the centrifugal barrier for two J values allow for a determination of C_v and v^* (v^* = 1–1.5). The dominant contributions to Q^*_{cent} come from J values between 0 and $2J_{max}(T)$. $J_{max}(T)$ corresponds to the maximum of the distribution, $f(J)$, and is given by

$$J_{max}(T) = \left(\frac{k_B T}{2v^* C_v}\right)^{1/2v^*} - \frac{1}{2} \tag{2.42}$$

Very simple expressions for the rigidity factors, f^{rigid}, are used in the expression for the thermal rate coefficients for simple unimolecular bond fission / radical recombination reactions:[43]

$$f^{rigid} \approx \frac{1}{\langle C \rangle^{3/4}} \qquad for\ b^{*}=1 \qquad (2.43)$$

$$f^{rigid} \approx \frac{1}{\langle C \rangle} \qquad for\ b^{*}=2 \qquad (2.44)$$

$$f^{rigid} \approx \frac{1}{\langle C \rangle^{3/2}} \qquad for\ b^{*}=3 \qquad (2.45)$$

$$f^{rigid} \approx \frac{3}{4\langle C \rangle} \qquad for\ b^{*}=4 \qquad (2.46)$$

where

$$\langle C \rangle = \frac{\langle \varepsilon_e \rangle^2}{2\langle B_m \rangle \Delta H_0^{\circ}} \qquad (2.47)$$

and where $b^{*} = b$ (the number of disappearing oscillators during the dissociation) - 1 (the dissociation reaction coordinate) - r (the number of hindered or free internal rotors), represents the number of the transitional oscillators which become fragment rotors. For a nonlinear reactant $b^{*} \leq 4$. $\langle \varepsilon_e \rangle$ is the geometric mean of the quanta of the b^{*} oscillators of the reactant, AB; and $\langle B_m \rangle$ is the geometric mean of all rotational constants of the fragments A + B.

2.1.3 Thermal Unimolecular Reactions in the Fall-off Range

In the intermediate fall-off regime between the low and high pressure limits, energy transfer effects, activated complex locations, lifetime distributions, centrifugal effects, etc.

contribute to the rate constant calculation simultaneously. A full calculation of the rate constants accounting for all of these effects is extremely difficult and has never been accomplished.[45] Troe[44] proposed focussing attention on the limiting rate constants, k_0 and k_∞, first, and then to use reduced fall-off curves which "interpolate k between k_0 and k_∞ in a most simple manner using $k_0[M]/k_\infty$ as a dimensionless pressure scale" (reduced with respect to k_∞).

k can be expressed in reduced form as[44-45]

$$\frac{k}{k_\infty} = F_{LH}(k_0[M]/k_\infty)\ F(k_0[M]/k_\infty, S_K, B_K, \beta_c) \qquad (2.48)$$

where F_{LH} is the Lindemann-Hinshelwood factor that was first given about 70 years ago[76]

$$F_{LH} = \frac{k_0[M]/k_\infty}{1 + k_0[M]/K_\infty} = \frac{[M]/[M]_c}{1 + [M]/[M]_c} \qquad (2.49)$$

with

$$[M]_c = \frac{k_\infty}{k_0} \qquad (2.50)$$

Fall-off curves are generally broader than predicted by the Lindemann-Hinshelwood expression. The broadening factor, F, has been derived from rigid RRKM-type models incorporating weak collision effects as determined by the solutions of the master equation.[44]

$$\log F = \frac{\log F_{cent}}{1+\left[\frac{\log([M]/[M]_c)}{N}\right]^2} \qquad (2.51)$$

where N is a scaling factor,

$$N = 0.75 - 1.27 \log F_{cent} \qquad (2.52)$$

F_{cent} gives the depression of the fall-off curve at the centre where $[M]=[M]_c$ relative to the Lindemann-Hinshelwood expression. F_{cent} can be expressed to a good approximation by the three parameters S_K , B_K , and β_c

$$S_K = \frac{H_T^o - H_0^o}{RT} - \frac{1}{2} \qquad (2.53)$$

$$B_K = \left(\frac{S_K - 1}{s-1+r/2}\right)\left(\frac{E_0 + \alpha(E_0)E_z}{k_B T}\right) \qquad (2.54)$$

$$F_{cent} = \beta_c^{0.14}\left\{F_1 + F_2 \exp(-B_K/19.5) + [1-F_1-F_2]\exp\left(-2.3\,[B_K/F_3]^{1.5}\right)\right\} \qquad (2.55)$$

$$F_1 = 1.32\exp(-S_K/4.2) - 0.32\exp(-S_K/1.4) \qquad (2.56)$$

$$F_2 = 1 - \exp(-S_K/30) \qquad (2.57)$$

$$F_3 = 7.5 + 0.43 S_K \qquad (2.58)$$

F_{cent} can be fitted into a much simpler form for easier use

$$F_{cent} = (1-a')\exp(-T/T^{***}) + a'\exp(-T/T^{*}) + \exp(-T^{**}/T) \qquad (2.59)$$

The pressure and temperature dependence of the rate coefficients for a unimolecular reaction and of its reverse reaction for a given bath gas can be calculated in terms of k_∞, k_0, and four fitting parameters, T^{***}, a', T^{*}, T^{**}, which are characteristic of a given species and bath gas M.

2.2 THE RATE OF METHYL RADICAL DECOMPOSITION

2.2.1 Calculation

Table 2.1 lists the parameters used in the calculation for the decomposition of CH_3.

There have been some experimental studies of collisional energy transfer in vibrationally highly excited species,[79-82] which relate to the collision efficiency, β_c. It seems reasonable to choose $-\langle\Delta E\rangle = 130\ cm^{-1}$, typical for argon.

Empirical values of the anisotropy ratio, α/β, are generally close to 0.5 for quite different types of reaction.[43,86-87] The ratio for methane decomposition equals 0.43. Because the lowest adiabatic channel potentials for methyl dissociation and methane decomposition are very similar, though they differ in zero-point energies, the value of α/β=0.43 is used also here to determine the maxima of the potential for $CH_3 \rightarrow CH_2 + H$.

To estimate f^{rigid}, only the higher frequency mode of the two disappearing oscillators is considered, ie. $\langle\varepsilon_e\rangle = 1383\ cm^{-1}$.

The equilibrium constant, K_C, which we used to relate $k_{diss.\infty}$ and $k_{rec.\infty}$ is[32]

$$K_c(mol.cm^{-3}) = 196.20T^{-0.269}\exp(-55200/T) \qquad (2.60)$$

Table 2.1 Parameters used in the calculation of the rate constant for CH_3 decomposition.

Low Pressure Limit			High Pressure Limit			
			$Q_{el}(CH_3) = 2$ $Q_{el}(CH_2) = 3$ $Q_{el}(H) = 2$			
Lennard-Jones parameters [a]			C-H bond distance in methyl /Å			1.079
			Dissociation energy D/cm^{-1}			40653
	σ_{LJ}/Å	ε_{LJ}/k_B /K	Morse parameter β/ Å^{-1}			1.865
CH_3	3.80	144	Anisotropy ratio α/β [b]			0.43
Ar	3.47	114	Quasi-diatomic centrifugal parameters [c]			
			C_{v^*} /cm^{-1} = 0.14		v^* = 1.17	
Average energy transferred per collision [b]			Rotational constants /cm^{-1}			
				A_R	B_R	C_R
- $\langle\Delta E\rangle$ /cm^{-1}		130	CH_3	9.576	9.576	4.788
			CH_2	73.811	8.450	7.184
			CH_2 frequencies/cm^{-1}	2954	3123	1056

$E_0 = \Delta H_0^\circ$ /cm^{-1}	37861.5	
CH_3 frequencies ν_i /cm^{-1}	3002	
	580	disappearing oscillator
	3184	reaction coordinate
	3184	
	1383	
	1383	disappearing oscillator

[a] from Ref. 25, 83

[b] see text

[c] determined by the procedure proposed in Ref. 43

remaining data taken or derived from Ref. 84-85

In the calculation of F_{cent}, S_K and B_K are evaluated by

$$S_K = 2.84405 + 3.06899\times10^{-3}T - 7.43448\times10^{-7}T^2$$

$$+9.46290\times10^{-11}T^3 - 4.90432\times10^{-15}T^4 - 234.931/T \qquad (2.61)$$

$$B_K = 12681\,(S_K-1)/T \qquad (2.62)$$

where S_K is derived from the polynomial fit[88] of H_T^o-H_{298}^o and the JANAF value of H_0^o-H_{298}^o for CH_3.

2.2.2 Results and Discussion

The various factors contributing to the methyl radical dissociation rate coefficients in the two limiting and fall-off pressure ranges are given in Table 2.2. Figure 2.3 shows the fall-off behaviour of methyl radical dissociation. Below 1000 K the reaction is apparently unlikely to occur at all. Methyl radical dissociation can occur with measurable rates only at high temperatures, far above 1000 K. Note that the centre of the fall-off curve, where $[M]/[M]_c = 1$, corresponds to total pressures of 900 atm and 2900 atm at the temperatures of 1500 K and 2000 K respectively. Much higher pressures have to be applied in order to come close to the high pressure limit of the reaction, *ie.* far away from the centre of the fall-off curve. Typical laboratory combustion pressures are about 10^{-3} times those corresponding to the fall-off centre or less. It can be seen from Figure 2.3 that the reaction can be considered to be at the low pressure limit when $[M]/[M]_c \leq 10^{-3}$, implying that measured rates are close to that limit. The resulting dissociation rate constants for the high pressure limit

Table 2.2 Calculation results for $CH_3(+Ar) \rightleftharpoons CH_2+H(+Ar)$ using the parameters in Table 2.1

T / K	1000	2000	3000	4000
β_c	0.1142	0.0599	0.0388	0.0276
Z_{LJ} / $cm^3 \cdot mol^{-1} \cdot s^{-1}$	3.003×10^{14}	3.743×10^{14}	4.287×10^{14}	4.732×10^{14}
$\rho_{vib,h}$ / J^{-1}	2.065×10^{24}	2.065×10^{24}	2.065×10^{24}	2.065×10^{24}
Q_{vib}	2.453	10.33	37.47	112.6
F_E	1.084	1.180	1.288	1.412
F_{anh}	1.372	1.372	1.372	1.372
F_{rot}	6.676	4.378	3.236	2.540
$F_{rot\ int}$	1.0	1.0	1.0	1.0
$k_{0,\ diss}$ / $cm^3 \cdot mol^{-1} \cdot s^{-1}$	8.70×10^{-6}	1.30×10^{6}	2.83×10^{9}	7.93×10^{10}
$^{\#}A_v$ / $cm^3 \cdot mol^{-1} \cdot s^{-1}$	7.718×10^{11}	5.457×10^{11}	4.456×10^{11}	3.859×10^{11}
Q^{*}_{cent}	1247	2251	3194	4060
f^{rigid}	0.726	0.726	0.726	0.726
$k_{rec,\infty}$ / $cm^3 \cdot mol^{-1} \cdot s^{-1}$	6.99×10^{14}	8.92×10^{14}	1.03×10^{15}	1.14×10^{15}
$k_{diss,\infty}$ / s^{-1}	2.28×10^{-8}	2.34×10^{4}	2.40×10^{8}	2.44×10^{10}
$[M]_c$ / $mol \cdot cm^{-3}$	2.62×10^{-3}	1.80×10^{-2}	8.50×10^{-2}	3.07×10^{-1}
F_{cent}	0.296	0.206	0.176	0.165

$$A_v = \frac{k_B T}{h}\left(\frac{h^2}{2\pi\mu k_B T}\right)^{3/2}\frac{Q_{el}(CH_3)}{Q_{el}(CH_2)\,Q_{el}(H)}$$

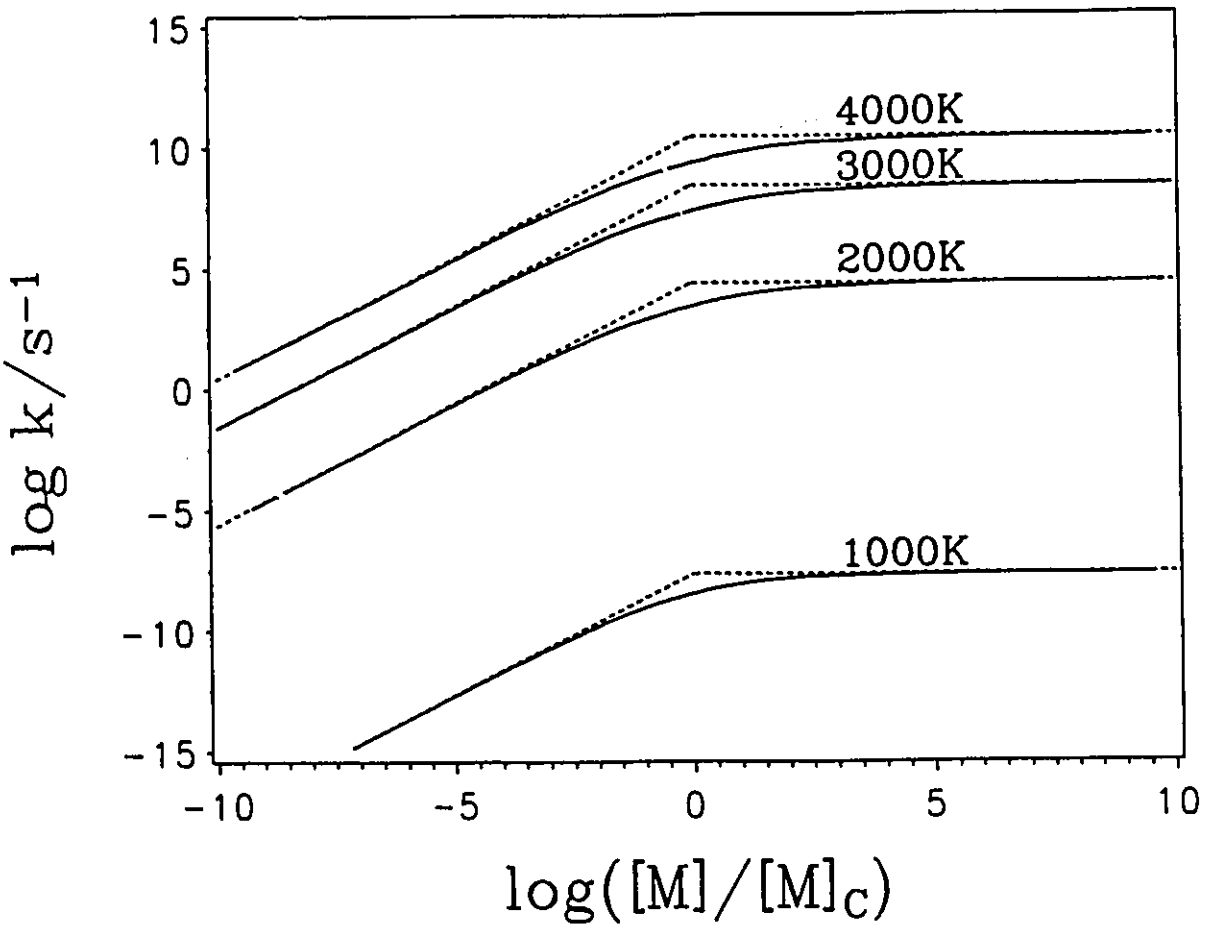

Figure 2.3 Fall-off curves for $\dot{C}H_3$ (+ Ar) → CH_2 + H (+ Ar). - $\langle \Delta E \rangle$ = 130 cm^{-1}.

and for the low pressure limit are

$$\text{High Pressure: } k_{diss,\infty}\,(s^{-1}) = 1.14\times10^{16}\,T^{0.08963}\,exp\,(-55190/T) \qquad (2.63)$$

$$\text{Low Pressure: } k_{0,diss}\,(cm^3\cdot mol^{-1}\cdot s^{-1}) = 2.72\times10^{36}\,T^{-5.309}\,exp\,(-58925/T) \qquad (2.64)$$

The only empirical parameter which could possibly affect our calculation of the low pressure limit is the average energy transferred per collision. The results, using five different values of $-\langle\Delta E\rangle$ = 70, 100, 130, 150, 200 cm^{-1} , are compared with each other and with the literature values in Figure 2.4. For each curve $\langle\Delta E\rangle$ is taken as a constant, independent of temperature. The value of $k_{0,diss}$ changes by a factor of 2.5 when $-\langle\Delta E\rangle$ changes from 70 to 200 cm^{-1}, but because of this relatively narrow spread it is hard to decide which curve best describes the experiments. **Equation (2.64)**, wherein the constant $-\langle\Delta E\rangle$ = 130 cm^{-1}, is our choice for the best fit to the experimental literature values.[2,32-34] Alternatively, the slope as well as the absolute values of *logk vs 1/T* for experiments are best reproduced if $-\langle\Delta E\rangle$ varies linearly from 130 to 200 cm^{-1} over the range 4000 to 1400 K, in accord with current thoughts on the temperature-dependence of $\langle\Delta E\rangle$.[80-82] In that case $k_{0,diss}$ is given by

$$k_{0,diss}\,(cm^3\cdot mol^{-1}\cdot s^{-1}) = 1.26\times10^{39}\,T^{-6.02}\,exp\,(-59800/T) \qquad (2.65)$$

Our calculation shows that at the low pressure limit the activation energy (calculated from $-dlnk_{0,diss}/d(1/RT)$) is less than the bond dissociation energy (486.3 $kJ\cdot mol^{-1}$) and that it

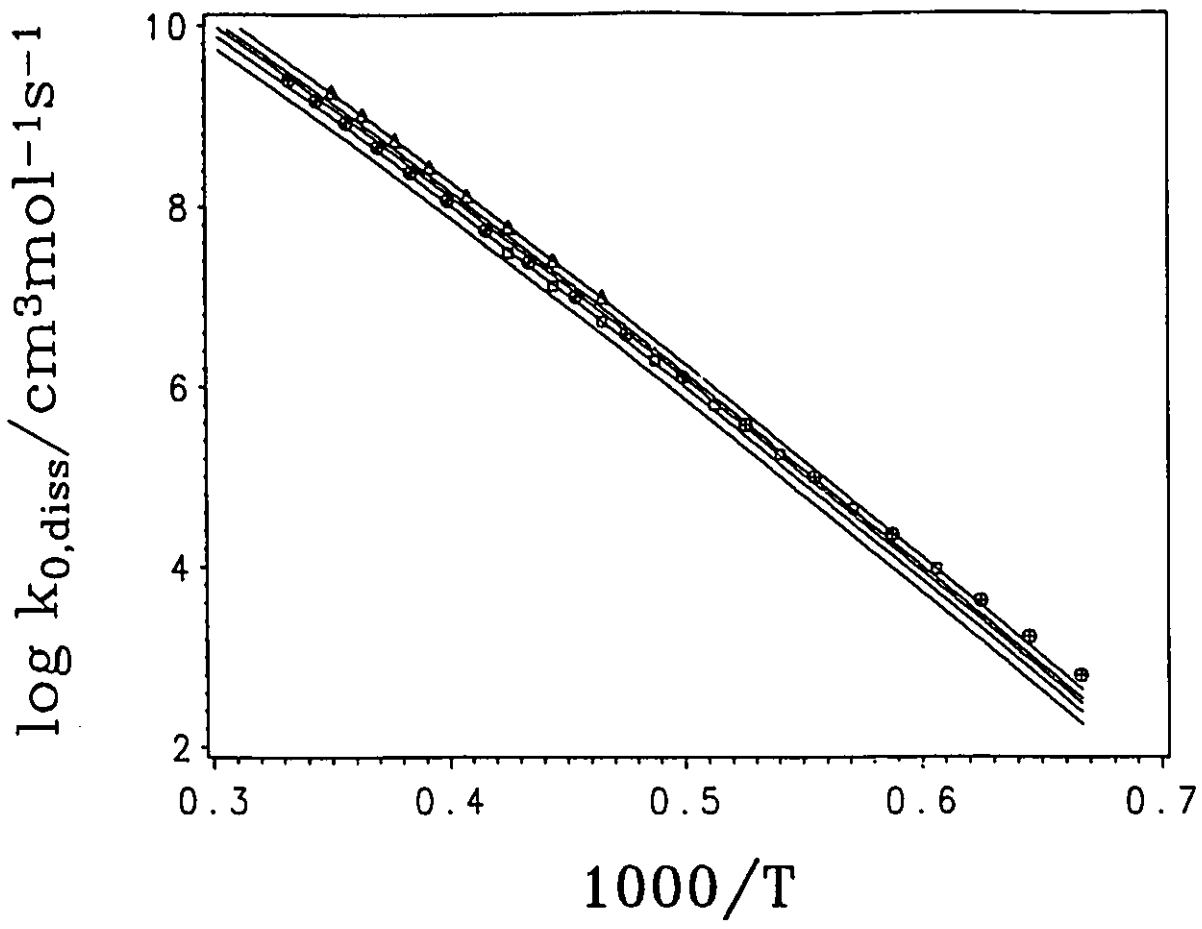

Figure 2.4 $k_{0,diss}$ for $CH_3 + Ar \rightarrow CH_2 + H + Ar$ compared with literature values.

From top to bottom - $\langle \Delta E \rangle$ = 200, 150, 130, 100 and 70 cm^{-1}.

⊕: evaluation from Ref. 2, 32; □: experiments from Ref. 33;

▲: experiments from Ref. 34.

decreases with increasing temperature (446, 402, 358, and 313 kJ·mol^{-1} at 1000, 2000, 3000, and 4000 K respectively). The average activation energy over the range 1000 – 4000 K is in very good agreement with the literature values of 373 – 383 kJ·mol^{-1}. [2,32-34]

Figure 2.5 is a plot of first order rate coefficients versus temperature for the dissociation of CH_3 at the high pressure limit and at various total densities. f^{rigid}, the rigidity factor, equals to 0.726 (see Table 2.2), implying a reaction with a nearly loose activated complex. In Merkel and Zulicke's study,[35] the molecular data set B corresponds to the "looser" transition state. It can be seen from Figure 2.5 that their $k_{diss.,\infty}$ of data set B ($[M]=\infty$) are very close to **equation (2.63)** (about a factor of 3 smaller at 2400 K). Their results for data set C (also $[M]=\infty$) are lower than their own data set B by factors of 22 – 105. The estimate of White and Gardiner[89] is simply double that of data set C.

By detailed balance, ie. using K_c, the reverse rate coefficients, $k_{rec.,\infty}$ and $k_{0,\,rec}$, can be easily obtained. Our results are in reasonably close agreement with a recent ab initio calculation of the high-pressure limiting rate constant, $k_{rec.,\infty}$, by Aoyagi *et al.*,[36] as shown in Figure 2.6. We find a very small positive temperature dependence ($\propto T^{0.36}$) for the high pressure rate coefficient for the reverse recombination. Our $k_{rec.,\infty}$ only changes by a factor of 2.5 over the range 300 – 4000 K. Merkel and Zulicke's values[35] of $k_{rec.,\infty}$ differ from Aoyagi *et al.*'s as well as our own. However, those of Merkel and Zulicke require reevaluation since their forward and reverse rate constants are not consistent with the true equilibrium constant, K_c, expressed by **equation (2.60)**. $k_{rec.,\infty}$ values for their data set C need to be reduced by a factor of 7.7; sets A and B need to be multiplied by 6 at 1500 K, by 3 at 1850 K, and by 1.4 at 2400 K. These reevaluated rate coefficients actually exhibit an even

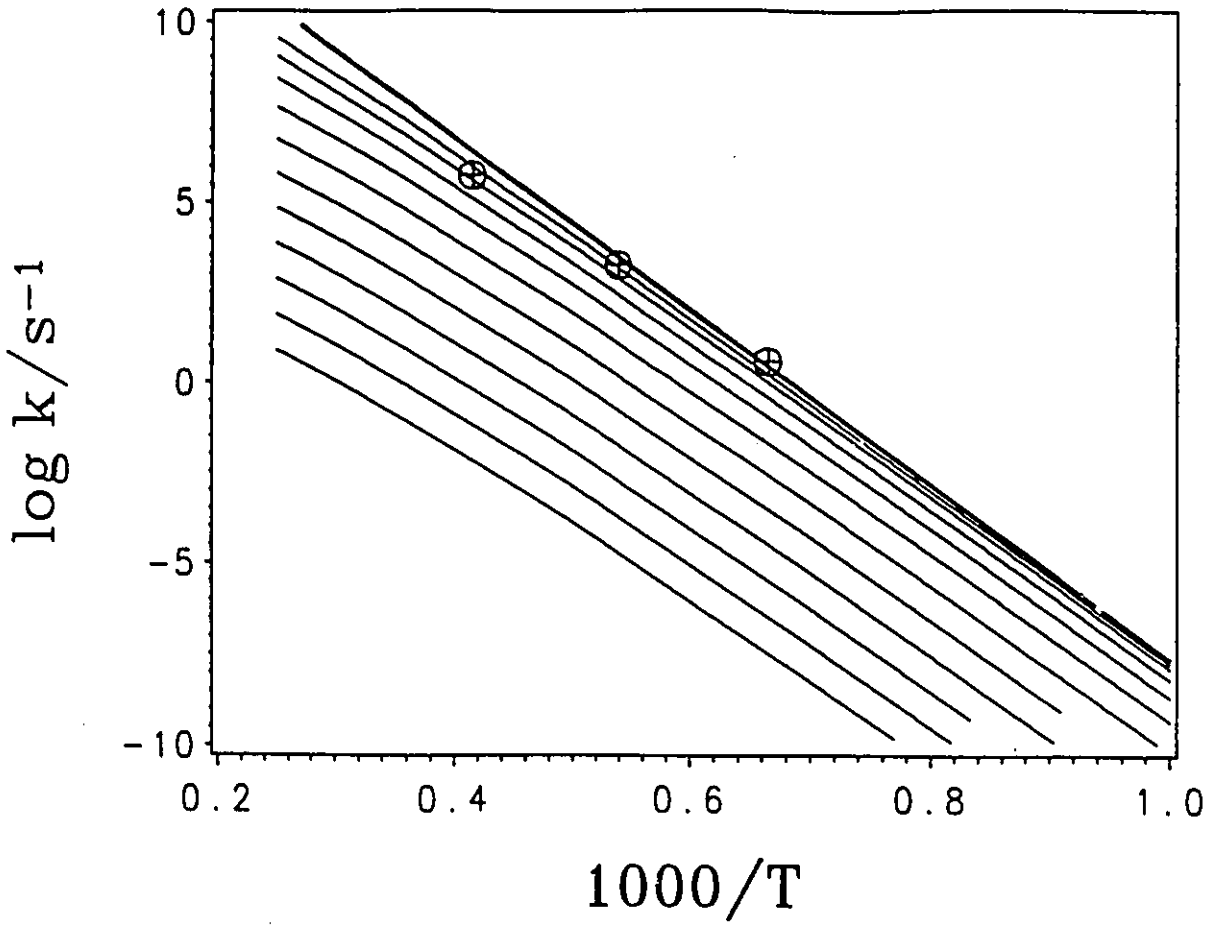

Figure 2.5 First order rate coefficients for the dissociation of CH_3 at the high pressure limit (equation (2.63): thick line), and at various total concentrations (thin lines) from top to bottom [M]= 1, 10^{-1}, 10^{-2}, 10^{-3}, 10^{-4}, 10^{-5}, 10^{-6}, 10^{-7}, 10^{-8}, 10^{-9}, 10^{-10} mol·cm^{-3}. ⊕: data set B of Ref. 35, with [M] = ∞

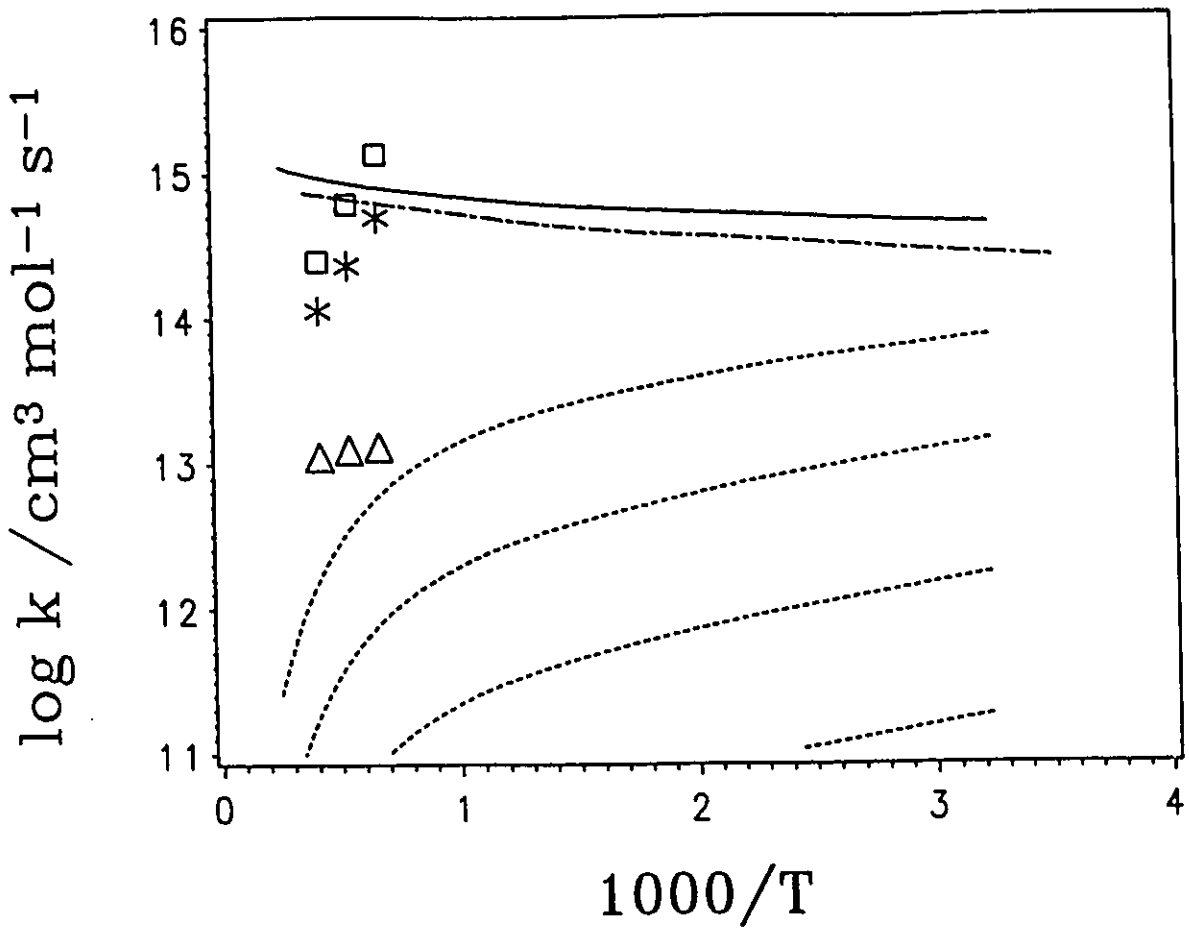

Figure 2.6 Second order rate coefficients for the recombination of CH_2 + H at the high pressure limit, [M] = ∞, (solid line: this work; -·-·-·-·-: Ref. 36; *, □, ▲: reevaluated from Ref. 35 for data sets A, B, C), and at various total concentrations (dashed lines: this work) from top to bottom [M]= 10^{-4}, 10^{-5}, 10^{-6}, 10^{-7} mol cm^{-3}.

steeper negative temperature dependence than their published ones do. Therefore the controversy persists.

Some experimental values[37-41] which propose a negative activation energy for the reaction of CH_2 + H are also somewhat controversial according to Aoyagi *et al.*[36] The latter try to explain the negative temperature dependence in terms of a rate determining formation of excited CH_3^*. However, the pressures are much too low for this to be reasonable. For example, Bohland and Temp's values[40] correspond to 10^{-7} *mol* cm^{-3}, and Frank *et al.*'s[41] to 10^{-5} *mol* cm^{-3}. Under such conditions CH_3 recombination is too slow, and it is more likely that a direct (and relatively fast) H-atom abstraction is occurring in the experiments to form the products CH + H_2 , as claimed by the experimenters. That comparison is, therefore, not fair.

Although **equation (2.13)** multiplied by the collision efficiency β_c is recommended for use in calculating the rate coefficients for low pressure unimolecular processes[42,45], it is strictly not correct to do so for high energy channels:[43] Bond breakage at the "low" threshold energy results in serious underpopulation of the vibrational energy levels which adversely compounds the underpopulation expected for the " upper" threshold channel (an effect which **equation (2.13)** ignores). Such is the situation in the present case, where CH_3 decomposition could, in principle, also result in the formation of CH + H_2 as an alternate channel. Since the barrier height for the latter process is not known it is worth while evaluating recent studies for clues to its possible effect on our calculations. Kiefer and Kumaran[31] recently performed an RRKM calculation for the low pressure limiting rate constant of the CH_2 + H channel, here denoted by $k_{0,diss}(H)$ as well as of the CH + H_2 channel, here denoted by

$k_{0,diss}(H_2)$. Unfortunately, the latter process is not a simple bond fission, and the energy barrier is thus not known. Kiefer and Kumaran (KK) simply assumed that it was equal to ΔH_0°, which is likely an underestimate. They find that $k_{0,diss}(H)/k_{0,diss}(H_2) \approx 0.78$ over the temperature range 3000 - 4000 K, suggesting that the H_2 channel's existence is likely to disturb the H-channel rate. Dean and Hanson[26] (DH) pyrolyzed CH_4 and were able to determine both rate constants indirectly by fitting their measurements of *[C]* and *[CH]* to kinetic simulations. They obtained $k_{0,diss}(H)/k_{0,diss}(H_2) \approx 1.8$ over the range 3000 - 4000 K, suggesting that the H_2 channel is not important, after all. Whether the KK or the DH results are correct, we note that both studies claim a temperature-independent branching ratio. This means that our calculation of the activation energy for $k_{rec,-}(H)$ above is not affected by the competing channel, and our conclusions regarding the controversy are at least qualitatively correct. Furthermore, as KK already noted,[31] not only do the KK or the DH sets of k's reproduce the DH data, but so do a third set due to Markus and Roth (MR)[30] who made direct measurements of *[CH]*. The MR study leads to $k_{0,diss}(H)/k_{0,diss}(H_2)$ varyir.g from 2 to 6 over the range 3000 - 4000 K. It suggests, additionally, that the energy barrier for CH + H_2 formation is significantly larger than ΔH_0°, as can be seen in Figure 2.7, where we have calculated the branching ratio, based on the use of **equation (2.13)**, for various choices of the energy barrier, E_0, for the formation of CH + H_2. Indeed if $E_0 = \Delta H_0^\circ$, the ratio is as KK predicts. The DH results are most simply explained if $E_0 = 1.05\Delta H_0^\circ$. At first sight the temperature dependence of the MR experimental branching ratio seems odd. In actual fact, as stated above, use of **equation (2.13)** for the channel of higher E_0 is problematical because of the excessively perturbed population distribution; (hence we do not recommend a value

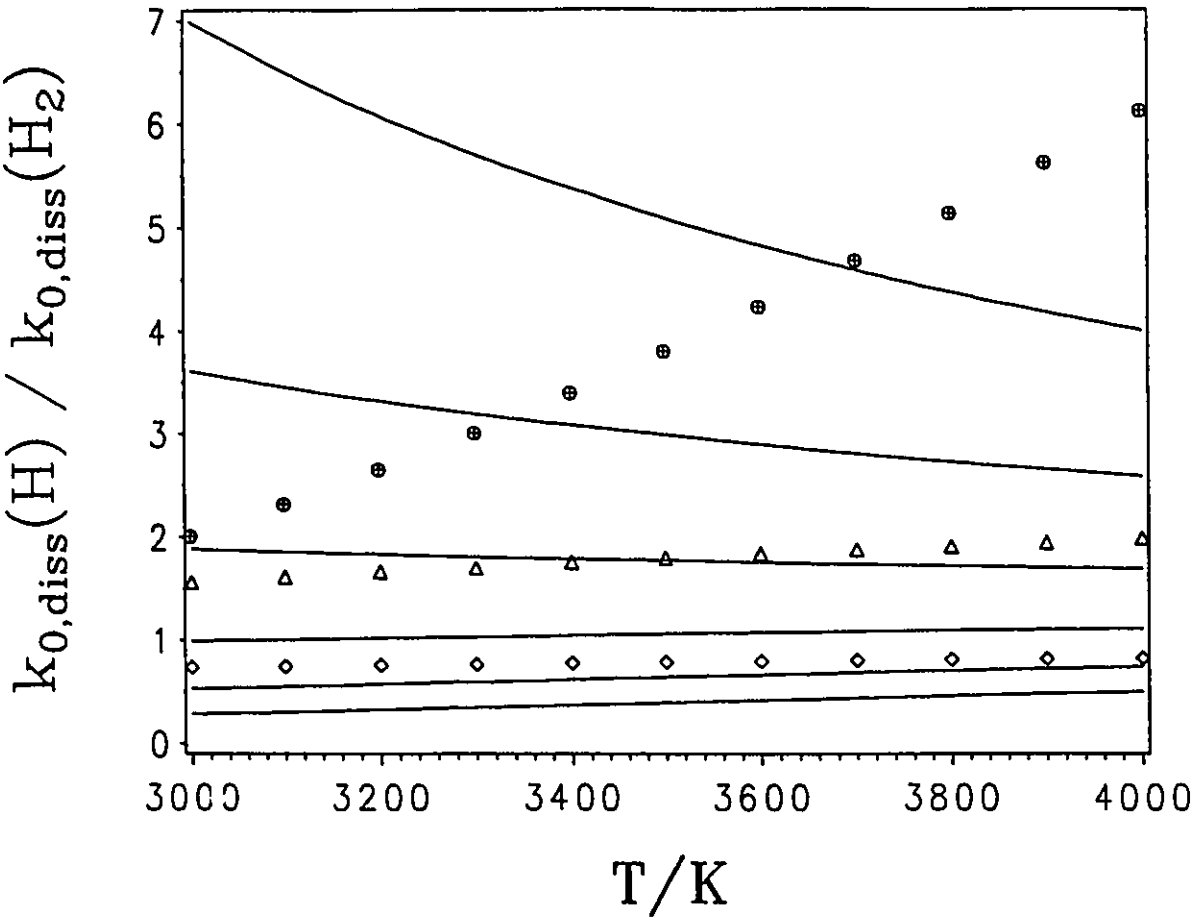

Figure 2.7 Branching ratio for $CH_3 + Ar \rightarrow CH_2 + H + Ar$ and $CH_3 + Ar \rightarrow CH + H_2 + Ar$ as predicted from this work (solid curves with $E_0 / \Delta H_0^\circ$ = 1.15, 1.10, 1.05, 1.00, 0.95, and 0.90 from top to bottom, and ΔH_0° = 105.6 kcal mol^{-1} for $CH + H_2$ formation). Also shown are RRKM calculations from Ref. 31 ◊, and experimental results from Ref. 26 ▲ and Ref. 30 ⊕.

for $k_{0,diss}(H_2)$). The higher the temperature the greater the perturbation and the more **equation (2.13)** overestimates $k_{0,diss}(H_2)$. (The severity of the double perturbation is underlined by the dramatically low activation energy observed for the CH + H_2 channel.[30]) The branching ratio , therefore, should indeed increase with temperature, as the MR data show. Consequently we believe that the MR study is not only a self-consistent proof that the H_2-channel is the relatively unimportant higher-energy channel, but also that our own calculation for the lower-energy channel is quantitatively correct.

2.3 THE PYROLYSIS OF AZOMETHANE

Azomethane is often used as a source of methyl radicals. However, its decomposition "proceeds via a complicated chain mechanism"[12,22,90-91] at low temperatures. At elevated temperatures (T ≥ 1300 K), "the decomposition of azomethane is sufficiently fast to exclude any CH_3 radical-parent molecule reactions", and there is an adequate amount of evidence that the decomposition follows the stoichiometry[8,15-16,21,92]

$$CH_3NNCH_3 \rightarrow 2\ CH_3 + N_2$$

To carry out the calculation, it is assumed that the decomposition of azomethane occurs in the following consecutive sequence

$$CH_3NNCH_3 \rightarrow CH_3NN + CH_3 \qquad (A)$$

$$CH_3NN \rightarrow CH_3 + N_2 \qquad (B)$$

and that step B is much faster than step A because of the instability of CH_3NN. Step B has

an exothermicity of at least 16 *kcal mol*$^{-1}$, a value estimated at room temperature by Y.-R. Luo. Therefore, the decomposition rate of azomethane according to the stoichiometry is determined by step A. The next sections are devoted to the calculation of the rate constant for step A, which will be used as an approximation to the whole rate.

The author was forced to make such an assumption because of the lack of spectroscopic data and thermodynamic properties for CH_3NN.

2.3.1 Calculation

The parameters used for the calculation of azomethane decomposition are listed in Table 2.3.

Six oscillators disappear during the reaction. They become fragment rotors. One of them (1008 cm^{-1}) is identified as the reaction coordinate. Two low frequencies (214, and 312 cm^{-1}) correspond to the torsional-type reactant oscillators. The remaining three frequencies (1179, 1112, and 353 cm^{-1}) are used to determine the rigidity factor.

There are no literature values of Lennard-Jones parameters for azomethane. The collision diameter is estimated from the value for C_4H_8.[83] The reduced collision integral is set to unity, *ie*. $\Omega^{(1,1)^*}_{A^2B^2M} = 1$. The collision frequency, Z_{LJ}, will be overestimated only by 10% to 30% from 1300 K to 4000 K.

All data for CH_3NN are estimated or identified from those for CH_3NNCH_3 and CH_3NNH.[93-96]

The equilibrium constant, K_c, is calculated by statistical thermodynamics. Appendix

Table 2.3 Parameters used in calculating the rate constant for azomethane decomposition

$E_0 = \Delta H_0^\circ$ /cm^{-1}	20454 [a]											
CH_3NNCH_3 frequencies[a] ν_i /cm^{-1}												
2989	2926	1583	1437	1381	1179[d]	919	591	2977	1416	1027	214[c, d]	
2981	1440	1111	312[d]	222[c]	2988	2925	1447	1384	1112[d]	1008[d, ‡]	353[d]	
Parameters for low pressure limit:												
Collision diameters[e] σ_{LJ}/Å	CH_3NNCH_3 : 5.176							Ar: 3.47				
Average energy transferred per collision - $\langle\Delta E\rangle$ /cm^{-1} = 130												
Parameters for high pressure limit:												
Electronic partition functions	$Q_{el}(CH_3NNCH_3) = Q_{el}(CH_3NN) = 1$							$Q_{el}(CH_3) = 2$				
C-N bond distance in azomethane /Å	1.482[a]											
Dissociation energy D/cm^{-1}	22748											
Morse parameter β/ Å^{-1}	2.7168											
Anisotropy ratio α/β	0.5											
Quasi-diatomic centrifugal parameters[f]	C_v. /cm^{-1} = 0.012							ν^* = 1.07				
Rotational constants /cm^{-1}			A_R			B_R			C_R			
	CH_3NNCH_3[a]		1.3569			0.1467			0.1398			
	CH_3NN[g]		1.997			0.3707			0.3323			
	CH_3[a]		9.576			9.576			4.788			
Frequencies/cm^{-1}												
	CH_3NN[g]	2992	2925	1559	1435	1382	1120					
		920	557	2988	1430	1140	170					
	CH_3[a]	3002	580	3184	3184	1383	1383					

[a] taken or derived from Ref. 85, 93, and 97. [c] torsional vibrations treated as hindered internal rotors. [d] disappearing oscillators. [‡] reaction coordinate. [e] taken or estimated from Ref. 25, 83. [f] determined by the procedure proposed in Ref. 43. [g] estimated from Ref. 96.

1 gives a brief summary of the calculation.

The following two formulae are used to evaluate S_K and B_K in the calculation of F_{cent}

$$S_K = 3.08690 + 1.26277\times10^{-2}T - 3.66333\times10^{-6}T^2$$

$$+5.42321\times10^{-10}T^3 - 3.18554\times10^{-14}T^4 + 24573/T \qquad (2.66)$$

$$B_K = 2185\,(S_K - 1)/T \qquad (2.67)$$

where S_K is derived from the polynomial fit of $H_T^o - H_{298}^o$ for azomethane.[93]

2.3.2 Results and Discussion

Table 2.4 tabulates the factors which contribute to the rate constant of azomethane decomposition. Figure 2.8 shows five curves of $k_{0,\,diss}$ with different $-\langle\Delta E\rangle$'s. The "direct" experimental studies[79-82] as well as the most recent modelling work[98] of weak collision effects in argon all suggest a value of 130 cm^{-1}. (There is no good theoretical reason for a constant $-\langle\Delta E\rangle$; it is only an empirical choice). As shown in Figure 2.8, $k_{0,\,diss}$ increases with increasing temperature below 2000 K and decreases above 2000 K. Equation (2.30) predicts a decrease in the weak collision coefficient, β_c, with increasing temperature as shown in Table 2.4. It gives good results as long as $F_E \leq 3$. This is the case for large polyatomic molecules only at sufficiently low temperatures. With increasing temperature this is no longer the case for large polyatomic molecules, *ie.* the expression for β_c breaks down: Equation (2.30) results in a serious underestimate of β_c.[44] Exact calculation for the C_7H_8 system by Gilbert, Luther, and Troe demonstrates that the decrease of β_c ceases at a

Table 2.4 Calculation results for azomethane decomposition using the parameters in Table 2.3

T / K	1000	2000	3000	4000
β_c	7.756×10^{-2}	1.786×10^{-2}	2.419×10^{-3}	1.840×10^{-4}
Z_{LJ} / $cm^3\cdot mol^{-1}\cdot s^{-1}$	3.346×10^{14}	4.723×10^{14}	5.796×10^{14}	6.693×10^{14}
$\rho_{vib,h}$ / J^{-1}	4.330×10^{31}	4.330×10^{31}	4.330×10^{31}	4.330×10^{31}
Q_{vib}	2.080×10^{3}	6.192×10^{6}	3.321×10^{9}	5.224×10^{11}
$exp(-E_0/kT)$	1.657×10^{-13}	4.071×10^{-7}	5.493×10^{-5}	6.380×10^{-4}
F_E	1.740	4.536	24.50	250.7
F_{anh}	1.141	1.141	1.141	1.141
F_{rot}	2.394	1.098	0.6684	0.4645
$F_{rot\ int}$	2.185	1.092	0.7284	0.5463
$k_{0,\ diss}$ / $cm^3\cdot mol^{-1}\cdot s^{-1}$	1.28×10^{10}	4.13×10^{12}	5.66×10^{11}	2.61×10^{10}
$^*A_v$ / $cm^3\cdot mol^{-1}\cdot s^{-1}$	2.838×10^{10}	2.007×10^{10}	1.639×10^{10}	1.419×10^{10}
Q^*_{cent}	2.539×10^{4}	4.860×10^{4}	7.112×10^{4}	9.312×10^{4}
f^{rigid}	0.0674	0.0674	0.0674	0.0674
$k_{diss,\infty}$ / s^{-1}	3.76×10^{4}	6.64×10^{10}	5.30×10^{12}	3.86×10^{13}
$[M]_c$ / $mol\cdot cm^{-3}$	2.93×10^{-6}	1.61×10^{-2}	9.35×10^{0}	1.48×10^{3}
F_{cent}	8.79×10^{-3}	7.45×10^{-2}	1.12×10^{-1}	1.12×10^{-1}

$$A_v = \frac{k_B T}{h}\left(\frac{h^2}{2\pi\mu k_B T}\right)^{3/2}\frac{Q_{el}(CH_3NNCH_3)}{Q_{el}(CH_3NN)\,Q_{el}(CH_3)}$$

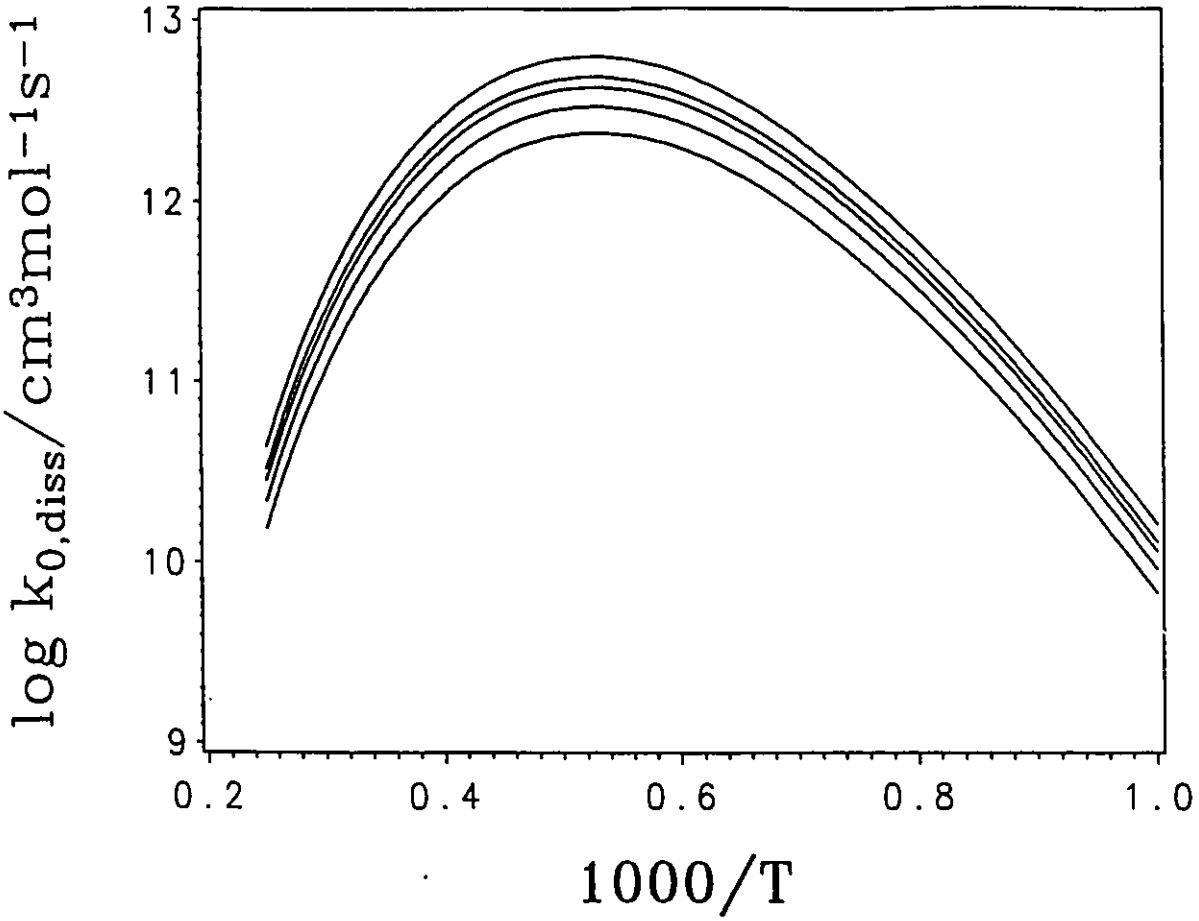

Figure 2.8 $k_{0,\,diss}$ for azomethane decomposition calculated using different values of the average energy transferred per collision (from top to bottom - $\langle\Delta E\rangle$ = 200, 150, 130, 100 and 70 cm^{-1}).

temperature corresponding to $F_E = 4$ where β_c starts to increase with temperature.[44] We can conclude that the results of our calculation are reasonable up to 2000 K. The results above 2000 K are underestimated since equation (2.30), based on a simplified exponential-up and -down collision model, becomes inadequate when F_E is much larger than 3.

Pseudo first order rate constants at different pressures are displayed in Figure 2.9. Also shown in the figure are the experimental results of Moller, Mozzhukhin, and Wagner.[15] Above 1300 K their results agree fairly well with the present calculation in the density range 10^{-6} to 10^{-5} mol cm^{-3}. This is also the range in which our experiments were carried out. The drop-off in the rate coefficients at higher temperatures is a reflection of the underestimate of $k_{0,\,diss}$.

Our calculation under the present experimental conditions is compared with the available literature data[8,15-16,21-22] in Figure 2.10. Taking account of the variation of the total densities, the present calculation is supported by those previous measurements. It is in excellent agreement with Moller, Mozzhukhin, and Wagner's experiment[15] above 1300 K. The drop-off in the first order rate coefficient at higher temperatures is present because of the increasing influence of $k_{0,\,diss}$. Even if the decomposition rate of azomethane had not been underestimated above 2000 K (as a consequence of underestimating $k_{0,\,diss}$ and β_c), the decomposition is still fast enough that we can safely exclude a bimolecular reaction between CH_3 radicals and the parent molecule from our mechanism of CH_3 reactions (below). It can be seen that the magnitude of k at 4000 K (even though it is severely underestimated) is about same as that at 1300 K. However, the real value of the rate coefficient for azomethane decomposition is still uncertain in the drop-off region. The absolute value of the rate constant

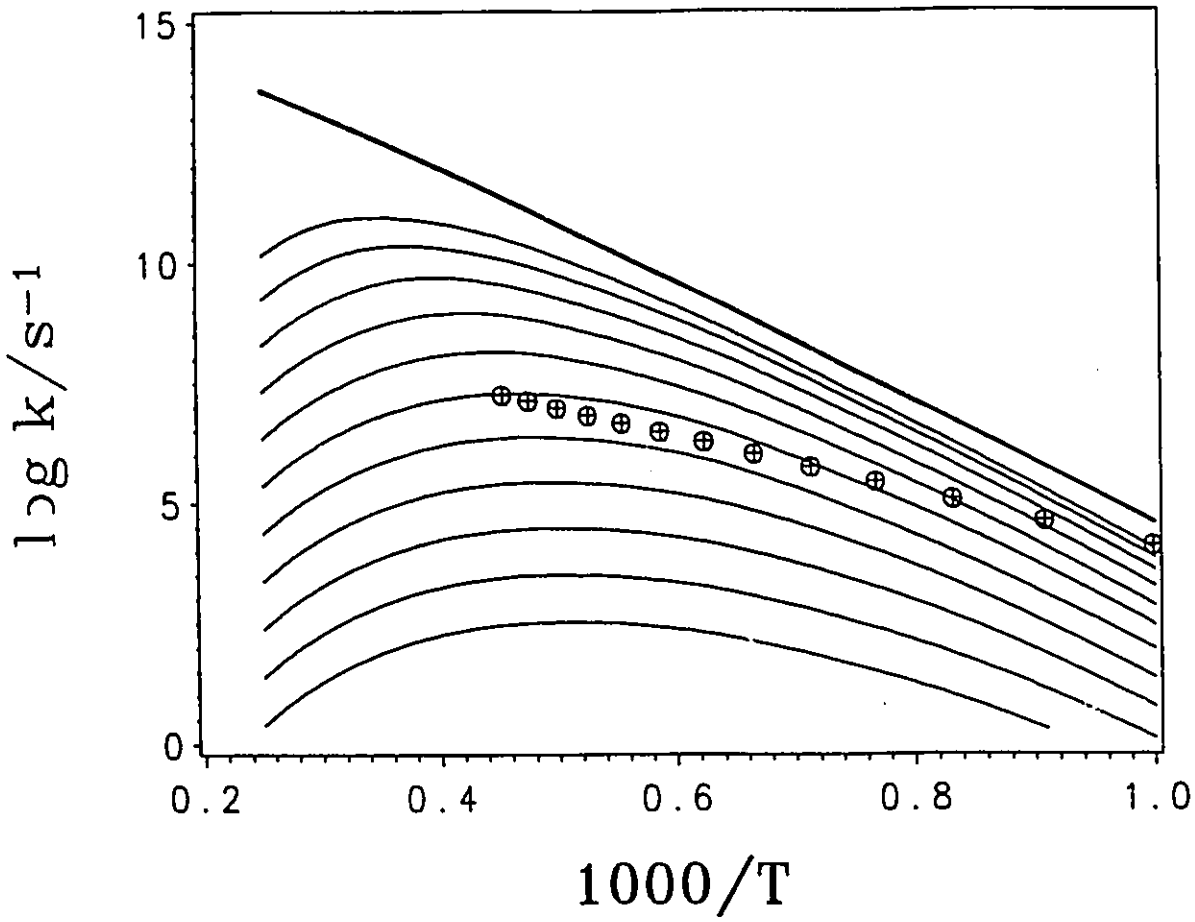

Figure 2.9 First order rate coefficients for the dissociation of azomethane at the high pressure limit (thick line), and at various total concentrations (thin lines). From top to bottom [M] = 1, 10^{-1}, 10^{-2}, 10^{-3}, 10^{-4}, 10^{-5}, 10^{-6}, 10^{-7}, 10^{-8}, 10^{-9}, 10^{-10} mol·cm^{-3}. ⊕: experiments from Ref. 15, with [M] = 3–8×10^{-6} mol·cm^{-3}.

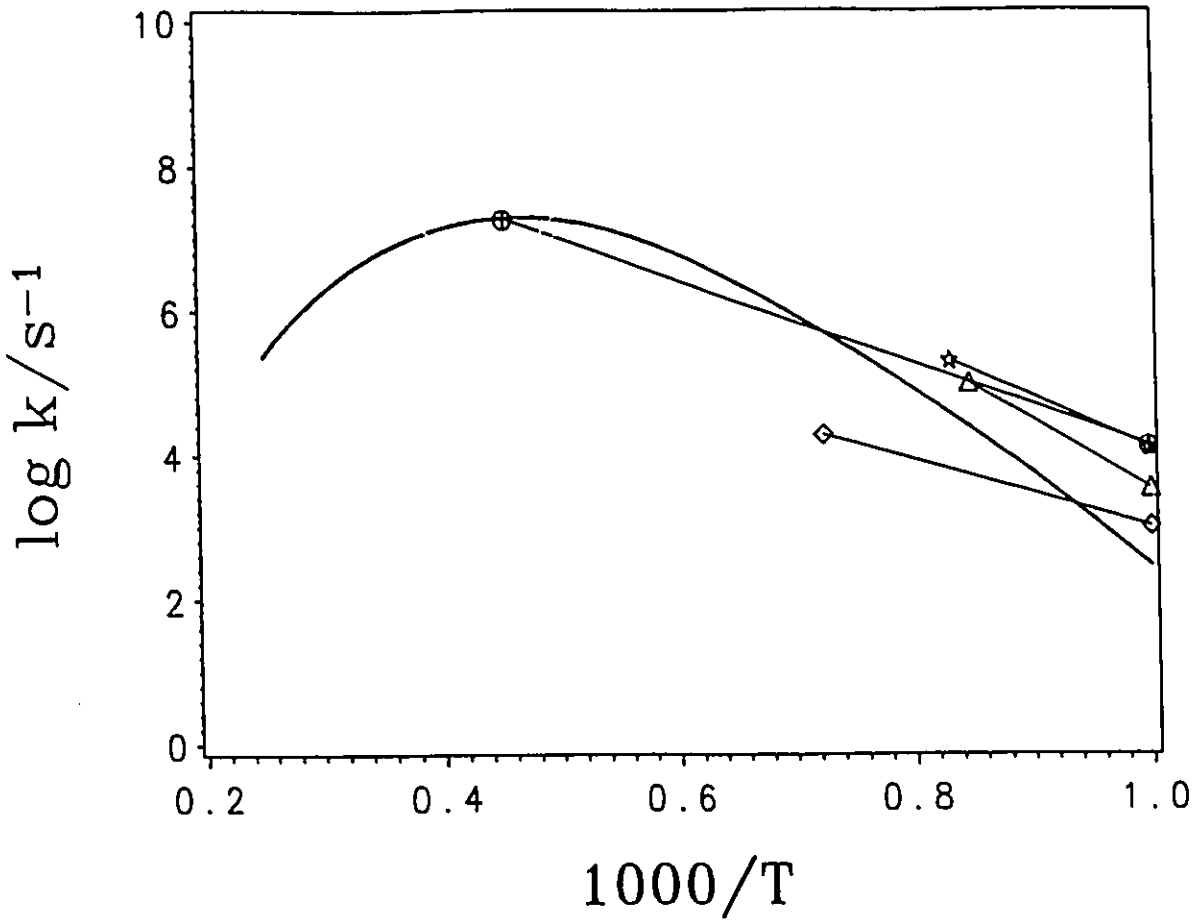

Figure 2.10 First order rate coefficient for the dissociation of azomethane calculated at a total concentration of 10^{-6} to 10^{-5} mol·cm^{-3} (thick line), and experimental data in the literature ⊕ Ref. 15 (3–8×10^{-6} mol·cm^{-3}); ★ Ref. 8 (3×10^{-5} to 1.7×10^{-4} mol·cm^{-3}); △ fitting from Ref. 16, 22 (2.5×10^{-6} mol·cm^{-3}); ◊ Ref. 21 (1×10^{-6} mol·cm^{-3}).

at such high temperatures remains to be calculated using a more exact collisional energy transfer model or remains to be verified by experiment. This will be discussed further in chapter 5 in the framework of a simulation of the full mechanism.

CHAPTER 3

EXPERIMENTAL

Experiments were carried out in a shock tube and designed to observe the primary reactions of CH_3. The thermal decomposition of azomethane at high temperature offers a clean source of methyl radicals to investigate their reactions. The laser schlieren technique was used to monitor the chemical reactions.

3.1 PRINCIPLE AND APPARATUS

3.1.1 Shock Waves and Shock Tubes

A sound wave is propagated through a gas by collisions between gas molecules. This is a perfect reversible adiabatic process consisting of a weak isoentropic compression. When a disturbance is forced through the gas with a velocity faster than the characteristic sound speed, an irreversible shock wave of a very different nature is generated.[99] Because the gas molecules in the path of the shock wave can only move away from the shock front with the sound wave speed, the temperature, pressure, and density of the gas suddenly increase in the shock wave. Obviously, a net motion of the gas following the shock wave results as well.

A shock wave can be conveniently initiated in a shock tube. A shock tube consists of a high pressure chamber--driver section and a low pressure chamber--test section (Fig. 3.1).

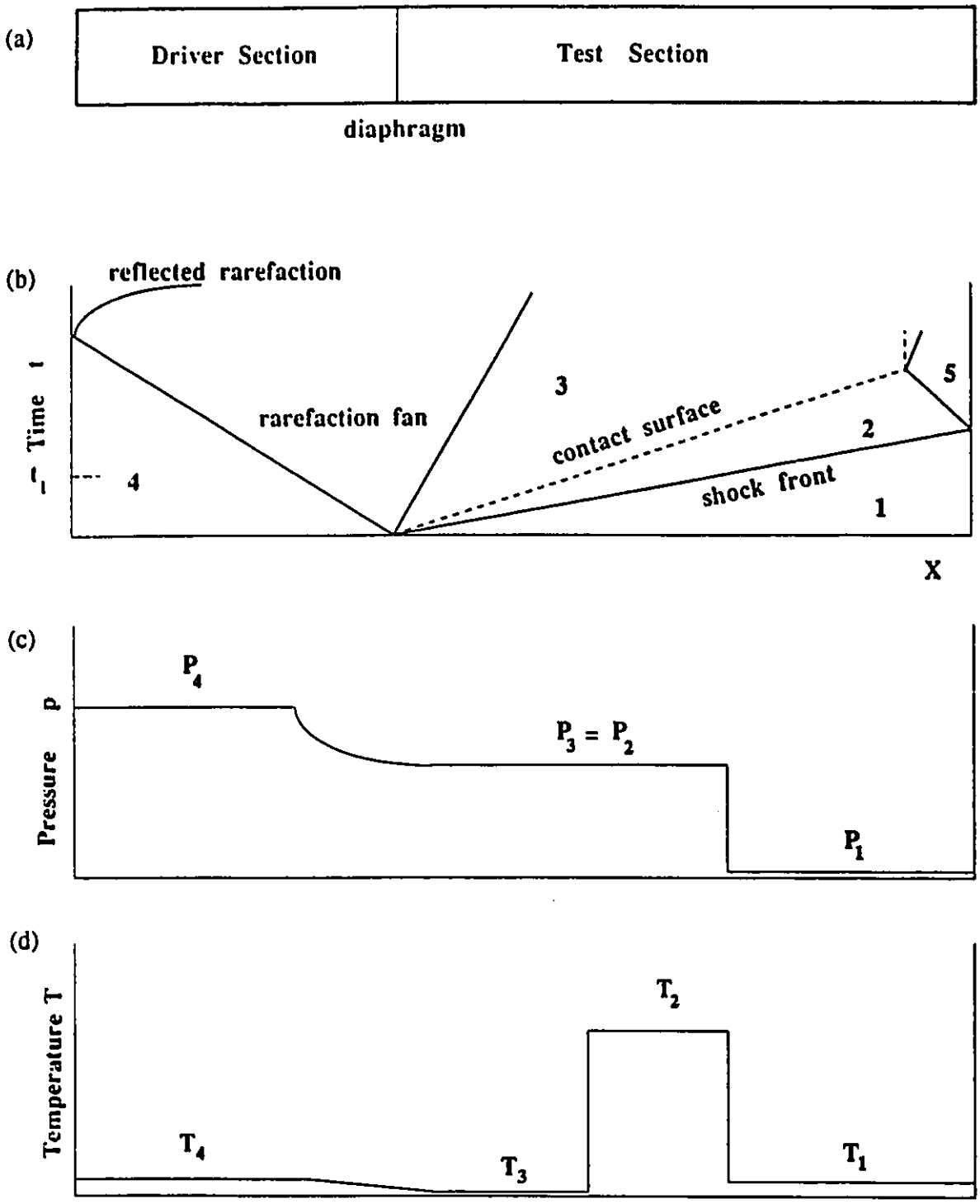

Figure 3.1 (a) Conventional shock tube. (b) A distance-time diagram showing progress of the shock wave, the rarefaction fan and the contact surface separating driver and test gases. (c) The pressure distribution along the tube at time t_1. (d) The temperature distribution along the tube at time t_1. (Adapted from reference 99).

The two sections (Figure 3.1(a)) are initially separated by a Mylar or aluminum diaphragm. A shock wave is generated by the spontaneous bursting of the diaphragm caused by increasing the pressure of the driver gas. A plane shock wave propagates with supersonic speed through the low-pressure test gas, exciting it suddenly to a new temperature and pressure. At the same time, an expansion or rarefaction wave moves back into the high-pressure driver gas at the speed of sound. In contrast to the shock wave, the expansion results in a smooth change in pressure, and thus the rarefaction wave is usually referred to as a fan. The test gas and driver gas make contact at the contact surface, where a temperature discontinuity separates the gas compressed by the shock from that cooled by the expansion. The contact surface moves rapidly along the tube behind the shock front. Conventionally the conditions in the undisturbed low-pressure test gas are symbolized by the subscript 1; so the initial pressure and temperature in this region are denoted by p_1 and T_1. The region between the shock front and the contact surface is symbolized by the subscript 2; hence the pressure and temperature are denoted by p_2 and T_2. The region between the contact surface and the rarefaction fan is symbolized by the subscript 3. The initial conditions in the high-pressure section are symbolized by the subscript 4. When the shock wave reflects from the end of the shock tube, there is a further rise in temperature and pressure, and this region is symbolized by the subscript 5.[99] Figure 3.1(b) displays the movements of the shock front, the contact surface, the rarefaction wave and the reflected shock wave in a distance-time diagram. The variations of pressure and temperature are illustrated in Figure 3.1(c) and (d). In the ideal case the temperature rises abruptly from room temperature, T_1, to a very high value, T_2, at the shock front, and it remains constant up

to the contact surface, where it falls subsequently to a value, T_3, well below room temperature. Finally in the rarefaction fan the temperature reapproaches its initial value, T_4.[99]

By means of a shock tube, the test gas can be brought almost instantly to a known and controlled high temperature in region 2, and this condition may be held for a few hundred microseconds.[99] During this time period the progress of chemical reactions can be monitored by various methods. In this study, all measurements were performed behind the incident shock (region 2) using the laser schlieren technique.

Two different shock tubes were used in this work. Each of the shock tubes consists of a rectangular cross-section test section coupled through a transition section to a tubular steel driver section. The first (old) shock tube, which has been described previously,[71] possesses a 5.4 *m* long steel test section of 8.9 *cm* × 11.4 *cm* cross-section and a 3.7 *m* long driver of 14.9 *cm* inner diameter. The main observation window is located 3.9 *m* downstream of the diaphragm. The second (new) shock tube's test-section was constructed of stainless steel plates welded together under ultra-high vacuum with an electron-beam. This created a 9.3 *cm* × 8.4 *cm* perfectly rectangular inner cross-section tube into which perfectly parallel pairs of observation windows could be attached absolutely flush with the inner walls of the shock tube. The test section was 7.3 *m* long, and the 15.3 *cm* inner diameter driver section was 3.8 *m* long. Measurements were made 6.1 *m* downstream of the diaphragm. Both shock tubes gave rate measurements which were indistinguishable from each other.

3.1.2 Detection System

3.1.2.1 Laser Schlieren Technique

Laser schlieren is a technique especially suited for studying reactions occurring on the submicrosecond time scale. Its excellent time resolution has allowed kineticists to probe the early stages of reactions. Its sensitivity to the thermochemistry of a process allows an accurate measure of the net rate of endothermic/exothermic reactions. The laser schlieren method has been fully described previously by its originators[67-70] and by Teitelbaum et al.[71]

Essentially, a 632.8 *nm* narrow beam from a helium-neon laser (Spectra Physics Model 120) passes through the shock tube. The laser beam deflection, resulting from the refractive index gradient generated by a chemical or physical process, is measured as a function of time. Due to the passage of the shock front and the chemical reactions, there is a dramatic refractive index gradient. At the observation window, the laser beam is deflected in the direction of increasing refractive index from its path perpendicular to the shock tube axis, and thus off the centre of a photodiode detector, as shown in Figure 3.2. The angular deflection, θ, is related to the refractive index gradient, dn/dy, by

$$\theta = l \frac{dn}{dy} \qquad (3.1)$$

provided that θ is small and that the refractive index, n, of the test gas is close to unity. l is the width of the shock tube. The displacement, Δ, of the laser beam on the surface of the detector can be expressed as

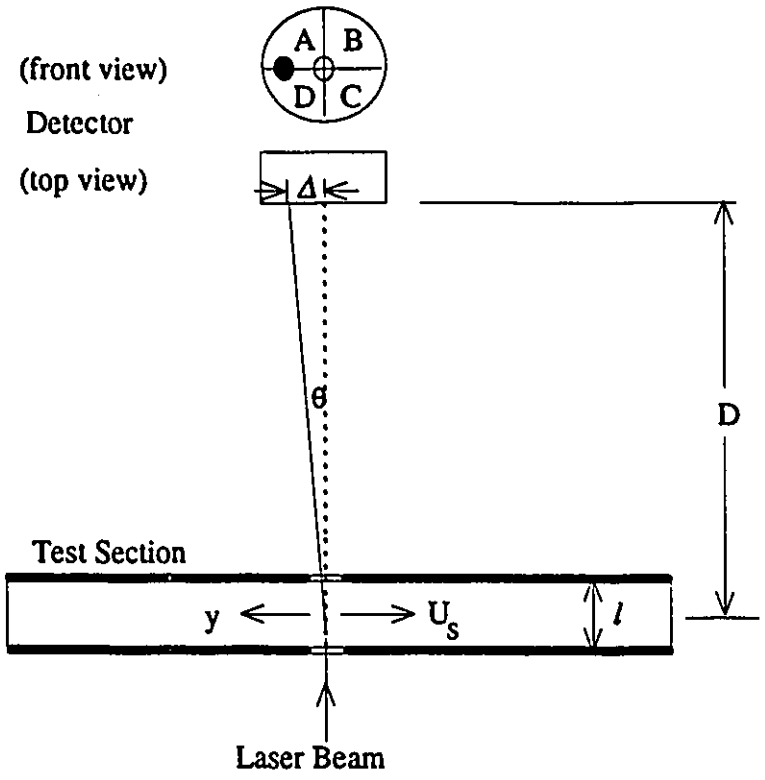

Figure 3.2 Schematic drawing of laser beam deflection on the surface of the quadrant photodiode detector.

$$\Delta = D\theta = Dl\frac{dn}{dy} \qquad (3.2)$$

where D is the distance between the shock tube axis and the detector. The quadrant photodiode detector is wired in a bridge configuration such that it can monitor the deflection precisely:[71] The outputs of quadrants A and C are fed to a differential amplifier to give an output signal $V_1 = V_A - V_C$. The voltages generated by the other two quadrants give a signal $V_2 = V_B - V_D$ through another differential amplifier. In each experiment, the laser beam is initially centred on the photodiode, and the signals from all four quadrants are equal. Any deflection of the laser beam causes the signals to become imbalanced. The horizontal deflection signal is, therefore, $V = V_1 - V_2$. The voltage generated by the detector is proportional to the displacement of the laser beam on its surface.

Figure 3.3 illustrates the detection system of the new shock tube. Electronic signals, V, generated by the quadrant photodiode detector are stored by a transient waveform recorder (Biomation 8100), with the fastest sampling being every 10 *ns*. They are subsequently displayed on a digital oscilloscope (Nicolet 290-111) and transferred onto disks for computer processing .

3.1.2.2 System Calibration

The proportionality between V and Δ can be deduced from a calibration procedure using a rotating mirror. The motor period, τ, of the mirror is 50.04 milliseconds. As the beam is swept across the split Si-photodiode, the signal generated by the sweep is recorded

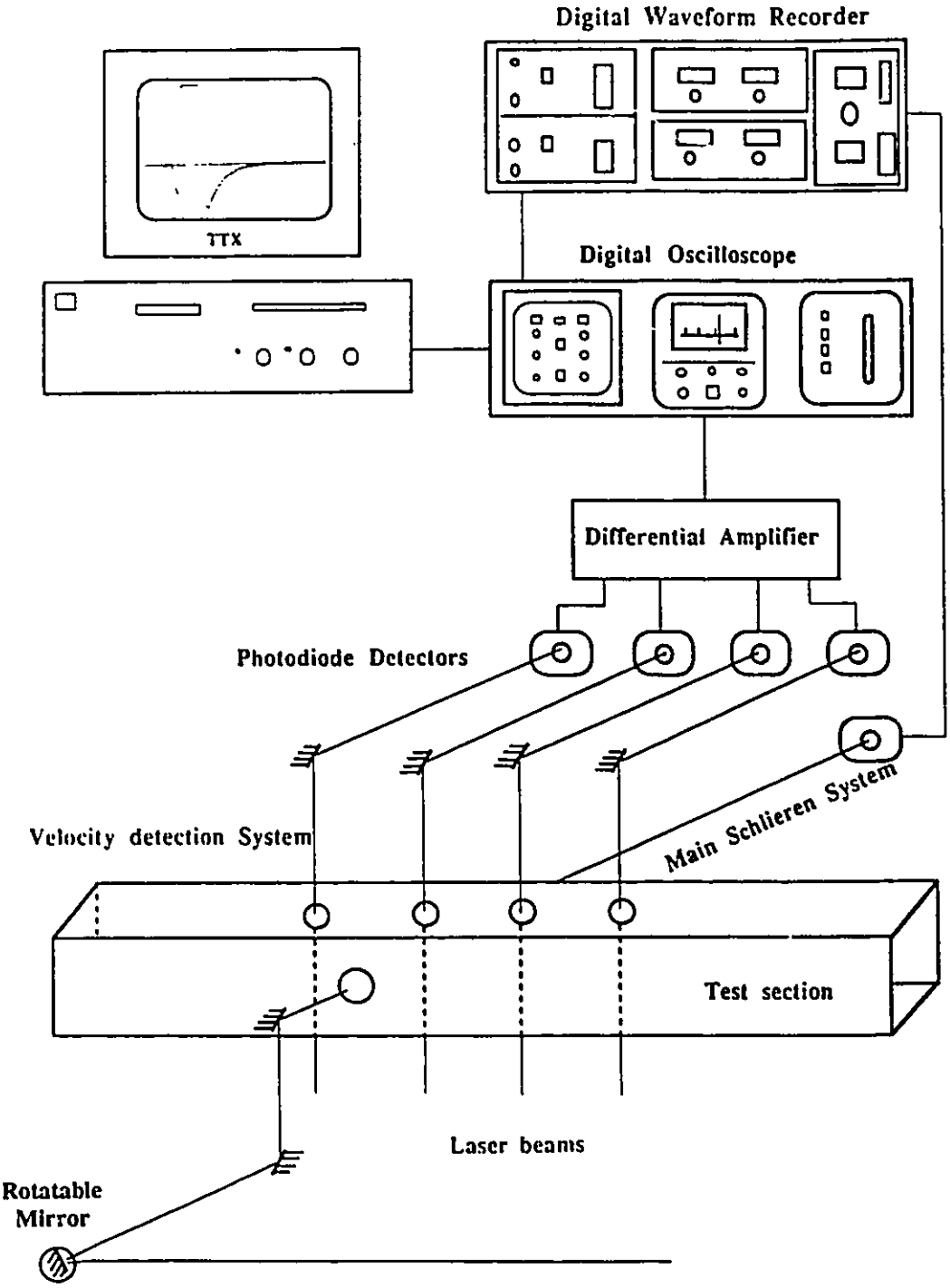

Figure 3.3 Laser-schlieren apparatus (Adapted from reference 102)

by the above-mentioned waveform recorder and oscilloscope. The slope of the signal at the central linear portion and the known sweep velocity are used to calculate the detector's angular sensitivity, $dV/d\Delta$, *ie*

$$\frac{dV}{d\Delta} = \frac{\tau}{4\pi L}\frac{dV}{dt} \qquad (3.3)$$

where L is the beam path length (from the rotating mirror to the detector). This calibration routine is carried out immediately before and after each experiment. The calibration factor, $C_b=(dV/d\Delta)Dl$, for each experiment is given in Appendix 2. Given the calibration factor, the refractive index gradient is related to the voltage signal by

$$\frac{dn}{dy} = \frac{V}{C_b} \qquad (3.4)$$

The uncertainty in the calibration is estimated to be less than 0.4%. The probable error in refractive index gradient is $(1–2)\times10^{-7}$ cm^{-1} mainly coming from the random noise of the detector.

3.1.2.3 Measurement of the Incident Shock Velocity

In the new shock tube, there are four additional laser-schlieren observation stations equipped with Uniphase Model 1105P He-Ne lasers (632.8 *nm*) spanning the main observation port at successive intervals of 305.0, 308.0, and 296.3 *mm*. They are used for the measurement of shock velocity. The velocity of the shock wave is determined by measuring the time intervals between 4 successive electronic pulses generated by the passage

of the shock front across the 4 stations. These signals are sequentially fed into and could be subsequently read directly from the digital oscilloscope. In the old shock tube, 4 gold thin-film resistance gauges (heat transfer gauges) are set at intervals of 133 *mm* spanning the main laser schlieren station. Their positions are accurately known to within 0.1 *mm*. A 6-channel, quartz-crystal controlled time-interval meter is employed to measure the transit times between the four gauges. The time resolution of the electronic time interval meter is 0.1 μs.

The observed shock velocities usually show a slight attenuation as the shock front moves from one station (or gauge) to another. Interpolation of the four time intervals gives the shock velocity at the main observation port. The error in estimating the velocity is less than 0.2%.

From the measured shock velocity, the state of the post-shock gas, such as temperature, pressure, and density, can be calculated from the conservation relations for mass, momentum, and energy.

3.1.3 Chemically Frozen Conditions behind the Incident Shock

It is necessary to introduce shock-fixed coordinates as distinguished from laboratory-fixed coordinates (see figure 3.4).[122] In laboratory coordinates, a shock wave propagates at velocity U_s into a still test gas and the gas behind the shock front moves with the speed, U_2 in the same direction; both velocities are determined with respect to a fixed observer. It is convenient to use shock-fixed coordinates for relating the pressures, temperatures, and densities immediately across the shock. Imagine a situation where an observer "sits on the

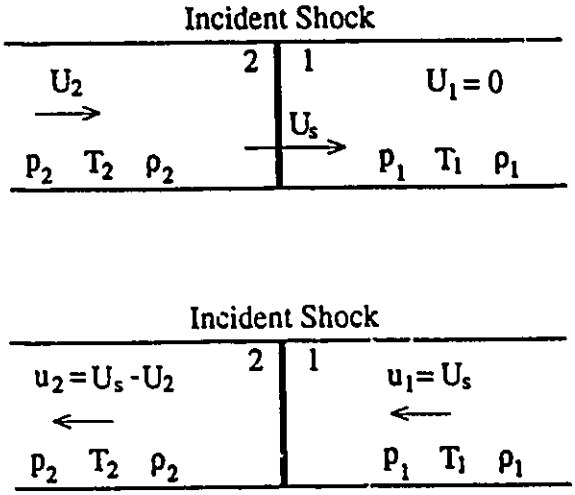

Figure 3.4 Laboratory-fixed coordinates (top) and shock-fixed coordinates (bottom).

shock front" and moves at the shock velocity. The shock is now fixed with respect to the observer and the gas motion is now relative to the shock front. In such a coordinate system, the test gas enters the shock front at a relative velocity u_1, and leaves with a relative velocity, u_2. U denotes the velocity in laboratory-fixed coordinates, and u in shock-fixed coordinates. These two coordinate systems are related by[122]

$$u_1 = U_s \tag{3.5}$$

$$u_2 = U_s - U_2 \tag{3.6}$$

The conditions immediately behind the incident shock wave, that is, before any chemical reaction has occurred, are calculated from the initial conditions of pressure, p_1, density, ρ_1, and temperature, T_1, together with a knowledge of the specific enthalpy, h_1, and the measured speed of the incident shock wave, u_1. This is accomplished by solving the following Rankine-Hugoniot equations[99] in conjunction with the ideal gas law

$$\rho_1 u_1 = \rho_2 u_2 \tag{3.7}$$

$$p_1 + \rho_1 u_1^2 = p_2 + \rho_2 u_2^2 \tag{3.8}$$

$$h_1 + u_1^2/2 = h_2 + u_2^2/2 \tag{3.9}$$

$$p_2 = \rho_2 R T_2/\mu \tag{3.10}$$

where μ is the effective molecular weight. h is a function of temperature alone since the calculation is under chemically frozen conditions. Hence, there are four unknowns (p_2, ρ_2, T_2, and u_2) and four equations. Thermodynamic quantities are obtainable directly from the

JANAF Thermochemical Tables.[85,93] An iterative method was used to calculate the chemically frozen conditions. Appendix 3 gives the shock wave parameters for each experiment.

It is very obvious that the initial conditions are important for the determination of the chemically frozen conditions. The 0.2% uncertainty in the shock velocity measurement results in less than only 10 K error at 1500 K and 20 K error at 4000 K.

3.2 OPERATION

3.2.1 Preparation of Gas Mixtures

Azomethane mixtures of 0.6% - 7.7% diluted in argon or nitrogen were prepared manometrically in a glass vessel and used after 48 hours. It was evacuated to a pressure of 10^{-5} torr before making a mixture. In this way the impurity level could be kept very low. The uncertainty in the azomethane mole fraction X_A is less than $0.01X_A$.

Azomethane was prepared for us by Cambridge Isotope Laboratories. Mass spectrometric analysis indicated 99% purity, with the main impurity being water, which was removed by trap-to-trap distillation. High purity argon and nitrogen (> 99.997% , Air Products) were used to dilute azomethane. The driver gas was helium or hydrogen of high purity grade > 99.997%.

3.2.2 Procedure

For each experiment, the optical detection system was first calibrated using the

rotating mirror. After the calibration, the rotating mirror was replaced by a static mirror. To make sure that the laser beam was centred on the quadrant photodiode detector, an electric chopper rotating at 3000 *rpm* was placed between the laser source and the detector. The voltage signals generated by the four quadrants were fed into the differential inputs of Textronix 2213 Oscilloscopes. The detector was adjusted both vertically and horizontally until the voltage differences, V_A-V_B, V_D-V_C, V_A-V_D, and V_B-V_C, were set to zero, thus ensuring that the laser beam was centred on the detector.

The shock tubes were evacuated using rotary and diffusion pumps (Edwards High Vacuum ED 250, EDM12, and E01, E02, the latter charged with Dow Corning 705 silicone fluid) to lower than 10^{-4} *torr*. The combined leak and out-gassing rate was less than 10^{-3} *torr/min*. Vacuum was monitored using an Edwards Model 14 Pirani gauge. The azomethane mixture was introduced into the test section within one minute.

Shock waves were generated by spontaneously pressure-bursting aluminium diaphragms with the driver gas. Usually, helium was used to produce the shock waves having velocities under 1800 *m/s* while hydrogen was employed to generate the stronger shock waves. The passage of the shock front past the observation window triggered the transient waveform recorder (Biomation), which thus captured the laser schlieren signal. With the pretriggering feature, the Biomation unit could record the zero base line prior to the arrival of the shock wave. The four successive electronic pulses from velocity detectors or gauges generated by the passage of the shock wave were captured by the Nicolet oscilloscope or by the velocity (time-interval) meter. After those signals were properly recorded on computer disks, the optical detection system was recalibrated.

All measurements were made behind incident shock waves, covering the very wide temperature range 560 - 4070 K in 0.6% - 7.7% azomethane diluted in argon or nitrogen to pressures of 0.05 - 1.1 atm. About ninety shocks were successfully fired.

3.3 OBSERVATIONS AND DISCUSSION

According to the Gladstone Dale Law,[100]

$$n = 1 + \kappa\rho \tag{3.11}$$

where κ is the specific refractivity of the test gas. Because the gas mixtures used in this study contain mostly argon or nitrogen, the change in specific refractivity in a given experiment is much smaller than the change in density. Therefore the observed refractive index gradients are basically density gradients. Since the pressure behind the incident shock wave is roughly constant, the temperature is inversely proportional to the density approximately, and so the observations are closely related to the temperature gradient and hence to the rate of reaction (weighted by the reaction enthalpy).

Figure 3.5 is a laser schlieren signal for pure argon. The large negative and positive spikes, caused by the interaction of the laser beam and the shock front, indicate the passage of the shock front. This is a purely physical process, and this experiment merely serves as a check of the performance of the experimental set-up.

The observed laser schlieren signals of azomethane mixtures can be classified into five different patterns associated with different temperature ranges. There are slight temperature overlaps in the pattern transitions depending on pressure and composition.

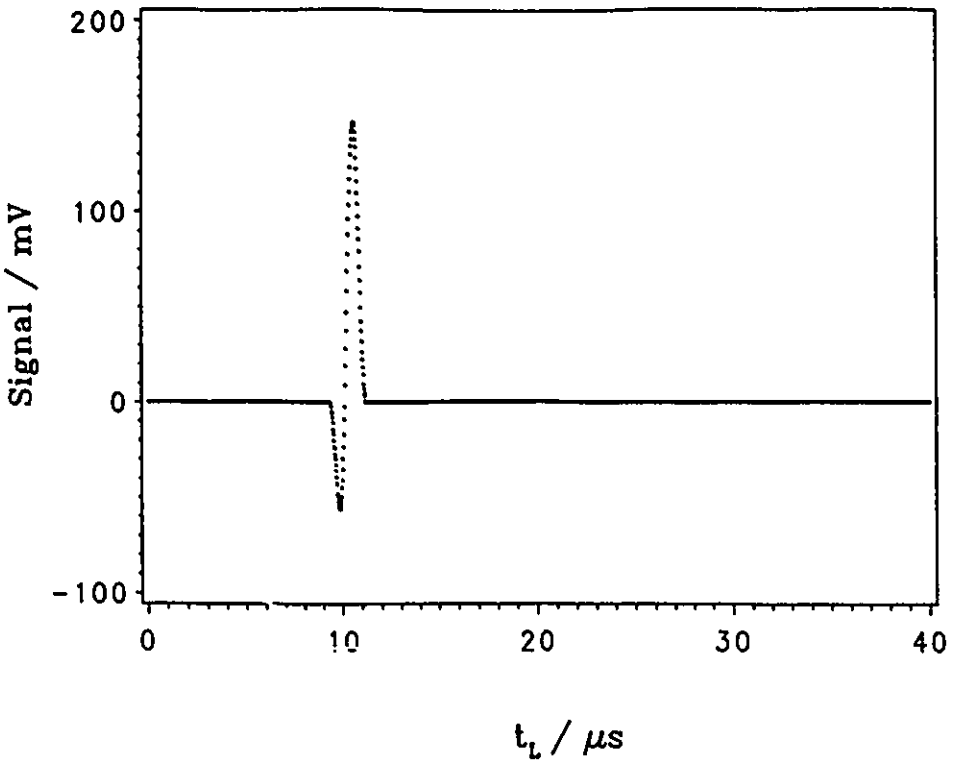

Figure 3.5 Laser schlieren signal for pure argon (U_s = 1420 m/s, T_1 = 294 K).

3.3.1 Laser Schlieren Signals at Low Temperatures (Pattern A)

Figure 3.6 shows some of the laser schlieren signals having pattern A. These were observed in the temperature range 560 - 900 K. After the passage of the shock front, there follows a very slowly decaying negative signal characteristic of exothermic processes. The half-life for the pyrolysis of azomethane requires more than a millisecond in this temperature range. It has been established that the mechanism for the decomposition of azomethane in this temperature range can be described as follows:[12,22,90-91]

$$CH_3N{=}NCH_3 \rightarrow 2\,CH_3\cdot + N_2 \qquad \text{(I)}$$

$$CH_3\cdot + CH_3N{=}NCH_3 \rightarrow CH_4 + CH_3N{=}NCH_2\cdot \qquad \text{(II)}$$

$$CH_3N{=}NCH_2\cdot \rightarrow CH_3\cdot + CH_2\cdot + N_2 \qquad \text{(III)}$$

$$CH_3\cdot + CH_3\cdot \rightarrow C_2H_6 \qquad \text{(IV)}$$

The chain is initiated by the endothermic step (I). In the propagation step (II), methyl radicals attack the parent azomethane. Although step (II) does not directly contribute to the laser schlieren signals (because it is nearly thermoneutral), the endothermicity of the subsequent step (III) does affect the signals. Methyl recombination terminates the chain. The four steps have an overall exothermicity of 16 *kcal mol*$^{-1}$, which accounts for the negative signals. In addition to these four main reactions, some other reaction pathways might also exist. Step (I) could occur in two successive steps (step A and step B) as described in the previous chapter (section 2.3). Step (II) could produce C_2H_6 and CH_3NN. Step (II) might also end up with the radical $(CH_3)_2N\text{-}NCH_3$,[22,91] which could attach to azomethane molecules, successively forming polymers of the form $(CH_3)_2N\text{-}N(CH_3)(A_n\text{-}R)$ [91] at a later time, where

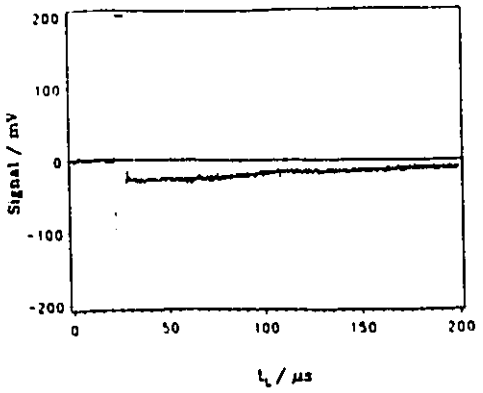

(1) 6.78% azomethane/Ar, T_2=566 K, P_2=115 Torr (exp12.35)

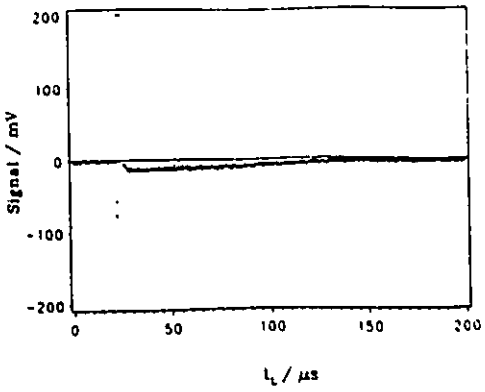

(2) 6.78% azomethane/Ar, T_2=745 K, P_2=52 Torr (exp12.48)

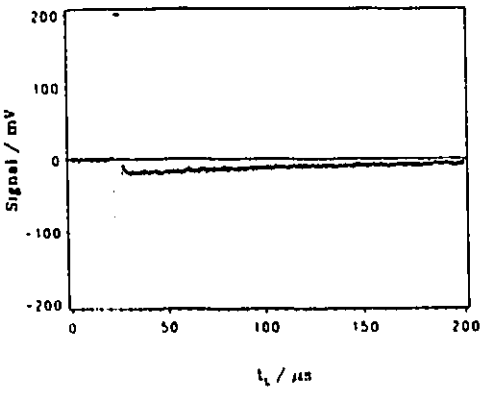

(3) 1.75% azomethane/Ar, T_2=691 K, P_2=69 Torr (exp13.12)

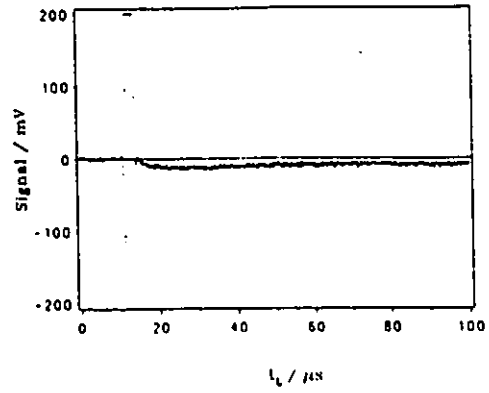

(4) 7.02% azomethane/N_2, T_2=614 K, P_2=45 Torr (exp14.32)

Figure 3.6 Laser schlieren signals with pattern A at low temperatures

A_n represents n units of azomethane and R represents a radical. The radical $CH_3N_2CH_2\cdot$ has two resonance structures, CH_3-N=N-$CH_2\cdot$ and CH_3-N-N=CH_2.[91] The reaction between $CH_3\cdot$ and $CH_3N_2CH_2\cdot$ could result in the production of methylethyldiimide ($CH_3N=NC_2H_5$) and dimethylhydrazone ($(CH_3)_2N$-N=CH_2). Ethyl radicals might also be involved in the mechanism. An alternative of step (III) could be the formation of CH_3 + N_2CH_2.

The aim of this thesis is to study the primary methyl-methyl reactions. Since methyl-methyl reactions at low temperatures (mainly methyl recombination) are well established, and since the complicated pyrolysis of azomethane cannot provide a clean source of methyl radicals at such low temperatures, there is no further analysis of these signals. This is merely a prelude to the secondary purpose of identifying when the system gets in and out of chaos.

3.3.2 Chaotic Laser Schlieren Signals (Pattern B)

When azomethane mixtures were shock-heated to 900 - 1300 K, chaotic or oscillatory signals were observed. Some of the signals are shown in Figure 3.7.1. The signals transformed from the well-behaved pattern A to the chaotic pattern B. This is the first experimental observation of chaos in the pyrolysis of azomethane, previously not even anticipated. Although the signals are irregular, they are reproducible and have some similarities. As shown in Figure 3.7.1, the two lower-temperature signals (Figure 3.7.1 (1) and (3)) are very similar except that chaotic behaviour in the azomethane mixture diluted by nitrogen begins at a slightly lower temperature than when diluted by argon. The two similar higher-temperature signals (Figure 3.7.1 (2) and (4)) are also shifted in temperature. At

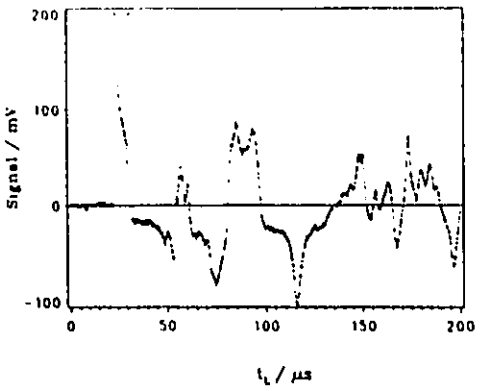

(1) 6.78% azomethane/Ar, T_2=911 K, P_2=42 Torr (exp12.55)

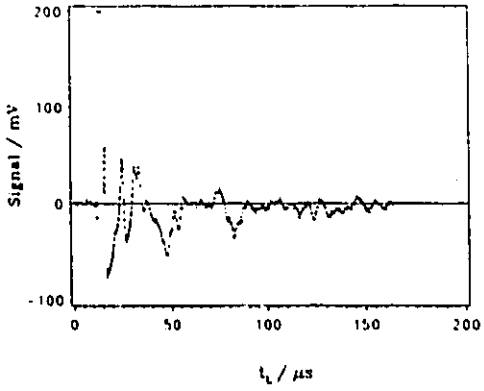

(2) 1.75% azomethane/Ar, T_2=1190 K, P_2=90 Torr (exp13.37)

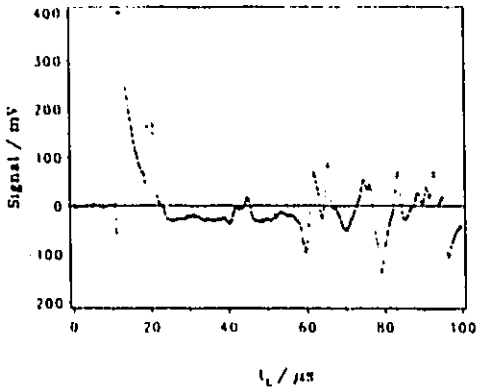

(3) 7.02% azomethane/N_2, T_2=830 K, P_2=70 Torr (exp14.26)

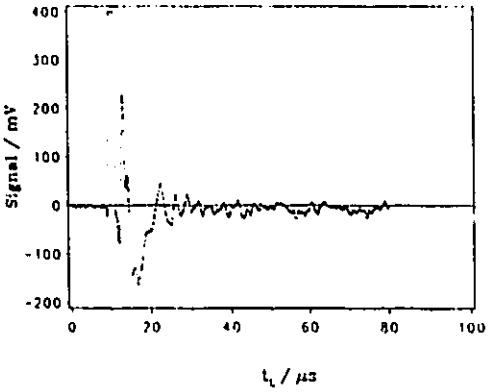

(4) 7.02% azomethane/N_2, T_2=1067 K, P_2=107 Torr (exp14.35)

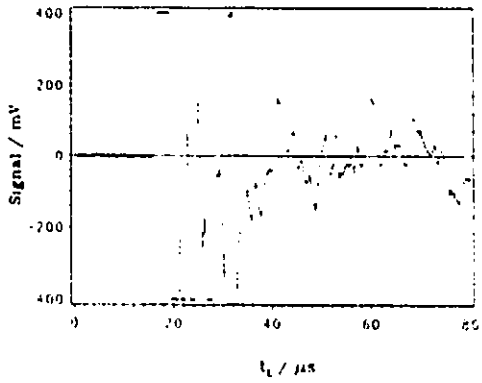

(5) 6.52% azomethane/Ar, T_2=1015 K, P_2=453 Torr (exp 9.2)

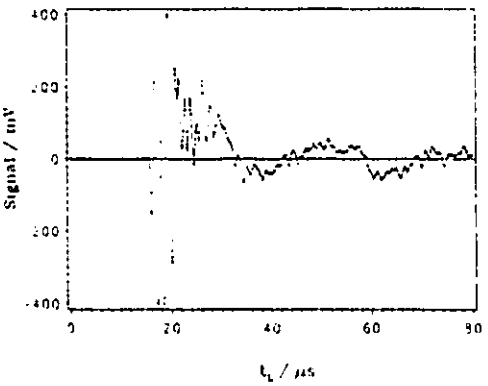

(6) 6.52% azomethane/Ar, T_2=1298 K, P_2=892 Torr (exp 9.3)

Figure 3.7.1 Chaotic laser schlieren signals with pattern B

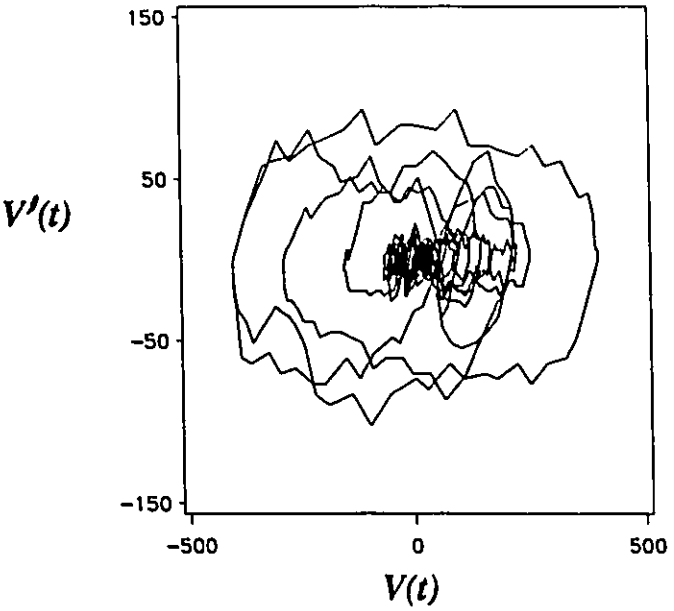

Liapunov characteristic exponent = 0.106 ± 0.020 (exp. 9.3)

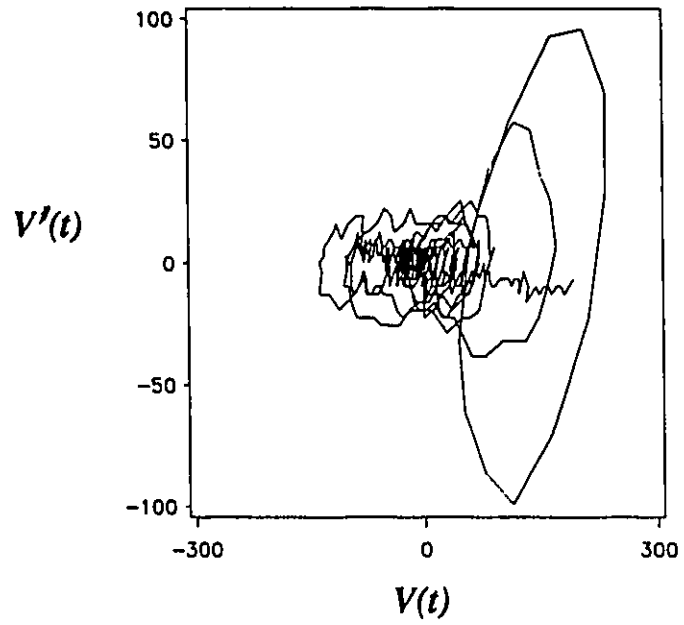

Liapunov characteristic exponent = 0.141 ± 0.019 (exp. 14.26)

Figure 3.7.2 Two-dimensional phase-space plots

higher pressures, experiments exhibit more chaotic signals (Figure 3.7.1 (5) and (6)). It appears that the signals have oscillatory components.

Figure 3.7.2 shows two phase-space pictures, where the derivatives, $V'(t)$, of the signals are plotted versus the magnitudes, $V(t)$, of the signals in the two-dimensional plots according to the techniques outlined by Packard et al.[137] Each of the two phase-space plots has an evident structure and an "attractor", suggesting a chaotic system.

The laser schlieren signal is proportional to the sum of the products of the elementary rate constants and their heats of reactions[101] ($\sum k_i \Delta H_i$). As temperature increases, the endothermic reactions in the pyrolysis mechanism (ie. step (I) and (III) etc) become faster. Therefore, there are opportunities for endothermic reactions to dominate the mechanism in certain periods of time, resulting in positive signals in those time periods. Initially, azomethane decomposes to methyl radicals, causing a temperature drop and a density rise. There should be a positive signal. At the same time, the temperature drop causes the endothermic reactions to slow down relative to the exothermic reactions. Methyl recombination and other exothermic reactions then overwhelm the mechanism. As the temperature increases and the density decreases, negative signals appear because of the exothermicity. In return, the high temperature accelerates the azomethane decomposition and other endothermic reactions as well. Superimposed on these swings are variations in the temperature-dependent equilibrium concentrations. The alternating domination of endothermic and exothermic reactions together with widely varying time lags and nonlinear thermal feedback is perhaps the reason for the oscillatory and chaotic behaviours.

There has been extensive interest in studying chemical chaos and developing methods

for coupling nonlinear systems in order to generate more exotic nonlinear phenomena.[137-139] Two such studies have been conducted in this laboratory. Oscillatory and chaotic phenomena were found for the condensation of Freon-11 (CCl_3F) vapour at about 400 K.[102, 103] These systems including ours are obviously nonlinear ones in some situations because rate constants and equilibrium concentrations depend nonlinearly on temperature. Therefore, they should be treated differently using nonlinear kinetics and dynamics. A full analysis is underway. Hopefully, this will help to understand irregular systems better.

3.3.3 Negative Laser Schlieren Signals (Pattern C)

As temperature goes beyond the chaotic regime, ie. T > 1300 K, laser schlieren signals become well-behaved again. This is illustrated in Figure 3.8, where the prominent negative signals decay on the microsecond time scale. Those signals are the signatures for strong exothermic reactions. In experiments at higher temperatures, up to 2400 K or more, the same shape of signal was observed with the decay time still on the microsecond time scale. Above 1300 K, an azomethane molecule decomposes into two methyl radicals plus a nitrogen molecule in less than one microsecond. This is fast enough to exclude the possibility of methyl-azomethane reactions.[8] The pyrolysis mechanism for azomethane becomes much simpler. By the earliest observable point in time (the second minimum of each signal in figure 3.8), azomethane is destroyed completely. Thus azomethane decomposition above 1300 K creates an almost instant source of methyl radicals, which makes it possible to investigate the primary reactions of methyl radicals.

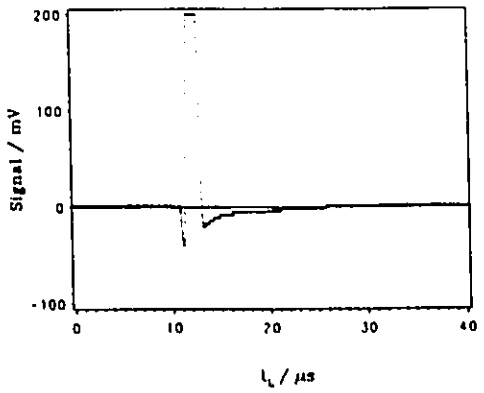

(1) 0.62% azomethane/Ar, T_2=1414 K, P_2=294 Torr (exp2.4)

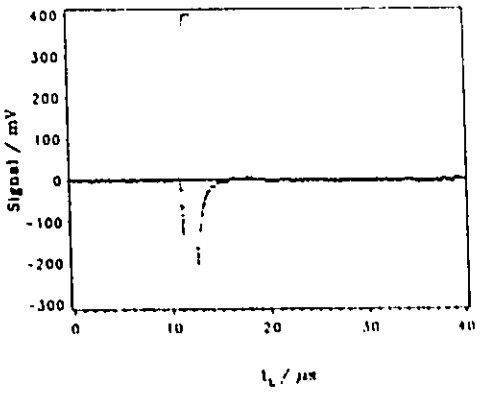

(2) 7.02% azomethane/N_2, T_2=1354 K, P_2=152 Torr (exp14.24)

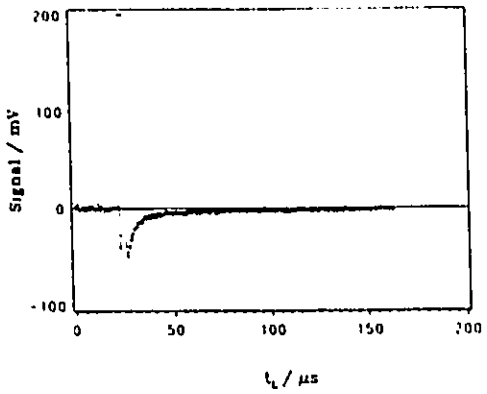

(3) 1.75% azomethane/Ar, T_2=1426 K, P_2=87 Torr (exp13.35)

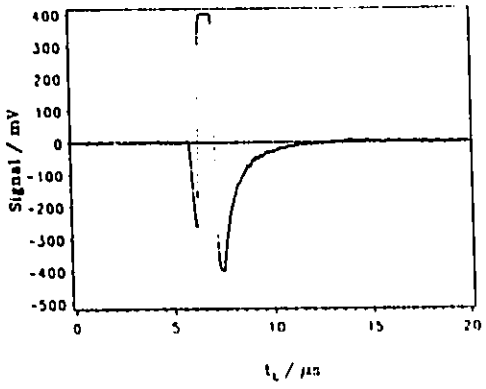

(4) 6.30% azomethane/Ar, T_2=1655 K, P_2=166 Torr (exp5.3)

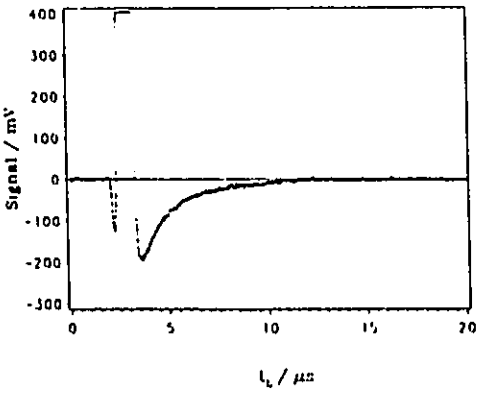

(5) 4.25% azomethane/Ar, T_2=1656 K, P_2=112 Torr (exp6.2)

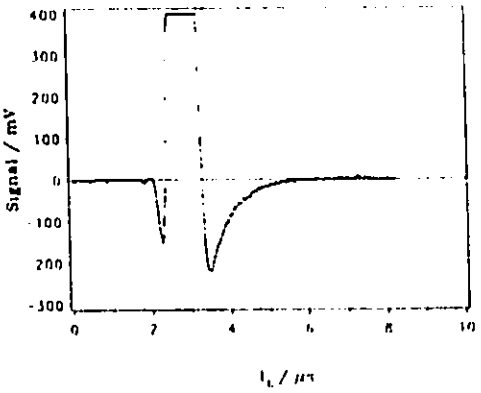

(6) 6.30% azomethane/Ar, T_2=2095 K, P_2=171 Torr (exp5.5)

Figure 3.8 Negative laser schlieren signals with pattern C

3.3.4 Pressure Effects at Intermediate Temperatures (Pattern D)

At higher pressures within the temperature range of pattern C, laser schlieren signals become progressively more positive. For each schlieren trace, as shown in Figure 3.9, a more slowly decaying positive component follows the very fast negative decay. This is called pattern D henceforth. The pressure threshold for the appearance of the positive component decreases at higher temperatures.

Possible reactions of methyl radicals as primary steps include six competing channels:

$$CH_3 + M \rightarrow CH + H_2 + M \qquad \Delta H^0_{298} = 448 \text{ kJ mol}^{-1} \qquad (1)$$

$$\rightarrow CH_2 + H + M \qquad \Delta H^0_{298} = 459 \text{ kJ mol}^{-1} \qquad (2)$$

$$CH_3 + CH_3 \rightarrow C_2H_5 + H \qquad \Delta H^0_{298} = 43.8 \text{ kJ mol}^{-1} \qquad (3)$$

$$C_2H_4 + H_2 \qquad \Delta H^0_{298} = -239 \text{ kJ mol}^{-1} \qquad (4)$$

$$C_2H_6 \qquad \Delta H^0_{298} = -375 \text{ kJ mol}^{-1} \qquad (5)$$

$$CH_4 + CH_2 \qquad \Delta H^0_{298} = 20.1 \text{ kJ mol}^{-1} \qquad (6)$$

It is obvious that reactions (4) and (5) are responsible for the negative laser schlieren signals (pattern C) and the negative components of the signals (pattern D). In order to identify which reactions cause positive components, some experiments were done at more reduced azomethane concentrations.

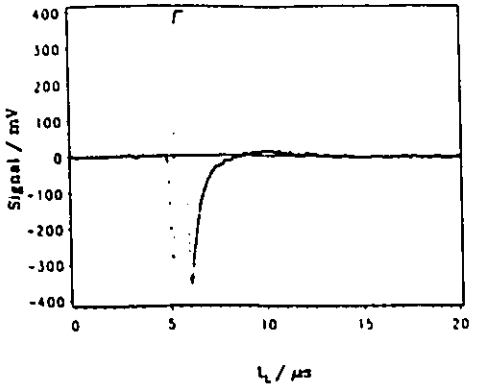

(1) 6.30% azomethane/Ar, T_2=2005 K, P_2=179 Torr (exp4.8)

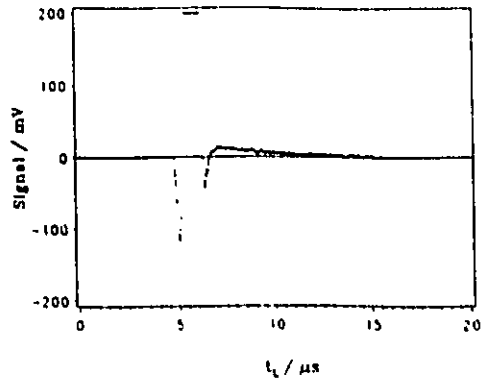

(2) 7.69% azomethane/Ar, T_2=2025 K, P_2=451 Torr (exp10.1)

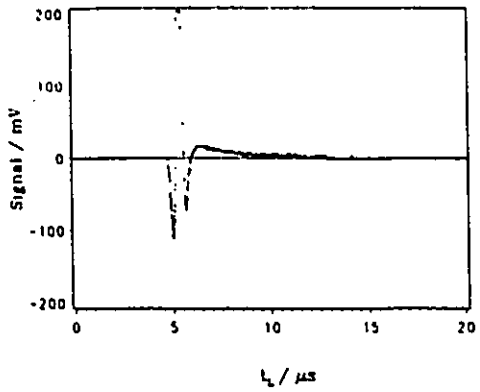

(3) 6.55% azomethane/Ar, T_2=2285 K, P_2=496 Torr (exp11.26)

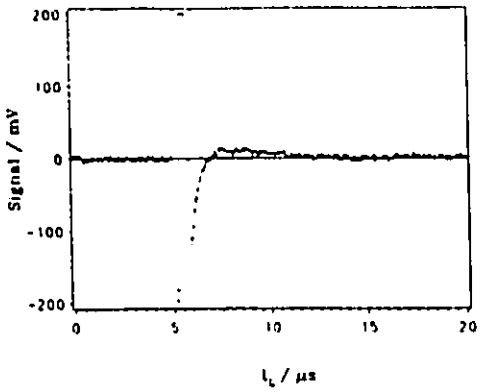

(4) 7.02% azomethane/N_2, T_2=1796 K, P_2=250 Torr (exp14.13)

Figure 3.9 Pressure effects on laser schlieren signals (pattern D)

3.3.5 Dilution Effects at Intermediate Temperatures (Pattern C+)

As azomethane was diluted more and more at intermediate temperatures, it was observed that not only did the signal decrease in magnitude, as expected, but the positive component shifted to longer and longer times, eventually separating completely from the negative component. Figure 3.10 shows six schlieren traces demonstrating the dilution effects. Figures 3.10, (2), (4), and (6) also demonstrate that the positive component shifts to longer times if the temperature drops. All of this indicates quite clearly that the positive components are caused by secondary or tertiary endothermic reactions rather than the dissociation of methyl radicals. Indeed, a recent theoretical calculation by us[104] (see also the previous chapter) and the numerical simulation to be described later show that the rates of reactions (1) and (2) are much too small to contribute significantly to the observed signals at intermediate temperatures. Rather, it is reactions (3)-(6) which are responsible for the exothermic signals or components, while subsequent dissociation reactions are responsible for the endothermic components:

$$C_2H_4 \rightarrow C_2H_3 + H \qquad \Delta H^0_{298} = 452 \text{ kJ mol}^{-1} \qquad (12)$$

$$C_2H_5 \rightarrow C_2H_4 + H \qquad \Delta H^0_{298} = 154 \text{ kJ mol}^{-1} \qquad (13)$$

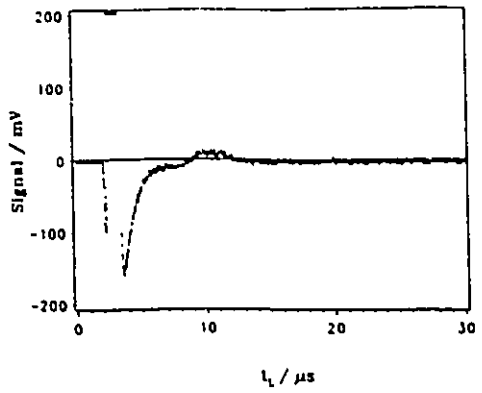

(1) 4.25% azomethane/Ar, T_2=1998 K, P_2=159 Torr (exp6.1)

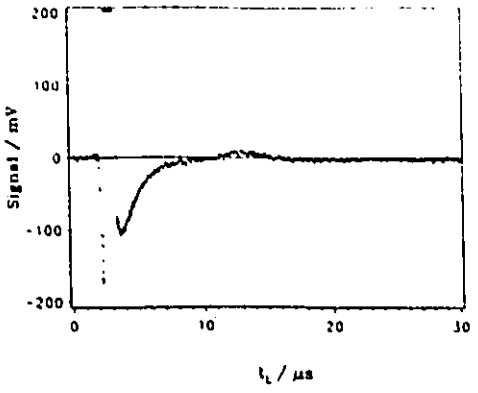

(2) 3.20% azomethane/Ar, T_2=1908 K, P_2=140 Torr (exp7.1)

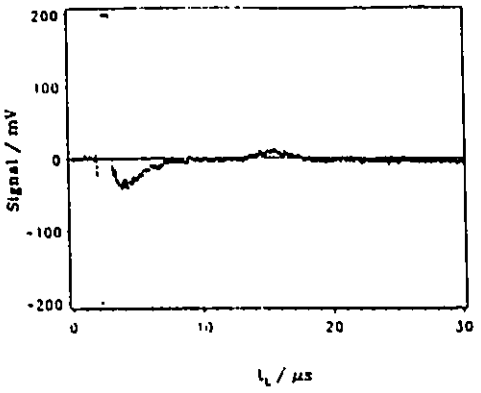

(3) 1.90% azomethane/Ar, T_2=2051 K, P_2=140 Torr (exp7.3)

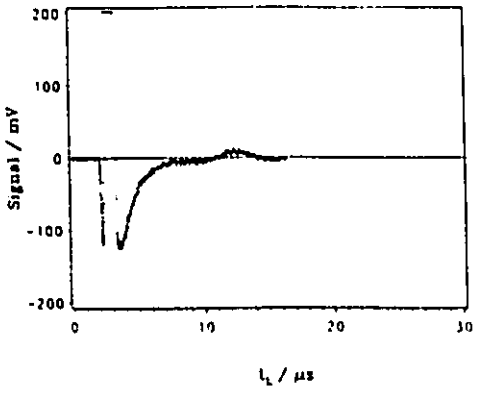

(4) 3.20% azomethane/Ar, T_2=2015 K, P_2=149 Torr (exp6.8)

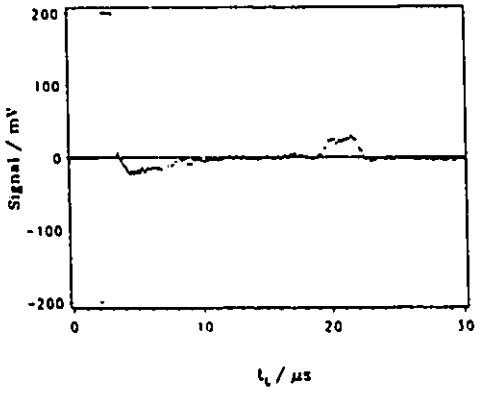

(5) 0.69% azomethane/Ar, T_2=2072 K, P_2=335 Torr (exp4.7)

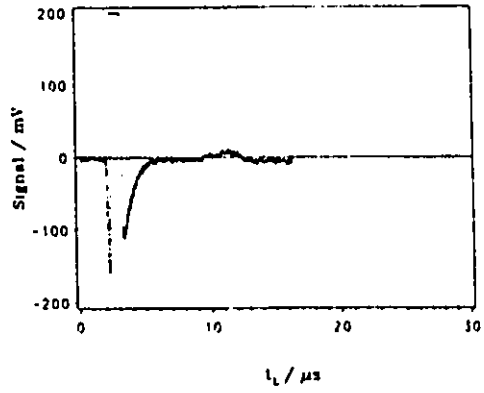

(6) 3.20% azomethane/Ar, T_2=2264 K, P_2=172 Torr (exp6.7)

Figure 3.10 Dilution and temperature effects on laser schlieren signals (pattern C+).

3.3.6 Positive Laser Schlieren Signals (Pattern E)

It was mentioned previously that the pressure threshold for the appearance of the positive component decreases at higher temperatures and that the positive component shifts to earlier times as the temperature increases. Starting from 2600 K, the signals are dominated by a positive component (see Figure 3.11) even at relatively low pressures. Such positive signals are characteristic of endothermic reactions. This is not to say that there are no exothermic reactions occurring. Rather, the overall thermochemistry, *ie* the net effect, is endothermic. Secondary dissociation reactions (such as of C_2H_4 and of C_2H_5 etc) still account for the positive signals at these high temperatures. In addition, the primary decomposition of methyl radicals might contribute to the observed signals above 3000 K.

The next two chapters will be devoted to the analysis of the observed laser schlieren traces with patterns C, D, and E.

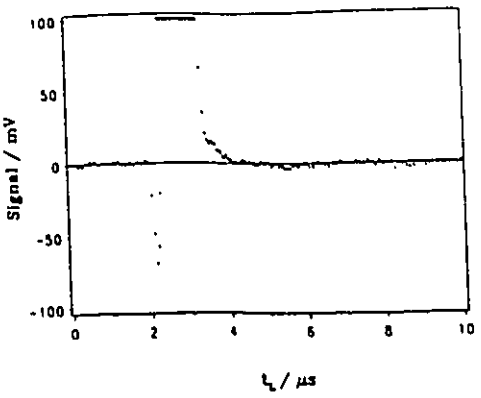

(1) 0.69% azomethane/Ar, T_2=2584 K, P_2=166 Torr (exp4.5)

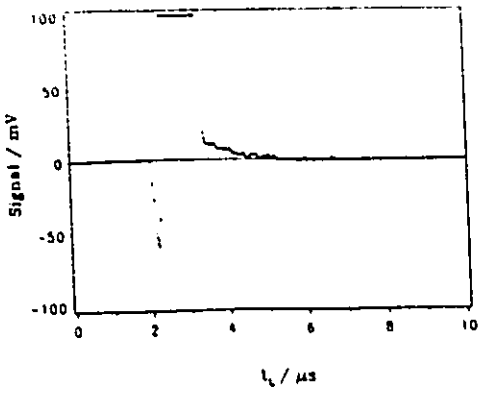

(2) 7.69% azomethane/Ar, T_2=2855 K, P_2=242 Torr (exp10.2)

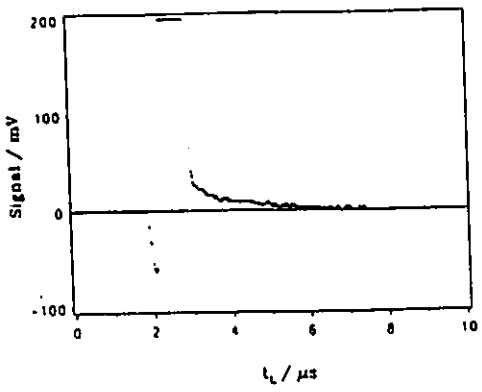

(3) 6.55% azomethane/Ar, T_2=3099 K, P_2=312 Torr (exp11.33)

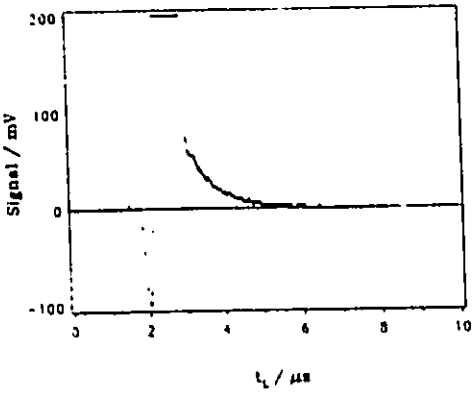

(4) 6.55% azomethane/Ar, T_2=3349 K, P_2=651 Torr (exp11.14)

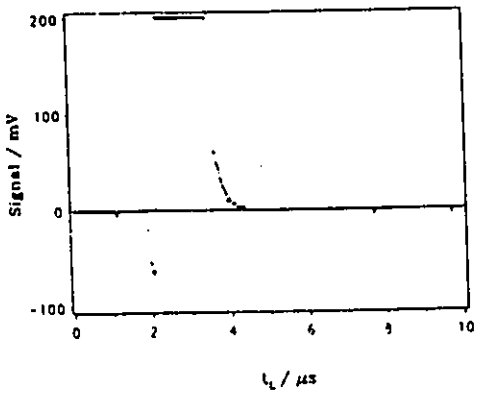

(5) 6.55% azomethane/Ar, T_2=4014 K, P_2=846 Torr (exp11.13)

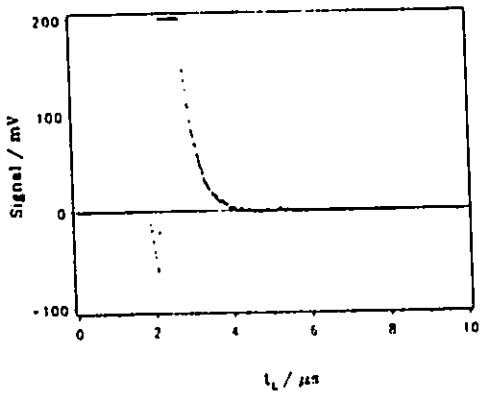

(6) 6.55% azomethane/Ar, T_2=4067 K, P_2=472 Torr (exp11.27)

Figure 3.11 Positive laser schlieren signals with pattern E

CHAPTER 4

POINT BY POINT ANALYSIS

In this chapter, we shall show our preliminary data analysis for the experiments with C-type signals. A more rigorous analysis based on a full simulation of the experiments will be discussed in the next chapter. As described in the previous chapter, the following set of bimolecular reactions are responsible for the exothermic component of the experimental signal,

$$CH_3 + CH_3 \rightarrow C_2H_5 + H \qquad \Delta H^0_{298} = 43.8 \text{ kJ mol}^{-1} \qquad (3)$$

$$C_2H_4 + H_2 \qquad \Delta H^0_{298} = -239 \text{ kJ mol}^{-1} \qquad (4)$$

$$C_2H_6 \qquad \Delta H^0_{298} = -375 \text{ kJ mol}^{-1} \qquad (5)$$

$$CH_4 + CH_2 \qquad \Delta H^0_{298} = 20.1 \text{ kJ mol}^{-1} \qquad (6)$$

while the subsequent dissociation reactions are responsible for the endothermic signal:

$$C_2H_4 \rightarrow C_2H_3 + H \qquad \Delta H^0_{298} = 452 \text{ kJ mol}^{-1} \qquad (12)$$

$$C_2H_5 \rightarrow C_2H_4 + H \qquad \Delta H^0_{298} = 154 \text{ kJ mol}^{-1} \qquad (13)$$

Defining α as the degree of reaction at time t_g, the amount of CH_3 remaining compared to the initial amount of CH_3, $n_{0,CH3}$, is $n_{CH3} = n_{0,CH3}\,(1 - 2\alpha)$. The rate of reaction $CH_3 + CH_3$

is given by

$$v = -\frac{1}{2V}\frac{dn_{CH_3}}{dt_g} = \frac{n_{0,CH_3}}{V}\frac{d\alpha}{dt_g} = \frac{X_0\rho}{\mu_0'}\frac{d\alpha}{dt_g} \qquad (4.1)$$

where the initial mole-fraction of CH_3 in the post-shock gas, $X_0 = 2X_A/(1+2X_A)$, with X_A being the mole fraction of azomethane in the preshock gas. The initial effective molecular weight of the postshock gas, $\mu'_0 = \mu_0/(1 + 2X_A)$, where μ_0 is the effective molecular weight of the preshock gas, ie of the initial mixture of azomethane and Ar. ρ is the gas density at time t_g. t_g is the real time that the gas has been processed at the high temperature, in distinction to the lab time, t_l, which corresponds to the distance from the shock front. $dy/dt_l = u_0$ = the shock velocity, while $dt_g / dt_l = \rho/\rho_0$.[71] V is the gas volume.

The power of the laser-schlieren technique lies in its ability to probe the primary reaction of a complicated mechanism.[101,105] Consequently, our first step in analyzing the negative signals is to ignore the endothermic steps (12) and (13). As has been shown in references 101, and 105, and as will be shown below, the observed signal in a laser schlieren experiment is proportional to the sum of the elementary rate coefficients, k_i, weighted by their heats of reaction. By virtue of this property a thermoneutral reaction will not contribute to the overall signal. Such is very nearly the case for reaction (6) relative to the other reactions. We can therefore analyze the exothermic signal very simply and analytically point-by-point if we consider merely reactions (3) - (5).

The rate coefficients, k_3 and k_4, for reactions (3) and (4) are not very well known. For example, the results of Frank and Braun-Unkhoff[18] for k_3 differ from those of Kiefer and Budach[54] by a factor of 30, while the results of Kern et al[59] for k_4 differ from those of Hidaka

et al[61] by more than a factor of 100. Even if we take the conservative choice, following the recommendations of Warnatz,[2] we still conclude that k_4 is larger than k_3 at all temperatures. In addition, the rate of reaction (3) is weighted by a much smaller heat of reaction. Thus our simple analysis reduces to considering only reactions (4) and (5).

4.1 THERMODYNAMIC AND KINETIC CONSIDERATIONS

k_5 decreases with increasing temperature, while k_4 increases with temperature. Somewhere between 1700 and 2300 K, C_2H_6 and C_2H_4 formation compete for domination. Note that it is exactly in this temperature range that k_5 is least well known (see Figure 1.2). It is also the region where thermodynamics and kinetics battle for control of the fate of CH_3: In this temperature range the equilibrium of reaction (5) is far to the left, whereas that of reaction (4) is far to the right. Thus thermodynamically, C_2H_4 formation is preferable to C_2H_6 formation. This will be discussed below.

(a) $CH_3 + CH_3 \rightarrow C_2H_6$

The rate of the reaction can be cast into the form

$$d\alpha/dt_g = k_5 [\,(1-2\alpha)^2 X_0 \rho/\mu'_0 - \alpha/K_c] \qquad (4.2)$$

with the effective molecular weight $\mu = \mu'_0/(1-X_0\,\alpha) = \mu_0/[1+2X_A(1-\alpha)]$. The maximum degree of this reaction, α_∞, can be obtained by setting $d\alpha/dt_g = 0$. At equilibrium

$$\alpha_\infty = \frac{1}{2}\left[\,\left(1+\frac{\mu_0}{8X_A\rho_\infty K_c}\right) \pm \sqrt{\left(1+\frac{\mu_0}{8X_A\rho_\infty K_c}\right)^2-1}\,\right] \qquad (4.3)$$

where ∞ denotes the equilibrium condition and K_c denotes the equilibrium constant. We use

$\alpha_{\infty(+)}$ and $\alpha_{\infty(-)}$ to distinguish between the 2 possibilities. The physically realistic choice is $\alpha_{\infty(-)}$ because α should not be larger than 1/2. It should be noted that the degree of the reaction depends on the gas composition and the total pressure (or density) in addition to the temperature.

(b) $CH_3 + CH_3 \rightleftharpoons C_2H_4 + H_2$ and/or $CH_3 + CH_3 \rightleftharpoons C_2H_5 + H$

The rate of either reaction can be cast into the form

$$d\alpha/dt_g = k[(1-2\alpha)^2 - \alpha^2/K_c]X_0\rho/\mu'_0 \qquad (4.2b)$$

with the effective molecular weight $\mu = \mu'_0 = \mu_0/(1+2X_A)$. The rate coefficient, k, is either k_4 or k_3. In the same manner, the maximum degree of either reaction is given by

$$\alpha_\infty = \frac{2 \pm K_c^{-1/2}}{4 - K_c^{-1}} \qquad (4.3b)$$

Note that the degree of reaction of each of these two reactions depends only on temperature.

$\alpha_{\infty(-)}$'s for the three reactions are plotted as a function of temperature in Figure 4.1. The degree of reaction for $CH_3 + CH_3 \rightleftharpoons C_2H_6$ drops dramatically starting from about 1700 K and declines to essentially zero at about 2300 K. The calculation was done for different gas compositions at a typical pressure of 0.2 atm. As can be seen from the figure, the smaller the content of azomethane, the lower the temperature where $\alpha_{\infty(-)} = 0$. It is also true that $\alpha_{\infty(-)}$ reaches zero at a lower temperature if one reduces the pressure. In contrast, $\alpha_{\infty(-)}$ for $CH_3 + CH_3 \rightleftharpoons C_2H_4 + H_2$ is almost a constant value of 0.5 in the whole temperature range. Also shown in Figure 4.1 is $\alpha_{\infty(-)}$ for $CH_3 + CH_3 \rightleftharpoons C_2H_5 + H$. It increases with increasing temperature. But it is small compared to the other two channels below 2000 K.

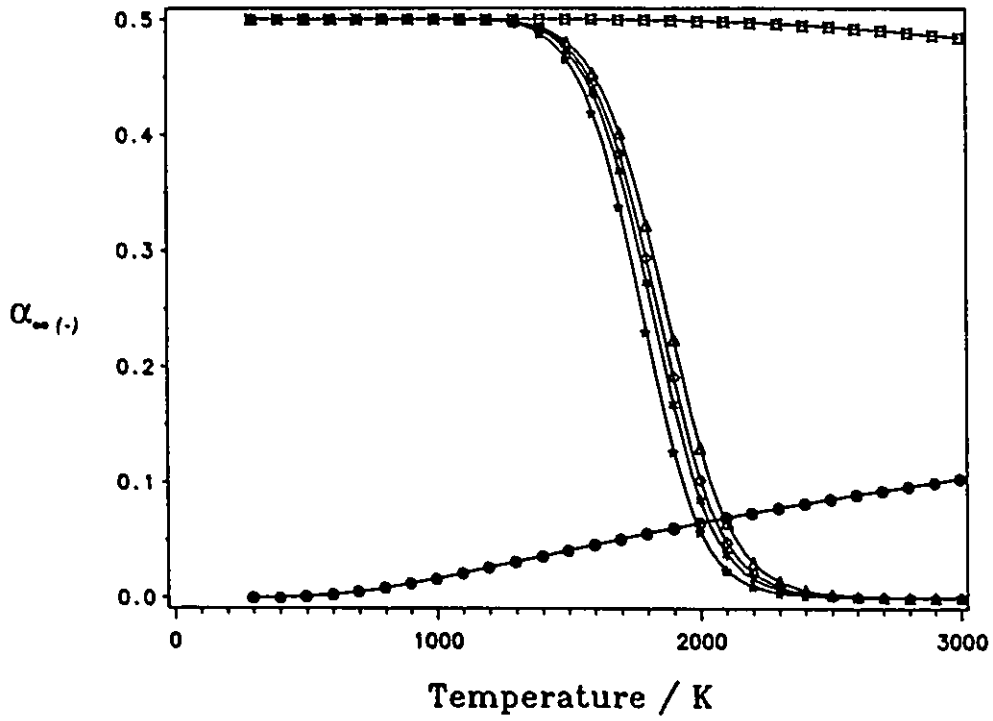

Figure 4.1 Maximum degrees of reaction for (1) $CH_3 + CH_3 \rightleftharpoons C_2H_6$: ▵ X_A= 6.30%; ◊ X_A= 4.25%; * X_A= 3.20%; ⋆ X_A= 1.9% and (2) $CH_3 + CH_3 \rightleftharpoons C_2H_4 + H_2$: □ as well as (3) $CH_3 + CH_3 \rightleftharpoons C_2H_5 + H$: ⊕.

$CH_3 + CH_3 \rightleftharpoons C_2H_4 + H_2$ has a high energy barrier compared to the zero activation energy for $CH_3 + CH_3 \rightleftharpoons C_2H_6$. Considering both thermodynamics and kinetics, we believe that methyl radical recombination forming C_2H_6 predominates below 1700 K, but it becomes prohibitive above 2300 K. Instead, $CH_3 + CH_3 \rightleftharpoons C_2H_4 + H_2$ is the major exothermic reaction above 2300 K. C_2H_6 and C_2H_4 formation compete for domination between 1700 and 2300 K. Total pressure and gas composition will play a key role in controlling the reaction pathway in this temperature range. Yet, k_4 is generally smaller than k_5 below 2000 K as best as we can make out from Figure 1.2 and Figure 1.4. It may be that in this range C_2H_4 is produced by other processes, e.g.

$$CH_3 + C_2H_6 \rightarrow CH_4 + C_2H_5 \qquad \Delta H^0_{298} = -19.5 \text{ kJ mol}^{-1} \qquad (34)$$

followed by the thermal decomposition of C_2H_5, ie reaction (13). Reaction (34) cannot directly affect our observations because it is nearly thermoneutral. Nevertheless it provides a pathway for satisfying the thermodynamic and kinetic requirements.

4.2 PROCEDURE

The first step in the analysis is to convert the observed signal to density gradient. The signal is proportional to the laser beam deflection, Δ, with the constant of proportionality deduced from a calibration using a rotating mirror. Δ in turn is related to the density gradient, $d\rho/dy$, by

$$\Delta = Dl\frac{d(\kappa\rho)}{dy} \qquad (4.4)$$

where l is the width of the shock tube, D is the distance between the shock tube axis and the detector, and κ is the Gladstone-Dale constant for the gas mixture.[71] The latter is a mass fraction average over the κ's of the individual component species. These components can be estimated for the unstable species according to the usual bond additivity rules.[106] However this is not crucial since κ is dominated by the contribution of Ar. In any case, the contribution of the disappearing CH_3 diminishes with time but is compensated by the increasing contribution of reaction products. Thus, κ is essentially constant. So

$$\Delta = Dl\kappa\frac{d\rho}{dy} \qquad (4.5)$$

The relationship between the density gradient and the reaction rate is found from the solution of the hydrodynamic equations of flow coupled to the rate equations:

$$\rho u = \rho_0 u_0 \qquad (4.6)$$

$$p + \rho u^2 = p_0 + \rho_0 u_0^2 \qquad (4.7)$$

$$h + u^2/2 = h_0 + u_0^2/2 \qquad (4.8)$$

$$p = \rho RT/\mu \qquad (4.9)$$

where $h\mu = \Sigma_n[(H-H^0_{298})_n + \Delta H^0_{f,n}(298)]X_n$ is the mixture enthalpy, μ is the effective molecular weight, u is the particle velocity, p is the pressure, T is the temperature, while X_n, $(H-H^0_{298})_n$, and $\Delta H^0_{f,n}(298)$, are the mole fraction, the molar enthalpy, and the standard heat of formation

of species n respectively. The latter 2 thermodynamic quantities are obtainable directly from the JANAF Thermochemical Tables.[85]

At low enough temperatures, reaction (5) alone is responsible for the signal. We can treat ρ as a known quantity, since it can be determined directly from the integral of the schlieren trace, using the first spike minimum as time zero.[132] Hence we have 5 unknowns (u, p, T, α, and k_5) and 5 equations. We can solve these equations (4.2), and (4.6) - (4.9) in terms of the observable $d\rho/dt_1$ and/or ρ. All 5 depend on time, even k_5 through its dependence on T. In fact, we shall use this property as a diagnostic tool below.

4.3 INTEGRATION OF LASER SCHLIEREN SIGNALS

To obtain $\rho(T(t))$ we have to integrate the schlieren trace. The exothermic components of the signals are fitted to the polynomial form

$$V(t_1) = C_b K \frac{d\rho}{dy} = C_b K \frac{d\rho}{u_0 dt_1} = \sum_{m=1}^{n} a_m t_1^{m-1} \qquad (4.10)$$

where C_b is the calibration factor and the a_m's are fitting parameters. Figure 4.2 illustrates the integration. The trace represents a typical C-type schlieren signal. The large spike (due to the passage of the shock front) is followed by a quickly decaying negative signal characteristic of an exothermic reaction. Point s is the earliest observable point. At point e the signal decays to zero, where a chemical equilibrium is assumed to be reached. Knowing the density at this equilibrium condition, ρ_∞, one can obtain $\rho(t_1)$ by integrating equation (4.10)

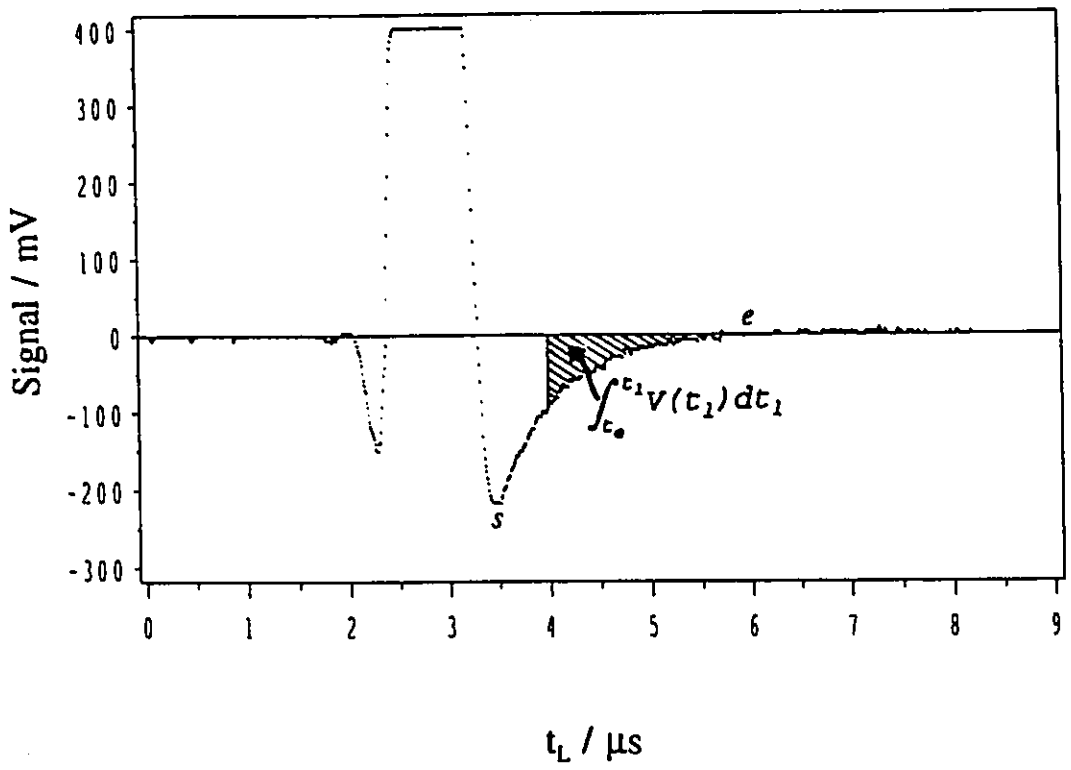

Figure 4.2 Illustration of the integration of a laser schlieren signal (*s*: earliest observable point; *e*: equilibrium point)

from e toward s

$$\rho(t_1) = \rho_\infty + \frac{u_0}{C_b K}\int_{t_e}^{t_1} V(t_1)\,dt_1 = \rho_\infty + \frac{u_0}{C_b K}\sum_{m=1}^{n}\frac{a_m}{m}(t_1^m - t_e^m) \qquad (4.11)$$

4.4 T, p, ρ, AND α AT THE EQUILIBRIUM CONDITION (at point e)

In principle, the answer to the problem is to solve equations (4.2), and (4.6) - (4.9) under equilibrium conditions (ie $d\alpha/dt_g = 0$) with the knowledge of T_0, h_0, X_A, p_0, μ_0, and ρ_0 in the preshock gas mixture and shock velocity U_s as well. By substitution and rearrangement those equations can be transformed into the following form

$$\frac{\rho_0}{\rho_e} = f(T_e, \alpha_{\infty(-)}) = \frac{1}{2T_0'}\left[\sqrt{(2\theta - T_e + T_0')^2 + 4T_0'T_e} - (2\theta - T_e + T_0')\right] \qquad (4.12)$$

$$\frac{p_e}{p_0} = 1 + \frac{\mu_0}{RT_0}u_0^2\left(1 - \frac{\rho_0}{\rho_e}\right) \qquad (4.13)$$

$$u_0 = \sqrt{\frac{2(h_e - h_0)}{1 - (\rho_0/\rho_e)^2}} \qquad (4.14)$$

$$\rho_\infty = \rho_e = \frac{\mu_0}{2X_A K_C}\frac{\alpha_{\infty(-)}}{(1 - 2\alpha_{\infty(-)})^2} \qquad (4.15)$$

where e denotes the equilibrium, $T_0' = T_0/[1+2X_A(1-\alpha_{\infty(-)})]$, $\theta = \mu_0(h_e - h_0)/[R[1+2X_A(1-\alpha_{\infty(-)})]]$, and $\mu_0(h_e - h_0) = X_A[2\alpha_{\infty(-)}\Delta H_5 + \Delta H_0 + (H_{A2D} - H^0_{A2D})] + (1-X_A)(H_{Ar} - H^0_{Ar})$. ΔH_0 is the heat of

dissociation of azomethane. The procedure is to treat T_e as known and to find the corresponding u_0 , p_e, ρ_∞, and α_∞. α_∞ is solved by iteration. It must satisfy equations (4.12) and (4.15) simultaneously. In other words, it has to obey

$$\rho_0 = \frac{\mu_0}{2X_A K_c} \frac{\alpha_{\infty(-)}}{(1-2\alpha_{\infty(-)})^2} f(T_e, \alpha_{\infty(-)}) \qquad (4.16)$$

The calculation is illustrated by the flow chart shown in Figure 4.3. For each chosen T_e, one can get a set of u_0 , p_e, ρ_∞, and $\alpha_{\infty(-)}$. T_e is varied until the calculated u_0 matches the experimental shock velocity U_s. Once ρ_∞ is determined, the integrated density profile can be very easily calculated using equation (4.11).

It should be pointed out that the determination of ρ_∞ (both its value and its location in time) is a crucial step. Our point-by-point analysis relies upon it. The advantage is that we do not have to worry about where time zero is and that we do not have to guess the part which is hidden behind the shock spikes.

4.5 FORMALISM

All flow and kinetic variables can be expressed in terms of the density, ρ, and density gradient $d\rho/dy$ (or $d\rho/dt_g$). For example, equations (4.6) - (4.9) can be rearranged into

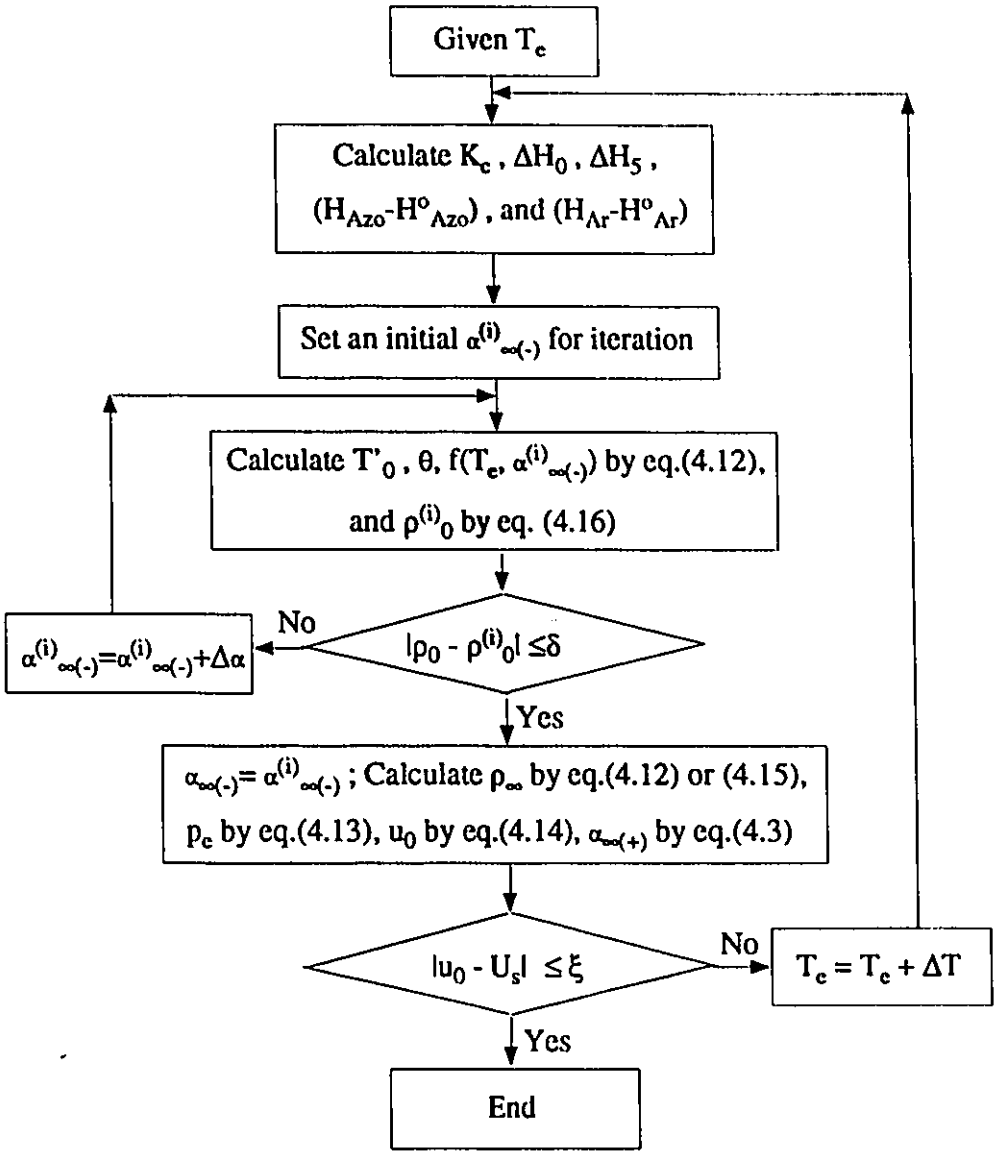

Figure 4.3 Procedure for calculating T_e, p_e, ρ_∞, and α_∞ assuming reaction $CH_3 + CH_3 \rightleftharpoons C_2H_6$ alone is responsible for the negative signals

$$u = u_0\rho_0/\rho \tag{4.17}$$

$$p = p_0+\rho_0 u_0^2 (1-\rho_0/\rho) \tag{4.18}$$

$$T = (\rho_0/\rho)\,[T_0+\mu_0 u_0^2 (1-\rho_0/\rho)/R]/[1+2X_A(1-\alpha)] \tag{4.19}$$

$$\alpha = \{\mu_0 u_0^2 [1-(\rho_0/\rho)^2]/2X_A - \Delta H_0 - (H_{Azo}-H^0_{Azo}) - (H_{Ar}-H^0_{Ar})\,(1-X_A)/X_A\}/2\Delta H_5 \tag{4.20}$$

where ΔH_0 is the heat of dissociation of azomethane. At each point in time, one determines T and α by combining and iterating with eqs. (4.19) and (4.20).

Differentiating equations (4.19) and (4.20) gives two differential equations relating T, ρ, and α. One resulting differential equation is substituted into the other, leading to the following expression:

$$\frac{d\alpha}{d\rho} = \frac{\mu_0 u_0^2 (\rho_0/\rho)^2\{[1+2X_A(1-\alpha)] - \overline{C}/R\} + \overline{C}T[1+2X_A(1-\alpha)]}{2X_A\rho\{\overline{C}T+\Delta H_5[1+2X_A(1-\alpha)]\}} \tag{4.21}$$

where ΔH_5 is the heat of the reaction $CH_3 + CH_3 \rightarrow C_2H_6$, and $\overline{C}$ is the effective heat capacity of the gas mixture at time, t_g,

$$\overline{C} = X_A\left[2\alpha\left(C_{p,C_2H_6} - 2C_{p,CH_3}\right) + \left(2C_{p,CH_3} + C_{p,N_2} + \frac{1-X_A}{X_A}C_{p,Ar}\right)\right] \tag{4.22}$$

The rate of reaction (equation (4.2)) can be related to the observable $d\rho/dt_g$ and ρ through the derivative $d\alpha/d\rho$

$$\frac{d\rho}{dt_g} = \frac{d\alpha}{dt_g} \Big/ \frac{d\alpha}{d\rho} \qquad (4.23)$$

Substituting the expressions for $d\alpha/dt_g$ and $d\alpha/d\rho$ into the formula above, we obtain

$$\frac{d\rho}{dt_g} = \frac{2X_A \rho k_5 \left[\frac{2X_A}{\mu_0}\rho(1-2\alpha)^2 - \alpha/K_c\right]\left\{\overline{C}T + \Delta H_5[1+2X_A(1-\alpha)]\right\}}{\mu_0 u_0^2 (\rho_0/\rho)^2\{[1+2X_A(1-\alpha)] - \overline{C}/R\} + \overline{C}T[1+2X_A(1-\alpha)]} \qquad (4.24)$$

Note that we have included the reverse dissociation reaction for cases close to equilibrium, and we have expressed the reverse rate coefficient in terms of the forward one through the equilibrium constant, K_c. Eq. (4.24) shows that the observable is roughly proportional to the product of k_5 and the effective heat of reaction, ΔH_5 , modulated by a term reflecting the decreasing amount of reagents. The 5 unknowns (u, p, T, α, and k_5) can be solved by the solution set of equations (4.17) - (4.20) and (4.24) at each point in time. k_5 can be deduced by one of the following three methods.

4.5.1 Direct Method

Inverting equation (4.24) directly gives an explicit expression for k_5. For convenience, we define a variable B

$$B = -\frac{\frac{2X_A}{\rho}\left(\overline{C}T+\Delta H_S[1+2X_A(1-\alpha)]\right)}{\mu_0 u_0^2(\rho_0/\rho)^2\{[1+2X_A(1-\alpha)]-\overline{C}/R\}+\overline{C}T[1+2X_A(1-\alpha)]} \qquad (4.25)$$

Consequently,

$$\frac{d\rho}{d\alpha} = -B\rho^2 \qquad (4.26)$$

$$\frac{d\rho}{dt_g} = \frac{d\rho}{d\alpha}\frac{d\alpha}{dt_g} = -B\rho^2 k_S\left[\frac{2X_A}{\mu_0}\rho(1-2\alpha)^2-\alpha/K_c\right] \qquad (4.27)$$

Therefore

$$k_S = -\frac{\frac{d\rho}{dt_g}}{B\rho^2\left[\frac{2X_A}{\mu_0}\rho(1-2\alpha)^2-\alpha/K_c\right]} \qquad (4.28)$$

This method exploits the proportionality of the observable to k_S .

4.5.2 Slope Method

Alternatively, one can focus on the time scale of the decay, ie on the slope of the observable, rather than bank on absolute calibration factors or worry about accumulating numerical errors arising from estimates of T, α, and ρ, based on the integration of the observable.

For simplicity, we use F to represent the absolute value of $d\rho/dt_g$ as the observable, ie.

$$F = -\frac{d\rho}{dt_g} = B\rho^2 k_5 \left[\frac{2X_A}{\mu_0}\rho(1-2\alpha)^2 - \alpha/K_c\right] \qquad (4.29)$$

It is fortunate that B is almost a constant for each C-type signal. For instance, B = 17.25 m^3 kg^{-1} at 1880 K and B = 17.19 m^3 kg^{-1} at 2030 K, both for experiment 5.4. Hence B is treated as constant in this and in the next methods. Differentiating F with respect to t_g, we obtain the derivative of the observable which can be rewritten into the form

$$k_5 = \frac{\left(\frac{E_a}{RT} - 3\right)\frac{F}{\rho} - \frac{d(\ln F)}{dt_g}}{\left(\frac{8X_A\rho}{\mu_0} + \frac{1}{K_c}\right) - \left(\frac{16X_A\rho}{\mu_0} + \frac{B\rho}{K_c}\frac{\Delta H_5}{RT}\right)\alpha} \qquad (4.30)$$

where E_a is the activation energy. k_5 can be deduced from this formula along with equations (4.17) - (4.20). It can be seen that in this method not only the absolute value of the observable but also its derivative (or shape) will contribute to the determination of k_5 .

4.5.3 Indirect Method

"Indirect" here means that the density gradient will not appear explicitly in the expression for k_5. First, integration of equation (4.26) gives a definite relation between α and ρ

$$\frac{1}{\rho} - \frac{1}{\rho_\infty} = B(\alpha - \alpha_{\infty(-)}) \qquad (4.31)$$

Because $\alpha_{\infty(-)}$ and $\alpha_{\infty(+)}$ are the two solutions of equation (4.2) when $d\alpha/dt_g = 0$, the rate equation can be rewritten as:

$$d\alpha/dt_g = k_5 \frac{8X_A\rho}{\mu_0} (\alpha-\alpha_{\infty(+)}) (\alpha-\alpha_{\infty(-)}) \qquad (4.32)$$

Substituting equation (4.31) into equation (4.32) and then separating the variables, after rearrangement we obtain

$$\frac{d(lnA)}{dt_g} = \frac{8X_A\rho_\infty}{\mu_0} k_5 (\alpha_{\infty(+)}-\alpha_{\infty(-)}) \qquad (4.33)$$

or

$$\frac{d(lnA)}{dt_l} = \frac{8X_A\rho\rho_\infty}{\mu_0\rho_0} k_5 (\alpha_{\infty(+)}-\alpha_{\infty(-)}) \qquad (4.34)$$

where

$$A = \frac{(\alpha_{\infty(+)}-\alpha)^{[B\rho_\infty(\alpha_{\infty(+)}-\alpha_{\infty(-)})+1]}}{\alpha_{\infty(-)}-\alpha} \qquad (4.35)$$

The rate constant can be found from the slope of a plot of lnA vs t_l .

4.5.4 Alternative Expression for α

Yet another choice is to solve equation (4.2) for α in terms of the observable, $d\rho/dt = (d\rho/d\alpha)(d\alpha/dt)$, and use it instead of eq. (4.20). Combining equations (4.26) and (4.32), we get

$$F = -\frac{d\rho}{dt_g} = k_5 \frac{8X_A B\rho^3}{\mu_0} (\alpha-\alpha_{\infty(+)}) (\alpha-\alpha_{\infty(-)}) \qquad (4.36)$$

The expression for α then has the form

$$\alpha = \frac{1}{2}\left[(\alpha_{\infty(+)}+\alpha_{\infty(-)}) - \sqrt{(\alpha_{\infty(+)}-\alpha_{\infty(-)})^2+4\sigma}\ \right] \qquad (4.37)$$

where

$$\sigma = \frac{1}{8X_A B\rho}\left(\frac{F\mu_0}{\rho^2 k_5}\right) \qquad (4.38)$$

For the slope and indirect method, one can use equation (4.37) to replace equation (4.20). Note that an iterative procedure is needed because k_5 is required to determine α.

4.6 RESULTS AND DISCUSSION

All three methods have been tried. Figure 4.4 , Figure 4.5, and Figure 4.6 illustrate the three methods graphically. The slopes are or contain the rate coefficient k_5. Figure 4.7 and Figure 4.8 compare k_5 obtained by the three methods for four experiments. The direct and slope methods give fairly close results, which agree within 40%. Note that reaction (5) is exothermic and that the temperature increases during the reaction. Although it has zero activation energy, k_5 will decrease with increasing temperature due to the fall-off effect, which has been discussed in chapter 2. The direct and slope methods indeed demonstrate this trend. The magnitudes of k_5 determined by the indirect method do not differ too much from those determined by the direct and slope methods. The largest difference is a factor of 2.8 and the smallest one is only 15%. However, k_5's obtained by the indirect method increase with increasing temperature, which is not reasonable according to the theory of unimolecular reactions. It is not surprising that the indirect method does not work very well because the

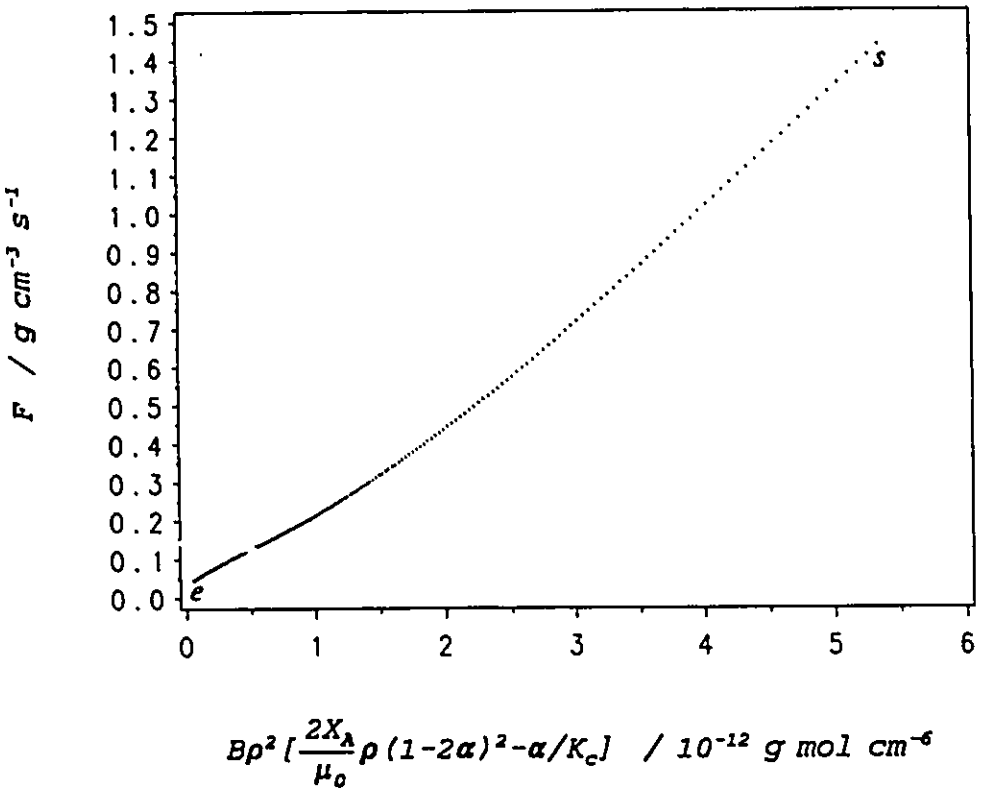

Figure 4.4 Illustration of the point-by-point analysis for experiment 4.8 using the direct method assuming that the reaction $CH_3 + CH_3 \rightleftharpoons C_2H_6$ alone is responsible for the negative signals (*s*: earliest observable point; *e*: equilibrium point)

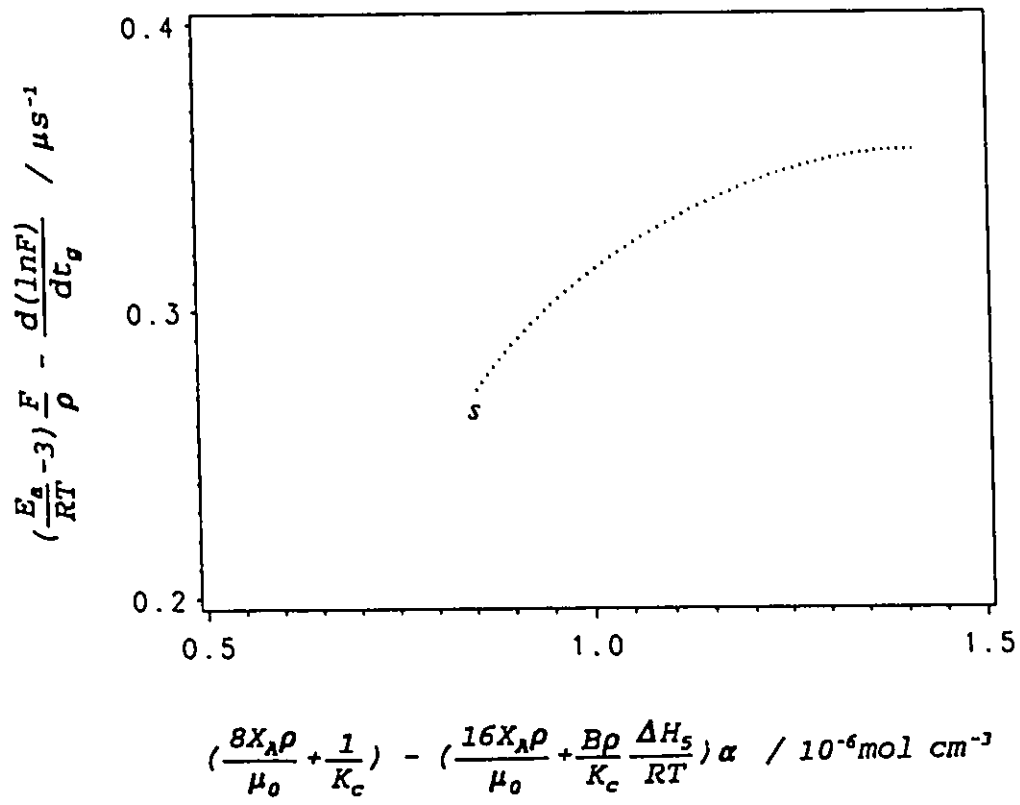

Figure 4.5 Illustration of the point-by-point analysis for experiment 4.8 using the slope method assuming that the reaction $CH_3 + CH_3 = C_2H_6$ alone is responsible for the negative signals (*s*: earliest observable point)

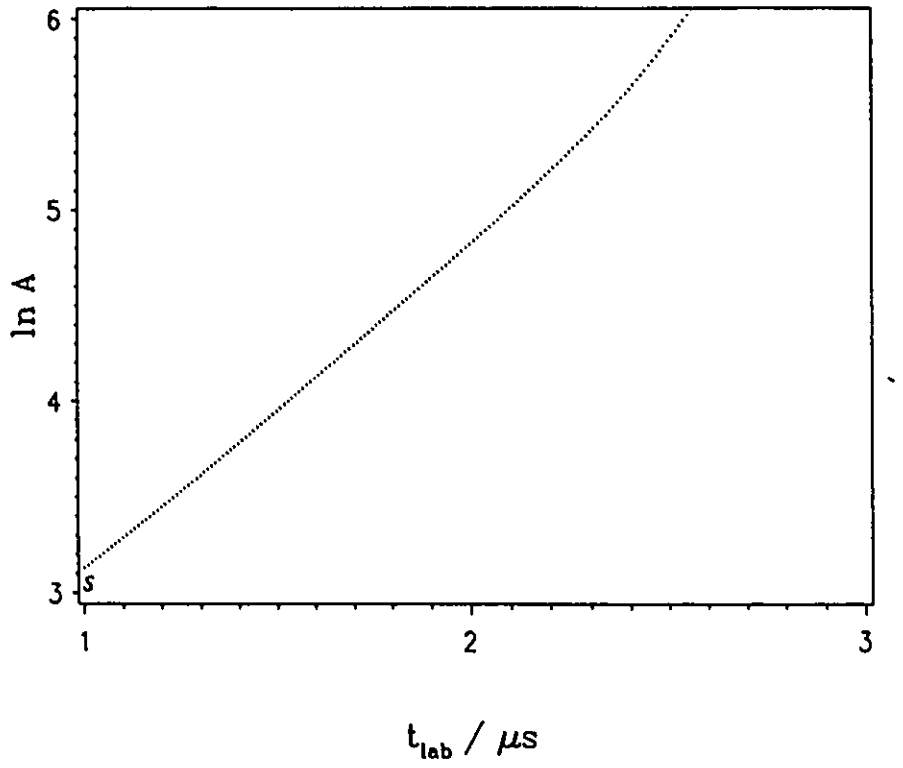

Figure 4.6 Illustration of the point-by-point analysis for experiment 4.8 using the indirect method assuming that the reaction $CH_3 + CH_3 \rightarrow C_2H_6$ alone is responsible for the negative signals (*s*: earliest observable point)

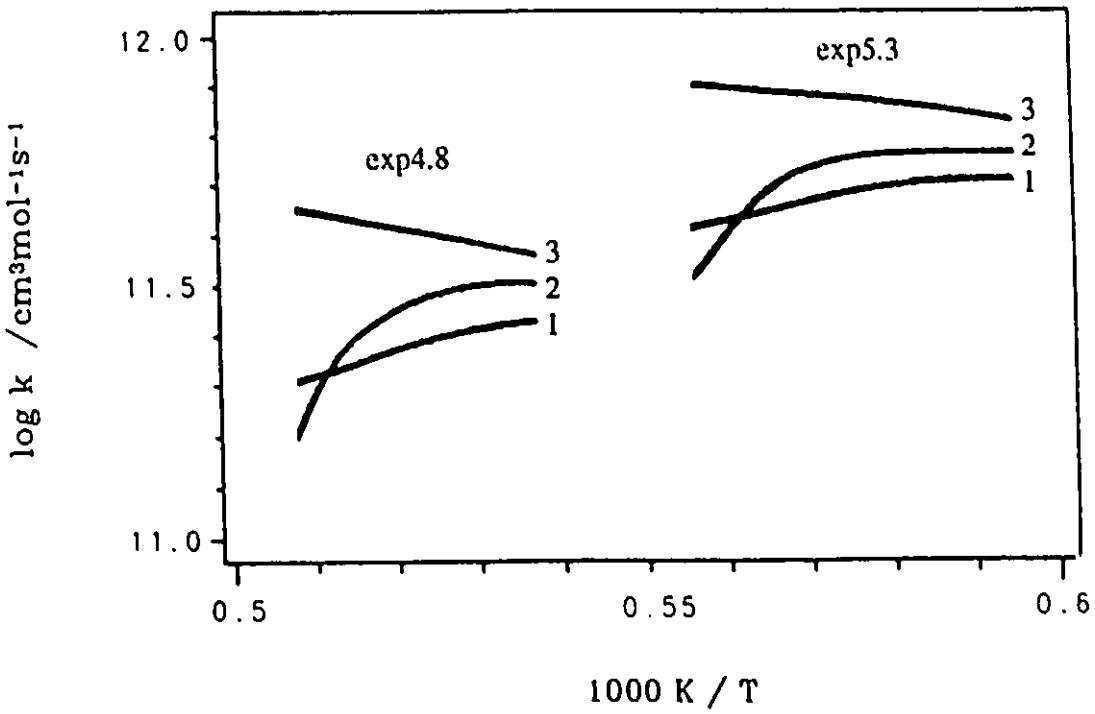

Figure 4.7 k_5 obtained by (1) direct, (2)slope, and (3) indirect methods for exp. 4.8 and 5.3

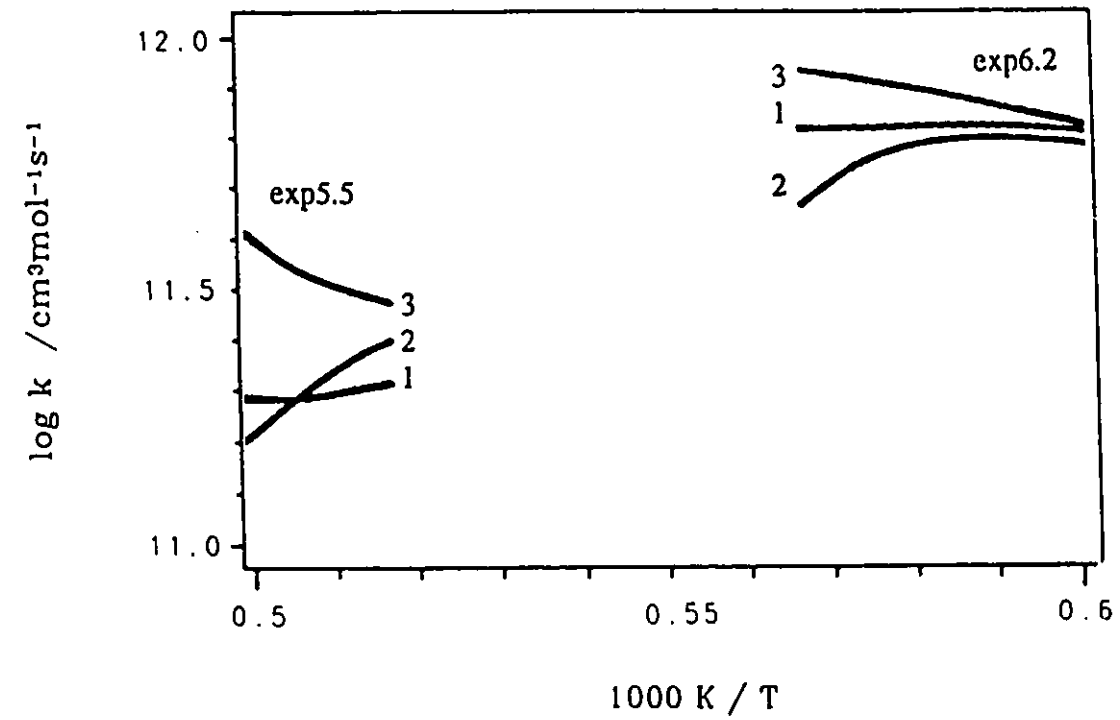

Figure 4.8 k_5 obtained by (1) direct, (2)slope, and (3) indirect methods for exp. 5.5 and 6.2

information available in the signals is not fully used in this method (for example, F and its derivative). In this sense the slope method is the most reliable one. The results in Figure 4.9 stem from the use of the direct and the slope methods, where we have drawn an Arrhenius plot of k_5 for selected experiments. Note that each experiment gives $k_5(T(t))$, ie an Arrhenius plot of its own. Only partial results are plotted for visual clarity.

We then repeated the analysis assuming that reaction (4) alone is responsible for the signal. The formalism is similar to that of reaction (5). The slight differences originate from the expressions for $d\alpha/dt_g$ and for μ. The differences are summarized in Appendix 4. The solution for k_4, in analogy to equation (4.24) now takes the form

$$\frac{d\rho}{dt_g} = \frac{4X_A^2\rho^2 k_4 [(1-2\alpha)^2 - \alpha^2/K_c]\Delta H_4 (1+2X_A)/\mu_0}{\mu_0 u_0^2 (\rho_0/\rho)^2\{(1+2X_A) - \overline{C}/R\} + \overline{C}T(1+2X_A)} \qquad (4.24b)$$

Again we drew the results as Arrhenius plots for selected experiments in Figure 4.9.

For internal consistency the rate coefficients must overlap if the temperature ranges overlap, ie. each experiment's Arrhenius plot must be a continuation of another one's. Clearly, k_5 shows the required internal consistency at temperatures less than 2100 K, whereas the assumption that reaction (4) is responsible for the signal leads to a contradiction at such temperatures. Note that for each individual curve, the low temperature end corresponds to the earliest observable point from the laser schlieren trace.

Figure 4.10 shows the results for k_5 classified according to the original mixture composition. Data points in the figure correspond to the earliest observable points from the laser schlieren traces. We saw no evident dependence on azomethane composition. This

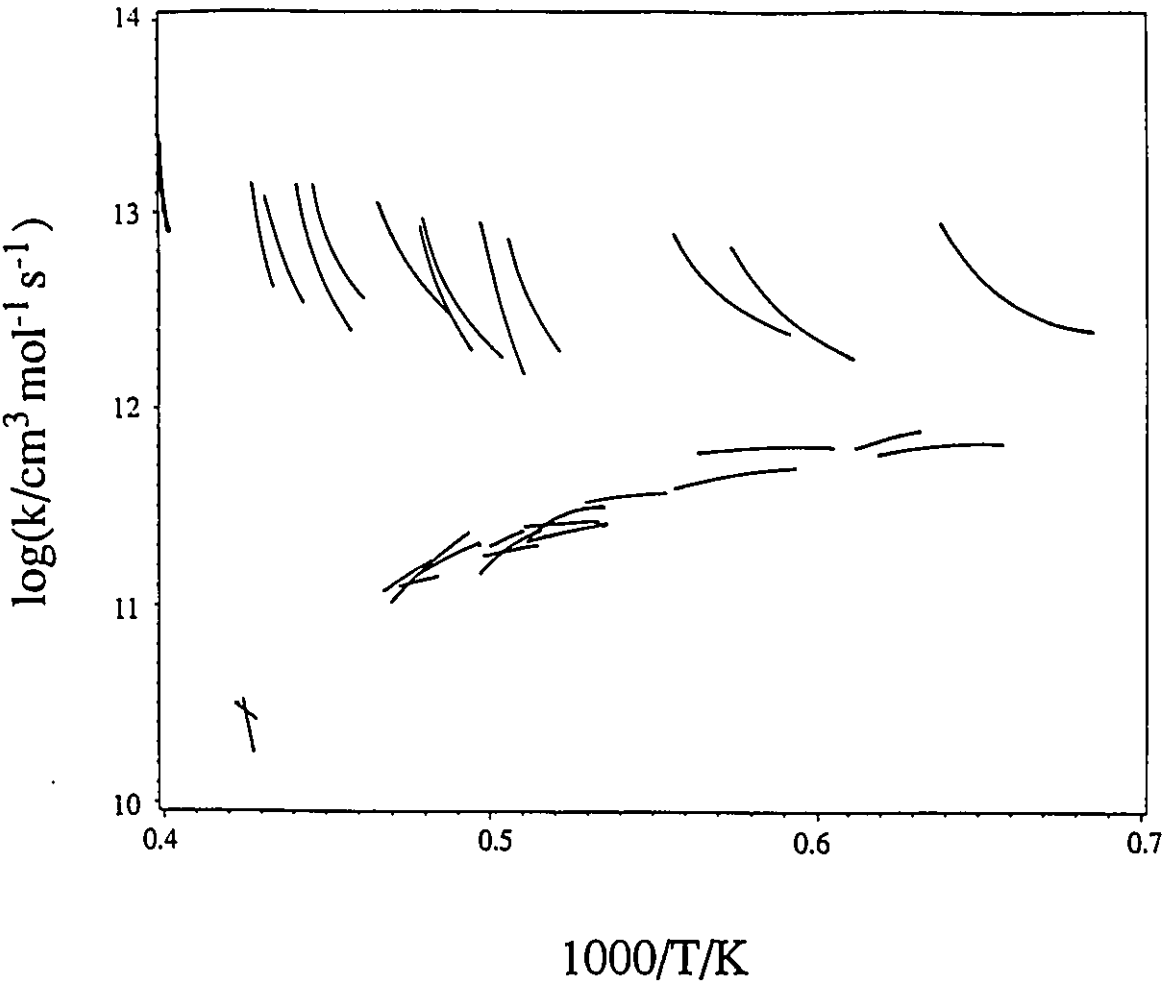

Figure 4.9 Rate coefficients for the disappearance of CH_3 as determined from a point-by-point analysis. Upper curves assume products are $C_2H_4 + H_2$. Lower curves assume products are C_2H_6.

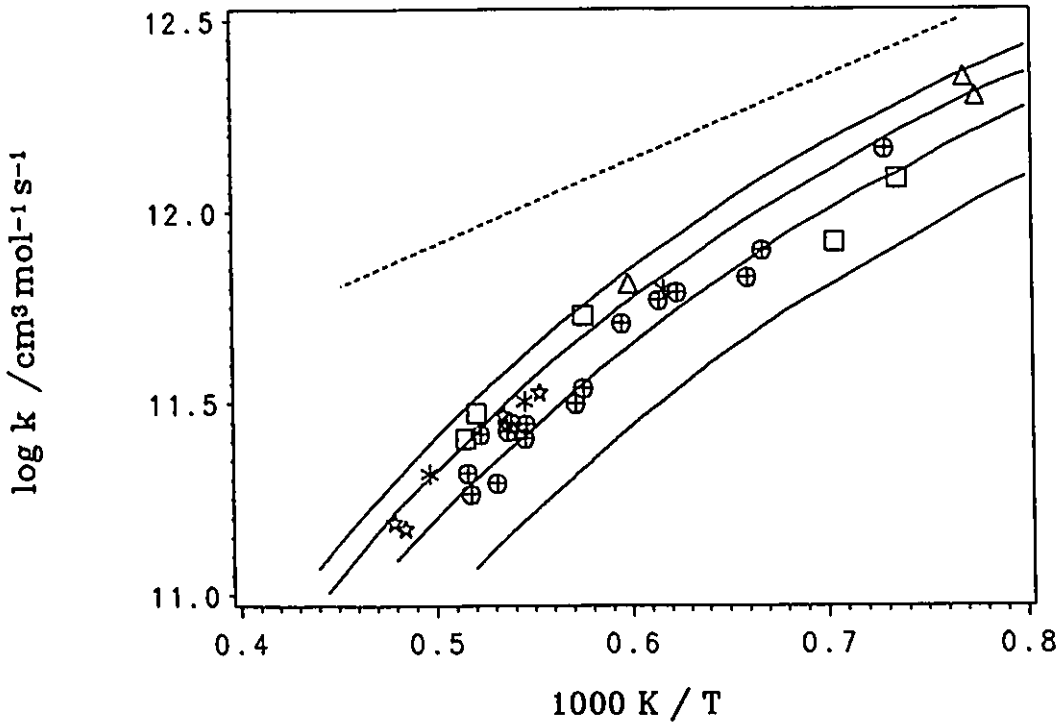

Figure 4.10 Rate coefficients for $CH_3 + CH_3 \rightarrow C_2H_6$. Azomethane molar composition: □ 1.75 %, 1.90 %; ★ 3.2 %; * 4.25 %; ⊕ 6.3%; ▵ 7.0%. Total density [M] = 0.6 - 1.6 × 10^{-6} mol cm^{-3}. Theoretical values (solid lines) are calculated from references 9, 32, and 50, where [M] = 0.5, 1.0, 1.5, and 2.0 × 10^{-6} mol cm^{-3} from bottom to top. The dashed line is the result from Moller et al,[15] where [M] = 5 × 10^{-6} mol cm^{-3}.

indicates that CH_3 is not too much more efficient than Ar as an energy transfer partner with excited C_2H_6. Also shown in Figure 4.10 are the theoretical values[9,32,50] calculated in the density range 0.5 - 2.0 × 10^{-6} *mol* cm^{-3}. These are in very good agreement with the present results. The slight spread in pressures may also contribute to the apparent scatter of the results. The present results (in the density range 0.6 - 1.6 × 10^{-6} mol cm^{-3}) support those of Moller et al,[15] which indicate a steeply declining rate coefficient as the temperature increases. Their results are shown in Figure 4.10 (dashed line) as well. Because they did experiments at a higher density (5 × 10^{-6} *mol* cm^{-3}) than we did, their results are higher than ours. Both results agree fairly well with each other and are also consistent with the theory of unimolecular reactions. Our rigorous simulation of the more detailed mechanism will confirm the assumption that reaction (5) alone is responsible for the negative signals of our lower-temperature experiments.

If one chooses the earliest observable points for k_4 instead of for k_5 in Figure 4.9, above 1900 K, to draw Figure 4.11, the values of k_4 appear to support the "large" rate constants.[2,19,55-56,58-60] However, Arrhenius plots obtained from the individual experiments are not consistent because they do not overlap. This contradiction is a clear indication that other primary reactions as well as secondary and tertiary reactions cannot be ignored at those temperatures. In view of the complications arising from the participation of endothermic processes, as noted above, it seems wiser not to rely on the point-by-point analysis for k_4. Rather, we have embarked on a numerical simulation of all of our signals using a 44-step mechanism. The details of the simulation will be given in the next chapter.

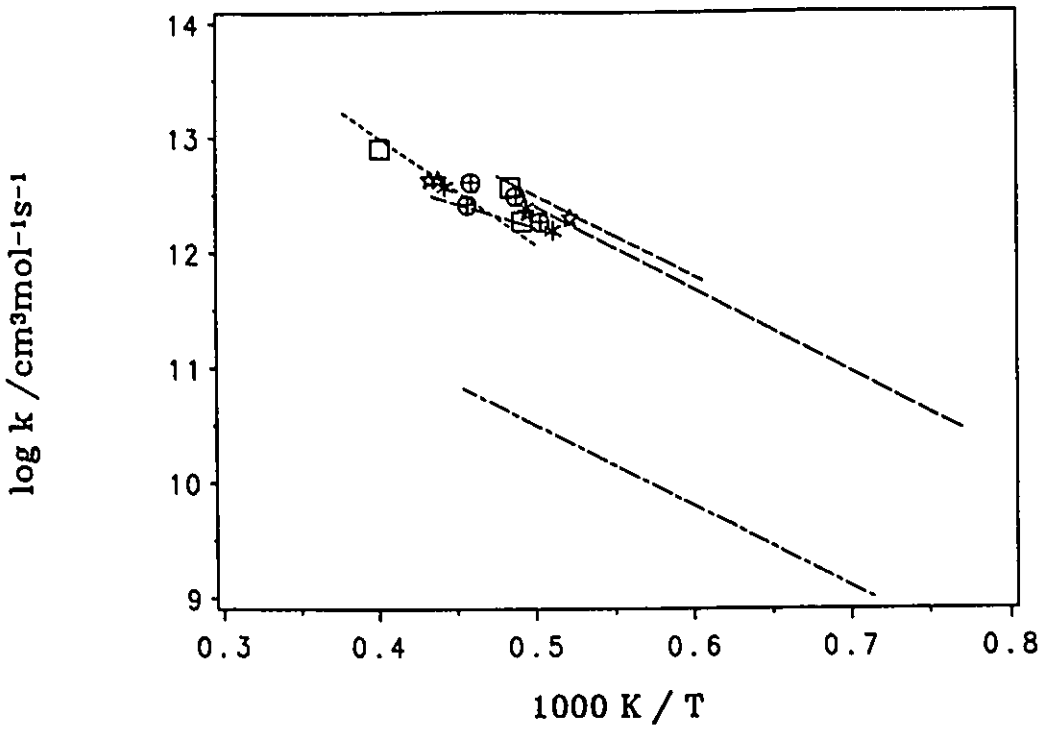

Figure 4.11 k_4 at earliest observable points compared with literature values for $CH_3 + CH_3 \rightarrow C_2H_4 + H_2$. Azomethane molar composition □ 1.90 %; ★ 3.20 %; * 4.25 %; ⊕ 6.30%.

---------- Ref. 2, 55

— — — — — — Ref. 59

·—·—·—·—· Ref. 19, 60

..... Ref. 56

·—·—·—·—· Ref. 61

CHAPTER 5

COMPUTER SIMULATION

The kinetics of the reactions of CH_3 radicals at high temperatures is rather complicated. Several primary channels compete for removal of CH_3. The secondary reactions also have a large impact on the whole mechanism. Such complications ultimately force one to extract the kinetic data from shock tube experiments by numerical simulation. Current computer technology allows for the rapid simulation of complex chemical processes. Simulation is now a common tool for the description of reacting systems. It is valuable for the interpretation of experimental results and for the understanding of chemical kinetic behaviour.

5.1 FUNDAMENTALS

The computer codes for simulation were provided to us by Sandia National Laboratories. Outlined in this section are the theoretical models of the Sandia computer codes.[120-122]

5.1.1 Chemical Reaction Rate Expression

Consider n elementary reactions involving m chemical species. The net molar production rate, v_j , of the jth species is a summation of the "rate-of-progress variables", ϕ_i, for all reactions involving the jth species:[120]

$$v_j = \sum_{i=1}^{n} \nu_{ji} \phi_i \tag{5.1}$$

where the stoichiometric coefficients of the jth species in the ith reaction, ν_{ji}, are the differences between the stoichiometric coefficients of the jth product species in the ith reaction, ν''_{ji}, and that of the jth reactant species, ν'_{ji}, i.e. $\nu_{ji} = \nu''_{ji} - \nu'_{ji}$. The rate-of-progress of the ith reaction, ϕ_i, is the difference between the forward rate and the reverse rate[120]

$$\phi_i = k_{f_i} \prod_{j=1}^{m} [X_j]^{\nu'_{ji}} - k_{r_i} \prod_{j=1}^{m} [X_j]^{\nu''_{ji}} \tag{5.2}$$

where $[X_j]$ is the molar concentration of the jth species and k_{fi} and k_{ri} are the forward and reverse rate constants of the ith reaction. In association and dissociation reactions (i.e., pressure-dependent reactions), equation (5.2) needs to be multiplied by the effective total concentration $[M]_{eff,i}$ of the ith reaction:[120]

$$[M]_{eff,i} = \sum_{j=1}^{m} \alpha_{ji} [X_j] \tag{5.3}$$

where α_{ji} is the third-body efficiency of the jth species in reaction i. In the present study it is assumed that all species in the mixture contribute equally as collisional partners in a reaction (i.e., all the $\alpha_{ji} = 1$). Then $[M]_{eff,i}$ equals the total concentration of the mixture, P/RT. We shall test the validity of this assumption later in this chapter.

5.1.2 Governing System of Ordinary Differential Equations

The well-established conservation laws of mass, momentum and energy transfer describe the distributions of density, ρ, velocity, u, and temperature, T, downstream of the shock.[99,122] For one-dimensional adiabatic flow, the conservation equations are given by[122]

$$\textit{Continuity:} \qquad \rho u A = \textit{constant} \tag{5.4}$$

$$\textit{Momentum:} \qquad \rho u \frac{du}{dy} + \frac{dp}{dy} = 0 \tag{5.5}$$

$$\textit{Energy:} \qquad \frac{dh}{dy} + u \frac{du}{dy} = 0 \tag{5.6}$$

$$\textit{Species:} \qquad \rho u \frac{dY_j}{dy} = v_j \mu_j \tag{5.7}$$

where A is the cross section of shock tube, y is the axial flow distance, p denotes pressure, and Y_j and μ_j denote mass fraction and molecular weight of species j respectively. Temperature is related to the specific enthalpy of the gas mixture, h, by

$$h = \sum_{j=1}^{m} h_j Y_j \tag{5.8}$$

and

$$h_j = (h_j)_0 + \int_{T_0}^{T} c_{pj}\, dT \tag{5.9}$$

The equation of state relates the intensive thermodynamic properties

$$p\mu = \rho RT \tag{5.10}$$

The molecular weight of the mixture, μ, is determined by

$$\mu = \frac{1}{\sum_{j=1}^{m} Y_j / \mu_j} \tag{5.11}$$

Differentiating equations (5.8), (5.9), (5.10), (5.11), and combining and rearranging equations (5.4), (5.5), (5.6), (5.7) leads to the following set of coupled, ordinary differential equations[122]

$$\frac{dY_j}{dt} = \frac{v_j \mu_j}{\rho} \tag{5.12}$$

$$\frac{du}{dt} = -\frac{u}{\rho}\frac{d\rho}{dt} - \frac{u^2}{A}\frac{dA}{dy} \tag{5.13}$$

$$\frac{dT}{dt} = \frac{u^2}{\rho c_p}\frac{d\rho}{dt} - \frac{1}{\rho c_p}\sum_{j=1}^{m} h_j v_j \mu_j + \frac{u^3}{A c_p}\frac{dA}{dy} \tag{5.14}$$

$$\frac{d\rho}{dt} = \frac{1}{p + \rho u^2/c_p T - \rho u^2}\left[\frac{R\rho}{\mu c_p}\sum_{j=1}^{m} v_j \mu_j \left(h_j - \frac{\mu c_p T}{\mu_j}\right) + \frac{\rho^2 u^3}{A}\left(1 - \frac{R}{\mu c_p}\right)\frac{dA}{dy}\right] \tag{5.15}$$

These (m+3) stiff ODEs serve as the governing equations which should be satisfied by the time histories of the measurable flow quantities. When chemically frozen conditions of the incident shock are determined by a procedure similar to that described in the previous chapter, the time histories of the flow quantities can be obtained by integrating the ODEs.

5.1.3 Laboratory Time and Gas-particle time

There is a time compression effect in shock waves. Consider a shock wave propagating at the velocity, U_s. A gas particle enters the shock front at time $t = 0$. At some later time t', the shock front has travelled a distance $U_s \cdot t'$. Since the gas particle is only moving at the velocity of $(U_s - u)$, it is not until time, t_g, referred to as the gas-particle time, that the particle has travelled the same distance. Therefore,

$$\int_0^{t_g} (U_s - u)\, dt = U_s t' \qquad (5.16)$$

where u is the post-shock gas velocity in shock-fixed coordinates. In laboratory coordinates, the particle is lagging behind the shock front by an amount of time equal to $(t_g - t') = t_L$, referred to as the laboratory time. In an experiment, therefore, the particle arrives at an observation window at a time t_L after the shock front. In other words, the test gas particle has been at the post-shock conditions for some time longer than the laboratory time. This longer gas-particle time is the time of interest with respect to rate processes in the test gas. Differentiating equation (5.16) and using the mass continuity relation (eq. 5.4) results in the following ordinary differential equation relating gas-particle and laboratory times[122]

$$\frac{dt_L}{dt_g} = \frac{\rho_1 A_1}{\rho A} \qquad (5.17)$$

When rate processes are measured using a shock tube method, the time as measured must be multiplied by the density-area ratio across the shock front in order to get the actual time referred to the test gas. Usually the subscript g for t_g is omitted. In the Sandia shock tube

code, equation (5.17) is integrated along with the other ODEs (5.12-5.15).

5.1.4 Boundary Layer Effects

A wall boundary is present in a shock tube, resulting in a velocity gradient normal to the gas flow and a non-uniform flow behind the shock front.[99] Mirels treated the flow as quasi-one-dimensional assuming a laminar boundary layer and proposed that[107]

$$\frac{\rho u}{(\rho u)_2} = \frac{A_2}{A} = 1-(y/l_m)^{1/2} \qquad (5.18)$$

where l_m is the distance between the shock and contact surface at infinite distance from the diaphragm. l_m can be estimated from the diluent viscosity[108] (2.272×10^{-4} $g\ s^{-1}\ cm^{-1}$ for Ar, and 1.786×10^{-4} $g\ s^{-1}\ cm^{-1}$ for N_2 at 300 K). Subscript 2 denotes conditions immediately behind the shock. Differentiating the right half of this equation yields the expression for the change in cross-sectional area with distance downstream of the shock[122]

$$\frac{1}{A}\frac{dA}{dy} = \frac{(y/l_m)^{-1/2}}{2\,l_m[1-(y/l_m)^{1/2}]} \qquad (5.19)$$

This expression accounts for the boundary layer effects and permits the calculation of the effective area through which the gas must flow. The expression is used in equations (5.13), (5.14) and (5.15). The distance of a fluid element from the shock, y, is related to the velocity by

$$\frac{dy}{dt} = u \qquad (5.20)$$

5.2 REACTION MECHANISM AND EVALUATION OF KINETIC DATA

A large reaction mechanism consisting of 44 reactions with 19 species was adopted for calculating the laser schlieren profiles. The reactions and rate coefficients used in the mechanism are summarized in Table 5.1. Where possible, the rate coefficient values are taken from the literature. The reverse rate constants are related to the forward ones through the equilibrium constants *ie* $k_f/k_r = K_c$. The change in enthalpy, $\Delta H°_{298}$, for each reaction is also listed in Table 5.1.

The thermal decomposition of azomethane at high temperatures offers a clean source of methyl radicals to investigate their reactions. "The initial decomposition step of azomethane at $T \geq 1300$ K is sufficiently fast to exclude a bimolecular reaction between CH_3 radicals and the parent molecule", and the decomposition leads to two methyl radicals.[8] The rate coefficient for this pressure-dependent reaction listed in the reaction mechanism is from the work of Moller, Mozzhukhin, and Wagner.[15] It is supplemented by the values calculated in chapter 2 for high temperatures. The calculated refractive-index-gradient profiles are not very sensitive to reasonable changes in the value of the rate coefficient. In practice, Wagner et al.'s rate constant should be reliable up to 2700 K without a large error. Beyond 2700 K, the decomposition rate definitely needs to be verified.

Reactions (1) - (6) are the six primary competing channels for CH_3 decay. The remaining reactions (7) - (43) include all the possible secondary reactions and some important tertiary reactions. This is to ensure that no crucial reactions have been omitted. Some of the reactions included are of little consequence. Sensitivity analysis shows that the simulation

Table 5.1. Reaction Mechanism

Reaction	ΔH°_{298} kJ mol^{-1}	$k = A\,T^b \exp(-E/RT)$ A s^{-1} $cm^3\,mol^{-1}\,s^{-1}$ $cm^6\,mol^{-2}\,s^{-1}$	b	E/R K	ref.
0. $CH_3NNCH_3 \rightleftharpoons N_2 + 2CH_3$	143	7.94×10^{9}	0.0	13300	15*
1. $CH_3 + M \rightleftharpoons CH + H_2 + M$	448	5.78×10^{13}	0.0	32834	30
2. $CH_3 + M \rightleftharpoons CH_2 + H + M$	459	2.72×10^{36}	-5.31	58925	this work
3. $CH_3 + CH_3 \rightleftharpoons C_2H_5 + H$	43.8	3.00×10^{13}	0.0	6800	18
4. $CH_3 + CH_3 \rightleftharpoons C_2H_4 + H_2$	-239	1.10×10^{14}	0.0	9026	this work
5. $CH_3 + CH_3\,(+M) \rightleftharpoons C_2H_6\,(+M)$	-375	3.61×10^{13}	0.0	0	9
Low pressure limit:		1.27×10^{41}	-7.0	1390	32,50
TROE centering:	$F_c = 0.38 \exp(-T/73) + 0.62 \exp(-T/1180)$				50
6. $CH_3 + CH_3 \rightleftharpoons CH_4 + CH_2$	20.1	4.30×10^{12}	0.0	5052	19
7. $CH_2 + M \rightleftharpoons H_2 + C + M$	330	1.30×10^{14}	0.0	29700	26
8. $CH_2 + M \rightleftharpoons H + CH + M$	425	1.20×10^{14}	0.0	30110	30
9. $CH_4\,(+M) \rightleftharpoons CH_3 + H\,(+M)$	439	2.40×10^{16}	0.0	52800	25
Low pressure limit: $T < 2200$ K		7.23×10^{17}	0.0	47000	32
$T \geq 2200$ K		1.90×10^{47}	-8.106	59100	31
TROE centering:	$F_c = \exp(-0.45 - T/3231)$				25
10. $C_2H_3\,(+M) \rightleftharpoons C_2H_2 + H\,(+M)$	158	2.00×10^{14}	0.0	20000	2,32
Low pressure limit:		4.16×10^{41}	-7.5	22900	32,109
TROE centering:	$F_c = 0.35$				32
11. $C_2H_4 + M \rightleftharpoons C_2H_2 + H_2 + M$	175	2.60×10^{17}	0.0	39900	2,110
12. $C_2H_4 + M \rightleftharpoons C_2H_3 + H + M$	452	3.80×10^{17}	0.0	49400	2,110
13. $C_2H_5 + M \rightleftharpoons C_2H_4 + H + M$	154	2.00×10^{15}	0.0	15640	65

Table 5.1. (Continued)

Reaction	ΔH°_{298} kJ mol^{-1}	k = A T^b exp (- E/RT) A s^{-1} cm^3 mol^{-1} s^{-1} cm^6 mol^{-2} s^{-1}	b	E/R K	ref.
14. $C_2H_6 + M \rightleftharpoons C_2H_4 + H_2 + M$	136	2.29×10^{17}	0.0	34040	52
15. C_2H_6 (+M) $\rightleftharpoons C_2H_5 + H$ (+M)	419	8.85×10^{20}	-1.23	51439	111
Low pressure limit:		6.90×10^{42}	-6.43	53938	111
TROE centering: F_c = 0.7 exp (-T/2200) + 0.3 exp (-T/12000) + exp (-6700/T)					*
16. $CH_2 + H \rightleftharpoons H_2 + CH$	-10.8	6.00×10^{12}	0.0	-900	32
17. $CH_3 + H \rightleftharpoons H_2 + CH_2$	61.0	1.69×10^{15}	-0.57	7640	32
18. $C_2H_3 + H \rightleftharpoons C_2H_2 + H_2$	-277	$1.2\text{~}3.8\times10^{13}$	0.0	0	2,32,65
19. $C_2H_4 + H \rightleftharpoons H_2 + C_2H_3$	15.8	5.42×10^{14}	0.0	7500	32
20. $C_2H_5 + H \rightleftharpoons H_2 + C_2H_4$	-282	1.81×10^{12}	0.0	0	109
21. $C_2H_6 + H \rightleftharpoons C_2H_5 + H_2$	-16.9	1.42×10^{9}	1.5	3725	32
22. $CH_3 + H_2 \rightleftharpoons CH_4 + H$	-2.6	6.87×10^{3}	2.74	4740	32
23. $CH_2 + CH_2 \rightleftharpoons C_2H_2 + 2H$	-111.3	1.10×10^{14}	0.0	400	32
24. $CH_2 + CH_3 \rightleftharpoons C_2H_4 + H$	-262	4.22×10^{13}	0.0	0	2,18,32
25. $CH_2 + C_2H_4 \rightleftharpoons C_3H_6$	-419	3.19×10^{12}	0.0	2660	112
26. $CH_2 + C_2H_5 \rightleftharpoons CH_3 + C_2H_4$	-305	1.81×10^{13}	0.0	0	109
27. $CH_2 + C_2H_6 \rightleftharpoons CH_3 + C_2H_5$	-36.6	6.50×10^{12}	0.0	3980	18,117
28. $CH_3 + CH_4 \rightleftharpoons C_2H_5 + H_2$	46.8	1.00×10^{13}	0.0	11570	74
29. $CH_3 + CH_4 \rightleftharpoons C_2H_6 + H$	64	8.00×10^{13}	0.0	20130	74
30. $CH_3 + C_2H_4 \rightleftharpoons CH_4 + C_2H_3$	13.2	4.16×10^{12}	0.0	5600	113
31. $CH_3 + C_2H_4 \rightleftharpoons n\text{-}C_3H_7$	-104	2.99×10^{11}	0.0	3830	*
32. $CH_3 + C_2H_5 \rightleftharpoons CH_4 + C_2H_4$	-285	1.20×10^{12}	0.0	0	109

Table 5.1. (Continued)

Reaction	ΔH°_{298} kJ mol^{-1}	k = A T^b exp (- E/RT) A s^{-1} / cm^3 mol^{-1} s^{-1} / cm^6 mol^{-2} s^{-1}	b	E/R K	ref.
33. $CH_3 + C_2H_5$ (+M) = C_3H_8 (+M)	-367	2.83×10^{13}	0.0	0	109
Fall-off factor :		see text			109
34. $CH_3 + C_2H_6 = CH_4 + C_2H_5$	-19.5	5.51×10^{-1}	4.0	4167	114
35. $C_2H_4 + C_2H_4 = C_2H_5 + C_2H_3$	298	4.82×10^{14}	0.0	36000	109
36. $CH_3 + C_2H_3 = CH_4 + C_2H_2$	-280	3.92×10^{11}	0.0	0	109
37. $C_3H_6 + M = CH_3 + C_2H_3 + M$	412	5.40×10^{75}	-15.7	60390	68
38. $C_3H_6 + H = CH_3 + C_2H_4$	-39.7	7.23×10^{12}	0.0	655	115
39. $C_2H_5 + C_2H_5 = C_2H_4 + C_2H_6$	-266	1.45×10^{12}	0.0	0	109
40. $C_2H_5 + C_2H_5 = C_4H_{10}$	-296	1.00×10^{13}	0.0	0	109
41. $C_2H_4 + C_2H_5 = C_2H_3 + C_2H_6$	33	6.32×10^{2}	3.13	9063	109
42. $H_2 + M = H + H + M$	436	2.23×10^{14}	0.0	48350	116
43. $CH + M = C + H + M$	340	1.90×10^{14}	0.0	33700	26

The reverse of each reaction is included via detailed balance, $k_r = k_f / K_c$.
* See text.

of the laser schlieren traces for different experimental conditions can be executed using a strongly reduced set of reactions, compared to the large scheme. This is so because of the dilution of the reactants, which reduces the importance of subsequent reactions considerably.

Reaction (1) and (2) are two competing channels of CH_3 decomposition. They have been fully addressed in our recent theoretical studies[104] as well as in chapter 2. At very high temperatures these reactions could compete with other primary reactions.

Recently Frank and Braun-Unkhoff[18] made more direct measurements for reaction (3). They chose the ARAS technique (atomic resonance absorption spectrometry) to monitor the thermal decay of azomethane, methyl iodide and ethane. The measurements of time dependent H-concentrations were performed behind the reflected shock wave in the temperature range 1320 to 2300 K. The rate coefficient is probably the best one for this reaction.

The present study determines the rate coefficient for reaction (4) which is derived from the fit of simulations to experimental observations. The experimental values for the rate coefficient are obtained by comparing laser schlieren profiles with the simulated refractive-index-gradient profiles. More details will be given in the following sections.

There have been a large number of studies of reaction (5). They cover effects arising from pressure as well as temperature.[53] The limiting high pressure rate coefficient of Troe et al[9] is preferred. It is temperature independent. The expressions for the limiting low pressure rate constant, which accommodates the chosen k_∞ value, and the centre-broadening factor are from the most recent evaluation[32] based on the modelling of Wagner and Wardlaw.[50] At high temperatures (T>1300 K) and ordinary pressures, reaction (5) is in the

fall-off region closer to the low pressure limit. Therefore, the low pressure limit, k_0, has a bigger impact on the effective second order rate coefficient than k_∞. Under our experimental conditions, where reaction (5) plays a role, it really doesn't matter whether we choose Troe et al.'s k_∞ or use Wagner and Wardlaw's $k_\infty(T)$. The effective second order rate coefficient, k_{Troe}, calculated using the set of expressions in Table 5.1 is very close to the effective second order rate coefficient, k_{Wagner}, computed using Wagner and Wardlaw's set of expressions of k_∞, k_0, and F_c,[50] ie. $k_{Troe}/k_{Wagner} = 0.98–1.12$ over the temperature range 1300~2300 K and the density range $0.6–3.5\times10^{-6}$ *mol* cm^{-3}.

Reaction (6) could produce carbene in both triplet and singlet states. No direct measurement has been made to distinguish singlet $^1CH_2$ from triplet $^3CH_2$. The rate coefficient for reaction (6) from Frank's work[19] could serve as the effective value for $^1CH_2$ and $^3CH_2$. Compared to other primary reactions, the thermal effect of reaction (6) is small. Therefore this reaction is less thermally influential than the other primary ones.

Two different groups performed experimental studies of reactions (7) and (8) recently.[26,30] C-atom concentrations were measured using atomic resonance absorption spectroscopy (ARAS) at 156.1 nm.[26] Using narrow-linewidth and ring dye laser absorption at 431 nm, the two groups detected CH concentration profiles generated during the high temperature pyrolysis of highly dilute mixtures of ethane or methane diluted in argon behind reflected shock waves. There are two sets of rate coefficients for k_7 and k_8 determined by the two groups, which differ by less than a factor of 2 over the range 3000 to 4000 K. No matter which set or combination of k_7 and k_8 is used, it really makes no difference in our simulation because these two reactions hardly contribute at all in our case. The rate

coefficient used in the scheme is merely our preference.

Shock tube experiments of methane dissociation over a wide pressure range have been reevaluated by Cobos and Troe using theoretical modelling.[25] Their high pressure limiting rate coefficient is consistent with a nearly temperature independent reverse rate coefficient. Their low pressure limiting rate coefficient was then compared to other experimental data, and this led to the recommended values (from 300 to 3000 K) given in reference 32 (and listed in our scheme for T < 2200 K). Kiefer and Kumaran, most recently, studied the rate of CH_4 dissociation at even higher temperatures (2800 - 4300 K).[31] Their low-pressure-limiting rate constant blends well with the recommendation below 2200 K, but it is six times smaller than that recommendation at 3500 K. We believe that Kiefer's expression is more appropriate at higher temperatures.

Kinetic modelling results of reaction (15) by Stewart, Larson, and Golden[111] are adopted in the present scheme. Their centre-broadening factor, $F_c = 47.61exp(-16182/T) + exp(-T/3371)$, has been refit to the general form as listed in Table 5.1.

Reaction (25) and reaction (31) are actually fall-off reactions. Sensitivity analysis indicates that these two reactions are not so important. We simply used the second order rate coefficients without considering the fall-off effects. The rate constant for reaction (31) is a fit of the values obtained from references 109, 118, and 119.

Tsang and Hampson have calculated the dependence of the rate coefficient, k_{33}, upon pressure and temperature.[109] This leads to three expressions for correction factors expressed in polynomial form at 0.1, 1, and 10 atms. Making use of those three expressions, we estimated the fall-off factor for reaction (33) using the Lagrange interpolation formula

$$\log \frac{k_{33}(T,P)}{k_{33,\infty}} = \sum_{j=1}^{4} \left[\frac{1}{2}\eta(\eta-1) f_{1j} - (\eta^2-1) f_{2j} + \frac{1}{2}\eta(\eta+1) f_{3j} \right] T^{j-1} \qquad (5.21)$$

where $\eta = log_{10} P\ (atm)$, and the f_{ij} are listed in the following array

	$j=1$	$j=2$	$j=3$	$j=4$	
$i=1$	-0.4870	$+1.985\times10^{-3}$	-1.8740×10^{-6}	$+2.1210\times10^{-10}$	(0.1 *atm*)
$i=2$	-0.3184	$+1.137\times10^{-3}$	-8.3530×10^{-7}	-2.1560×10^{-11}	(1.0 *atm*)
$i=3$	-0.0968	$+2.233\times10^{-4}$	$+8.8824\times10^{-8}$	-2.0494×10^{-10}	(10 *atm*)

At relatively low temperatures and high pressures, methyl can react with vinyl forming propene, the reverse of reaction (37). The rate constant for the forward reaction is from Kiefer et al.'s shock tube experiments.[68]

At high temperatures and low pressures C_2H_5 is so unstable that the small pressure dependence is unimportant for practical purposes.[109] Thus the second order high pressure rate coefficient is used without any fall-off correction for reaction (40).

Both Dean et al.[26] and Roth et al.[30] studied reaction (43) experimentally. The former measured simultaneously C-atom concentrations using ARAS and CH concentrations using laser absorption. The latter only monitored CH laser absorption.

After careful evaluation and selection of kinetic data, we believe that the reaction scheme presented in Table 5.1 is sufficient to interpret our experiments. The following sections will demonstrate that this reaction mechanism is successfully used in the simulation of our laser schlieren traces.

5.3 SIMULATION OF LASER SCHLIEREN SIGNALS

Integration of the ODEs (5.12), (5.13), (5.14), (5.15), (5.17), and (5.20) using the kinetic data listed in Table 5.1 was made using the generalized chemical kinetics code CHEMKIN-II package,[120] the stiff ordinary differential equation solver LSODE,[121] and the Sandia shock tube code[122] with some modifications by the present author. The output from the shock tube code gives the state of the gas (T, p, ρ), the mole fractions x_j of the mixture, and the laboratory time t_L etc. as functions of gas-particle time t_g (or t). The results are used for additional processing in order to obtain the refractive-index-gradient (dn/dy vs t_L).

For a given wavelength of light the refractive index, n, of the gas is related to its density, ρ, by the well-established Gladstone-Dale Law, which may be written as[100]

$$n = 1 + \kappa\rho \tag{5.22}$$

κ is known as the Gladstone-Dale constant, or specific refractivity which can be evaluated by the mixture rule

$$\kappa = \frac{\sum x_j \mu_j \kappa_j}{\sum x_j \mu_j} \tag{5.23}$$

Differentiating equations (5.22) and (5.23) yields

$$\frac{dn}{dt} = \kappa\frac{d\rho}{dt} + \rho\frac{\sum (\kappa_j - \kappa)\,\mu_j \frac{dx_j}{dt}}{\sum x_j \mu_j} \tag{5.24}$$

Noticing that

$$\frac{dn}{dy} = \frac{dn}{dt}\frac{dt}{dt_L}\frac{dt_L}{dy} \qquad (5.25)$$

and

$$\frac{dt_L}{dy} = \frac{1}{U_s} \qquad (5.26)$$

equation (5.24) can be rewritten as

$$\frac{dn}{dy} = \frac{1}{U_s(dt_L/dt)}\left[\kappa\frac{d\rho}{dt} + \rho\frac{\sum(\kappa_j-\kappa)\mu_j\frac{dx_j}{dt}}{\sum x_j\mu_j}\right] \qquad (5.27)$$

The author made use of the subroutine INTDY of LSODE[121] to evaluate the derivatives of t_L, ρ, and x_j with respect to gas-particle time. Equation (5.27) was used to calculate the refractive-index-gradient. This information was then compared with the observed laser-schlieren signal. The specific refractivities used are listed in Appendix 5.

5.4 RESULTS AND DISCUSSION

5.4.1 Simulated profiles

The proposed mechanism predicts the measured refractive-index-gradient profiles reasonably well above 1300 K. Figure 5.1 shows the simulated profiles compared with two measured C-pattern signals. The top simulated profile reproduces the experiment with the initial postshock temperature of 1655 K. A one-step mechanism (assuming that only ethane

is formed via reaction (5)) is also used in a second simulation of this signal. It turns out to be indistinguishable from the result determined from the full mechanism. This verifies that methyl recombination alone is responsible for the negative signals at relatively low temperatures, as described in the point-by-point analysis. Figure 5.1(b), where the initial postshock temperature is 2095 K, looks similar to Figure 5.1(a). However, the mechanism has changed here. Methyl recombination has little effect on the simulated profile: whether open or closed this channel gives no obvious contribution. Reaction (5) alone is no longer able to account for the negative signal. This is essentially because the fall-off effect has reduced the value of k_5 too much. In contrast, closing reaction channel (4) results in a very poor simulation. Therefore, the primary reaction, $CH_3+CH_3 \rightarrow C_2H_4+H_2$, is more important than methyl recombination, in this case.

At higher pressures, experiments (pattern D) exhibit progressively more positive signals. Our simulation with the proposed mechanism also successfully reproduces laser-schlieren signals of this type, as shown in Figure 5.2. Like the case of Figure 5.1(b), $CH_3+CH_3 \rightarrow C_2H_4+H_2$ is still the principal exothermic reaction for the two D-pattern signals. The major contributor to the slowly decaying positive component is the secondary decomposition of ethyl radical following the primary reaction (3).

At higher temperatures, we believe that an extrapolation of the azomethane decomposition rate of Wagner et al.[15] could serve as an upper boundary and that our calculation results, as shown in Figures 2.9 and 2.10, could serve as a lower bound. The real value must be in between. Our simulation confirms that Wagner et al.'s rate constant for azomethane decomposition, listed in Table 5.1, can be used up to 2700 K. Indeed, at about

2700 K it makes no difference in practice whether one uses Wagner et al.'s value or our theoretical results, except for considerations of incubation times (see below).

Figure 5.3 displays the simulation results at the temperatures above 3000 K. Using Wagner et al.'s rate coefficient for azomethane decomposition always gives a good simulation result. However, it is not appropriate to extrapolate their rate coefficient for azomethane decomposition to such high temperatures. An attempt to use our own calculated result for azomethane decomposition, as shown in Figure 2.10, has been made at those extremely high temperatures. It is quite successful in the simulation of experiments near 3000 K, such as shown in Figure 5.3 (a). However, at about 4000 K, simulation leaves no doubt that our calculation is an under-estimate of the azomethane decomposition rate coefficient. Without raising the rate coefficient of our calculation, attempts to fit failed. A good fit for Figure 5.3 (b), for example, is achieved only when the rate coefficient of our calculation is increased by at least a factor of 10. Simulation suggests a drop-off from a linear extrapolation of Wagner et al.'s rate coefficient for azomethane decomposition. But, this drop-off is much weaker than the theoretical prediction using the simplified collisional model (see chapter 2). This also suggests the need for a more exact collisional energy transfer model in the theoretical calculation of the rate coefficient for azomethane decomposition. It might alternatively imply that a slight positive temperature dependence for $-\langle \Delta E \rangle$, rather than a constant, should be adopted in the theoretical calculation, so that the collision efficiency, β_c, does not decrease so strongly with increasing temperature at the upper temperature range.

In the experimental profiles of Figure 5.3, only positive components of the gradients show up. Endothermic reactions, such as the decomposition of ethyl and methyl radicals,

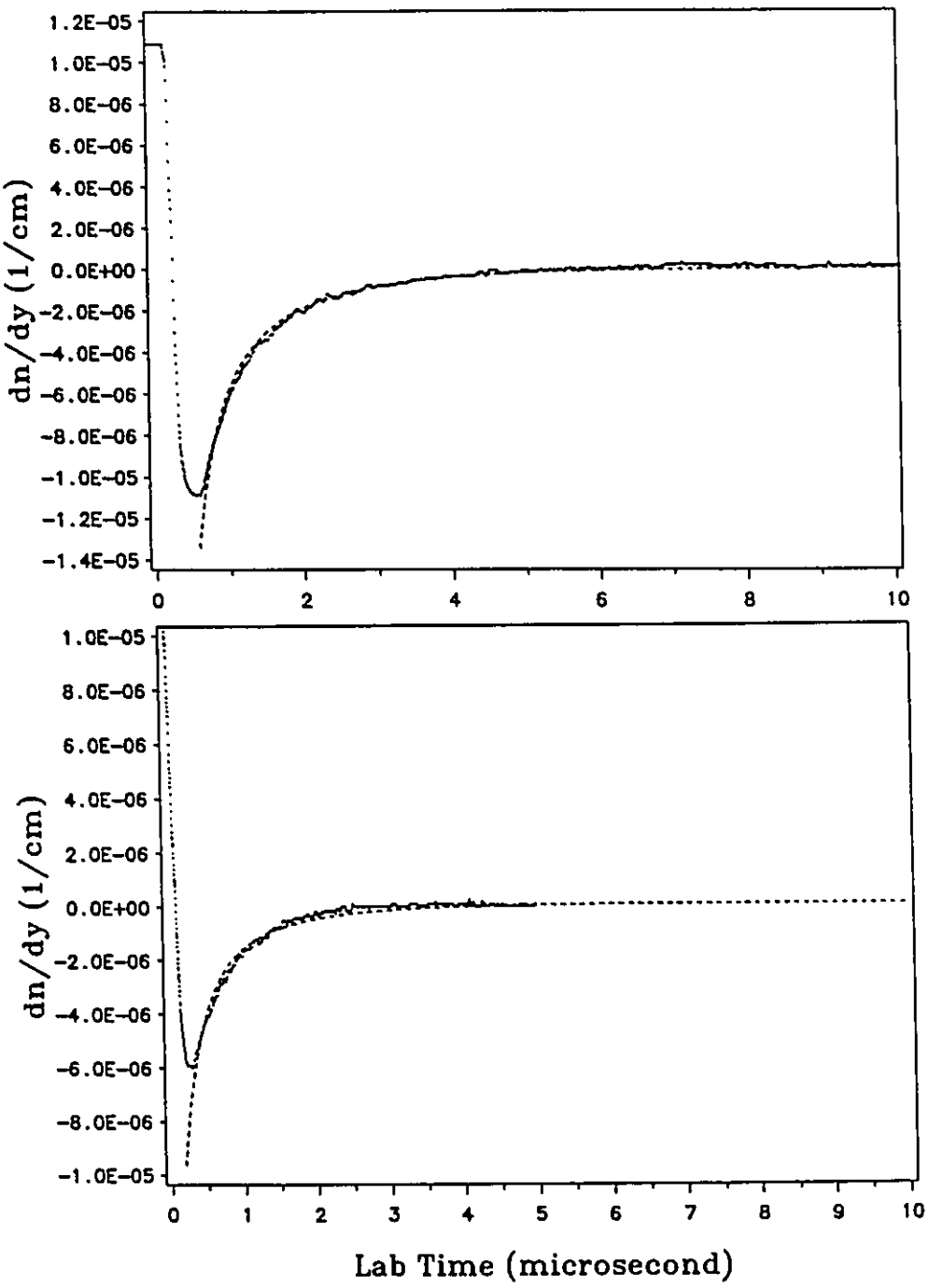

Figure 5.1 Comparison of simulated profiles with experimental signals (pattern C).

Top: (a) Experiment 5.3 (T_2 = 1655 K, P_2 = 0.218 atm)

Bottom: (b) Experiment 5.5 (T_2 = 2095 K, P_2 = 0.225 atm)

----------: Simulated profiles

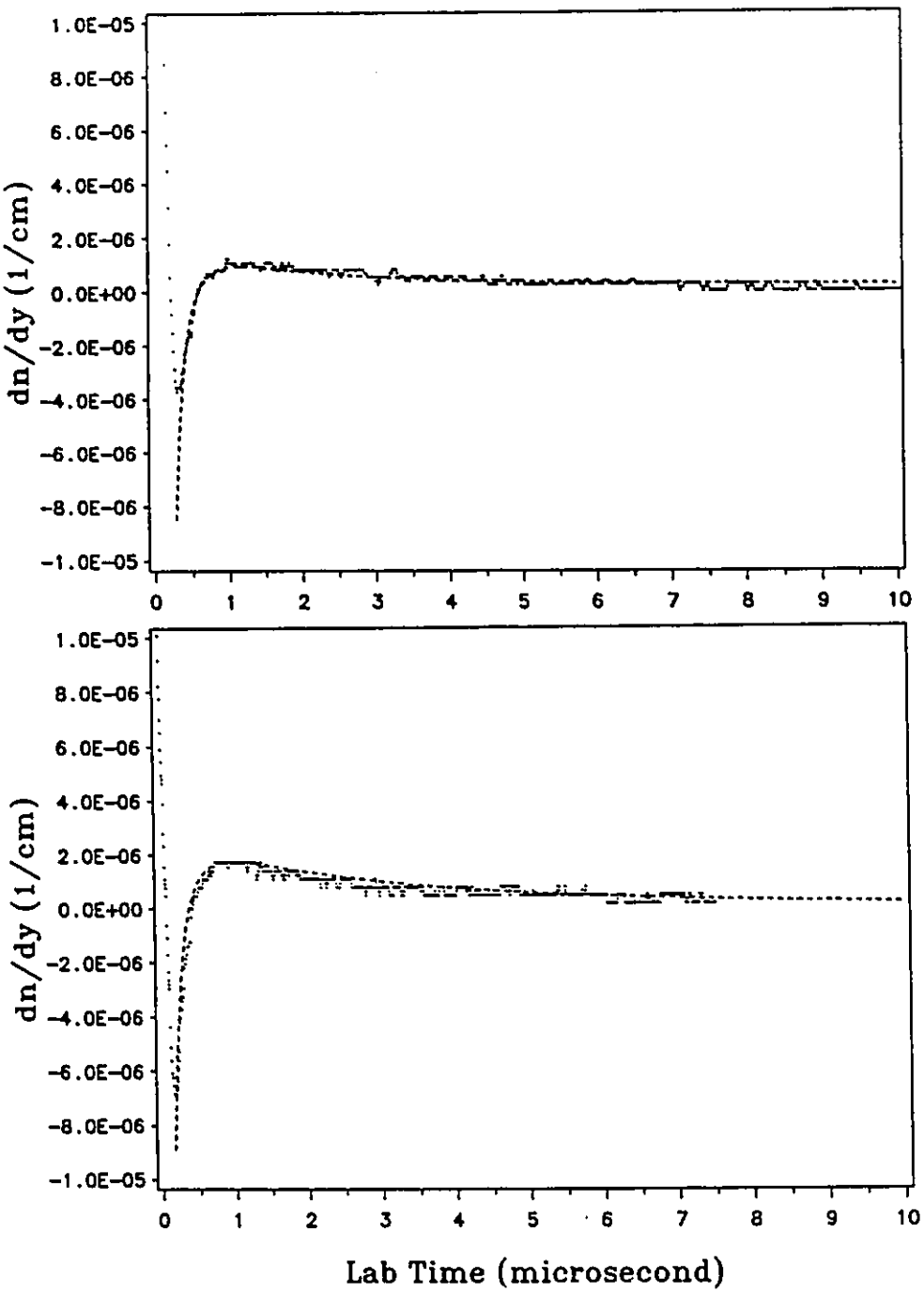

Figure 5.2 Comparison of simulated profiles with experimental signals (pattern D).

Top: (a) Experiment 10.1 (T_2 = 2025 K, P_2 = 0.594 atm)

Bottom: (b) Experiment 11.26 (T_2 = 2285 K, P_2 = 0.652 atm)

----------: Simulated profiles

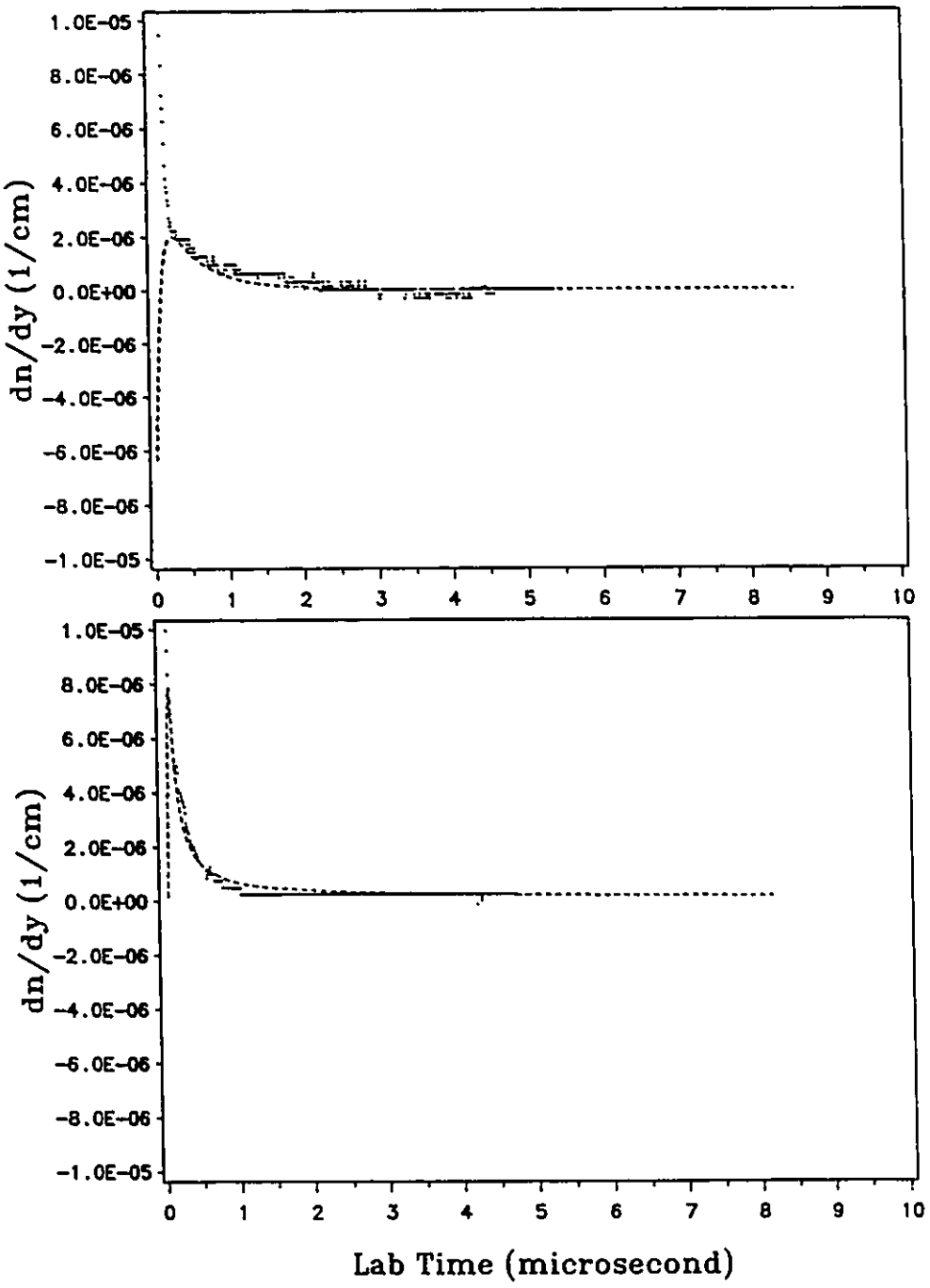

Figure 5.3 Comparison of simulated profiles with experimental signals (pattern E).

Top: (a) Experiment 11.33 (T_2 = 3099 K, P_2 = 0.411 atm)

Bottom: (b) Experiment 11.13 (T_2 = 4014 K, P_2 = 1.113 atm)

----------: Simulated profiles

definitely contribute to the positive signals. This does not mean that there are no exothermic reactions. On the contrary, exothermic reaction (4), $CH_3+CH_3 \rightarrow C_2H_4+H_2$, is very important, and ethylene decomposes very fast via endothermic channels at those temperatures. This is proved by the fact that omitting reaction (4) gave very poor simulated signals. More simulation results can be found in Appendix 6 and Appendix 7.

5.4.2 Sensitivity Analysis

Sensitivity analysis is performed using the SENKIN program code from Sandia National Laboratories,[124] which involves the integration of the system of ordinary differential rate equations with respect to time. It is a powerful, objective, and systematic tool to determine quantitatively and efficiently how the solution to a model depends on the various elementary reaction rate coefficients without solving the problem repetitively using different input values. It also helps to identify the important reaction pathways and it provides insight to the kinetics.

Because temperature is closely related to the experimental observable, it is chosen as the sensitive object. The first-order sensitivity coefficients of temperature with respect to the individual reaction rate coefficients are defined as

$$\delta_i = \frac{\partial T}{\partial k_i} \qquad i=1,2,\ldots\ldots,43 \qquad (5.28)$$

Note that the sensitivity coefficients change with time because temperature evolves with time. Figure 5.4 displays both the sensitivities of the individual reactions at early times when the primary reactions (1-6) are just starting, as well as the maximum sensitivities of the reactions

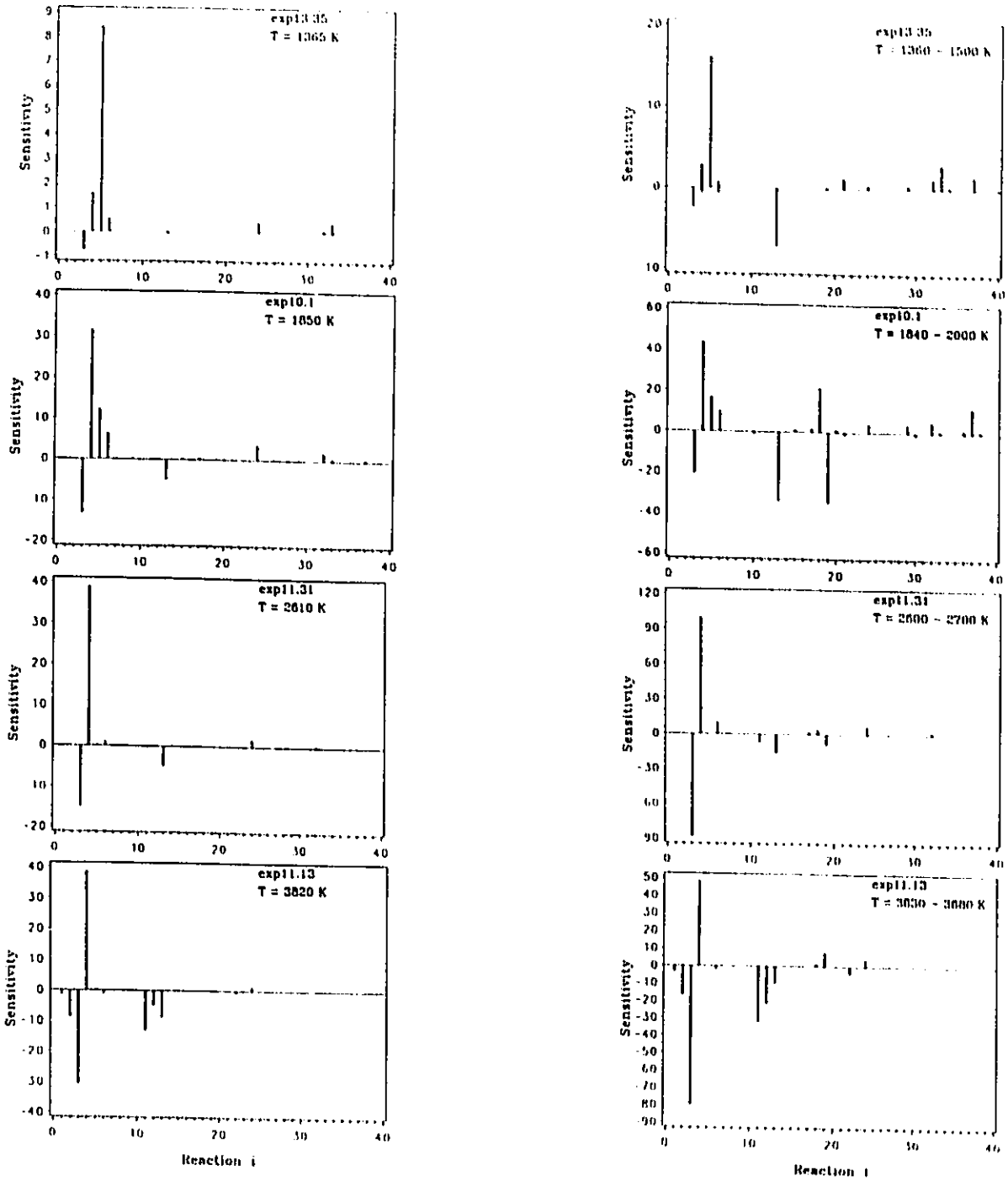

Figure 5.4 Sensitivity analysis for temperature evolution for the reaction mechanism of Table 5.1 under typical experimental conditions. Left column: sensitivities at various temperatures and early times. Right column: collection of the maximum sensitivities of the individual reactions in the given temperature ranges.

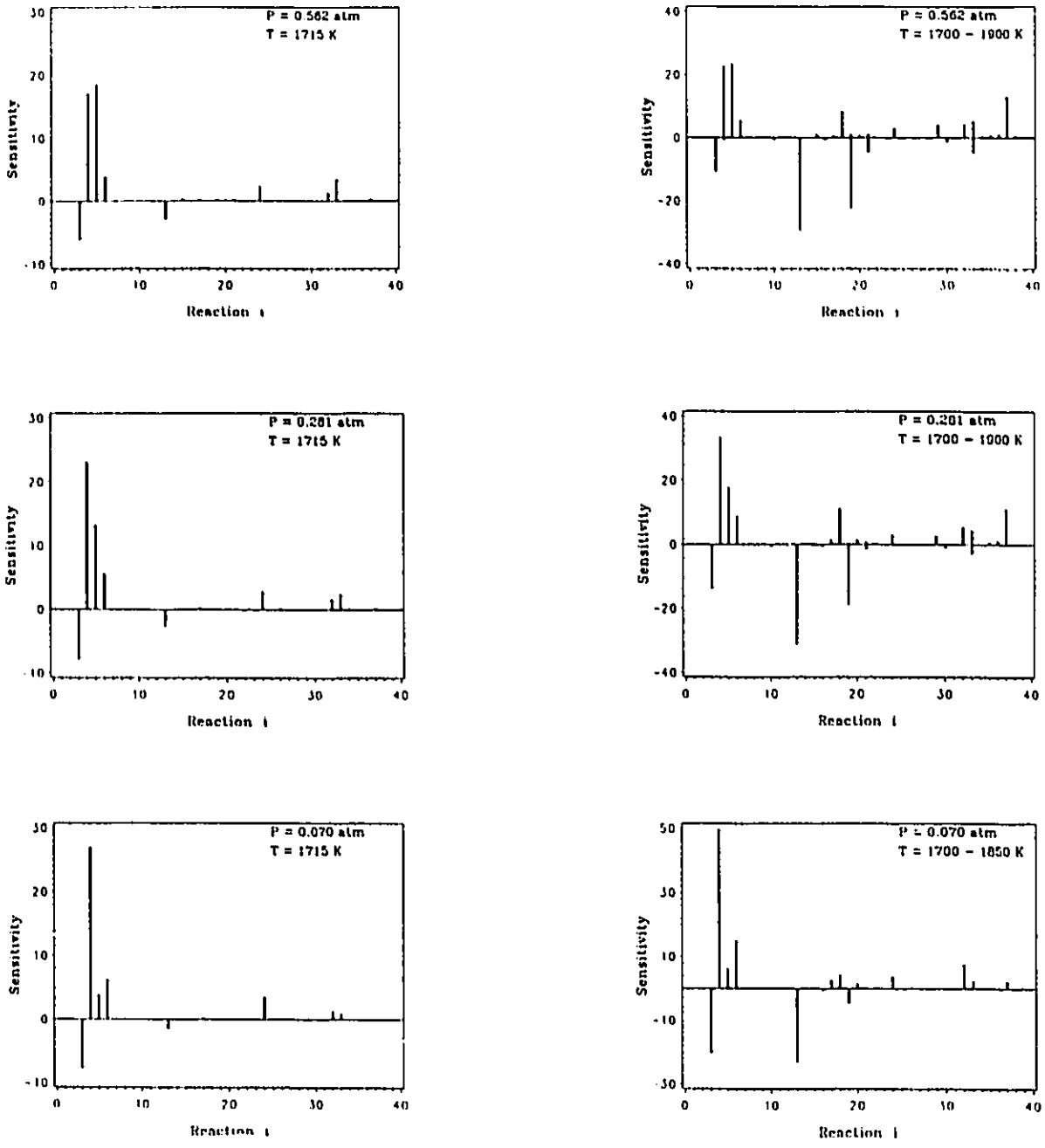

Figure 5.5 Effect of pressure on the sensitivity analysis for temperature evolution for the reaction mechanism of Table 5.1. Left column: sensitivities at early times at 1715 K. Right column: collection of the maximum sensitivities of the individual reactions in the given temperature ranges.

in the given time periods or temperature ranges. The plots in the left column mainly show how the primary reactions compete with one another in the early stages. The maximum sensitivities in the right column give an overall impression of the important reactions in the mechanism. Of course, each reaction reaches its peak sensitivity at different times or temperatures. Although the sets of the maximum sensitivities in the right column of Figure 5.4 illustrate basically the temperature effect, it should be pointed out that the variation among the four pictures is also due to different integration time periods and different pressures. Figure 5.5 demonstrates the effect of pressure.

A combined consideration of the endothermicity (or exothermicity), the sensitivity of each reaction, and the experimental (or simulated) signals leads to the following proposal for the major reaction pathways as shown in Figures 5.6.1-5.6.5.

The dominant reaction over the temperature range 1360 - 1500 K (see Figure 5.6.1) is the exothermic reaction (5). Methyl recombination alone is sufficient to reproduce the negative experimental signal in this temperature range. Three other primary reactions (3), (4), and (6) are not capable of competing against the ethane formation channel, although they may consume a small portion of methyl radicals. Sensitivity analysis reveals more details of the subsequent reactions. Ethane, reacting with H atoms, produces most of the ethyl radicals, which quickly dissociate to ethylene plus H. Two other radical association reactions, (33) and (-37), have large exothermicity. However, propane formation is a tertiary reaction and propene is formed at an even later time. Their contributions to the negative signal, therefore, are much smaller than that of reaction (5).

In the temperature range 1510 - 1780 K, the picture (see Figure 5.6.2) is not

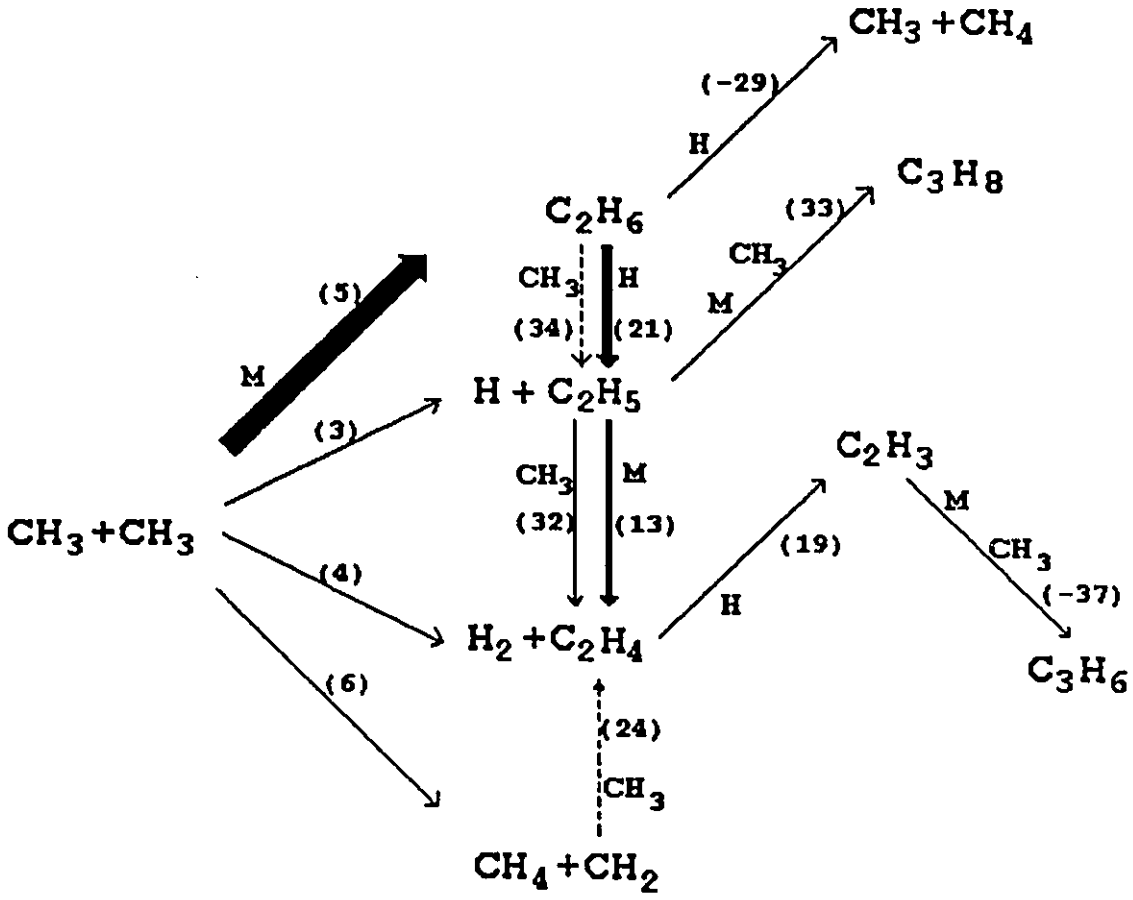

1360 - 1500 K

Figure 5.6.1 Reaction pathways for the decay of CH_3 under the conditions of Exp. 13.35

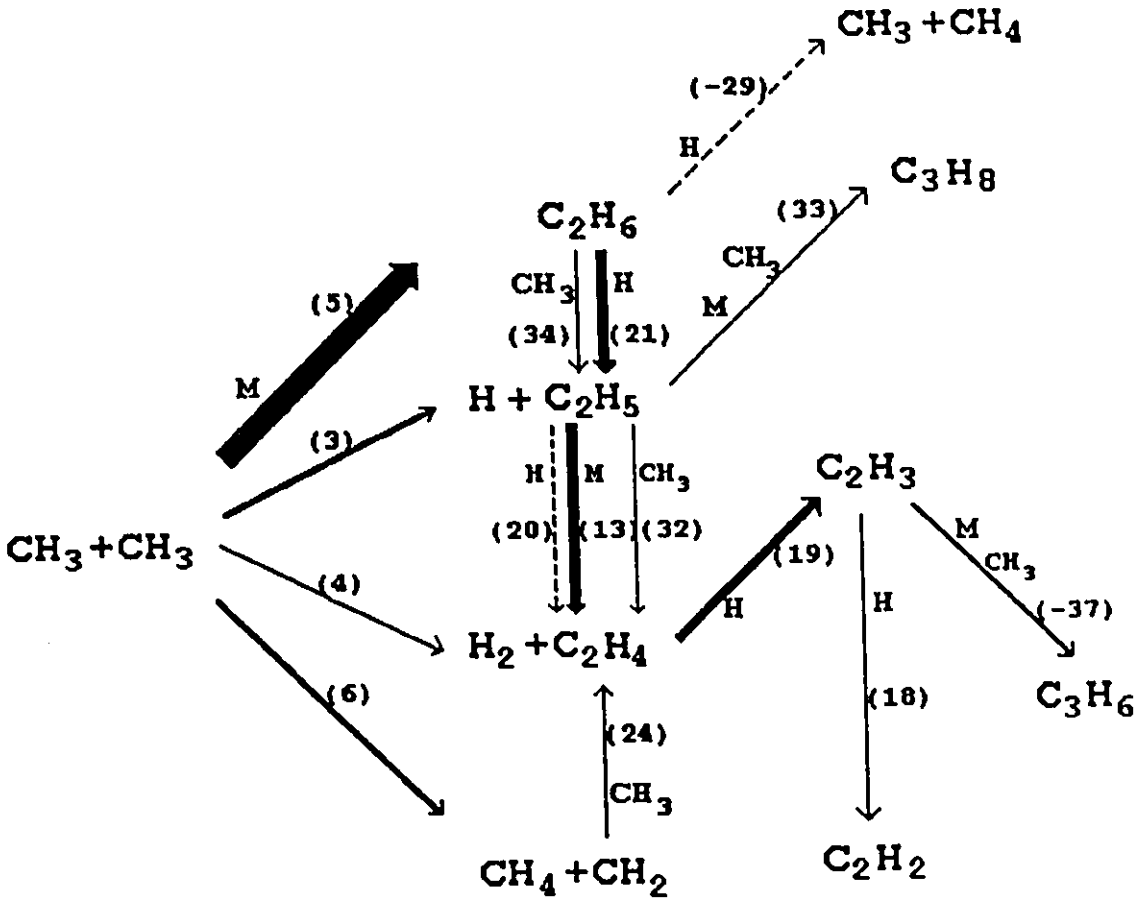

1510 - 1800 K

Figure 5.6.2 Reaction pathways for the decay of CH_3 under the conditions of Exp. 5.3

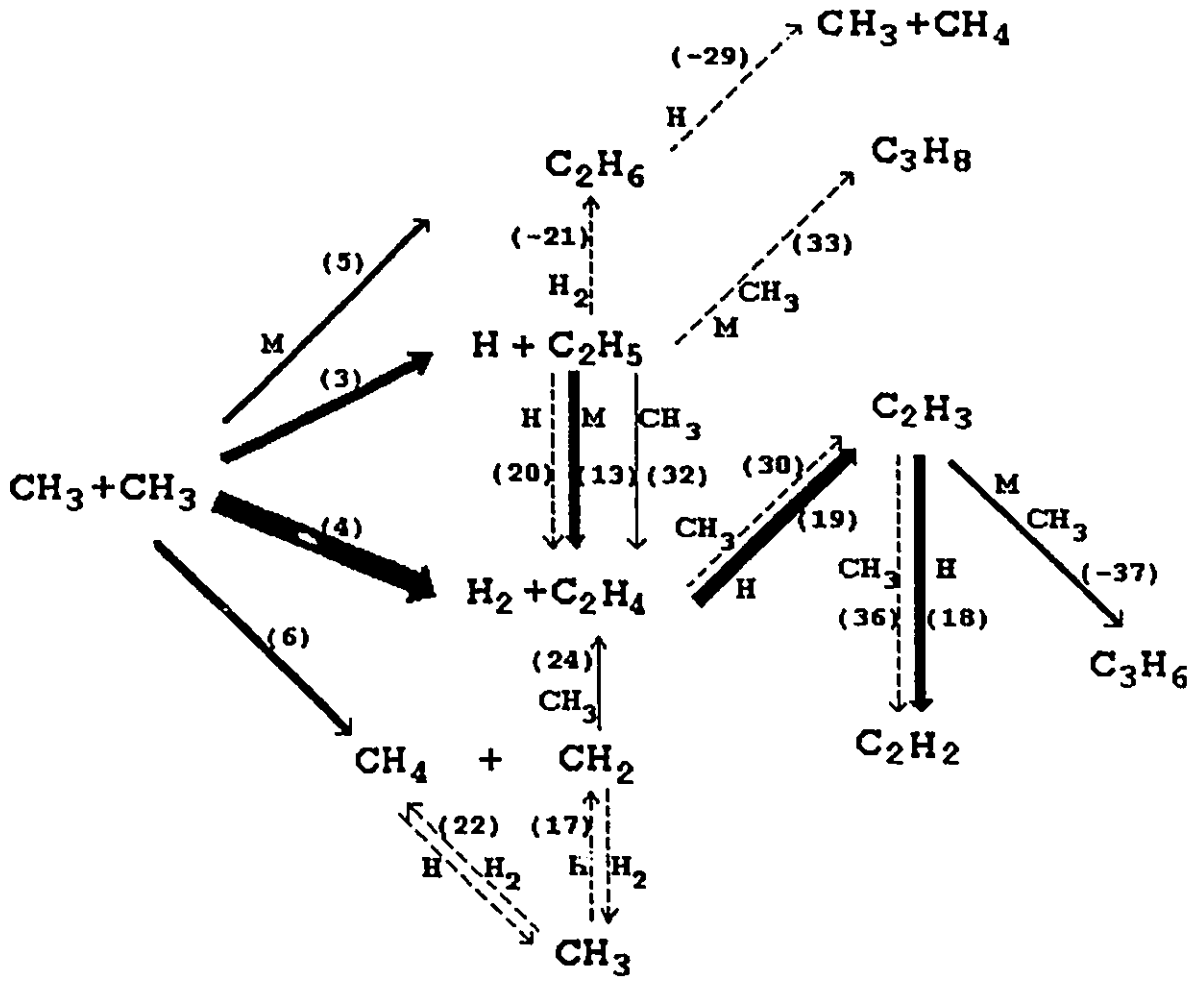

1840 - 2000 K

Figure 5.6.3 Reaction pathways for the decay of CH_3 under the conditions of Exp. 10.1

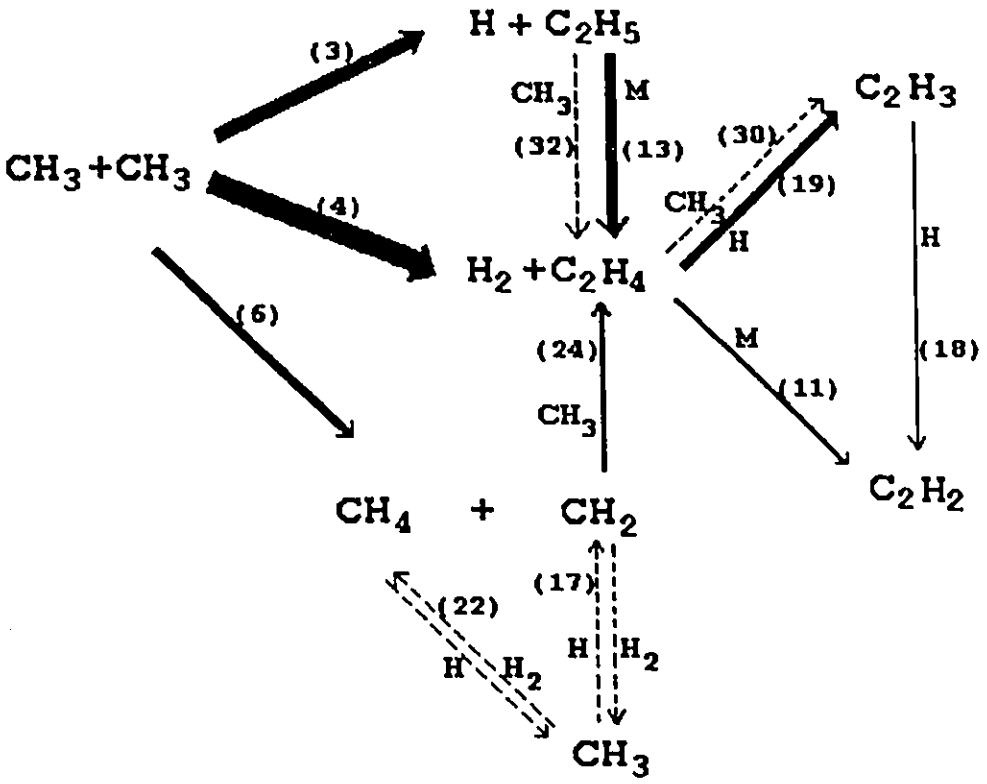

2600 - 2700 K

Figure 5.6.4 Reaction pathways for the decay of CH_3 under the conditions of Exp. 11.31

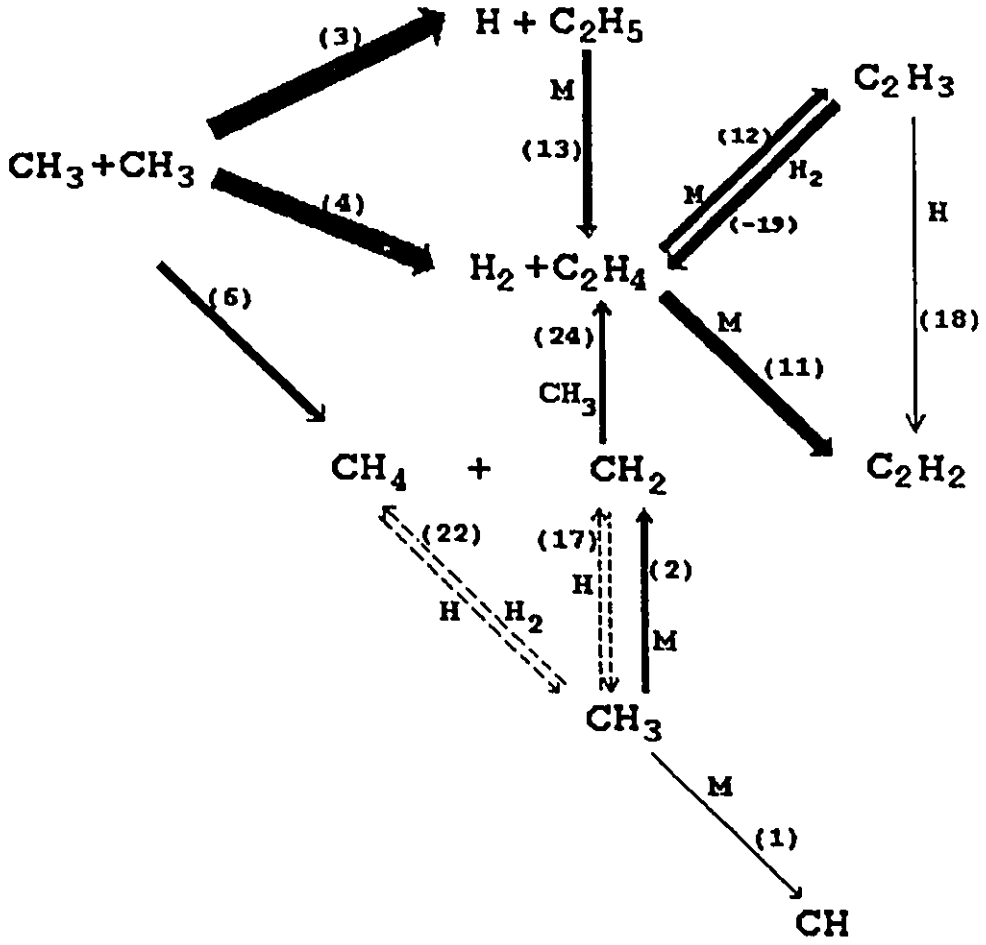

3830 - 3680 K

Figure 5.6.5 Reaction pathways for the decay of CH_3 under the conditions of Exp. 11.13

substantially different, and methyl recombination still dominates the mechanism. An increase in the temperature certainly accelerates the dissociation of the ethyl radical, which results in a faster H-atom transfer in reaction (21). Since more vinyl radicals are formed at these higher temperatures, the propene and acetylene content of the gas rises, (cf Figure 5.6.1).

When the temperature increases further, as shown in Figure 5.6.3, the most remarkable change is that reaction (5) becomes less important because of fall-off behaviour. Before drawing any conclusion, one should be very careful to notice the pressure range, which sometime is crucial in the competition of the primary methyl radical reactions. (This is clearly demonstrated in Figure 5.5). Under the conditions of experiment 10.1, the exothermic reaction (4), forming ethylene plus a hydrogen molecule, gains the upper hand in the battle for control. The disproportionation reaction (6) increases its rate accordingly. Another loss process for methyl radicals, reaction (3), also becomes an important step. Even though its low heat of reaction makes it practically invisible, the sequence of reactions (3) and (13) results in two highly reactive hydrogen atoms. Since ethylene and H concentrations are relative high in the early stages, reaction (19) then produces more vinyl radicals. The endothermic reactions, (13) and (19), are responsible for the positive components following the negative components of the laser schlieren signals (see Figure 5.2). At later times, vinyl further reacts with H producing a substantial amount of acetylene via reaction (18), and vinyl also combines with methyl forming propene at not too low a pressure. One can also see that above 1800 K reaction (33) has little influence on the scheme because of the fall-off effect. Under those conditions, C_2H_5 prefers to react with CH_3 via bimolecular disproportionation, ie. reaction (32).

Fall-off effects are demonstrated particularly well in Figure 5.5, which clearly explains the pressure influence on some of the reactions, such as reactions (5), (13), (33) and (-37). As temperature is continuously increased from 2000 K, reactions (5), (33), and (-37) gradually disappear from the sensitivity plots because of simultaneously lower pressure. In addition to the fall-off effect, thermodynamic effects also slow down reaction (5) (formation of ethane). Eventually this reaction becomes forbidden above 2300 K (the standard Gibbs free energy changes for reaction (5), ΔG°, are -41, -8, and +8 kJ mol^{-1} at 2000, 2200, and 2300 K respectively). This issue has been addressed previously in our point-by-point analysis. In this case, the formation of ethylene plus H_2 by reaction (4) is the only thermodynamically favoured exothermic reaction in the primary steps of CH_3 decay, as shown in Figure 5.6.4. The second major source of ethylene is ethyl dissociation following reaction (3). An additional ethylene source is the bimolecular reaction between methyl and carbene. At these high temperatures, ethylene then decomposes via a molecular channel, ie. endothermic reaction (11). Although the sequence of reactions ($C_2H_4 \rightarrow C_2H_3$ and $C_2H_3 \rightarrow C_2H_2$) will result in the same product, there is strong evidence that the main reaction in ethylene decomposition involves a H_2-molecular channel.[72-73,110]

Methyl radical decompositions (reactions (1) and (2)) gain in influence at higher temperatures, ie. $T \geq 3000$ K. Endothermic reactions are favoured at these high temperatures. As shown in Figure 5.6.5, endothermic effects resulting from reactions (1), (2), (3), (11), (12), and (13) are so strong that we can no longer see the negative profile but only a positive trace (see Figure 5.3). However, the simulation remains very sensitive to reaction (4) because the two-channel decomposition of ethylene (reactions (11) and (12)) account for the positive

signals. As already mentioned, those very high temperature experiments (signals with pattern E) cannot be reproduced if reaction (4) is omitted.

5.4.3 Rate Constant for $CH_3 + CH_3 = C_2H_4 + H_2$

The rate data for the reaction, $CH_3 + CH_3 = C_2H_4 + H_2$, deduced from shock tube experiments were obtained by comparing observed laser-schlieren profiles with the profiles calculated by numerical integration of the postulated mechanism. Considering the sensitivity of the simulation to k_4, and since k_4 is basically the only unknown, we have a fairly unambiguous and definitive measurement of k_4. The values of the rate coefficient, k_4, at the earliest observable points are displayed as an Arrhenius plot in Figure 5.7. This figure also illustrates the previous experimental values in the literature.[2,19,55-56,59-61] It can be seen that our results are generally in good agreement with the values of references 2, 19, 55, 56, 59, and 60 but quite different from that of reference 61. In Hidaka and coworkers' study of methane pyrolysis,[61] reaction (4) is merely one of their secondary steps. If their values for k_4 are used in our simulation, the calculated profiles are way off the experimental signals. In contrast to those studies where CH_3 reactions were secondary to the dissociation of precursors such as CH_4 and C_2H_6 on the same time scale, our pyrolysis of azomethane at temperatures > 1300 K in our experiments provides an essentially instantaneous and clean source of CH_3, and reaction (4) is a primary reaction. Therefore, our results not only confirm that much higher values of k_4 (than Hidaka et al 's) should be adopted, but also make the higher temperature kinetic data for this reaction available up to 4000 K. A least-squares fit gives

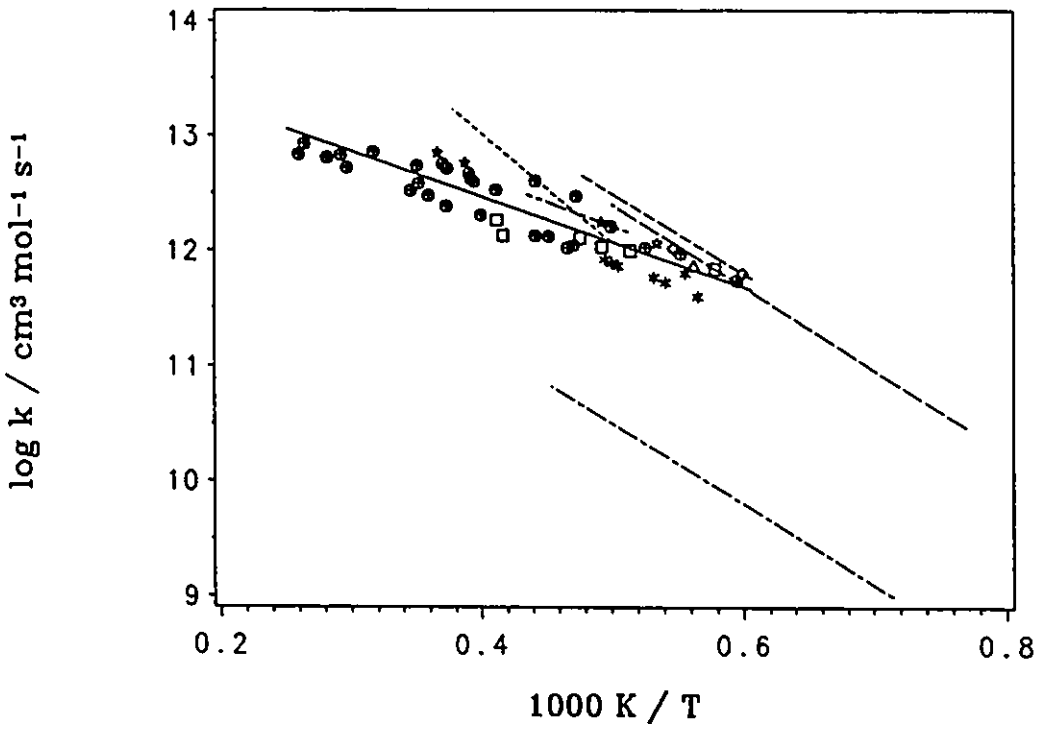

Figure 5.7 Arrhenius plot of derived rate constants for $CH_3 + CH_3 = C_2H_4 + H_2$

Azomethane molar composition □ 4.2%, * 6.3%, • 6.5%, ▵ 6.8%, ◇ 7.0%, ⋆ 7.7%: this work

———————— This work, equation (5.29)

- - - - - - - - - - - - - Ref. 2, 55

— — — — — — — — — Ref. 59

·· — · — · — · — Ref. 19, 60

..... Ref. 56

— · — · — · — · — Ref. 61

$$k_4 \ / cm^3 mol^{-1} s^{-1} = (1.1 \pm 0.4) \times 10^{14} \exp[-(9026 \pm 668)/T] \qquad (5.29)$$

covering the temperature range from 1800 to 4000 K. This is the first experimental study for the reaction $CH_3 + CH_3 = C_2H_4 + H_2$ over such a wide range of temperature. Rate coefficient data above 2650 K were not previously available. The k_4 which we have obtained is also supported by Davidson et al.'s latest shock tube study of ethane decomposition monitored by laser absorption of methyl radicals over the temperature range 1350 - 2110 K.[136]

Since methyl recombination generally dominates the mechanism at lower temperatures, k_4 cannot be uniquely determined below 1700 K. Methyl recombination above 2300 K is forbidden, and thus its rate constant should have no effect on the value of k_4 above that temperature. The region between 1700 and 2300 K is problematical, and it is therefore worth examining it more carefully: Figure 5.8 shows the influence of the variation of k_4 by a factor of 2 on the calculated refractive-index-gradient profile at about 2000 K. Dividing k_4 by 2 gives less positive a profile at early times, while multiplying k_4 by 2 renders the profile more positive at later times than the experimental one. It is strictly not correct to assume that all the $\alpha_{ji} = 1$ (see section 5.1.1). This assumption is most likely to affect the rate coefficient for methyl recombination. If one takes into account the different collision efficiencies of each species in the mixture and if one uses an overestimated value (10 times as efficient as Ar) for anything else besides Ar, k_5 would be increased by at most a factor of 2 under our experimental conditions. Fortunately, it hardly affects k_4 in practice, since simultaneously changing the effective second order rate coefficient, k_5, by a factor of 2 does not alter the picture. This is because of the much larger Ar concentration than anything else. Therefore

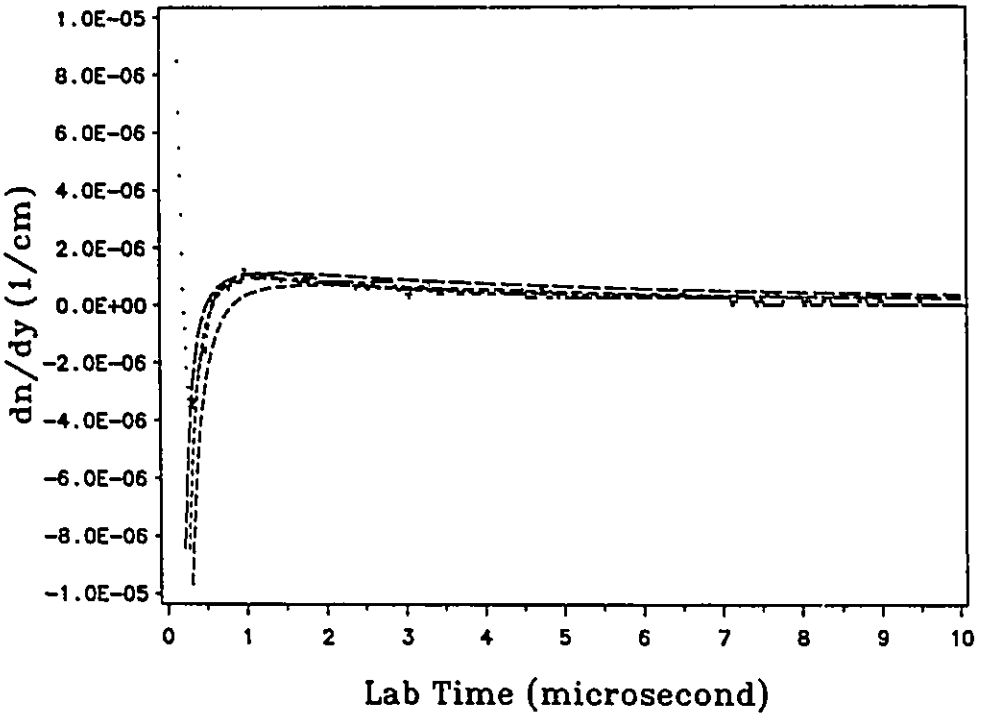

Figure 5.8 Influence of the variation of k_4 on the simulation of experiment 10.1

$k_4 \times 1$: ..... $k_4/2$: - - - - - - - - - - - - - $k_4 \times 2$: ———————

we are fairly confident of equation (5.29) even at 2000 K.

Methyl decomposition is important only when the temperature is above 3000 K. There are three different sets of rate coefficients for reactions (1), (2), (7), (8), and (43) due to Kiefer and Kumaran[31] (KK), Dean and Hanson[26] (DH), as well as Markus and Roth[30] (MR). There is also another set listed in Table 5.1, which is a combined set due to KK, DH, MR, and us.[104] No matter which set is used, our high-temperature experiments are well reproduced, with k_4 varying by less than 50%. This is just as Kiefer and Kumaran already indicated that comparably satisfactory simulations of the DH results can be achieved using any one of the KK, DH, and MR sets.[31] The fact that those different choices of rate constants for methyl decomposition give satisfactory simulations of our laser schlieren traces is good evidence for the reliability of our determination of k_4. On the other hand, our experiments are not able to identify which set is closer to reality.

The reliability of k_4 at higher temperatures is associated with that of k_3 and k_6. The rate coefficient, k_3, was measured by Frank and Braun-Unkhoff (FB) using ARAS in the temperature range 1320-2300 K.[18] Extrapolation of k_3 to 4000 K certainly involves some uncertainty. The disproportionation reaction (6) could produce carbene in both triplet and singlet states. There has been no experimental study which could measure the triplet and the singlet rate constants separately. All of these uncertainties are inter-related. However, our simulation shows that FB's k_3 still is the best choice. An absolutely precise determination of k_4 is only possible if the triplet and the singlet rate constants of reaction (6) and k_3 are measured accurately and separately over the entire temperature range.

Arrhenius plots of the six primary methyl radical reactions (1-6) are drawn in Fig. 5.9.

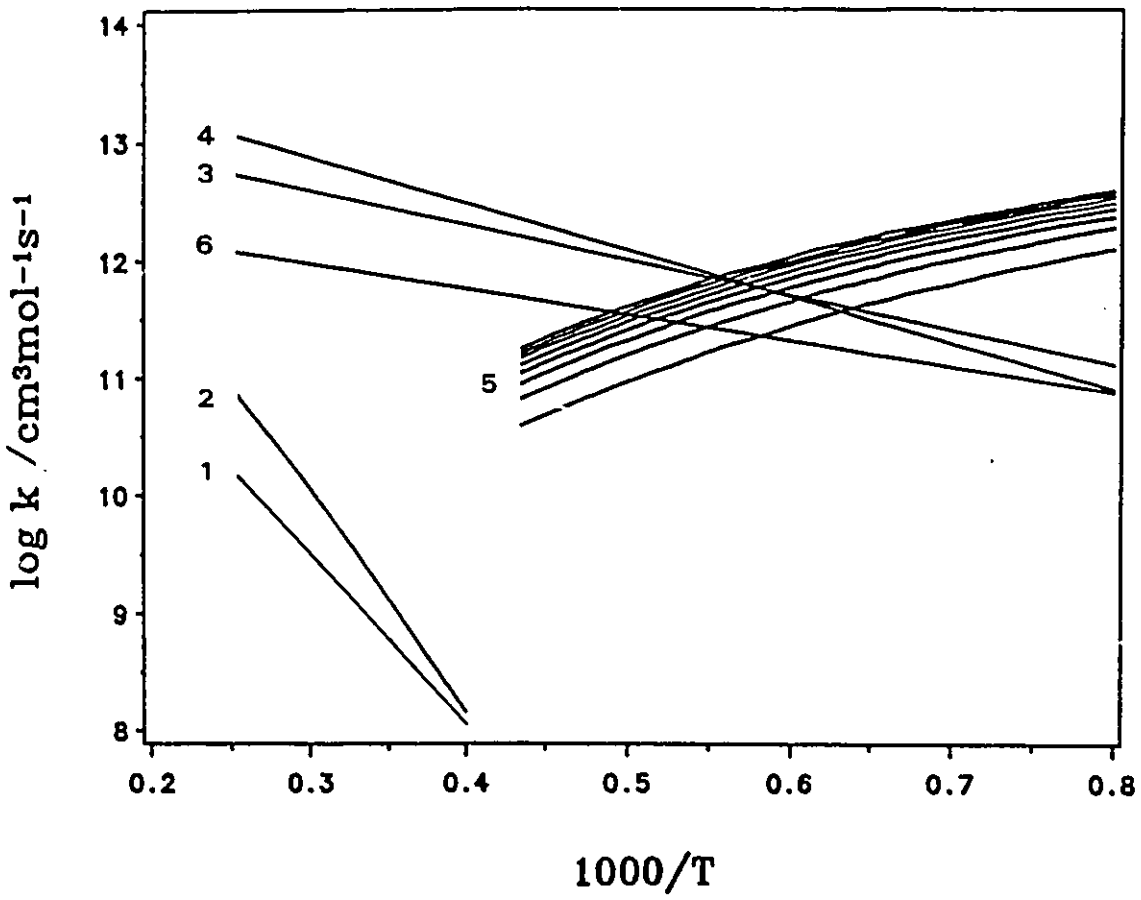

Figure 5.9 Arrhenius plots of primary methyl radical reactions (1)-(6). The "unimolecular" reaction (5) is evaluated at total densities of 0.5, 1.0, 1.5, 2.0, 2.5, 3.0, 3.5, 4.0 $\times 10^{-6}$ *mol* cm^{-3} (from bottom to top).

This picture shows roughly how the primary reactions compete with one another under different conditions.

5.4.4 Significance of Results

In many hydrocarbon pyrolysis and combustion studies, the reaction, $CH_3 + CH_3 \rightarrow C_2H_4 + H_2$, was often ignored. It was either omitted completely or it was assigned a very small rate coefficient.[7,14,31,61,65,68,74,141-143] Significant errors in the extraction of rate coefficients or in the prediction of the behaviour of various combustors are generated by ignoring such an important reaction. On the basis of our results, a revision should be made of many previous combustion and pyrolysis studies.

One hypothesis assumes that reaction (4) forms excited "ethane" in the first step and then this activated complex decomposes to the products:

$$CH_3 + CH_3 \rightleftharpoons C_2H_6^* \rightarrow C_2H_4 + H_2$$

It used to be thought that the energy barrier is enormous, and it has been estimated to be 130 *kcal mol*$^{-1}$. [144] This is the reason reaction (4) is often ignored. However, the present study gives a much lower activation energy of 17.9 ± 0.6 *kcal mol*$^{-1}$. In order to interpret our observation, a search for a low energy path has to be made. According to Melius's BAC-MP4 calculation of heats of formation for stable and unstable species,[97] we can identify a low energy path, as shown in Figure 5.10. The barrier for this low energy path is 18.4 *kcal mol*$^{-1}$,

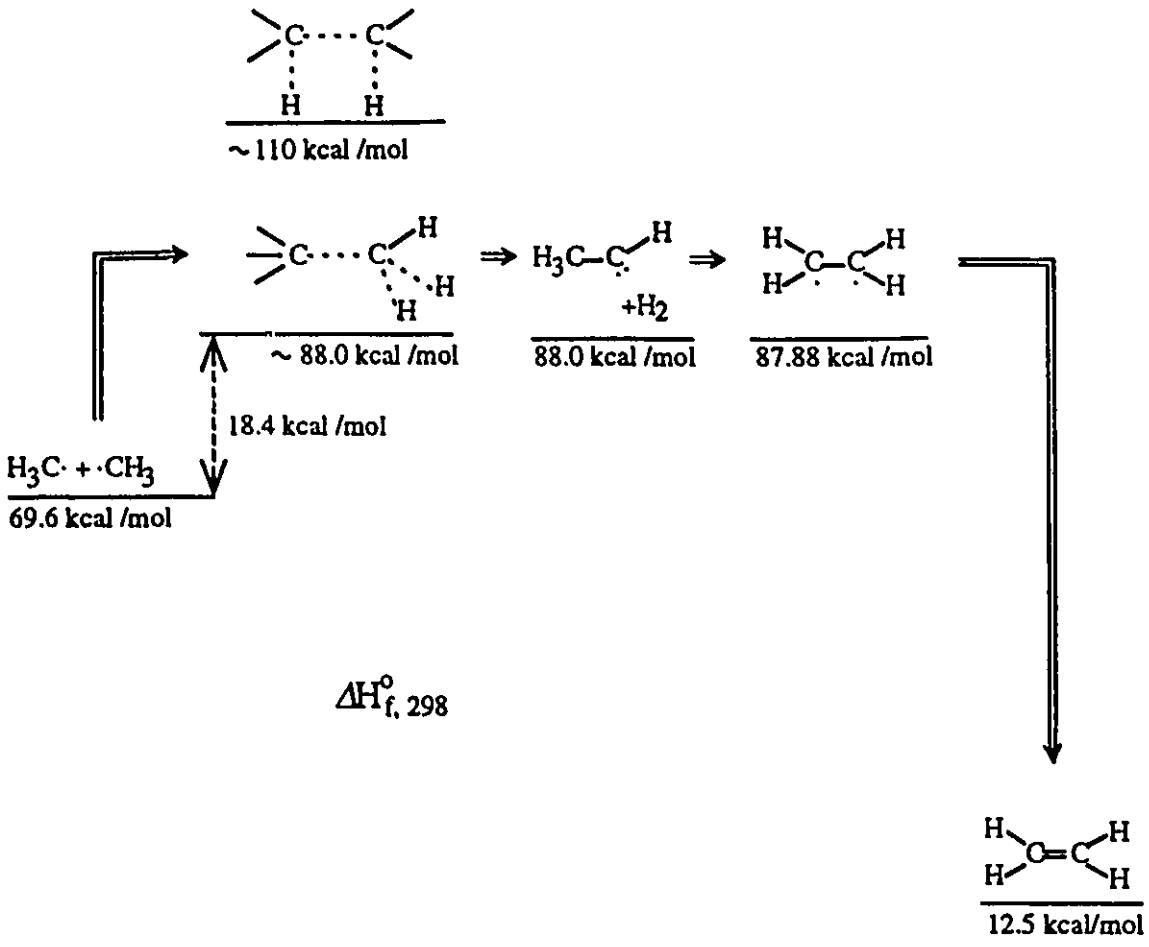

Figure 5.10 A low energy path for $CH_3 + CH_3 \rightarrow C_2H_4 + H_2$

and it agrees very nicely with the activation energy which we have found. In other words, our experiments show that C_2H_6* loses two H-atoms from the same carbon rather than from two separate carbons.

5.4.5 Incubation Times

When shock heated, a gaseous reactant is adiabatically compressed, and its translational temperature is raised nearly instantaneously from room temperature to several thousand degrees. However, translational-vibrational (T-V) energy transfer is comparatively ineffective.[125] The vibrational energy content of the gas molecules, on which the unimolecular reaction rate depends, lags well behind that of the other degrees of freedom. Therefore, unimolecular dissociation exhibits a delay while the vibrational energy distribution is relaxing to that corresponding to the higher kinetic temperature of the shock.[126] The effect is also manifested in the reverse or recombination process. The delay of the onset of chemical reaction after the sudden heating of a gaseous reactant has been termed "incubation" in the literature on thermal reactions.[127] Its determination is an important goal, because it is an additional diagnostic for the evaluation of theories of unimolecular reaction. Unfortunately it is rather difficult to measure it for large molecules because the incubation zone lasts for only a few vibrational relaxation times, typically less than 0.1 μs. However in the present study, it is the "unimolecular" reaction $2CH_3 \rightarrow C_2H_6$ which concerns us, and C_2H_6 may be small enough a molecule to make such a measurement feasible.

Incubation times can be measured by the use of the very fast and sensitive laser-

schlieren technique. Dove, Nip, and Teitelbaum observed, for the first time, incubation periods in the dissociation of a polyatomic molecule, during a shock tube study of the thermal decomposition of nitrous oxide (N_2O).[105] Recently, Kiefer, Kumaran, and Sundaram conducted a shock tube study of the highly strained norbornene (bicyclo[2,2,1]hept-2-ene, C_7H_{10}) dissociation, which provided the first measurements of unimolecular incubation times for the dissociation of a large polyatomic molecule.[128] It was found in several other studies too that a relative shift between observations and simulations of dissociation reactions had to be postulated in order to obtain a good fit to experiment,[31,68,129-131] and this is perfectly understandable and expected according to the theory of unimolecular reactions.

In shock tube experiments, the incubation time is the period between the shock arrival, "time origin", and the "starting point" at which molecules are dissociating at the maximum rate after the establishment of a quasi-steady vibrational distribution. The moment when the shock front passes through the centre of the laser beam corresponds to the "time origin", and the temperature of the system is increased instantly at that moment. Estimation of the incubation time is possible only if one knows the exact time origin. There has been a long argument about this location. Dove and Teitelbaum located the time origin at the first minimum in a laser schlieren signal,[132] while Kiefer et. al. assigned the positive portion of a laser schlieren signal near the zero-crossing for the time origin. (This is 0.2 to 0.4 μs, in gas time, later than the first signal minimum[68-70,129,133]). Consequently, this represents a limit to our precision. The data presented in Figure 5.11 are based on Dove and Teitelbaum's assignment for the time origin. They might be over-estimated if Kiefer et. al.'s assignment is applied.

In the present study, the introduction of an incubation time was necessary in order for our experiments to agree with our computer simulations. In practice, the incubation time was assigned as the time which was required to shift an experimental signal to the left so that it coincided with its simulated profile. Each estimated incubation time, $\Delta t_{gas} = \Delta t_{lab} (\rho_2/\rho_1)$, multiplied by the initial postshock pressure, p_2, is drawn against the reciprocal of the temperature in a semi-logarithmic plot, Figure 5.11. The accurate determination of incubation times is rather difficult because they are less than 1 microsecond in duration and are hidden by the schlieren spike due to the shock front. Nevertheless, the plot does show a trend that incubation time becomes longer at higher temperatures, apparently indicating that energy transfer becomes less efficient. This is a curious result, because it is the opposite of what is observed in the case of N_2O. Furthermore, it is expected that in the case of C_2H_6* where the vibrational relaxation time is very short (less than 0.02 μs at room temperature[140] and hence much less than that at our high temperatures) the incubation time should be no more than 0.2 μs at 1 atmosphere. Therefore, we believe that Figure 5.11 may well reflect the incubation times for "unimolecular" recombination of CH_3 at temperatures less than 2300 K, but that at higher temperatures it reflects an anomalous slowing down of the dissociation of the parent azomethane itself. This is echoed by our theoretical calculation and computer simulation where a drop in the rate of azomethane decomposition is claimed at upper temperatures because of less efficient energy transfer. Clearly, more work is required to understand the energy transfer properties of highly excited azomethane.

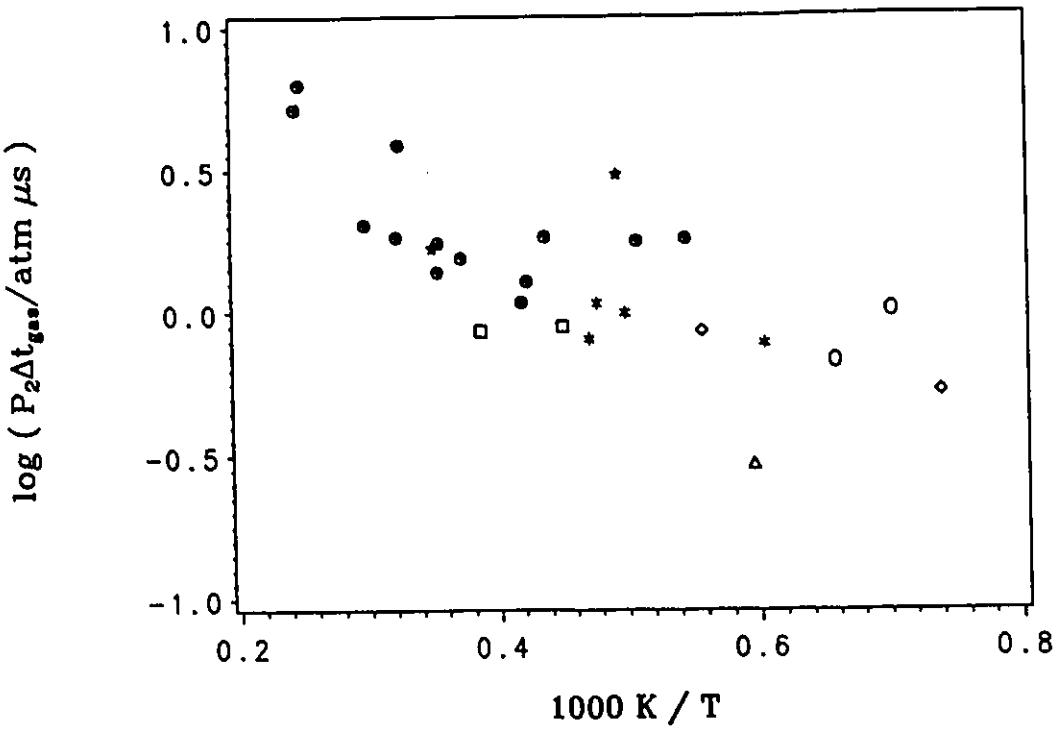

Figure 5.11 Incubation times

(azomethane molar composition ∘ 1.7%, □ 4.2%, . 6.3%, • 6.5%, ▵ 6.8%, ◇ 7.0%, ⋆ 7.7%)

CHAPTER 6

CONCLUSIONS

This study involved shock tube experiments using a laser-schlieren detection system, designed to observe the primary reactions of methyl radicals. The rate of disappearance of methyl radicals was monitored over the temperature range 1400 to 4000 K behind incident shock waves. Experimental results were analyzed with the aid of analytical models and numerical modelling to evaluate the rates of methyl radical reactions. This study leads to the following major conclusions:

1. Under typical combustion conditions, methyl recombination is in the fall-off regime. The rate constant for methyl recombination obtained from the analytical point-by-point analysis supports the unimolecular reaction theory developed by Troe, and is in very good agreement with the recommendation from a recent compilation.[32] That recommendation was then used in a numerical simulation of the complete reaction because of its explicit expression of the temperature and pressure dependence, and because it best reproduces our experiments. Our computer simulation and point-by-point analysis confirm that below 1700K $CH_3 + CH_3$ (+ M) ⇌ C_2H_6 (+ M) dominates the mechanism, and it is responsible for the observed negative signals. Due to the involvement of other competing channels, its influence begins to decrease above 1700 K. Between 1700 and 2000 K, its influence depends on pressure. Above 2000 K this reaction has little effect, and eventually it becomes forbidden

thermodynamically when $T > 2300$ K. Incubation times for low pressure "unimolecular" recombination of CH_3 / dissociation of C_2H_6 were deduced for the first time.

2. The rate constant for $CH_3 + CH_3 \rightarrow C_2H_4 + H_2$, which was basically unknown at high temperatures, was determined by comparing experimental signals with those from numerical integration of a postulated mechanism of 44 reactions. Although this was an indirect determination, our signals are sensitive to the value of k_4 over virtually the entire range, 1800 - 4000 K. Above 2000 K, it becomes the most important exothermic reaction, so that combined with the literature data the present measurements lead to an unambiguous value of k_4 over the range 1800 - 4000 K. Our results support large values of the rate coefficient. The fit, equation (5.29), has an uncertainty of a factor of 2. The value of k_4 depends upon an assumed reaction mechanism and the associated rate parameters for all contributing reactions, but the only possible parameters, which could change our results at the highest temperatures, are the rate coefficients, k_3 and k_6. However, the k_4 which we obtained should not be too far away from reality unless there is a dramatic change in the values of k_3 or k_6. Our measured activation energy is proof that C_2H_4 is produced via H_3CCH rather than via $H_2C\text{-}CH_2$ transition states.

3. $CH_3 + CH_3 \rightleftharpoons C_2H_5 + H$ and the secondary decomposition of C_2H_5 are important reactions, partially responsible for the positive part of the laser-schlieren signals. The best choice of the rate constant for the former reaction, recommended by this work, is that of reference 18. Direct measurement of the rate constant for this reaction, over a wider range

of temperature, is clearly needed. Probably the best technique for this is ARAS detection of H atoms.

4. The disproportionation reaction $CH_3 + CH_3 \rightarrow CH_2 + CH_4$ has the smallest reaction enthalpy compared to the other primary reactions. Thus our studies are essentially blind to this reaction. There has been no reliable experiments where singlet- and triplet-carbene channels are measured separately. This lack of specificity might be a source of uncertainty in our value of k_4.

5. Fall-off behaviour in the thermal decomposition of the methyl radical was studied theoretically using Troe's factorization approach. Methyl radical dissociation, in practice, takes place in the lower fall-off region very close to the low pressure limit. The dissociation rate coefficient at the low pressure limit, given by equation (2.64) or (2.65), is in good agreement with experimental values published in the literature. It also demonstrates an activation energy smaller than the bond dissociation energy. Our high pressure dissociation rate constant expression is consistent with the calculations of Merkel and Zulicke for data set B. We have confirmed Aoyagi *et al.*'s results that the rate coefficient for the high pressure recombination of $CH_2 + H$ increases mildly with increasing temperature. Low pressure experimental rate data for $CH_2 + H \rightarrow CH + H_2$ appear not to involve recombination phenomena. The CH_3 decomposition system is a good test case for evaluating theories of multichannel unimolecular dissociation. Substantial disagreement persists regarding which decomposition channel (reaction (1) or (2)) has a higher energy barrier, and our simulation

was unable to identify this either. CH_3 decomposition has an effect on the reaction only at temperatures above 3000 K.

6. Although azomethane has often been used as a precursor of CH_3, fall-off behaviour in its thermal decomposition has been ignored up until now. A theoretical calculation of the decomposition rate using a constant value for $-\langle\Delta E\rangle$ gives a good fit to the experimental results of Moller, Mozzhukhin, and Wagner,[15] but it predicts a severe "drop-off" in the decomposition rate at temperatures above 3000 K due to the use of the inadequate collisional energy transfer model. The numerical simulation of our experiments, however, suggests a much weaker drop in the rate than the theoretical prediction, and a slight positive temperature dependence for $-\langle\Delta E\rangle$ instead of a constant. The drop-off in the rate coefficient is supported by our observation of anomalously large incubation times for methyl radical reactions at high temperatures. Similar drop-offs in the decomposition rates of cyclohexene and vinylcyclohexene have been reported in the literature: Above a certain temperature, the rate constants fall far below a linear extrapolation of an Arrhenius plot through the lower temperature results.[134-135] More experiments are required to characterize the unimolecular decomposition of azomethane at very high temperatures.

7. Chemical chaos and oscillation were observed in the pyrolysis of azomethane at 900-1300 K for the first time.

Appendix 1. Statistical Equilibrium Constant for $CH_3NNCH_3 \rightarrow CH_3NN+CH_3$

The equilibrium constant of the title reaction is related to the partition functions of the species involved

$$K_p = \frac{\frac{q^0}{N_A}(CH_3NN)\ \frac{q^0}{N_A}(CH_3)}{\frac{q^0}{N_A}(CH_3NNCH_3)} \exp(-\frac{E_0}{RT})$$

where q^0's are the molar partition functions at standard pressure, N_A is Avogadro's constant, and E_0 is the dissociation threshold energy. The molecular partition function can be factorized into contributions from each mode, namely translation, rotation, vibration, and electronic (only the translational components depend on the pressure):

$$q = q_e\, q_v\, q_r\, q_t$$

$$q_e = \sum_i g_i \exp(-\epsilon_i / kT)$$

$$q_v = \prod_{j=1}^{s} [1-\exp(-\frac{1.43879\ \tilde{\nu}_j / cm^{-1}}{T/K})]^{-1}$$

$$q_r = \frac{1.0270}{\sigma} \frac{(T/K)^{3/2}}{(A_R B_R C_R / cm^{-3})^{1/2}}$$

$$\frac{q_t^0}{N_A} = 2.561\times10^{-2} (T/K)^{5/2} (\mu / g\ mol^{-1})^{3/2}$$

where g_i and ϵ_i are the degeneracy and the energy of the electronic states, s is the number of oscillators, ν_j is the vibrational frequency (in wave numbers), σ is the symmetry number,

A_R, B_R, C_R are the rotational constants, and μ is the molecular weight.

The procedure leads to K_p, which can be converted to K_c using the ideal gas law

$$K_c\ /mol\ cm^{-3} = \frac{K_p\ /atm}{82.0578\ T/K}$$

Some of the results are listed in Table A.1. The values of K_c are fit to the following equation in the temperature range 1000 to 4000 K

$$K_c\ /mol\ cm^{-3} = 1.965\times10^{13}\ T^{-2.8244}\ \exp(-32080/T)$$

Table A.1 Statistical Equilibrium Constant for $CH_3NNCH_3 \rightleftharpoons CH_3NN + CH_3$

T /K	1000	2000	3000	4000
q_v(AB)	2.08002×10^{3}	6.19252×10^{6}	3.32098×10^{9}	5.22387×10^{11}
q_v(A)	3.13492×10^{1}	1.45735×10^{3}	3.16547×10^{4}	3.83666×10^{5}
q_v(B)	2.45308×10^{0}	1.03268×10^{1}	3.74667×10^{1}	1.12610×10^{2}
q_r(AB)	9.73418×10^{4}	2.75324×10^{5}	5.05803×10^{5}	7.78735×10^{5}
q_r(A)	6.54791×10^{4}	1.85203×10^{5}	3.40240×10^{5}	5.23833×10^{5}
q_r(B)	2.58320×10^{2}	7.30639×10^{2}	1.34227×10^{3}	2.06656×10^{3}
q_t^0(AB)/N_A	3.58495×10^{8}	2.02795×10^{9}	5.58838×10^{9}	1.14718×10^{10}
q_t^0(A)/N_A	2.28738×10^{8}	1.29394×10^{9}	3.56568×10^{9}	7.31963×10^{9}
q_t^0(B)/N_A	4.72125×10^{7}	2.67074×10^{8}	7.35970×10^{8}	1.51080×10^{9}
q^0(AB)/N_A	7.25856×10^{16}	3.45756×10^{21}	9.38716×10^{24}	4.66675×10^{27}
q^0(A)/N_A	4.69536×10^{14}	3.49241×10^{17}	3.84031×10^{19}	1.47108×10^{21}
q^0(B)/N_A	5.98352×10^{10}	4.03023×10^{12}	7.40245×10^{13}	7.03175×10^{14}
K_p /atm	6.41419×10^{-5}	1.65718×10^{2}	1.66340×10^{4}	1.41425×10^{5}
K_c /mol cm^{-3}	7.81667×10^{-10}	1.00976×10^{-3}	6.75701×10^{-2}	4.30870×10^{-1}

AB: CH_3NNCH_3, A: CH_3NN, B: CH_3. $q_e(AB) = q_e(A) = 1$, $q_e(B) = 2$.
Symmetry number CH_3NNCH_3: 2, CH_3NN: 1, CH_3: 6.

Appendix 2. Calibration Factors of the Optical Detection System

Exp.	C_b 10^7mV·cm	Exp.	C_b 10^7mV·cm	Exp.	C_b 10^7mV·cm	Exp.	C_b 10^7mV·cm
4.8	3.67920	5.1	3.67920	5.2	3.67920	5.3	3.67920
5.4	3.67920	5.5	3.67920	5.6	3.67920	5.8	3.67920
6.2	3.67920	6.4	3.67920	6.5	3.66953	6.6	3.66953
6.7	3.66953	6.8	3.66953	7.1	3.66953	7.2	3.66953
7.3	3.66953	7.4	3.66953	7.5	3.66953	9.2	1.02136
9.3	1.02136	9.4	1.02136	9.5	1.02136	10.1	1.16953
10.2	1.27226	11.12	1.28040	11.13	1.28040	11.14	1.12438
11.15	1.12438	11.18	1.07426	11.24	1.02876	11.26	1.02876
11.27	1.06644	11.31	1.06644	11.32	0.99446	11.33	0.99446
11.36	0.92247	12.12*	2.12150	12.16*	2.12150	12.22*	1.91997
12.25*	1.91997	12.33*	1.75427	12.35*	1.75427	12.38*	1.96430
12.45*	1.96430	12.48*	1.96430	12.55*	1.96430	13.13*	2.44293
13.15*	2.44293	13.25*	2.07745	13.28*	2.07745	13.33*	2.09604
13.35*	2.09604	13.37*	2.09604	13.42*	2.09604	13.48*	1.96793
14.12*	2.56499	14.14*	2.31204	14.22*	2.36615	14.23*	2.31204
14.24*	2.31204	14.26*	2.12182	14.32*	2.12182	14.35*	2.24020

*: Experiments in new shock tube; others in old one.

Appendix 3. Initial Conditions and Chemically Frozen Conditions Behind Incident Shock

Exp. no	x_{azo} %	P_1 torr	P_4/P_1	U_0 m/s	T_1 K	P_2 atm	$\rho_2 \times 10^6$ mol·cm^{-3}	T_2 K	pattern
1.1	6.82	51.0	23.0	746.8	293.15	0.503	8.998	682	A
1.2	6.82	3.0	211.0	1220.0	293.15	0.082	0.7644	1306	B
1.3	6.82	3.0	305.0	1443.0	293.15	0.116	0.8401	1679	C
1.5	6.82	11.0	67.0	1127.0	293.15	0.255	2.666	1166	B
1.6	6.82	10.5	119.0	1264.0	293.15	0.308	2.733	1376	BC
1.8	6.82	11.0	119.0	1263.0	293.15	0.320	2.856	1368	BC
2.1	6.82	6.0	82.0	1203.0	294.65	0.158	1.507	1281	BC
2.2	0.62	19.5	55.0	1074.0	296.15	0.360	3.455	1270	C
2.3	0.62	21.0	44.0	1013.0	295.65	0.345	3.626	1158	BC
2.4	0.62	18.0	70.0	1150.0	292.15	0.387	3.339	1414	C
2.5	0.62	16.0	64.0	1107.0	292.15	0.323	2.929	1343	C
2.6	0.62	13.0	90.0	1210.0	292.15	0.312	2.463	1545	C
2.7	0.62	13.0	98.0	1226.0	292.15	0.319	2.473	1571	C
2.8	0.62	13.0	58.0	1080.0	296.15	0.244	2.312	1287	C
3.1	0.62	5.0	131.0	1288.0	294.15	0.135	0.9605	1708	C
3.2	0.69	13.0	122.0	1305.0	295.65	0.358	2.506	1743	C
3.3	0.69	10.0	164.0	1412.0	295.65	0.324	1.978	1994	C
3.4	0.69	21.0	112.0	1275.0	294.15	0.555	4.039	1675	C
3.5	0.69	12.0	201.0	1466.0	294.15	0.421	2.414	2126	C
3.6	0.69	6.0	394.0	1641.0	295.15	0.264	1.239	2595	E
3.7	0.69	7.0	341.0	1605.0	295.15	0.294	1.437	2494	C+
3.8	0.69	6.0	400.0	1622.0	295.15	0.258	1.235	2542	E
4.3	0.69	4.0	600.0	1758.0	293.15	0.203	0.8450	2935	E
4.5	0.69	5.0	470.0	1637.0	295.15	0.219	1.032	2584	E
4.7	0.69	13.0	182.0	1444.0	295.15	0.441	2.539	2072	C+

Appendix 3. (Continued)

Exp. no	x_{azo} %	P_1 torr	P_4/P_1	U_0 m/s	T_1 K	P_2 atm	$\rho_2 \times 10^6$ mol·cm^{-3}	T_2 K	pattern
4.8	6.30	5.0	473.0	1600.0	295.15	0.235	1.429	2005	D
5.1	6.30	5.0	323.0	1568.0	296.15	0.225	1.410	1942	C
5.2	6.30	5.0	152.0	1319.0	296.15	0.158	1.291	1487	C
5.3	6.30	6.0	217.0	1415.0	296.15	0.218	1.609	1655	C
5.4	6.30	4.0	487.0	1658.0	296.15	0.202	1.157	2123	C
5.5	6.30	4.5	508.0	1645.0	294.15	0.225	1.307	2095	C
5.6	4.25	5.0	483.0	1634.0	294.15	0.238	1.306	2221	C+
6.1	4.25	5.0	317.5	1532.0	294.15	0.209	1.272	1998	C+
6.2	4.25	4.5	169.0	1363.0	294.15	0.148	1.087	1656	C
6.4	4.25	5.0	255.0	1495.0	294.15	0.198	1.259	1920	C+
6.5	4.25	3.0	788.0	1790.0	294.15	0.172	0.8095	2589	C+
6.6	3.20	5.0	410.0	1602.0	296.15	0.222	1.212	2237	C+
6.7	3.20	5.0	452.0	1614.0	294.15	0.227	1.224	2264	C+
6.8	3.20	5.0	297.0	1505.0	295.15	0.196	1.188	2015	C+
7.1	3.20	5.0	245.0	1456.0	295.15	0.184	1.173	1908	C+
7.2	1.90	5.0	452.0	1639.0	294.15	0.228	1.132	2451	C+
7.3	1.90	5.0	266.0	1477.0	295.15	0.184	1.091	2051	C+
7.4	1.90	5.0	250.0	1460.0	294.15	0.180	1.091	2010	C+
7.5	1.90	5.0	152.0	1335.0	294.15	0.150	1.055	1731	C
9.2	6.52	32.0	31.8	1016.0	293.15	0.596	7.160	1015	B
9.3	6.52	44.0	52.5	1209.0	293.15	1.174	11.02	1298	B
9.4	6.52	6.0	385.2	1922.0	293.15	0.414	1.881	2683	D
9.5	6.52	5.0	307.2	1790.0	293.15	0.299	1.526	2385	D
10.1	7.69	11.5	201.0	1654.0	293.15	0.594	3.574	2025	D

Appendix 3. (Continued)

Exp. no	x_{ato} %	P_1 torr	P_4/P_1	U_0 m/s	T_1 K	P_2 atm	$\rho_2 \times 10^6$ mol·cm^{-3}	T_2 K	pattern
10.2	7.69	4.0	577.9	2043.0	293.15	0.318	1.357	2855	E
11.12	6.55	11.0	163.1	1520.0	293.15	0.470	3.126	1833	C
11.13	6.55	10.0	1032.7	2431.0	293.15	1.113	3.379	4014	E
11.14	6.55	9.5	706.0	2191.0	293.15	0.856	3.116	3349	E
11.15	6.55	9.5	188.9	1589.0	293.15	0.445	2.757	1966	C
11.18	6.55	10.0	593.1	2085.0	293.15	0.815	3.229	3076	E
11.24	6.55	10.5	220.1	1618.0	293.15	0.510	3.072	2023	D
11.26	6.55	11.5	335.9	1745.0	293.15	0.652	3.477	2285	D
11.27	6.55	5.5	1360.5	2449.0	293.15	0.621	1.862	4067	E
11.31	6.55	5.5	608.3	1982.0	293.15	0.404	1.746	2823	E
11.32	6.55	5.5	561.3	1979.0	293.15	0.403	1.745	2815	E
11.33	6.55	5.0	772.6	2094.0	293.15	0.411	1.617	3099	E
11.36	6.55	5.5	420.3	1780.0	293.15	0.325	1.677	2361	D
12.12	6.78	5.5	138.2	1294.0	294.15	0.169	1.443	1426	BC
12.16	6.78	6.5	116.9	1200.0	297.15	0.169	1.611	1279	B
12.22	6.78	9.0	42.1	977.9	295.15	0.154	1.960	961	B
12.25	6.78	6.0	42.0	1010.0	295.65	0.110	1.335	1004	B
12.33	6.78	15.0	10.0	635.8	295.65	0.105	2.234	571	A
12.35	6.78	22.0	9.1	630.0	295.65	0.151	3.245	566	A
12.38	6.78	13.5	9.3	641.3	295.15	0.0961	2.033	576	A
12.45	6.78	10.0	15.0	695.5	295.15	0.0844	1.633	630	A
12.48	6.78	6.0	16.6	801.9	295.15	0.0682	1.116	745	A
12.55	6.78	3.5	35.7	940.0	295.15	0.0553	0.7401	911	B
13.13	1.75	11.0	11.4	714.8	295.15	0.0903	1.591	691	A
13.15	1.75	5.5	22.7	881.8	295.15	0.0698	0.9273	918	A

Appendix 3. (Continued)

Exp. no	x_{azo} %	P_1 torr	P_2/P_1	U_0 m/s	T_1 K	P_2 atm	$\rho_2 \times 10^6$ mol·cm^{-3}	T_2 K	pattern
13.25	1.75	8.0	15.6	770.6	295.15	0.0768	1.228	762	A
13.28	1.75	18.0	28.1	767.6	296.15	0.171	2.742	759	A
13.33	1.75	8.5	50.6	1022.0	295.85	0.146	1.560	1140	B
13.35	1.75	5.0	86.0	1180.0	296.15	0.115	0.9847	1426	C
13.37	1.75	6.5	54.4	1051.0	295.65	0.118	1.212	1190	B
13.42	1.75	5.0	60.6	1043.0	296.15	0.0894	0.9265	1176	B
13.48	1.75	3.0	134.8	1229.0	295.15	0.0754	0.6040	1521	C
14.12*	7.02	6.0	187.0	1414.0	294.65	0.169	1.925	1071	B
14.14*	7.02	5.5	1267.0	2046.0	295.15	0.329	2.236	1796	D
14.22*	7.02	6.0	127.0	1326.0	295.15	0.148	1.830	985	B
14.23*	7.02	5.0	462.0	1675.0	295.65	0.199	1.797	1348	C
14.24*	7.02	5.0	462.0	1680.0	296.15	0.200	1.797	1354	C
14.26*	7.02	5.0	80.8	1155.0	296.15	0.0926	1.359	830	B
14.32*	7.02	5.5	22.7	884.5	296.15	0.0589	1.169	614	A
14.35*	7.02	5.0	183.0	1411.0	294.15	0.141	1.604	1067	B

*: azomethane diluted by N_2.
A, B, C, D, E: signal patterns.

Appendix 4. Summary of Point-by-Point Analysis for $2CH_3 \rightarrow C_2H_4 + H_2$

We repeated the point-by-point analysis (appearing on p. 89) assuming that reaction (4) alone is now responsible for the signal. The rate of reaction $CH_3 + CH_3 \rightarrow C_2H_4 + H_2$ can be cast into the form

$$d\alpha/dt_g = k_4 [(1-2\alpha)^2 - \alpha^2/K_c] X_0 \rho/\mu'_0 \qquad (4.2b)$$

where the effective molecular weight $\mu = \mu'_0 = \mu_0/(1+2X_A)$. The formalism and its development are similar to that for reaction (5). Some equations remain the same. The slight differences originate from the expressions for $d\alpha/dt_g$ and μ. Only differences will be mentioned here. For consistency, the equations which are different from those for reaction (5), are denoted by the same equation numbers followed with a letter *b*.

(1) *T*, *p*, ρ, and α at the Equilibrium Condition (at point *e*)

$$\frac{\rho_0}{\rho_e} = f(T_e, \alpha_{e(-)}) = \frac{1}{2T'_0}\left[\sqrt{(2\theta - T_e + T'_0)^2 + 4T'_0 T_e} - (2\theta - T_e + T'_0)\right]$$

(4.12b)

$$\rho_\infty = \rho_e = \frac{\rho_0}{f(T_e, \alpha_{e(-)})} \qquad (4.15b)$$

where $\theta = \mu_0(h_e - h_0)/[R(1+2X_A)]$, $\mu_0(h_e - h_0) = X_A[2\alpha_{e(-)}\Delta H_4 + \Delta H_0 + (H_{A2e} - H^0_{A2e})] + (1-X_A)(H_{Ae} - H^0_{Ar})$, and $T'_0 = T_0/(1+2X_A)$. As α_e depends on temperature only, no iteration is involved. For each chosen T_e, one can get a set of u_0, p_e, ρ_e, and α_e. We keep changing T_e until the calculated u_0 matches the experimental shock velocity U_s. This is illustrated in the following flow chart.

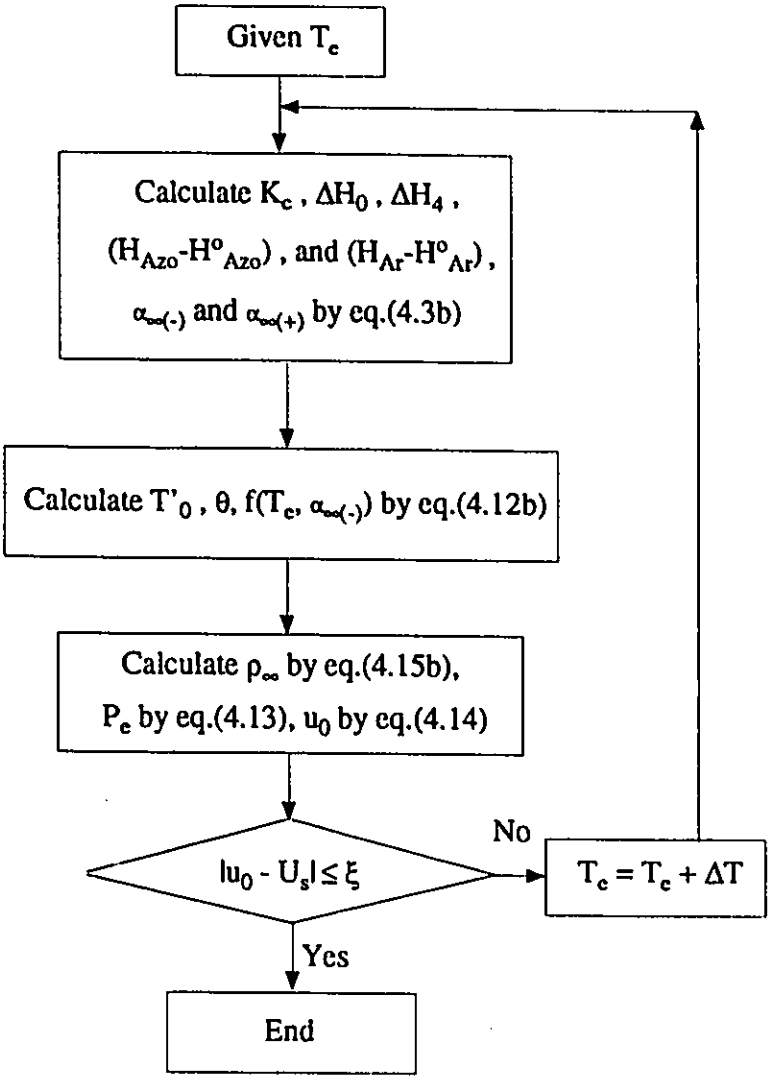

Procedure for calculating T_e, p_e, ρ_∞, and α_∞ assuming reaction $CH_3 + CH_3 \rightarrow C_2H_4 + H_2$ alone is responsible for the negative signals

(2) T, p, ρ, α and $d\rho/dt$ at time t_g

$$T = (\rho_0/\rho)\,[T_0+\mu_0 u_0^2\,(1-\rho_0/\rho)/R]/(1+2X_A) \qquad (4.19b)$$

$$\alpha = \{\mu_0 u_0^2\,[1-(\rho_0/\rho)^2]/2X_A-\Delta H_0-(H_{Azo}-H^0_{Azo})-(H_{Ar}-H^0_{Ar})\,(1-X_A)/X_A\}/2\Delta H_4 \qquad (4.20b)$$

At each point in time, the determination of T and α does not involve iteration.

$$\frac{d\alpha}{d\rho} = \frac{\mu_0 u_0^2\,(\rho_0/\rho)^2\,[(1+2X_A)-\overline{C}/R]+\overline{C}T(1+2X_A)}{2X_A\rho\Delta H_4\,(1+2X_A)} \qquad (4.21b)$$

where ΔH_4 is the heat of the reaction $CH_3 + CH_3 = C_2H_4 + H_2$, and $\overline{C}$ is the effective heat capacity of the gas mixture at time t_g

$$\overline{C} = X_A\left[2\alpha\,(C_{p,C_2H_4}+C_{p,H_2}-2C_{p,CH_3})+\left(2C_{p,CH_3}+C_{p,N_2}+\frac{1-X_A}{X_A}C_{p,Ar}\right)\right] \qquad (4.22b)$$

$$\frac{d\rho}{dt_g} = \frac{4X_A^2\rho^2 k_4\,[(1-2\alpha)^2-\alpha^2/K_c]\,\Delta H_4\,(1+2X_A)/\mu_0}{\mu_0 u_0^2\,(\rho_0/\rho)^2\{(1+2X_A)-\overline{C}/R\}+\overline{C}T(1+2X_A)} \qquad (4.24b)$$

(2A) Direct Method

$$B = -\frac{\frac{2X_A}{\rho}\Delta H_4\,(1+2X_A)}{\mu_0 u_0^2\,(\rho_0/\rho)^2\,[(1+2X_A)-\overline{C}/R]+\overline{C}T(1+2X_A)} \qquad (4.25b)$$

$$\frac{d\rho}{dt_g} = \frac{d\rho}{d\alpha}\frac{d\alpha}{dt_g} = -\frac{2X_A}{\mu_0}B\rho^3 k_d[(1-2\alpha)^2-\alpha^2/K_c] \qquad (4.27b)$$

$$k_d = -\frac{\frac{d\rho}{dt_g}}{\frac{2X_A}{\mu_0}B\rho^3[(1-2\alpha)^2-\alpha^2/K_c]} \qquad (4.28b)$$

(2B) Slope Method

$$F = -\frac{d\rho}{dt_g} = \frac{2X_A}{\mu_0}B\rho^3 k_d[(1-2\alpha)^2-\alpha^2/K_c] \qquad (4.29b)$$

$$k_d = \frac{(\frac{E_a}{RT}-3)\frac{F}{\rho} - \frac{d(lnF)}{dt_g}}{\frac{2X_A\rho}{\mu_0}[4-2\alpha(4-\frac{1}{K_c})-\frac{\alpha^2}{K_c}\frac{\Delta H_d}{RT}B\rho]} \qquad (4.30b)$$

(2C) Indirect Method

$$d\alpha/dt_g = k_d\frac{2X_A\rho}{\mu_0}(4-\frac{1}{K_c})(\alpha-\alpha_{\infty(+)})(\alpha-\alpha_{\infty(-)}) \qquad (4.32b)$$

$$\frac{d(lnA)}{dt_g} = \frac{2X_A\rho_\infty(4-\frac{1}{K_c})}{\mu_0}k_d(\alpha_{\infty(+)}-\alpha_{\infty(-)}) \qquad (4.33b)$$

$$\frac{d(lnA)}{dt_1} = \frac{2X_A\rho\rho_\infty(4-\frac{1}{K_c})}{\mu_0\rho_0}k_d(\alpha_{\infty(+)}-\alpha_{\infty(-)}) \qquad (4.34b)$$

(2D) Alternative Expression for α

$$F = -\frac{d\rho}{dt_g} = k_4 \frac{2X_A B\rho^3}{\mu_0} \left(4-\frac{1}{K_c}\right) (\alpha-\alpha_{\infty(+)}) (\alpha-\alpha_{\infty(-)}) \qquad (4.36b)$$

$$\sigma = \frac{1}{2X_A B\rho} \left(\frac{F\mu_0}{\rho^2 k_4}\right) \left(\frac{K_c}{4K_c-1}\right) \qquad (4.38b)$$

The above equations replace those in Chapter 4 which have matched equation numbers. The rest of the equations in Chapter 4 remain unchanged except that equation (4.16) is no longer used in this case.

Appendix 5. Specific Refractivities of the Species in the Reaction Scheme

Species j	Molecular Weight μ_j / g·mol^{-1}	Specific Refractivity[123] κ_j / cm^3·g^{-1}
1. CH_3NNCH_3	58.08352	0.4158*
2. CH_3	15.03506	0.5646
3. C_2H_4	28.05418	0.5693
4. C_2H_5	29.06215	0.5311
5. C_2H_6	30.07012	0.5628
6. H	1.00797	1.5407
7. H_2	2.01594	1.5407
8. CH_4	16.04303	0.6149
9. CH_2	14.02709	0.4952
10. CH	13.01912	0.4152
11. C_2H_2	26.03824	0.5050
12. C_2H_3	27.04621	0.5423
13. C_3H_6	42.08127	0.5581
14. n-C_3H_7	43.08924	0.5211*
15. C_3H_8	44.09721	0.5458
16. C_4H_{10}	58.12430	0.5323
17. N_2	28.01340	0.2388
18. Ar	39.94800	0.1577
19. C	12.01115	0.3216

* estimated from molar refraction, R_j, data[106] using group contributions ($\kappa_j = 3R_j/2\mu_j$).

Appendix 6. Additional Simulations of Laser Schlieren Profiles

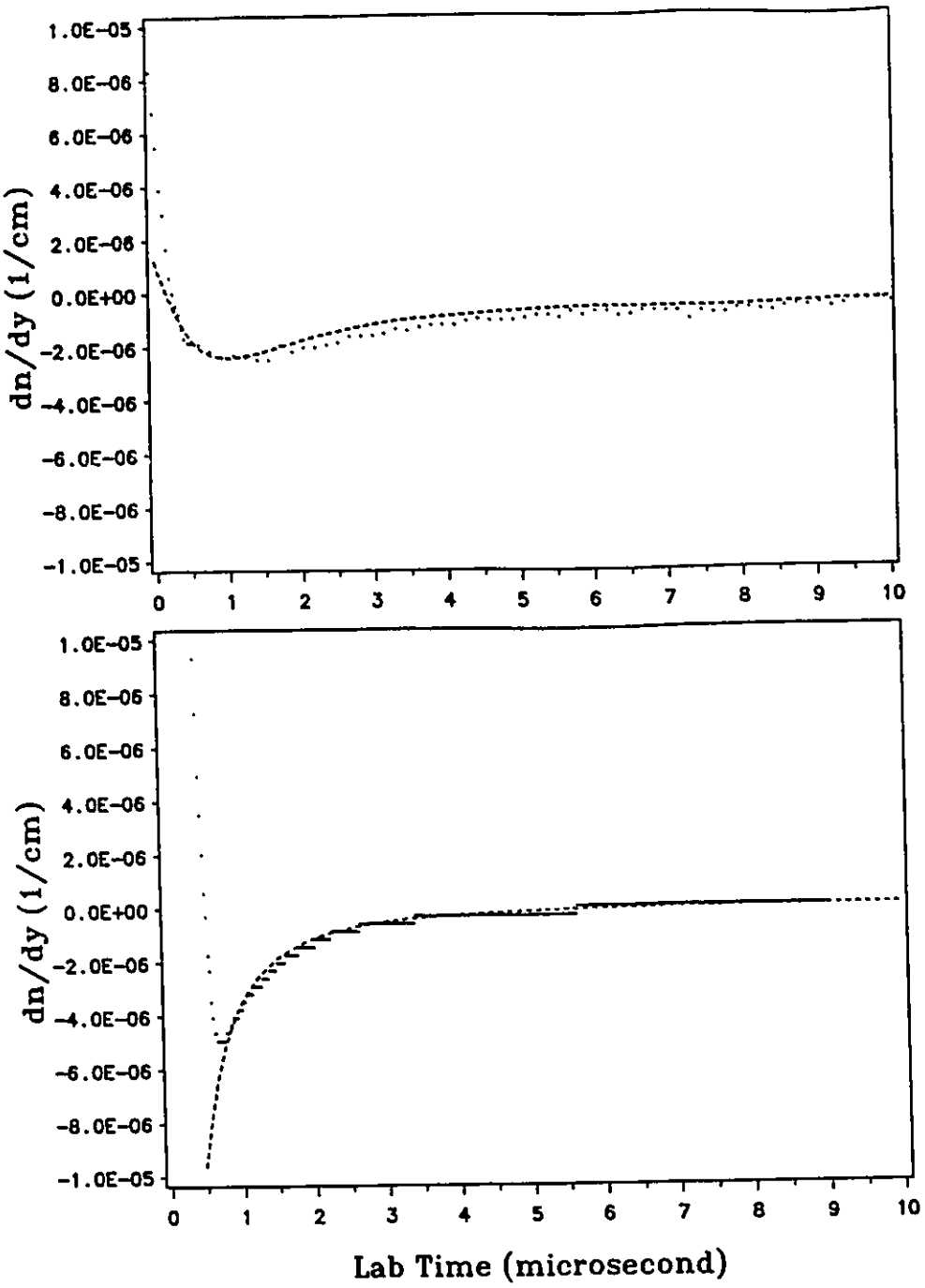

Figure A6.1 Comparison of simulated profiles with experimental signals.

Top: (a) Experiment 13.35 (T_2 = 1426 K, P_2 = 0.115 atm)

Bottom: (b) Experiment 1.3 (T_2 = 1679 K, P_2 = 0.116 atm)

---------- : Simulated profiles

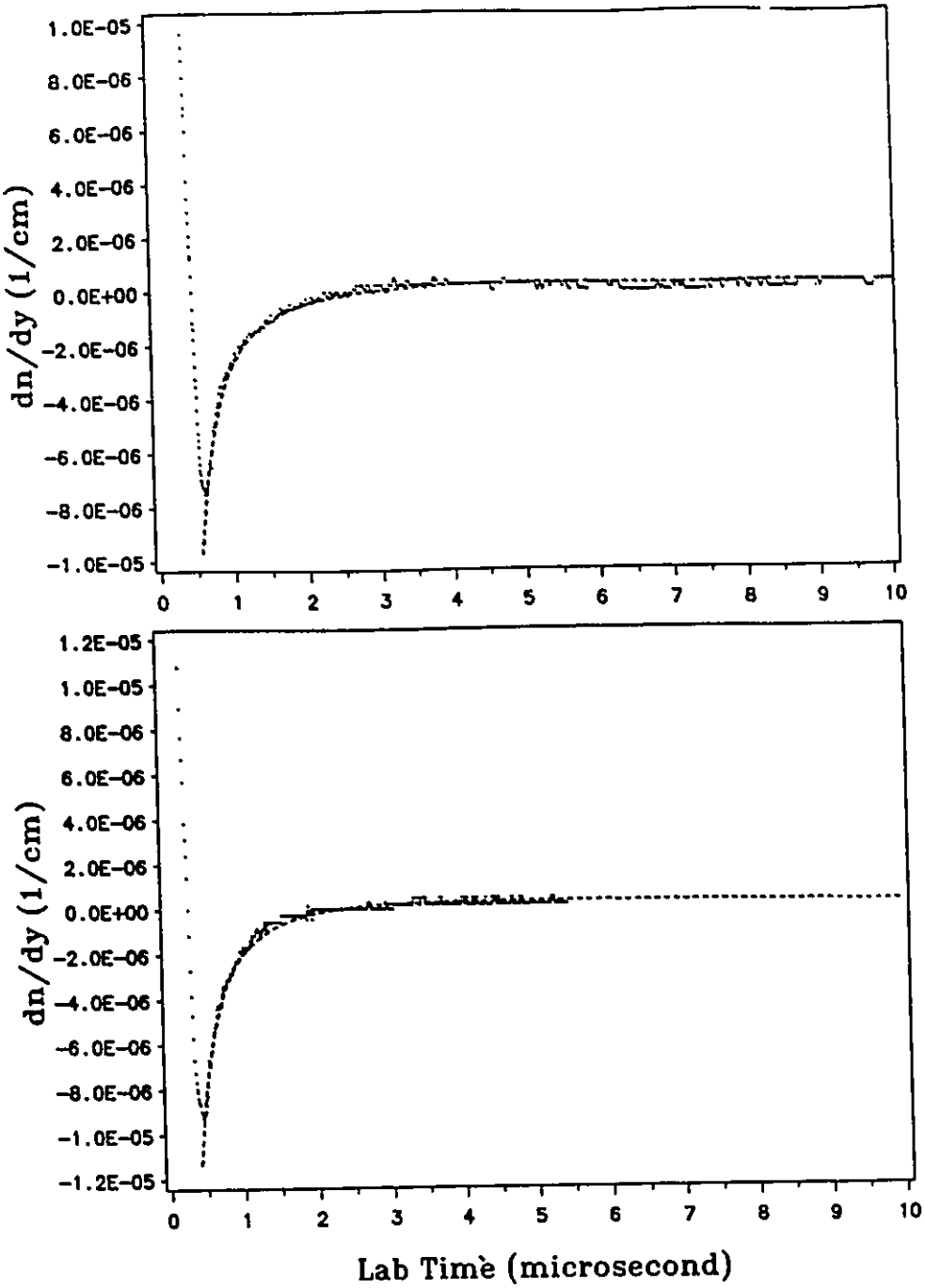

Figure A6.2 Comparison of simulated profiles with experimental signals.

Top: (a) Experiment 11.12 (T_2 = 1833 K, P_2 = 0.470 atm)

Bottom: (b) Experiment 11.15 (T_2 = 1966 K, P_2 = 0.445 atm)

----------: Simulated profiles

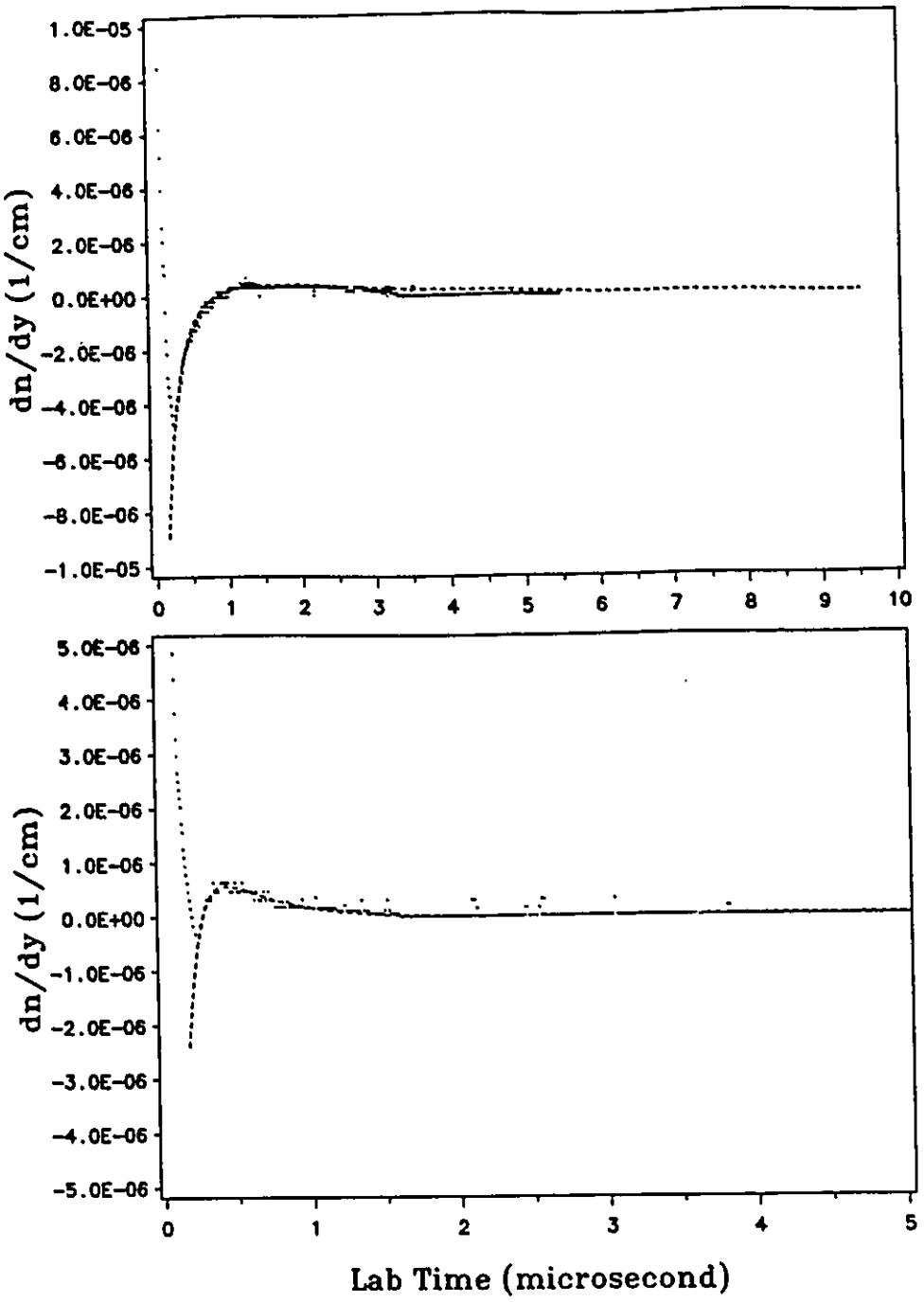

Figure A6.3 Comparison of simulated profiles with experimental signals.

Top: (a) Experiment 11.36 (T_2 = 2361 K, P_2 = 0.325 atm)

Bottom: (b) Experiment 9.4 (T_2 = 2683 K, P_2 = 0.414 atm)

..... : Simulated profiles

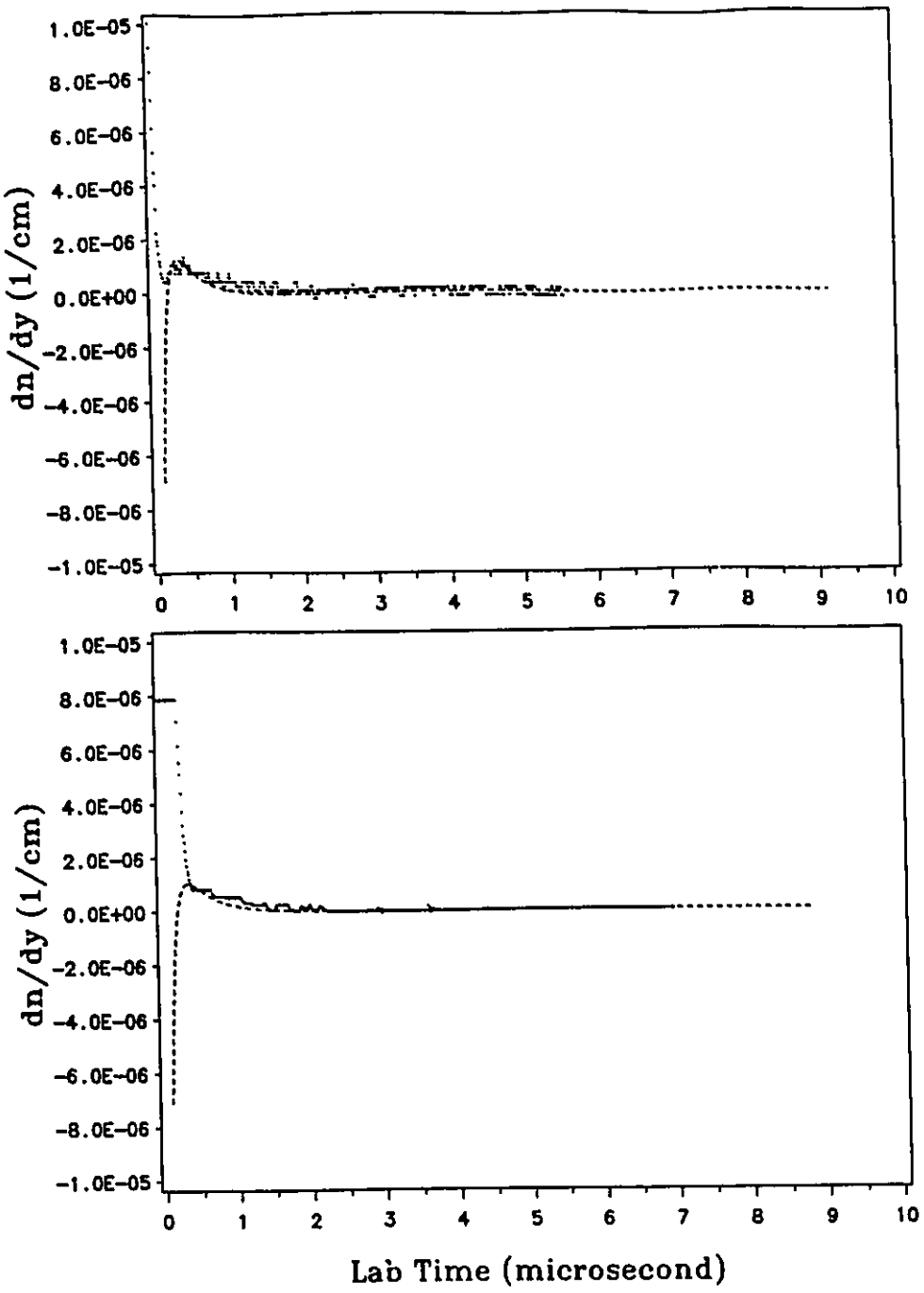

Figure A6.4 Comparison of simulated profiles with experimental signals.

Top: (a) Experiment 11.31 (T_2 = 2823 K, P_2 = 0.404 atm)

Bottom: (b) Experiment 10.2 (T_2 = 2855 K, P_2 = 0.318 atm)

----------: Simulated profiles

Appendix 7. Simulated Gas-Composition Time Profiles

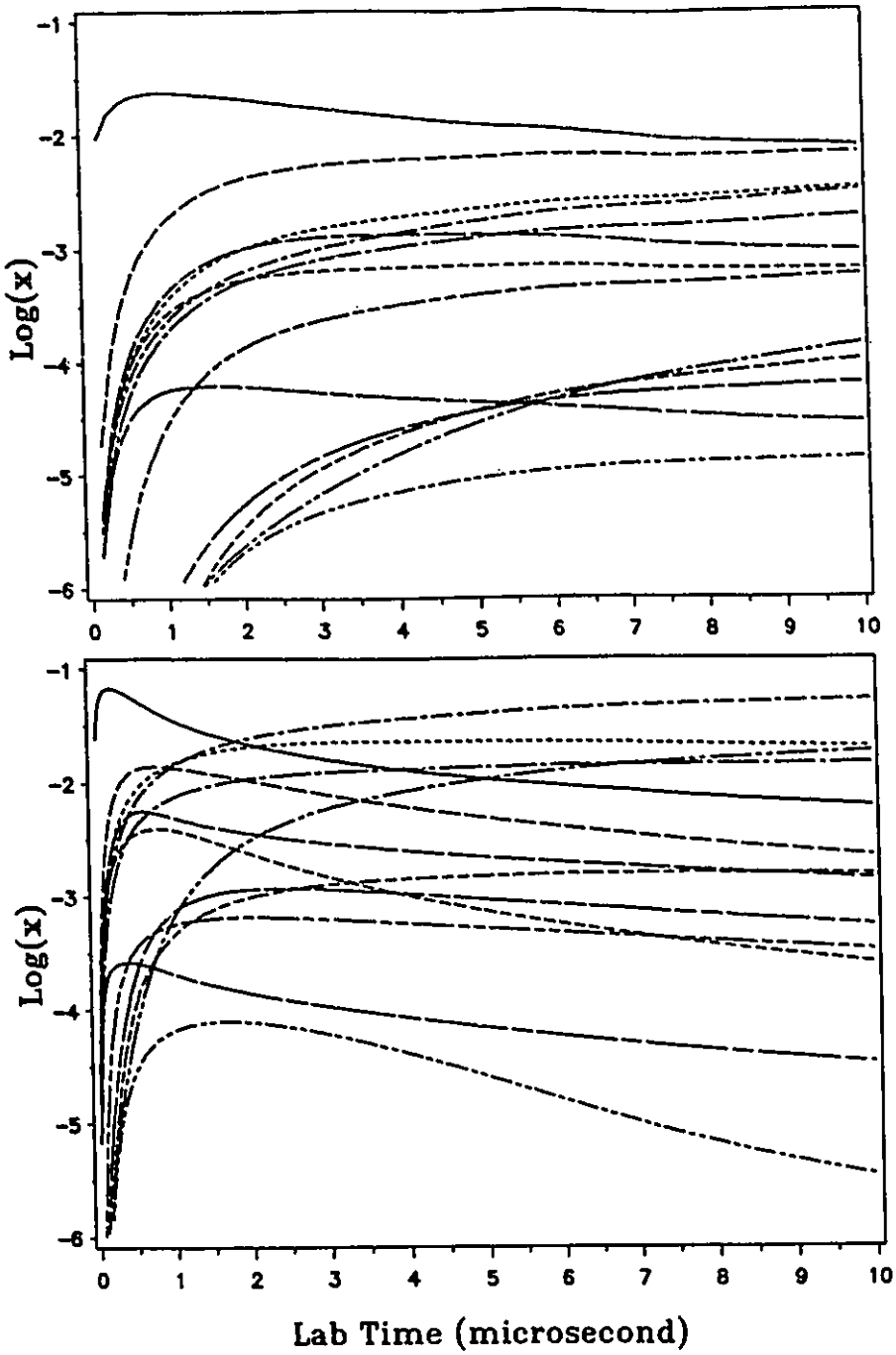

Figure A7.1 Simulated gas-composition time profiles.
Top: (a) Experiment 13.35 (T_2 = 1426 K, P_2 = 0.115 atm)
Bottom: (b) Experiment 5.3 (T_2 = 1655 K, P_2 = 0.218 atm)

CH_3 C_2H_4 C_2H_5
C_2H_6 H H_2
CH_4 CH_2 CH
C_2H_2 C_2H_3 C_3H_6
C_3H_8

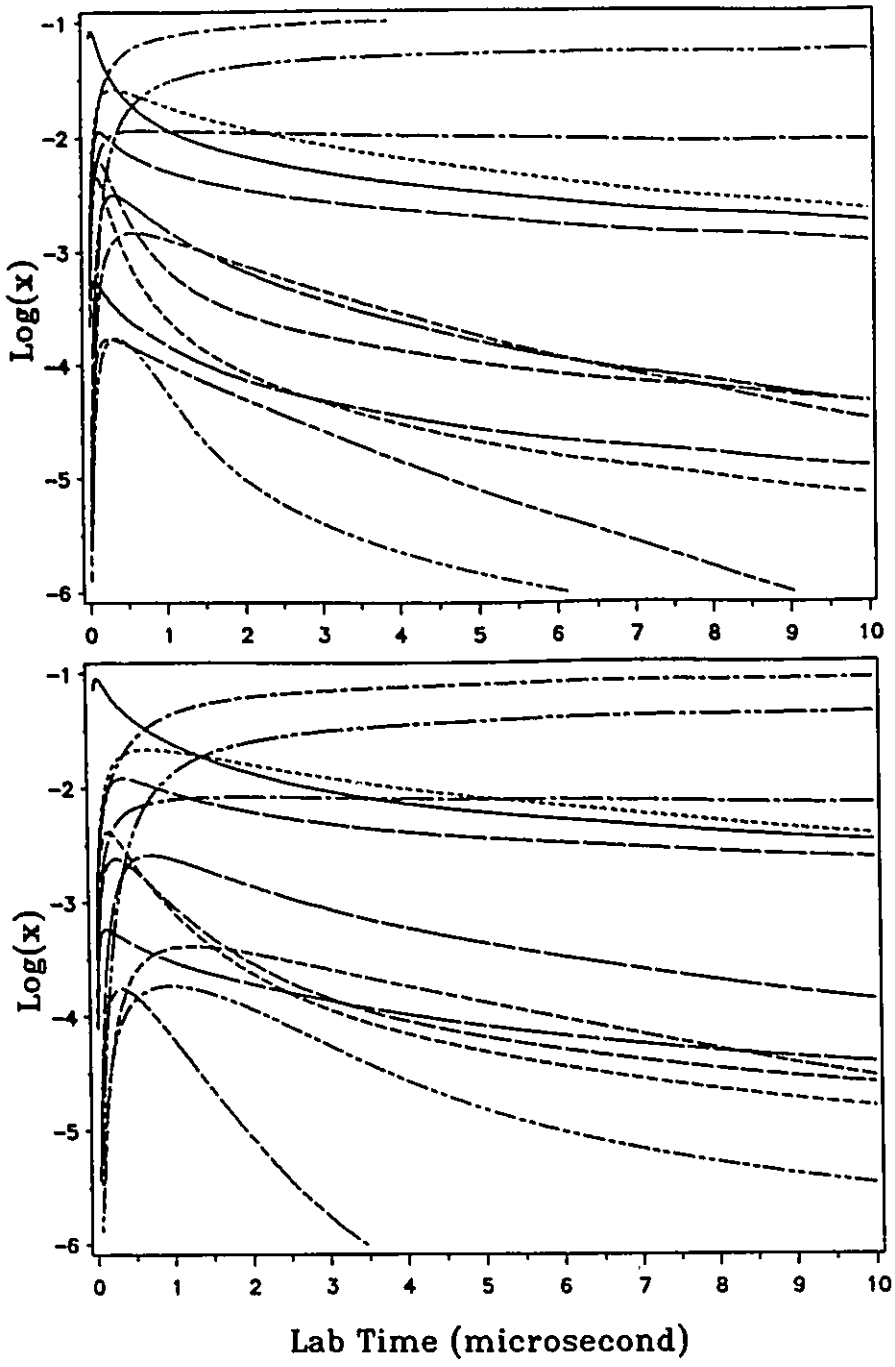

Figure A7.2 Simulated gas-composition time profiles.
Top: (a) Experiment 10.1 (T_2 = 2025 K, P_2 = 0.594 atm)
Bottom: (b) Experiment 5.5 (T_2 = 2095 K, P_2 = 0.225 atm)

CH_3 C_2H_4 C_2H_5
C_2H_6 H H_2
CH_4 CH_2 CH
C_2H_2 C_2H_3 C_3H_6
C_3H_8

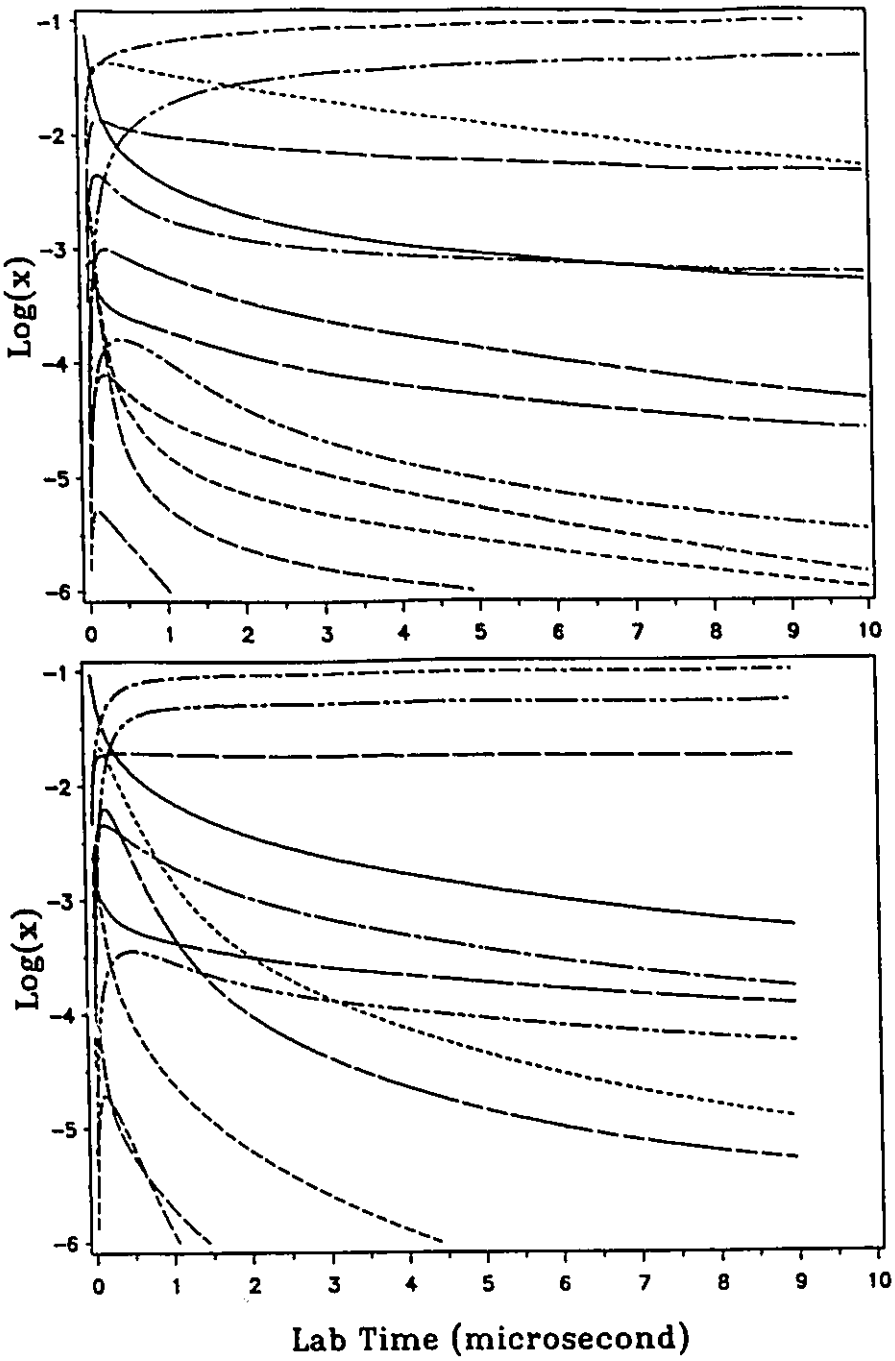

Figure A7.3 Simulated gas-composition time profiles.
Top: (a) Experiment 11.26 (T_2 = 2285 K, P_2 = 0.652 atm)
Bottom: (b) Experiment 11.31 (T_2 = 2823 K, P_2 = 0.404 atm)

CH_3 C_2H_4 C_2H_5
C_2H_6 H H_2
CH_4 CH_2 CH
C_2H_2 C_2H_3 C_3H_6
C_3H_8

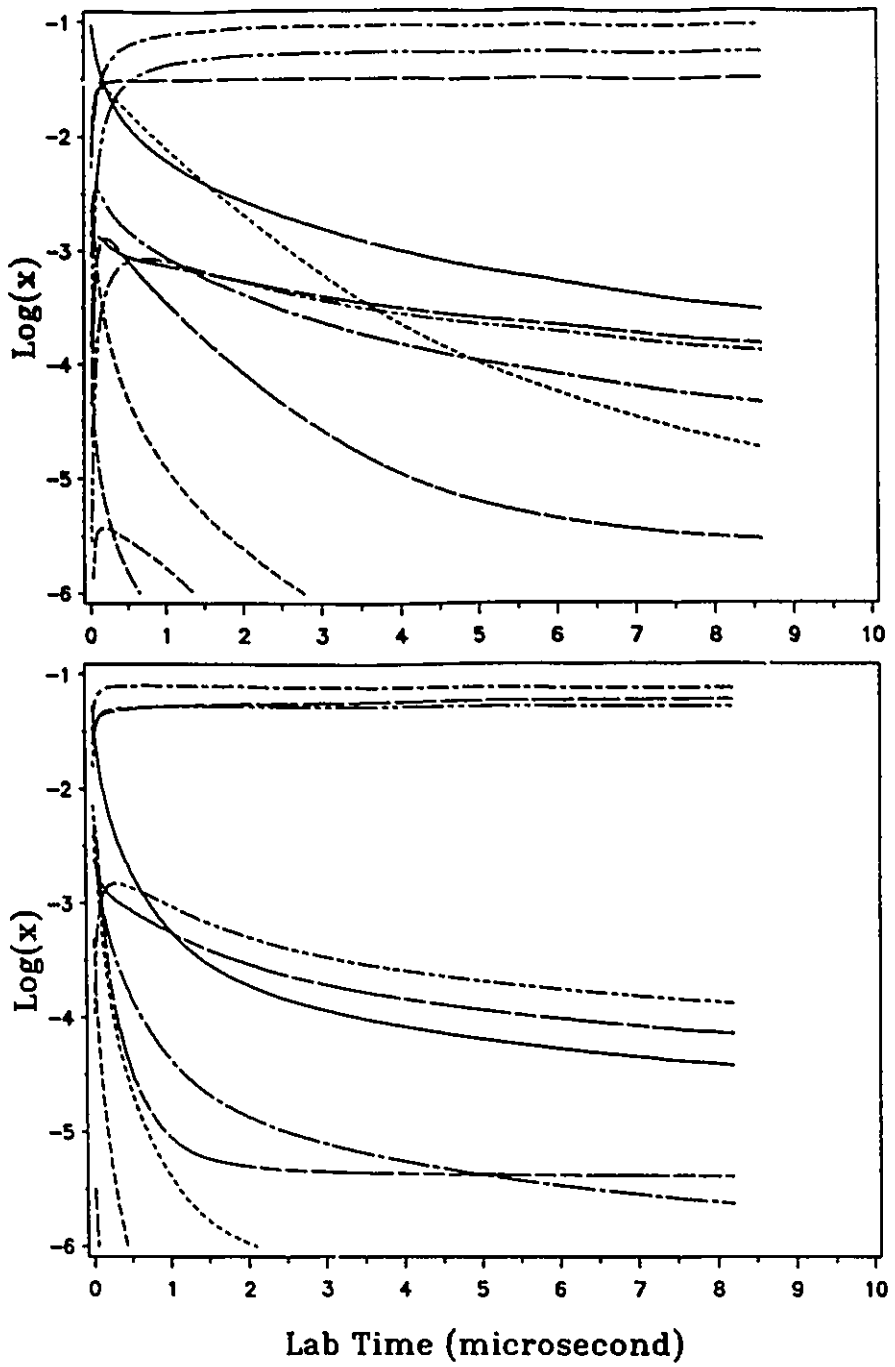

Figure A7.4 Simulated gas-composition time profiles.
Top: (a) Experiment 11.33 (T_2 = 3099 K, P_2 = 0.411 atm)
Bottom: (b) Experiment 11.13 (T_2 = 4014 K, P_2 = 1.113 atm)

CH_3 C_2H_4 C_2H_5
C_2H_6 H H_2
CH_4 CH_2 CH
C_2H_2 C_2H_3 C_3H_6
C_3H_8

Appendix 8. Computer Code: Unimrxn Fortran

This program is the implementation of Troe's factorization approach to the prediction of rate constants for unimolecular reaction.

```
      PROGRAM UNIMRXN
C
      IMPLICIT DOUBLE PRECISION (A-H,O-Z), INTEGER (I-N)
C
      PARAMETER (IST=2, KLOW=3, KHIGH=4, KFALL=5, LVAZ=7, LOUT=6, NT=31)
      DIMENSION VAB(6), VA(3), VB(3), FC(NT)
C     CHARACTER CA(LCA)*16, ITITL*76, PREC*16, VERS*16
C     LOGICAL KERR
      COMMON /NUM/ NABS, NAS, NBS, M, NR, NBSTAR
C
      COMMON /ENERGY/ E0, EE, BE, BOO, AETPC, VRC, EKAB, EKM, DH0
C
      COMMON /GET/ EZAB, EZA, EZB, D, DEZ, AE0, FRIGID, FANH, PVIBH,
     1             BMORSE, A1, A2, E0AEZ
C
      COMMON /PARAM/ CDAB, CDM, QEAB, WMAB, WMA, WMB, WMM, QAB, QA,
     1              QB, AKC, BKC, CKC, ADIVB
      COMMON /SANDIA/ SA1, SA2, SA3, SA4, SA5, SA6
C
      COMMON /ACPAR/ VSTAR, CVSTAR
C
      DATA VAB/ 3002.0,  580.0, 3184.0, 3184.0, 1383.0, 1383.0/
      DATA VA / 2954.0, 3123.0, 1056.0 /
      DATA VB / 0.0, 0.0, 0.0/
C        SET INPUT PARAMETERS
C
C                                        [V(*)]=1/CM
      VSTAR =1.170D0
      CVSTAR=0.140D0
C               VSTAR:DIMENSIONLESS     [CVSTAR]=1/CM
      NABS=6
      NAS =3
      NBS =0
      CDAB=3.8
```

```
      CDM =3.47
      QEAB=1.079
C       [QEAB]=[CD*]=A   (1A=10E-10 M)
      EKAB=144.0
      EKM =114.0
C             [EK*]=K   (KELVIN)
      WMAB = 15.03482
      WMA  = 14.02688
      WMB  =  1.00794
      WMM  = 39.948
C           WM*   MOLECULAR WEIGHT
      DH0 = 37861.5
      E0  = 37861.5
C       [DH0]=[E0]=1/CM
      M  = 3
      NR = 0
      NBSTAR = 1
C     NBSTAR = M - 1 - NR
      AETPC=130.0
C             [AETPC]=1/CM  AVERAGE ENERGY TRANSFERRED PER COLLISION
      VRC=VAB(3)
      QAB =2.0
      QA  =3.0
      QB  =2.0
C
       AKC=196.20
       BKC=-0.269
       CKC=55200.0
C        KC=(AKC)*T**(BKC)*EXP(-(CKC)/T)        [MOLE/CM3]
      ADIVB=0.43
      BE = 7.182
      BOO= 16.486
      EE = 1383.0
C     EE = 1396.0
C         [BE]=[BOO]=[EE]=1/CM
      SA1= 2.844051D0
      SA2= 6.137974D-3
      SA3=-2.230345D-6
      SA4= 3.785161D-10
      SA5=-2.452159D-14
      SA6=-234.931D0
C               [SA*]=DIMENSIONLESS
      EZAB=0.0
      DO 100 I=1,NABS
```

```
      EZAB=EZAB+VAB(I)
  100 CONTINUE
      EZAB=EZAB/2.0D0
      EZA=0.0
      DO 200 I=1,NAS
      EZA=EZA+VA(I)
  200 CONTINUE
      EZA=EZA/2.0D0
      EZB=0.0
      DO 300 I=1,NBS
      EZB=EZB+VB(I)
  300 CONTINUE
      EZB=EZB/2.0D0
      DEZ=EZAB-(EZA+EZB)-VRC/2.0D0
      D  =DH0+EZAB-(EZA+EZB)
C           [EZ*]=[DEZ]=[D]=1/CM
      BMORSE=0.1217788D0*SQRT(WMA*WMB/(WMA+WMB)/D)*VRC
C              [BMORSE]=1/A     (1A=10E-10 M)
      A1=2.0D0/(BMORSE*QEAB)
      A2=1.0D0/(BMORSE*QEAB)**2
C                              [A*]=DIMENSIONLESS
      IF (IST .EQ. 1) THEN
        WRITE (LVAZ, 20) D, DEZ, ADIVB, EZA+EZB, BE, A1, A2
      ELSE
        SUM1 = 0.0D0
        SUM2 = 0.0D0
        SUM3 = 0.0D0
        SUM4 = 0.0D0
        SUM5 = 0.0D0
        SUM8 = 0.0D0
        SUM9 = 0.0D0
        SUM10= 0.0D0
        SUM11= 0.0D0
        SUM12= 0.0D0
        SUM13= 0.0D0
        SUM14= 0.0D0
        SUM15= 0.0D0
        SUM16= 0.0D0
        SUM17= 0.0D0
        DO 400 I=1,NT
          T=1000.0D0 + 100.0D0*DBLE(I-1)
          CALL LOWPK (T, VAB, ZLJ, VIBT, EXPT, FE, FROT,FINT, BC, PLOWK)
          CALL HIGHPK (T, PREA,QCENT, RECK, HIGHK)
          WRITE(KLOW, 30)T, ZLJ, VIBT, EXPT, FE, FROT, FINT, BC, PLOWK
```

```
      WRITE(KHIGH, 40)T, PREA, QCENT, RECK, HIGHK
      DO 500 J=1,11
        CMMC=10.0D0**(-DBLE(J-1))
      CALL FALLOFF(T, BC, CMMC, PLOWK, HIGHK, FLH, F, FCENT, CM, FALLK)
        WRITE(J+9 ,50)T, CMMC, CM, FLH, F, FCENT, FALLK
500    CONTINUE
      FC(I)=FCENT
      SUM1 = SUM1 + T
      SUM2 = SUM2 + T**2
      SUM3 = SUM3 + T**(-2)
      SUM4 = SUM4 + LOG(FC(I))
      SUM5 = SUM5 + T*LOG(FC(I))
      SUM8 = SUM8 + 1.0D0/T
      SUM9 = SUM9 + LOG(T)
      SUM10= SUM10+ (LOG(T))**2
      SUM11= SUM11+ LOG(T) /T
      SUM12= SUM12+ LOG(PLOWK)
      SUM13= SUM13+ LOG(PLOWK) /T
      SUM14= SUM14+ LOG(PLOWK) * LOG(T)
      SUM15= SUM15+ LOG(HIGHK)
      SUM16= SUM16+ LOG(HIGHK) /T
      SUM17= SUM17+ LOG(HIGHK) * LOG(T)
400   CONTINUE
C     FITTING  FCENT: T***...T3S     1-A.....ACENT
      T3S = (SUM1**2 - NT*SUM2)/(NT*SUM5 - SUM1*SUM4)
      ALN = SUM4/NT + SUM1/NT/T3S
      ACENT = EXP(ALN)
C     FITTING  ARRHENIUS PARAMETERS
      TER9 = SUM3  - SUM8**2/NT
      TER11= SUM11 - SUM9*SUM8/NT
      TER13= SUM10 - SUM9**2/NT
C           LOW PRESSURE K
      TER10= SUM13 - SUM12*SUM8/NT
      TER12= SUM14 - SUM12*SUM9/NT
      PLKC =(TER10/TER11 - TER12/TER13)/(TER11/TER13 - TER9/TER11)
      PLKB =PLKC*(TER11/TER13) + (TER12/TER13)
      PLKLNA = (SUM12 - PLKB*SUM9 + PLKC*SUM8) /NT
      PLKA = EXP(PLKLNA)
C           HIGH PRESSURE K
      TER20= SUM16 - SUM15*SUM8/NT
      TER22= SUM17 - SUM15*SUM9/NT
      HPKC =(TER20/TER11 - TER22/TER13)/(TER11/TER13 - TER9/TER11)
      HPKB =HPKC*(TER11/TER13) + (TER22/TER13)
      HPKLNA = (SUM15 - HPKB*SUM9 + HPKC*SUM8) /NT
```

```
      HPKA = EXP(HPKLNA)
C     FITTING  FCENT: T*...T1S
C       SUM6 = 0.0D0
C       DO 410 I=1,NT
C         T=1000.0D0 + 100.0D0*DBLE(I-1)
C         SUM6 = SUM6 + T*LOG((FC(I)-ACENT*EXP(-T/T3S))/(1.0D0-ACENT))
C410    CONTINUE
C       T1S = - SUM2 / SUM6
C       SUM7 = 0.0D0
C       DO 420 I=1,NT
C         T=1000.0D0 + 100.0D0*DBLE(I-1)
C         SUM7 = SUM7 +
C    &      LOG( FC(I)-ACENT*EXP(-T/T3S)-(1.0D0-ACENT)*EXP(-T/T1S) ) /T
C420    CONTINUE
C       T2S = - SUM7 / SUM3
C       WRITE(LOUT, 70) ACENT, T3S, 1.0D0-ACENT, T1S, T2S
        WRITE(LOUT, 72) HPKA, HPKB, HPKC
        WRITE(LOUT, 74) PLKA, PLKB, PLKC
      ENDIF
      STOP
C
C       FORMATS
 20   FORMAT (5(1PE15.5),/' J ', 2(1PE15.5) )
 30   FORMAT (9(1PE14.5))
 40   FORMAT (5(1PE14.5))
 50   FORMAT (7(1PE14.5))
 70   FORMAT (/'Fcent =',1PE14.5,'exp( -T/',1PE14.5,') +',1PE14.5,
     1        'exp( -T/',1PE14.5,') + exp( -',1PE14.5,'/T)'  )
 72   FORMAT (/'High Pressure  k (1/s) =',1PE14.5,' T**(',1PE14.5,
     1        ') exp( -',1PE14.5,'/T)' )
 74   FORMAT (/'Low Pressure  k (cm3/mole.s) =',1PE14.5,' T**(',1PE14.5,
     1        ') exp( -',1PE14.5,'/T)' )
CCC   FORMAT (/59X,'T1  =',1PE10.3,/59X,'T2  =',1PE10.3,/59X,
C     1  'DT  =',1PE10.3,/59X,'RTOL =',1PE10.3,/59X,'ATOL =',1PE10.3)
      END
C
      SUBROUTINE LOWPK (T, VAB,ZLJ, VIBT, EXPT, FE, FROT,FINT,BC, PLOWK)
      IMPLICIT DOUBLE PRECISION (A-H,O-Z), INTEGER (I-N)
      COMMON /NUM/ NABS, NAS, NBS, M, NR, NBSTAR
      COMMON /ENERGY/ E0, EE, BE, BOO, AETPC, VRC, EKAB, EKM, DH0
      COMMON /GET/ EZAB, EZA, EZB, D, DEZ, AE0, FRIGID, FANH, PVIBH,
     1             BMORSE, A1, A2, E0AEZ
      COMMON /PARAM/ CDAB, CDM, QEAB, WMAB, WMA, WMB, WMM, QAB, QA,
     1               QB, AKC, BKC, CKC, ADIVB
```

```
      DIMENSION VAB(NABS)
C
      CDABM=(CDAB+CDM)/2.0D0
      WMABM=WMAB*WMM/(WMAB+WMM)
      EKABM=SQRT(EKAB*EKM)
      RCI=1.0D0/( 0.697D0+0.5185D0*LOG10(T/EKABM) )
      ZLJ=4.87D14*SQRT(T/1000.0D0)*SQRT(20/WMABM)*(CDABM/5.0D0)**2*RCI
C
      QVIB=1.0D0
      SIGMA1=0.0D0
      SIGMA2=0.0D0
      DO 600 I =1, NABS
      QVIB=QVIB / ( 1.0D0 - EXP(-1.438786*VAB(I)/T) )
      SIGMA1=SIGMA1+VAB(I)
      SIGMA2=SIGMA2+VAB(I)**2
  600 CONTINUE
      BSTAR=DBLE(NABS-1)*SIGMA2/SIGMA1**2
      IF ( E0/EZAB .GE. 1.0D0) THEN
        W=10.0D0**( -1.0506*(E0/EZAB)**0.25 )
      ELSE
        W=1.0D0 / ( 5.0D0*E0/EZAB + 2.73*(E0/EZAB)**0.5 + 3.51 )
      ENDIF
      AE0=1.0D0-W*BSTAR
      E0AEZ=E0+AE0*EZAB
      HVI=1.0D0
      DO 700 I =1, NABS
      HVI=HVI*VAB(I)
  700 CONTINUE
      SM1=1.0D0
      DO 710 I =1, NABS-1
      SM1=SM1*DBLE(I)
  710 CONTINUE
      PVIBH=E0AEZ**(NABS-1) /SM1/HVI
      VIBT=PVIBH*(0.6950304*T)/QVIB
      EXPT=EXP(-E0/(0.6950304*T))
      FE=0.0D0
      DO 720 I =0, NABS-1
      SM1MI=1.0D0
       DO 725 J=1, NABS-1-I
       SM1MI=SM1MI*DBLE(J)
  725  CONTINUE
      FE=FE +(SM1/SM1MI)*( 0.6950304*T / E0AEZ )**I
  720 CONTINUE
      FANH=( DBLE(NABS-1) / (DBLE(NABS)-1.5D0) )**M
```

```
      SP1D2=0.8862269D0
      DO 730 I =1, NABS
      SP1D2=SP1D2*(DBLE(I)+0.5D0)
  730 CONTINUE
      FRMAX=(SM1/SP1D2)*( E0AEZ/(0.6950304*T) )**1.5
      RATIOI=2.15D0*(E0/(0.6950304*T))**(1.0/3.0)
      FROT = FRMAX * RATIOI / ( RATIOI - 1.0D0 + FRMAX )
      IF ( MOD(NR, 2) .EQ. 0) THEN
        SM1PR2=1.0D0
        DO 740 I =1, NABS-1+NR/2
        SM1PR2=SM1PR2*DBLE(I)
  740   CONTINUE
      ELSE
        SM1PR2=0.8862269D0
        DO 750 I =1, NABS-1+NR/2
        SM1PR2=SM1PR2*(DBLE(I)+0.5D0)
  750   CONTINUE
      ENDIF
      FINT =(SM1/SM1PR2)*( E0AEZ/(0.6950304*T) )**(NR/2)
      BC0= 1.438786*AETPC/T/FE
  800 BC =(1.438786*AETPC/T/FE)*(1.0D0-SQRT(BC0))
      IF ( ABS(BC-BC0) .GT. 0.0001D0)  THEN
        BC0=BC
        GOTO 800
      ENDIF
      PLOWK = BC*ZLJ*VIBT*EXPT*FE*FANH*FROT*FINT
      RETURN
      END
C
      SUBROUTINE HIGHPK (T, PREA,QCENT, RECK, HIGHK)
      IMPLICIT DOUBLE PRECISION (A-H,O-Z), INTEGER (I-N)
      COMMON /NUM/ NABS, NAS, NBS, M, NR, NBSTAR
      COMMON /ENERGY/ E0, EE, BE, BOO, AETPC, VRC, EKAB, EKM, DH0
      COMMON /GET/ EZAB, EZA, EZB, D, DEZ, AE0, FRIGID, FANH, PVIBH,
     1             BMORSE, A1, A2, E0AEZ
      COMMON /PARAM/ CDAB, CDM, QEAB, WMAB, WMA, WMB, WMM, QAB, QA,
     1              QB, AKC, BKC, CKC, ADIVB
      COMMON /ACPAR/ VSTAR, CVSTAR
      WMAPB = WMA*WMB/(WMA+WMB)
      PREA  =( 6.6768948D13/SQRT(T*WMAPB**3) ) * (QAB/QA/QB)
C             UNIT:  CM3/MOLE/S
      JMAX= (0.6950304*T / (2.0D0*VSTAR*CVSTAR))**(0.5D0/VSTAR)
      QCENT=0.0D0
      DO 820 J=0, 2*JMAX
```

```
      QCENT = QCENT +
     &   DBLE(2*J+1)*EXP(- CVSTAR*(DBLE(J*(J+1)))**VSTAR/(0.6950304*T))
  820 CONTINUE
      RECK = PREA*QCENT
      CCC = EE**2 /(2.0D0*BOO*DH0)
      IF (NBSTAR .EQ. 1)    FRIGID = 1.0D0 / CCC**(3.0D0/4.0D0)
      IF (NBSTAR .EQ. 2)    FRIGID = 1.0D0 / CCC
      IF (NBSTAR .EQ. 3)    FRIGID = 1.0D0 / CCC**(3.0D0/2.0D0)
      IF (NBSTAR .EQ. 4)    FRIGID = 3.0D0 / (4.0D0*CCC)
      RECK = RECK*FRIGID
C        KC=(AKC)*(T**(BKC))*EXP(-(CKC)/T)       [MOLE/CM3]
      HIGHK=(AKC)*(T**(BKC))*EXP(-(CKC)/T) * RECK
C                                        [HIGHK]=[1/S]
      RETURN
      END
C
      SUBROUTINE FALLOFF(T, BC, CMMC, PLOWK, HIGHK, FLH, F, FCENT, CM,
     1                   FALLK)
      IMPLICIT DOUBLE PRECISION (A-H,O-Z), INTEGER (I-N)
      COMMON /NUM/ NABS, NAS, NBS, M, NR, NBSTAR
      COMMON /ENERGY/ E0, EE, BE, BOO, AETPC, VRC, EKAB, EKM, DH0
      COMMON /GET/ EZAB, EZA, EZB, D, DEZ, AE0, FRIGID, FANH, PVIBH,
     1             BMORSE, A1, A2, E0AEZ
      COMMON /SANDIA/ SA1, SA2, SA3, SA4, SA5, SA6
C
      CM = HIGHK/PLOWK
      CMMC =CMMC/CM
      FLH = CMMC/(1.0D0 + CMMC)
      SK = SA1 + SA2*T/2.0D0 + SA3*T**2/3.0D0
     1                       + SA4*T**3/4.0D0 + SA5*T**4/5.0D0 + SA6/T
C     SK = SK - 0.5D0
C     SK = SK + 0.5D0
      BK =((SK -1.0D0)/DBLE(NABS-1+NR/2)) * (E0AEZ/(0.6950304*T))
      F1 =1.32D0*EXP(-SK/4.2D0) - 0.32D0*EXP(-SK/1.4D0)
      F2 =1.0D0 - EXP(-SK/30.0D0)
      F3 =7.5D0 + 0.43D0*SK
      FCENT = BC**0.14*
     &    (F1+F2*EXP(-BK/19.5D0)+(1.0D0-F1-F2)*EXP(-2.3D0*(BK/F3)**1.5))
      FN = 0.75D0 - 1.27D0*LOG10(FCENT)
      FLOG =LOG10(FCENT)/(1.0D0 +(LOG10(CMMC)/FN)**2)
      F  = 10.0D0**FLOG
      FALLK = FLH*F*HIGHK
      RETURN
      END
```

Appendix 9. Computer Code: Pbpanaly Fortran

This program is the implementation of the analytical models for the point-by-point analysis.

```
      PROGRAM PBPANALY
C     POINT BY POINT ANALYSIS (2CH3=C2H6) ----USING FITTING SIGNAL
      IMPLICIT REAL*8 (A-H,O-Z)
      REAL*8 DEN(1135),DENG(1135),V(1135),TIME(1135),U(1135),P(1135),
     1 ARFA(1135),T(1135),XD(1135),AXISX(1135),TE(40),CK1(40),CK2(40),
     2 CK(1135),F(1135),S(1135),B(1135),RECK1(1135),RECK2A(1135),A(10),
     3 RECK2B(1135),RECK3A(1135),RECK3B(1135),CX(1135),WAY3A(1135),
     4 WAY3B(1135),WBDR(1135),CAFA3(1135),SIGMA3(1135),EA1(1135)
      HAZO(X)=-16340.0D0+25.7372D0*X+0.103687D0*X**2
     1        -2.7678D-5*X**3+2.93112D-9*X**4
      HAR(X)=-6197.454455D0+20.786056D0*X
C     DHR1(X)=134882.4893D0+3.31501D1*X-2.71425494D-2*X**2
C     1        +4.3543D-6*X**3-3.91001D-13*X**4
C     DHR2(X)=-366001.564D0-41.7907D0*X+3.80D-2*X**2-1.19614D-5*X**3
C     1         +1.42457D-9*X**4
      DHR1(X)=155480.9995D0-5.8945D0*X-4.4533468D-3*X**2+1.13534D-8*X**3
     1         +1.01249D-10*X**4
      DHR2(X)=-377244.0639D0-14.4371D0*X+1.4686862D-2*X**2
     1         -3.6277D-6*X**3+3.60466D-10*X**4
      CPN2(X)=26.96997054D0+6.89227D-3*X-1.19D-6*X**2
      CPH3(X)=26.82237579D0+4.340938D-2*X-1.257D-5*X**2+1.26725D-9*X**3
      CPH6(X)=9.2235781D0+1.67673449D-1*X-6.3542D-5*X**2+8.49443D-9*X**3
C     H###,AND DHR# WITH UNIT OF J/MOL ;CP## J/MOL/K
      R=8.314D0
      M=29
      DO 17 I=1,M
      READ(5,*)TE(I),CK1(I),CK2(I)
CK1 (CH3=C2H6) IN UNIT LITER PER MOLE;  CK2 (CH3=C2H4) DEMENSIONLESS
      CK1(I)=CK1(I)/1.0D3
CK1 CONVERTED TO CUBIC METER PER MOLE
 17   CONTINUE
      TEST=5.4
      T0=296.15D0
      XAZO=0.063D0
```

```
      WM0=0.0410905D0
C         KG/MOL
      U0=1658.0D0
C         M/S
      P0=4.0D0
C         TORR
      P0=133.322D0*P0
C         N/SQUARE METER
      N=649
CHOOSE N AND MAKE SURE ABSOLUTE VOLTAGE DECREASED
      DEN0=8.9D-3
      DEN(N)=4.39183D-2
C         KG/CUBIC METER
      ARFA(N)=0.1143349D0
      ARFAPO=2.1865574D0
      BTA=0.180D-3
C         CUBIC METER/KG
      C=9.125D-3
C         1/V/M
      NV=4
C  NV IS THE NUMBER OF THE POLYNOMIAL PARAMETERS
      A(1)=-117.4326530D-3
      A(2)=97.6507119D3
      A(3)=-26.7350786D9
      A(4)=2.4000137D15
C  A(I)S FROM FITTING EQUATION OF VOLTAGE (V) AND TIME (SECOND)
      DT=0.005D-6
C  DT IN UNIT OF SECOND
      INITL=193
C  AT EARLIEST OBSERVABLE POINT
      EA2=0.0D0
C     ACTIVATION ENERGY FOR METHOD 2 (J/MOL)
C**1-CALCULATE DENSITY & ITS GRADIENT AFTER INCIDENT SHOCK WAVE***
      DO 10 I=INITL,N
      TIME(I)=DBLE(I-1)*DT
      V(I)=A(1)
      DO 12 J=2,NV
      V(I)=V(I)+A(J)*TIME(I)**(J-1)
   12 CONTINUE
      DENG(I)=C*U0*V(I)/BTA
   10 CONTINUE
      DO 30 I=INITL,N-1
      DEN(I)=0.0D0
      DO 20 J=1,NV
```

```
      DEN(I)=DEN(I)+A(J)*(TIME(N)**J-TIME(I)**J)/DBLE(J)
   20 CONTINUE
      DEN(I)=DEN(N)-C*U0*DEN(I)/BTA
   30 CONTINUE
      DO 40 I=INITL,N
      XT=DEN0/DEN(I)
      DENG(I)=DENG(I)*XT
      F(I)=-DENG(I)
   40 CONTINUE
C ***************2-POINT BY POINT ANALYSIS **********************
      DO 50 I=INITL,N-1
      XT=DEN0/DEN(I)
      U(I)=U0*XT
      P(I)=P0+DEN0*U0*U0*(1.0D0-XT)
      TRY=XT*(T0+WM0*U0*U0*(1.0D0-XT)/8.314D0)/(1.0D0+2.0D0*XAZO)
   51 ARFA(I)=WM0*U0*U0*(1.0D0-XT**2)/2.0D0/XAZO/DHR2(TRY)
      ARFA(I)=ARFA(I)-DHR1(TRY)/DHR2(TRY)-(HAZO(TRY)-HAZO(T0))/DHR2(TRY)
      ARFA(I)=ARFA(I)-(1.0D0-XAZO)*(HAR(TRY)-HAR(T0))/XAZO/DHR2(TRY)
      ARFA(I)=ARFA(I)/2.0D0
      T(I)=XT*(T0+WM0*U0*U0*(1.0D0-XT)/8.314D0)
      T(I)=T(I)/(1.0D0+2.0D0*XAZO*(1.0D0-ARFA(I)))
      IF(DABS(T(I)-TRY)-0.0005D0)50,50,55
   55 TRY=T(I)
      GOTO 51
   50 CONTINUE
      XT=DEN0/DEN(N)
      U(N)=U0*XT
      P(N)=P0+DEN0*U0*U0*(1.0D0-XT)
      T(N)=XT*(T0+WM0*U0*U0*(1.0D0-XT)/8.314D0)
      T(N)=T(N)/(1.0D0+2.0D0*XAZO*(1.0D0-ARFA(N)))
      DO 90 I=INITL,N
      CX(I)=2.0D0*XAZO*ARFA(I)*(CPH6(T(I))-2.0D0*CPH3(T(I)))
      CX(I)=CX(I)+2.0D0*XAZO*CPH3(T(I))+XAZO*CPN2(T(I))
      CX(I)=CX(I)+20.786D0*(1.0D0-XAZO)
      XT=DEN0/DEN(I)
      B(I)=CX(I)*T(I)+DHR2(T(I))*(1.0D0+2.0D0*XAZO*(1.0D0-ARFA(I)))
      W3=(1.0D0+2.0D0*XAZO*(1.0D0-ARFA(I))-CX(I)/8.314D0)*WM0*(U0*XT)**2
      W4=CX(I)*T(I)*(1.0D0+2.0D0*XAZO*(1.0D0-ARFA(I)))
      B(I)=-2.0D0*XAZO*B(I)/(W3+W4)/DEN(I)
      IF(I.NE.N) S(I)=XT*DLOG(F(I+1)/F(I))/DT
      DO 95 J=2,M
      IF(TE(J).LT.T(I))GOTO 95
      FACTOR=(T(I)-TE(J-1))/(TE(J)-TE(J-1))
      CK(I)=CK1(J-1)*(CK1(J)/CK1(J-1))**(FACTOR*TE(J)/T(I))
```

```
      GOTO 90
 95   CONTINUE
 90   CONTINUE
C  *********** METHOD 1 ***************
      DO 100 I=INITL,N
      W1=2.0D0*XAZO*DEN(I)*(1.0D0-2.0D0*ARFA(I))**2/WM0-ARFA(I)/CK(I)
      AXISX(I)=-B(I)*DEN(I)**2*W1
      RECK1(I)=DENG(I)/AXISX(I)
 100  CONTINUE
C     DO 200 I=INITL,N-1
C     EA1(I)=8.314D0*T(I)*T(I+1)*DLOG(RECK1(I+1)/RECK1(I))/(T(I+1)-T(I))
C     WRITE(6,*)EA1(I)
C200  CONTINUE
C  *********** METHOD 2  ****************
      DO 92 I=INITL,N-2
      W1=ARFAPO+ARFA(N)
      W2=ARFAPO-ARFA(N)
      WAI=B(I)*DEN(I)*DHR2(T(I))/(2.0D0*CK(I)*8.314D0*T(I))
      WBI=DEN(I)/DEN(N)/CK(N)-1.0D0/CK(I)+WAI*W1
      WAI=8.0D0*XAZO*DEN(I)/WM0+WAI
      WCI=F(I)*WM0/(2.0D0*XAZO*B(I)*DEN(I)**3)
      WDI=F(I)*(EA2/8.314D0/T(I)-3.0D0)/DEN(I)-S(I)
C  *********** METHOD 2A ****************
      RECK2A(I)=8.0D0*XAZO*DEN(I)/WM0+1.0D0/CK(I)-2.0D0*WAI*ARFA(I)
      RECK2A(I)=WDI/RECK2A(I)
C  *********** METHOD 2B ****************
      EQA=(WAI*W2+WBI)*(WAI*W2-WBI)
      EQB=WAI**2*WCI-2.0D0*WBI*WDI
      EQC=-WDI**2
      RECK2B(I)=(DSQRT(EQB**2-4.0D0*EQA*EQC)-EQB)/EQA/2.0D0
C  *********** METHOD 3A ****************
      WBDR(I)=B(I)*DEN(N)*(ARFAPO-ARFA(N))+1.0D0
      WAY3A(I)=(ARFAPO-ARFA(I))**WBDR(I)/(ARFA(N)-ARFA(I))
 92   CONTINUE
      DO 110 I=INITL,N-3
      XT=DEN0/DEN(I)
      W4=XT*DLOG(WAY3A(I+1)/WAY3A(I))/DT
      RECK3A(I)=W4*WM0/(8.0D0*XAZO*DEN(N))/(ARFAPO-ARFA(N))
 110  CONTINUE
C  *********** METHOD 3B ****************
      DO 120 I=INITL,N-3
      L=I+1
      TRYK=RECK3A(I)
 122  SIGMA3(I)=(F(I)*WM0/DEN(I)**2/TRYK)/(8.0D0*XAZO*B(I)*DEN(I))
```

```
      W1=ARFAPO+ARFA(N)
      W2=ARFAPO-ARFA(N)
      CAFA3(I)=(W1-DSQRT(W2**2+4.0D0*SIGMA3(I)))/2.0D0
      WAY3B(I)=(ARFAPO-CAFA3(I))**WBDR(I)/(ARFA(N)-CAFA3(I))
      SIGMA3(L)=(F(L)*WM0/DEN(L)**2/TRYK)/(8.0D0*XAZO*B(L)*DEN(L))
      CAFA3(L)=(W1-DSQRT(W2**2+4.0D0*SIGMA3(L)))/2.0D0
      WAY3B(L)=(ARFAPO-CAFA3(L))**WBDR(L)/(ARFA(N)-CAFA3(L))
      XT=DEN0/DEN(I)
      W3=XT*DLOG(WAY3B(L)/WAY3B(I))/DT
      RECK3B(I)=W3*WM0/(8.0D0*XAZO*DEN(N))/(ARFAPO-ARFA(N))
      ERROR=DABS((TRYK-RECK3B(I))/RECK3B(I))
      IF(ERROR-0.001D0)120,121,121
  121 TRYK=RECK3B(I)
      GOTO 122
  120 CONTINUE
      WRITE(6,80) TEST,EA2
      WRITE(6,85)T0,P0/133.322D0,DEN0,U0,XAZO,WM0,BTA
      WRITE(6,86)(A(J),J=1,NV)
      WRITE(6,170)
      WRITE(6,171)
      DO 165 I=INITL,N-2
      WRITE(6,131)TIME(I)*1.0D6,T(I),RECK1(I),RECK2A(I),RECK2B(I),
     1 RECK3A(I),RECK3B(I),SIGMA3(I)
      BONE=DBLE(I-INITL+1)/48.0D0
      BONE=BONE-DBLE(INT(BONE))
      IF(BONE.NE.0.0D0)GOTO 165
      WRITE(6,80) TEST,EA2
      WRITE(6,85)T0,P0/133.322D0,DEN0,U0,XAZO,WM0,BTA
      WRITE(6,86)(A(J),J=1,NV)
      WRITE(6,170)
      WRITE(6,171)
  165 CONTINUE
      WRITE(6,80) TEST,EA2
      WRITE(6,85)T0,P0/133.322D0,DEN0,U0,XAZO,WM0,BTA
      WRITE(6,86)(A(J),J=1,NV)
      WRITE(6,70)
      DO 65 I=INITL,N-1
      WRITE(6,60)TIME(I)*1.0D6,T(I),U(I),DEN(I),P(I),ARFA(I),F(I),S(I),
     1 CX(I),B(I),CAFA3(I)
      BONE=DBLE(I-INITL+1)/49.0D0
      BONE=BONE-DBLE(INT(BONE))
      IF(BONE.NE.0.0D0)GOTO 65
      WRITE(6,80) TEST,EA2
      WRITE(6,85)T0,P0/133.322D0,DEN0,U0,XAZO,WM0,BTA
```

```
      WRITE(6,86)(A(J),J=1,NV)
      WRITE(6,70)
   65 CONTINUE
   60 FORMAT(3G9.4,4G11.4,G10.4,G12.4,G9.4,2G12.4)
  131 FORMAT(8G13.5)
   70 FORMAT(8HTIME(MS),1X,4HT(K),5X,6HU(M/S),5X,8HD(KG/M3),4X,
     17HP(N/M2),4X,4HARFA,4X,10HF(KG/M3/S),3X,6HS(1/S),2X,10HC(J/MOL/K),
     22X,8HB(M3/KG),4X,5HCAFA3)
   80 FORMAT(51HPOINT BY POINT ANALYSIS OF SHOCK TUBE EXPEIMENT NO.,
     1  F3.1,2X,11H(2CH3=C2H6),6H  EA2=,F7.0,8HJ/MOL/K /)
   85 FORMAT(10HINITIAL:  ,F6.2,1HK,2X,F4.1,4HTORR,2X,E9.3,5HKG/M3,2X,
     1 F6.1,3HM/S,2X,5HXAZO=,F6.4,2X,G12.6,6HKG/MOL,2X,5H(BTA=,G8.3,
     2 7H M3/KG))
   86 FORMAT(6HV(V)=(,4G16.8,22H)*(LAB TIME IN SECOND)/)
  170 FORMAT(4X,4HTIME,6X,11HTEMPERATURE,14X,
     1  23HRATE CONSTANT(M3/S/MOL))
  171 FORMAT(2X,9HMICROSEC.,8X,1HK,9X,7HMETHOD1,5X,9HMETHOD 2A,
     1   4X,9HMETHOD 2B,4X,9HMETHOD 3A,4X,9HMETHOD 3B,4X,6HSIGMA3)
      STOP
      END
```

Appendix 10. Computer Code: Dndytlab Fortran

This code is run in conjunction with CHEMKIN-II and the Sandia shock tube code (both as modified by the author of this thesis to calculate the refractive-index-gradient as function of laboratory time for the comparison with laser-schlieren signal).

```
      PROGRAM DNDYTLAB
C
C*****double precision
      IMPLICIT DOUBLE PRECISION (A-H,O-Z), INTEGER (I-N)
C*****END double precision
C*****single precision
C     IMPLICIT REAL (A-H,O-Z), INTEGER (I-N)
C*****END single precision
C
      PARAMETER (NSPEC=100, LIN=5, LOUT=6, LPLOT=88)
      DIMENSION X(NSPEC), DXDT(NSPEC), WTM(NSPEC), BETA(NSPEC)
C
      REWIND( UNIT=LPLOT )
      READ( UNIT=LPLOT, END=100, FMT=200) KK
      READ(LIN,310) ( BETA(K), K=1,KK)
      READ( UNIT=LPLOT, END=100, FMT=300) U0
      DO 818 K1=1,KK,10
        K2=MIN(K1+9,KK)
        READ( UNIT=LPLOT, END=100, FMT=300) (  WTM(K), K=K1,K2 )
  818 CONTINUE
   50 CONTINUE
      READ( UNIT=LPLOT, END=100, FMT=300) TL,DTLDT,RHO,DRHODT,TEMP,PA
      DO 828 K1=1,KK,10
        K2=MIN(K1+9,KK)
        READ( UNIT=LPLOT, END=100, FMT=300) (    X(K), K=K1,K2 )
        READ( UNIT=LPLOT, END=100, FMT=300) ( DXDT(K), K=K1,K2 )
  828 CONTINUE
      SUMXU  = 0.0D0
      SUMXUB = 0.0D0
      SBBUXT = 0.0D0
      DO 20 K = 1, KK
        SUMXU  = SUMXU  + X(K)*WTM(K)
```

```
      SUMXUB = SUMXUB + X(K)*WTM(K)*BETA(K)
20  CONTINUE
    BETAM = SUMXUB/SUMXU
    DO 30 K = 1, KK
      SBBUXT = SBBUXT + (BETA(K)-BETAM)*WTM(K)*DXDT(K)
30  CONTINUE
    DNDY = ( BETAM*DRHODT + RHO*SBBUXT/SUMXU ) / ( U0*DTLDT )
    WRITE(LOUT,400) TL, DNDY, TEMP, PA, RHO
    GOTO 50
100  STOP
200  FORMAT(I3)
300  FORMAT(10(1PE11.3))
310  FORMAT(8(1PE10.3))
400  FORMAT(5(1PE11.3))
     END
```

Appendix 11. Computer Code: Postsens Fortran

This code is run in conjunction with Sandia CHEMKIN-II and SENKIN to calculate sensitivity coefficients with respect to the rate constants of the reactions in the mechanism.

```
      PROGRAM POSTSENS
C
C  THIS PROGRAM WILL WRITE OUT THE SENSITIVITY COEFFICIENTS
C
      IMPLICIT DOUBLE PRECISION (A-H,O-Z), INTEGER (I-N)
C
      PARAMETER (NSPEC=100, NRXN=100, LOUT=6, LSAVE=7, LPAR=5)
      DIMENSION Z(NSPEC, NRXN)
      LOGICAL LSENS
C
      OPEN ( UNIT=LSAVE, STATUS='OLD', FORM='UNFORMATTED',FILE='SAVE$')
      REWIND( UNIT=LSAVE )
      READ ( UNIT=LSAVE, END=100 ) LSENS
C     WRITE( UNIT=LOUT , FMT=150 ) LSENS
      READ ( UNIT=LSAVE, END=100 ) NSYS, KK, II
C     WRITE( UNIT=LOUT , FMT=200 ) NSYS, KK, II
   50 CONTINUE
      READ ( UNIT=LSAVE, END=100 ) TIM, P, Z(1,1)
C     WRITE( UNIT=LOUT , FMT=300 ) TIM, P, Z(1,1)
      DO 818 I1 = 2, NSYS, 10
        I2 = MIN (I1+9, NSYS)
        READ ( UNIT=LSAVE, END=100 ) (Z(I,1), I = I1, I2)
C       WRITE( UNIT=LOUT , FMT=400 ) (Z(I,1), I = I1, I2)
  818 CONTINUE
      IF (LSENS) THEN
        DO 828 J = 2, II+1
          DO 838 I1= 1, NSYS, 10
            I2 = MIN (I1+9, NSYS)
            READ ( UNIT=LSAVE, END=100 )    ( Z(I,J), I=I1, I2)
C           WRITE( UNIT=LOUT , FMT=500 ) J-1,( Z(I,J), I=I1, I2)
  838     CONTINUE
  828   CONTINUE
      ENDIF
C
```

```
         WRITE( UNIT=LPAR, FMT=410) TIM, Z(1,1), Z(3,1)
       DO 808 J1 = 2, II+1, 8
         J2 = MIN (J1+7, II+1)
         WRITE( J1, FMT=450)  (J-2, Z(1,J), J=J1, J2)
       IF(J2 .NE. J1) WRITE( J2, FMT=450)  (J-2, Z(3,J), J=J1, J2)
       IF(J2 .EQ. J1) WRITE( J2+1, FMT=450)  (J-2, Z(3,J), J=J1, J2)
 808   CONTINUE
C
     GOTO 50
 100 CLOSE (LSAVE)
     STOP
 150 FORMAT(A)
 200 FORMAT('Variable No.=', I3, '    Species No.=', I3,
    *       '    Reaction No.=', I3 )
 300 FORMAT('Time =', 1PE12.3, '(s)   Pres =', 1PE12.3,
    *       '(dyne/cm2)   Temp =',1PE12.3, ' (K)' )
 400 FORMAT( 'Y (mass fraction):',   10(1PE12.3))
 410 FORMAT(3(1PE12.3))
 450 FORMAT(8(I4, 1PE12.3))
 500 FORMAT('RXN',I3,10(1PE12.3))
     END
```

REFERENCES

1. J. Warnatz, *18th Symp. (Int.) on Combustion*, The Combustion Institute, Pittsburgh, 1981, p. 369.
2. J. Warnatz, in *Combustion Chemistry*, W. C. Gardiner, Jr., Ed., Springer-Verlag, New York, 1984, p. 197.
3. Y. Hirose, *First International Conference on the New Diamond Science and Technology*, Japan New Diamond Forum, 1988, p. 38.
4. S. Matsumoto, Y. Sato, M. Tsutsumi, and N. Setaka, *J. Mater. Sci.* **17**, 3160 (1982).
5. S. Matsumoto, Y. Sato, M. Kamo, and N. Setaka, *Jap. J. Appl. Phys.* **21**, L183 (1982).
6. M. Murayama, and K. Uchida, *Combustion and Flame* **91**, 239 (1992).
7. E. Meeks, R. J. Kee, D. S. Dandy, and M. E. Coltrin, *Combustion and Flame* **92**, 144 (1993).
8. K. Glanzer, M. Quack, and J. Troe, *Chem. Phys. Letters* **39**, 304 (1976); *16th symp. (Int.) on Combustion*, The Combustion Institute, Pittsburgh, 1976, p. 949.
9. H. Hippler, K. Luther, A. R. Ravishankara, and J. Troe, *Z. Phys. Chem. Neue Folge* **142**, 1 (1984).
10. P. Borrell, C. J. Cobos, A. E. Croce de Cobos, H. Hippler, K. Luther, A. R. Ravishankara, and J. Troe, *Ber. Bunsenges. Phys. Chem.* **89**, 337 (1985).
11. J. M. Roscoe, C. Blatt, and R. A. Back, *Int. J. Chem. Kinet.* **23**, 633 (1991).
12. R. A. Back, *Can. J. Chem.* **61**, 916 (1983).

13. M. T. Macpherson, M. J. Pilling, and M. J. C. Smith, *J. Phys. Chem.* **89**, 2268 (1985); *Chem.Phys. Letters* **94**, 430 (1983).

14. S. M. Hwang, H. Gg. Wagner, and Th. Wolff, *23rd Symp. (Int.) on Combustion*, The Combustion Institute, Pittsburgh, 1990, p.99.

15. W. Moller, E. Mozzhukhin, and H. Gg. Wagner, *Ber. Bunsenges. Phys. Chem.* **90**, 854 (1986).

16. M. Klatt, and H. Gg. Wagner, *Ber. Bunsenges. Phys. Chem.* **93**, 841(1989).

17. W. Moller, E. Mozzhukhin, and H. Gg. Wagner, *Ber. Bunsenges. Phys. Chem.* **91**, 660 (1987).

18. P. Frank, and M. Braun-Unkhoff, *Proc. 16th. Int. Symp. on Shock Tubes and Waves*, Aachen, West Germany, 1987, p.379.

19. P. Frank, *Proc. 15th. Int. Symp. on Rarefied Gas Dynamics*, Grado, B. G. Teubner Stuttgart, 1986, p. 422.

20. D. S. Y. Hsu, W. M. Shaub, T. Creamer, D. Gutman, and M. C. Lin, *Ber. Bunsenges. Phys. Chem.* **87**, 909 (1983).

21. T. C. Clark, T. P. J. Izod, M. A. Di Valentin, and J. E. Dove, *J. Chem. Phys.* **53**, 2982 (1970).

22. V. H. Knoll, K. Scherzer, G. Geiseler, *Z. Phys. Chem. (Leipzig)* **249**, 359 (1972).

23. G. Acs, and A. Peter, *Int. J. Chem. Kinet.* **19**, 929 (1987).

24. D. B. Olson, and W. C. Gardiner, Jr., *Combustion and Flame* **32**, 151 (1978).

25. C. J. Cobos, and J. Troe, *Z. Phys. Chem. Neue Folge* **167**, 129 (1990).

26. A. J. Dean, and R. K. Hanson, *Int. J. Chem. Kinet.* **24**, 517 (1992).

27. M. Frenklach, H. Wang, and M. J. Rabinowitz, *Progr. Energy Comb. Sci.* **18**, 47 (1992).

28. M. Frenklach, and H. Wang, *J. Appl. Phys.* **65**, 5142 (1989).

29. M. Frenklach, and H. Wang, *Phys. Rev.* **B43**, 1520 (1991).

30. M. W. Markus, and P. Roth, *Int. J. Chem. Kinet.* **24**, 433 (1992).

31. J. H. Kiefer, and S. S. Kumaran, *J. Phys. Chem.* **97**, 414 (1993).

32. D. L. Baulch, C. J. Cobos, R. A. Cox, C. Esser, P. Frank, Th. Just, J. A. Kerr, M. J. Pilling, J. Troe, R. W. Walker, and J. Warnatz, *J. Phys. Chem. Ref. Data* **21**, 411 (1992).

33. K. A. Bhaskaran, P. Frank, and Th. Just, *Proc. 12th. Int. Symp. on Shock Tubes and Waves*, Jerusalem, Magnes Press, 1979, p. 503.

34. P. Roth, U. Barner, and R. Lohr, *Ber. Bunsenges. Phys. Chem.* **83**, 929 (1979).

35. A. Merkel, and L. Zulicke, *Mol. Phys.* **60**, 1379 (1987).

36. M. Aoyagi, R. Shepard, A. F. Wagner, T. H. Dunning, Jr., and F. B. Brown, *J. Phys. Chem.* **94**, 3236 (1990).

37. J. Peeters, and C. Vinckier, *15th Symp. (Int.) on Combustion*, The Combustion Institute, Pittsburgh, 1975, p. 969.

38. R. Lohr, and P. Roth, *Ber. Bunsenges. Phys. Chem.* **85**, 153 (1981).

39. J. Grebe, and K. H. Homann, *Ber. Bunsenges. Phys. Chem.* **86**, 581 (1982).

40. T. Bohland, and F. Temps, *Ber. Bunsenges. Phys. Chem.* **88**, 459 (1984); T. Bohland, F. Temps, and H. Gg. Wagner, *J. Phys. Chem.* **91**, 1205 (1987).

41. P. Frank, and K. A. Bhaskaran, *J. Phys. Chem.* **90**, 2226 (1986).

42. J. Troe, *J. Chem. Phys.* **66**, 4745 (1977); **66**, 4758 (1977).

43. J. Troe, *J. Chem. Phys.* **75**, 226 (1981); *22nd Symp. (Int.) on Combustion*, The Combustion Institute, Pittsburgh, 1988, p. 843; *Z. Phys. Chem. Neue Folge* **161**, 209 (1989); C. J. Cobos, and J. Troe, *J. Chem. Phys.* **83**, 1010 (1985).

44. J. Troe, *Ber. Bunsenges. Phys. Chem.* **87**, 161 (1983); R. G. Gilbert, K. Luther, and J. Troe, *Ber. Bunsenges. Phys. Chem.* **87**, 169 (1983).

45. J. Troe, *J. Phys. Chem.* **83**, 114 (1979); in *Combustion Chemistry*, W. C. Gardiner, Jr., Ed., Springer-Verlag, New York, 1984, p. 173.

46. D. L. Baulch, and J. Duxbury, *Combustion and Flame* **37**, 313 (1980).

47. I. R. Slagle, D. Gutman, J. W. Davies, and M. J. Pilling, *J. Phys. Chem.* **92**, 2455 (1988).

48. M. Quack, and J. Troe, *Ber. Bunsenges. Phys. Chem.* **78**, 240 (1974); **79**, 170 (1975); **79**, 469 (1975).

49. D. M. Wardlaw, and R. A. Marcus, *J. Phys. Chem.* **90**, 5383 (1986).

50. A. F. Wagner, and D. M. Wardlaw, *J. Phys. Chem.* **92**, 2462 (1988).

51. D. Walter, H.-H. Grotheer, J. W. Davies, M. J. Pilling, and A. F. Wagner, *23rd Symp. (Int.) on Combustion*, The Combustion Institute, Pittsburgh, 1990, p.107.

52. W. G. Mallard, F. Westley, J. T. Herron, R. F. Hampson, and D. H. Frizzell, *NIST Chemical Kinetics Database - Ver. 5.0*, NIST Standard Reference Data, Gaithersburg, Maryland (1993), and references therein.

53. M. J. Pilling, and V. K. Proudler, *International Reviews in Physical Chemistry*, 1990, Vol. 9, No. 4, p. 329.

54. J. H. Kiefer, and K. A. Budach, *Int. J. Chem. Kinet.* **16**, 679 (1984).

55. P. Roth, and Th. Just, *Ber. Bunsenges. Phys. Chem.* **83**, 577 (1979).

56. W. C. Gardiner, Jr., J. H. Owen, T. C. Clark, J. E. Dove, S. H. Bauer, J. A. Miller, and W. J. McLean, *15th Symp. (Int.) on Combustion*, The Combustion Institute, Pittsburgh, 1975, p. 857.

57. C. C. Chiang, and G. B. Skinner, *J. Phys. Chem.* **85**, 3126 (1981).

58. T. Tsuboi, *Jap. J. Appl. Phys.* **17**, 709 (1978).

59. R. D. Kern, H. J. Singh, and C. H. Wu, *Int. J. Chem. Kinet.* **20**, 731 (1988).

60. Th. Just, *Proc. 13th. Int. Symp. on Shock Tubes and Waves*, Niagara Falls, State University of New York Press, 1981, p.54.

61. Y. Hidaka, T. Nakamura, H. Tanaka, K. Inami, and H. Kawano, *Int. J. Chem. Kinet.* **22**, 701 (1990).

62. M. Brouard, and M. J. Pilling, *Chem.Phys. Letters* **129**, 439 (1986).

63. M. Brouard, M. T. Macpherson, and M. J. Pilling, *J. Phys. Chem.* **93**, 4047 (1989).

64. T. C. Clark, T. P. J. Izod, and G. B. Kistiakowsky, *J. Chem. Phys.* **54**, 1295 (1971).

65. D. B. Olson, T. Tanzawa, and W. C. Gardiner, Jr., *Int. J. Chem. Kinet.* **11**, 23 (1979).

66. J. M. Simmie, W. C. Gardiner, Jr., and C. S. Eubank, *J. Phys. Chem.* **86**, 799 (1982).

67. J. H. Kiefer,and R. W. Lutz, *J. Chem. Phys.* **44**, 658 (1966)

68. J. H. Kiefer, M. Z. Al-Alami, and K. A. Budach, *J. Phys. Chem.* **86**, 808 (1982).

69. J. H. Kiefer, and A. C. Manson, *Rev. Sci. Instrum.* **52**, 1392 (1981).

70. J. H. Kiefer, and J. C. Hajduk, *Proc. 12th. Int. Symp. on Shock Tubes and Waves*, Jerusalem, The Magnes Press, 1980, p.97.

71. J. E. Dove and H. Teitelbaum, *Chem. Phys.* **6**, 431 (1974)

72. T. Tanzawa, and W. C. Gardiner, Jr., *Combustion and Flame* **39**, 241(1980).

73. J. H. Kiefer, S. A. Kapsalis, M. Z. Al-Alami, and K. A. Budach, *Combustion and Flame* **51**, 79 (1983).

74. K. Tabayashi, and S. H. Bauer, *Combustion and Flame* **34**, 63 (1979).

75. R. K. Hanson, *Proc. 19th. Int. Symp. on Shock Tubes and Waves*, Marseille, France, 1994, p.000. (in press)

76. K. J. Laidler, *Chemical Kinetics*, 3rd ed., Harper & Row, Publishers, New York, 1987, p. 152.

77. J. O. Hirschfelder, C. F. Curtiss, and R. B. Bird, *Molecular Theory of Gases and Liquids*, 2nd ed., Wiley, London, 1963.

78. R. C. Reid, and T. K. Sherwood, *The Properties of Gases and Liquids*, 2nd ed., McGraw-Hill, New York, 1966.

79. M. Damm, H. Hippler, H. A. Olschewski, J. Troe, and J. Willner, *Z. Phys. Chem. Neue Folge* **166**, 129 (1990).

80. M. Heymann, H. Hippler, D. Nahr, H. J. Plach, and J. Troe, *J. Phys. Chem.* **92**, 5507 (1988).

81. M. Heymann, H. Hippler, H. J. Plach, and J. Troe, *J. Chem. Phys.* **87**, 3867 (1987).

82. M. Heymann, H. Hippler, and J. Troe, *J. Chem. Phys.* **80**, 1853 (1984).

83. R. J. Kee, G. Dixon-Lewis, J. Warnatz, M. E. Coltrin, and J. A. Miller, *A Fortran Computer Code Package for the Evaluation of Gas-Phase Multicomponent Transport Properties*, Sandia Report SAND86-8246 UC-401, September 1991.

84. M. E. Jacox, *J. Phys. Chem. Ref. Data* **19**, 1387 (1990); **17**, 269 (1988); **13**, 945 (1984).

85. M. W. Chase, Jr., C. A. Davies, J. R. Downey, Jr., D. J. Frurip, R. A. McDonald, and A. N. Syverud, *JANAF Thermochemical Tables* (3rd edition), *J. Phys. Chem. Ref. Data* **14**, Suppl.1 (1985); D. Stull and H. Prophet, *JANAF Thermochemical Tables*, 2nd. ed. NBS, Washington (1971).

86. J. Troe, *Combustion and Flame* **78**, 59 (1989).

87. C. J. Cobos, and J. Troe, *Chem. Phys. Letters* **113**, 419 (1985).

88. R. J. Kee, F. M. Rupley, and J. A. Miller, *The Chemkin Thermodynamic Data Base*, Sandia Report SAND87-8215B UC-4, February 1992.

89. J. N. White, and W. C. Gardiner, Jr., *J. Phys. Chem.* **83**, 562 (1979).

90. A. Peter, and G. Acs, *Kinetics and Catalysis* **27**, 189 (1986).

91. Y. Paquin, and W. Forst, *Int. J. Chem. Kinet.* **5**, 691 (1973).

92. P. C. Durban, and R. M. Marshall, *Int. J. Chem. Kinet.* **12**, 1031 (1980).

93. K. M. Pamidimukkala, D. Rogers, and G. B. Skinner, *J. Phys. Chem. Ref. Data* **11**, 83 (1982).

94. N. C. Craig, M. N. Ackermann, and R. A. MacPhail, *J. Chem. Phys.* **68**, 236 (1978).

95. T. Shimanouchi, *J. Phys. Chem. Ref. Data* **6**, 993 (1977).

96. M. N. Ackermann, J. J. Burdge, and N. C. Craig, *J. Chem. Phys.* **58**, 203 (1973).

97. C. F. Melius, *Heats of Formation and Free Energies*, Sandia National Laboratories, 1993.

98. P. W. Seakins, S. H. Robertson, M. J. Pilling, I. R. Slagle, G. W. Gmurczyk, A. Bencsura, D. Gutman, and W. Tsang, *J. Phys. Chem.* **97**, 4450 (1993).

99. A. G. Gaydon, and I. R. Hurle, *The Shock Tube In High-Temperature Chemical Physics*, Chapman and Hall Ltd., London, 1963.

100. J. K. Wright, *Shock Tubes*, Wiley, New York, 1961, p. 40.

101. J. Z. Su, and H. Teitelbaum, *Proc. 19th. Int. Symp. on Shock Tubes and Waves*, Marseille, France, 1994, p.000.(in press)

102. Z. Cheng, *Ph. D. Thesis*, University of Ottawa, 1993.

103. D. N. S. Permann, *Ph. D. Thesis*, University of Ottawa, 1993.

104. J. Z. Su, and H. Teitelbaum, *Int. J. Chem. Kinet.* **26**, 159 (1994).

105. J. E. Dove, W. S. Nip and H. Teitelbaum, *Proc. 15th Internat. Symp. on Combustion*, The Combustion Institute, Pittsburgh, (1975), p. 903

106. R. C. Weast, ed., *Handbook of Chemistry and Physics*, CRC Press, Cleveland, 1974, p.E222; 70th edition (1989 - 1990), p. E-383.

107. H. Mirels, *Physics of Fluids* **6**, 1201 (1963).

108. Y. S. Touloukian, S. C. Saxena, and P. Hestermans, *Viscosity, Thermophysical Properties of Matter*, IFI/Plenum, New York, Vol. 11, p. 5 and p. 51.

109. W. Tsang, and R. F. Hampson, *J. Phys. Chem. Ref. Data* **15**, 1087 (1986).

110. Th. Just, P. Roth, and R. Damm, *16th Symp. (Int.) on Combustion*, The Combustion Institute, Pittsburgh, 1977, p. 961.

111. P. H. Stewart, C. W. Larson, and D. M. Golden, *Combustion and Flame* **75**, 25 (1989).

112. T. Bohland, F. Temps, and H. Gg. Wagner, *Ber. Bunsenges. Phys. Chem.* **90**, 486 (1986).

113. J. A. Kerr, and M. J. Parsonage, *Evaluated Kinetic Data on Gas Phase Hydrogen Transfer Reactions of Methyl Radicals*, Butterworths, London, 1976.

114. T. C. Clark, and J. E. Dove, *Can. J. Chem.* **51**, 2147 (1973).

115. W. Tsang, *J. Phys. Chem. Ref. Data* **20**, 221 (1991).

116. D. L. Baulch, D. D. Drysdale, D. G. Horne, and A. C. Lloyd, *Evaluated Kinetic Data for High Temperature Reactions*, vol. 1: *Homogeneous Gas phase Reactions of the H_2 - O_2 System*, Butterworths, London, 1972.

117. T. Bohland, S. Dobe, F. Temps, and H. Gg. Wagner, *Ber. Bunsenges. Phys. Chem.* **89**, 1110 (1985).

118. J. A. Kerr, and M. J. Parsonage, *Evaluated Kinetic Data on Gas Phase Addition Reactions*, Butterworths, London, 1972.

119. P. M. Holt, and J. A. Kerr, *Int. J. Chem. Kinet.* **9**, 185 (1977).

120. R. J. Kee, F. M. Rupley, and J. A. Miller, *Chemkin-II: A Fortran Chemical Kinetics Package for the Analysis of Gas Phase Chemical Kinetics*, Sandia Report SAND89-8009B·UC-706, April 1992.

121. A. C. Hindmarsh, *LSODE and LSODI: Two New Initial Value Differential Equation Solvers, ACM Signum Newsletter* **15**, No. 4, December 1980.

122. R. E. Mitchell, and R. J. Kee, *A General Purpose Computer Code for Predicting Chemical Behavior behind Incident and Reflected Shocks*, Sandia Report SAND82-8205·UC-401, February 1992.

123. W. C. Gardiner, Jr., Y. Hidaka, and T. Tanzawa, *Combustion and Flame* **40**, 213 (1981).

124. A. E. Lutz, R. J. Kee, and J. A. Miller, *Senkin: A Fortran Program for Predicting Homogeneous Gas Phase Chemical Kinetics with Sensitivity Analysis*, Sandia Report SAND87-8248·UC-401, February 1991.

125. J. T. Yardley, *Introduction to Molecular Energy Transfer*, Academic Press, New York, 1980.

126. J. Shi, and J. R. Barker, *Int. J. Chem. Kinet.* **22**, 187 (1990).

127. J. E. Dove, and J. Troe, *Chem. Phys.* **35**, 1 (1978).

128. J. H. Kiefer, S. S. Kumaran, and S. Sundaram, *"Vibrational Relaxation, Dissociation, and Dissociation Incubation Times in Norbornene", Third International Conference on Chemical Kinetics*, Gaithersburg, USA, July 12-16, 1993.

129. J. H. Kiefer, and J. N. Shah, *J. Phys. Chem.* **91**, 3024 (1987).

130. W. D. Breshears, P. F. Bird, and J. H. Kiefer, *J. Chem. Phys.* **55**, 4017 (1971).

131. G. Yahav, Y. Haas, B. Carmeli, and A. Nitzan, *J. Chem. Phys.* **72**, 3410 (1980).

132. J. E. Dove, and H. Teitelbaum, *Proc. 11th. Int. Symp. on Shock Tubes and Waves*, University of Washington Press, Seattle, 1978, p. 474.

133. J. H. Kiefer, in *Shock Waves in Chemistry*, A. Lifshitz, Ed., Marcel Dekker, New York, 1981, p. 219.

134. J. A. Barnard, and T. K. Parrott, *J. Chem. Soc., Faraday Trans. I* **72**, 2404 (1976).

135. Y. Hidaka, T. Chimori, S. Shiba, and M. Suga, *Chem. Phys. Letters* **111**, 181 (1984).

136. D. F. Davidson, M. D. Di Rosa, R. K. Hanson, and C. T. Bowman, *Int. J. Chem. Kinet.* **25**, 969 (1993).

137. N. H. Packard, J. P. Crutchfield, J. D. Farmer, and R. S. Shaw, *Phys. Rev. Lett.* **45**, 712 (1980).

138. J. M. T. Thompson, and H. B. Stewart, *Nonlinear Dynamics and Chaos*, John Wiley & Sons, Chichester, 1986.

139. S. Vohra, M. Spano, M. Shlesinger, L. Pecora, and W. Ditto (eds.), *Proc. 1st Experimental Chaos Conference*, World Scientific, Singapore, 1992.

140. J. D. Lambert, and R. Salter, *Proc. Roy. Soc.* **253A**, 277 (1959); T. L. Cottrell, and J. C. McCoubrey, *Molecular Energy Transfer in Gases*, Butterworths, London, 1961, p. 111; R. Holmes, G. R. Jones, and N. Pusat, *J. Chem. Phys.* **41**, 2512 (1964); A. S. Kozhevnikov, and V. F. Yakovlev, *Russ. J. Phys. Chem.* **56**, 1254 (1982).

141. J. A. Miller, and C. F. Melius, *Combustion and Flame* (in press).

142. K. Y. Lee, M. H. Yang, and I. K. Puri, *Combustion and Flame* **92**, 419 (1993).

143. K. Y. Lee, and I. K. Puri, *Combustion and Flame* **94**, 191 (1993).

144. M. S. Gordon, T. N. Truong, and J. A. Pople, *Chem. Phys. Lett.* **130**, 245 (1986).

145. L. Teng, and W. E. Jones, *J. Chem. Soc., Faraday Trans. I* **68**, 1267 (1972).

146. A. M. Bass, and A. H. Laufer, *Int. J. Chem. Kinet.* **5**, 1053 (1973).

147. H. E. Van den Bergh, *Chem. Phys. Letters* **43**, 201 (1976).

148. A. M. Held, K. C. Manthorne, P. D. Pacey, and H. P. Reinholdt, *Can. J. Chem.* **55**, 4128 (1977).

149. A. Sepehrad, R. M. Marshall, and H. Purnell, *J. Chem. Soc., Faraday Trans. I* **75**, 835 (1979).

150. I. S. Zaslonko, and V. N. Smirnov, *Kinetics and Catalysis* **20**, 575 (1979).

151. P. D. Pacey, and J. H. Wimalasena, *J. Phys. Chem.* **84**, 2221 (1980).

152. N. L. Arthur, and C. Anastasi, *Bull. Soc. Chim. Belg.* **92**, 647 (1983).

153. N. L. Arthur, and J. C. Biordi, *Aust. J. Chem.* **39**, 1257 (1986).

154. P. D. Pacey, and J. H. Wimalasena, *Chem. Phys. Letters* **53**, 593 (1978).

155. C. Anastasi, and N. L. Arthur, *J. Chem. Soc., Faraday Trans. II* **83**, 277 (1987).

156. R. Gomer, and G. B. Kistiakowsky, *J. Chem. Phys.* **19**, 85 (1951).

157. A. Shepp, *J. Chem. Phys.* **24**, 939 (1956).

158. P. Kebarle, *J. Phys. Chem.* **67**, 351 (1963).

159. E. V. Waage, and B. S. Rabinovitch, *Int. J. Chem. Kinet.* **3**, 105 (1971).

160. M. P. Halstead, D. A. Leathard, R. M. Marshall, and J. H. Purnell, *Proc. Roy. Soc. London A* **316**, 575 (1970).

January 3, 1994

To Whom It May concern:

I, the author of the Ph.D. thesis "Studies of the Kinetics of Cluster Redistribution in CCl_3F Vapours", Chemistry Department, University of Ottawa, authorize Mr. (Joseph) Zhichun Su to use and to revise Figures 2.1.4 and 2.1.7 of my Ph.D. thesis for his Ph.D. thesis entitled "The Kinetics of the Decay of Methyl Radicals at High Temperatures".

Zhikai Cheng

Zhikai Cheng

United States Department of Commerce
National Institute of Standards & Technology

Dr. W. Gary Mallard, Research Chemist
Chemical Kinetics and Thermodynamics Division
Bldg 222 Rm. A-260
Gaithersburg,MD 20899

Bitnet gmallard@nbsenh
Internet gmallard@enh.nist.gov
Phone: (301)-975-2564
FAX: (301)-926-4513

Joseph Zhichun Su
Chemistry Department
10 Marie Curie
PO Box 450 Stn A
University of Ottawa
Ottawa, ON K1N 6N5
CANADA

Dear Mr. Su:

Any graph that you generate from the NIST Chemical Kinetics Database may be used in the publication of your thesis or any other publication. The only requirement is that the origin of the data be properly given. The reference for the database is available by selecting Credits/Citation on the main menu. For the current version - version 5 the citation is

W.G.Mallard, F.Westley, J.T.Herron, R.F.Hampson, and D.H.Frizzell
NIST Chemical Kinetics Database - Ver. 5.0
NIST Standard Reference Data, Gaithersburg,MD (1993).

The citation is as if the database is a book, and NIST Standard Reference Data is the publisher. You will probably have to change the format slightly to conform with the standards of the university. Please note that the exact authorship does change from version to version.

Sincerely